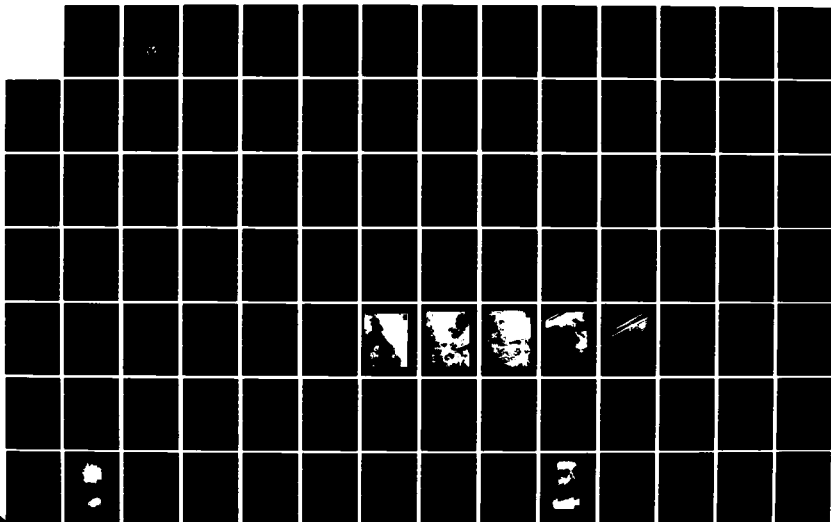


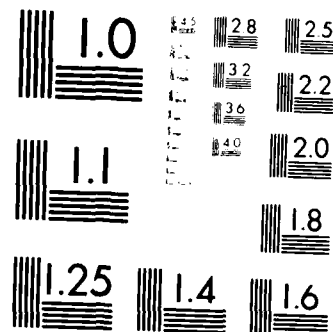
AD-A152 047

FUNDAMENTAL STUDIES OF GROWTH DOPING AND TRANSFORMATION 1/2
IN BETA SILICON C. (U) NORTH CAROLINA STATE UNIV AT
RALEIGH DEPT OF MATERIALS ENGINE. R F DAVIS ET AL

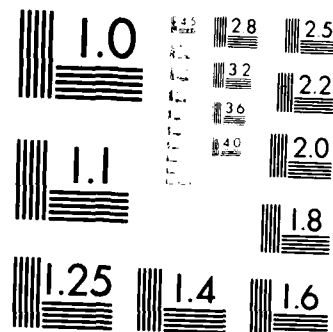
UNCLASSIFIED

20 FEB 85 NCSU-243-043-006 N00014-84-K-0182 F/G 20/12 NL





MICROCOPY RESOLUTION TEST CHART
NATIONAL BUREAU OF STANDARDS-1963-A



MICROCOPY RESOLUTION TEST CHART
NATIONAL BUREAU OF STANDARDS-1963-A

AD-A152 047

DTIC FILE COPY

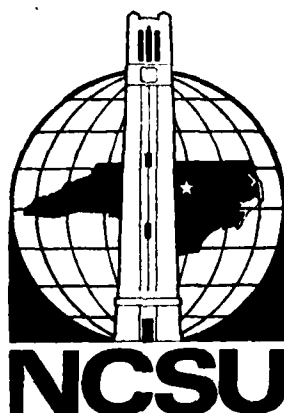
Final Technical Report

on

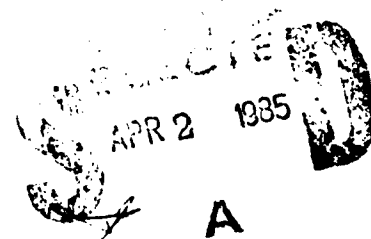
FUNDAMENTAL STUDIES OF GROWTH, DOPING AND TRANSFORMATION
IN BETA SILICON CARBIDE

Supported by ONR Under Contract N00014-82-K-0182

For the Period February 1, 1982 - January 31, 1985



School of Engineering
North Carolina State University
Raleigh, North Carolina



This document has been approved
for release and sale, its
distribution is unlimited.

AD-A152 047

DTIC FILE COPY

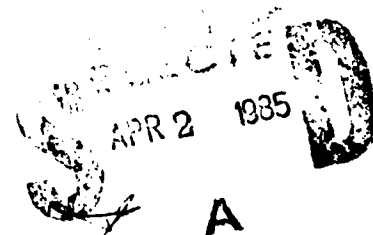
Final Technical Report

on

FUNDAMENTAL STUDIES OF GROWTH, DOPING AND TRANSFORMATION
IN BETA SILICON CARBIDE

Supported by ONR Under Contract N00014-82-K-0182

For the Period February 1, 1982 - January 31, 1985



School of Engineering
North Carolina State University
Raleigh, North Carolina

This document has been approved
for release and sale, its
distribution is unlimited.

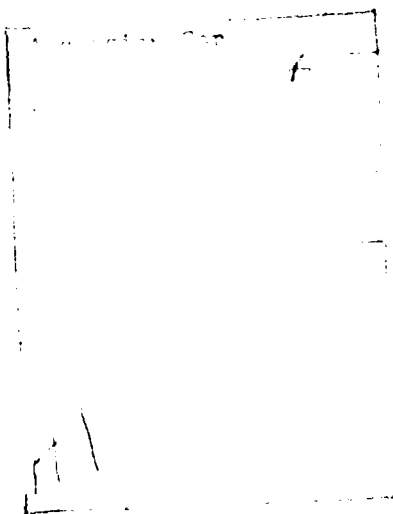
Final Technical Report

on

FUNDAMENTAL STUDIES OF GROWTH, DOPING AND TRANSFORMATION
IN BETA SILICON CARBIDE

Supported by ONR Under Contract N00014-82-K-0182

For the Period February 1, 1982 - January 31, 1985



REPORT DOCUMENTATION PAGE		READ INSTRUCTIONS BEFORE COMPLETING FORM
1. REPORT NUMBER	2. GOVT ACCESSION NO.	3. RECIPIENT'S CATALOG NUMBER
243-043-006	AD-A152 647	
4. TITLE and Subtitle	5. TYPE OF REPORT & PERIOD COVERED	

REPORT DOCUMENTATION PAGE		READ INSTRUCTIONS BEFORE COMPLETING FORM
1. REPORT NUMBER 243-043-006	2. GOVT ACCESSION NO. AD-A152 647	3. RECIPIENT'S CATALOG NUMBER
4. TITLE and Subtitle Fundamental Studies of Growth, Doping and Transformation in Beta Silicon Carbide	5. TYPE OF REPORT & PERIOD COVERED Final Technical Report	
6. AUTHOR Robert F. Davis P. H. Giedelmaier	8. CONTRACT OR GRANT NUMBER N00014-82-K-0182	
7. PERFORMING ORGANIZATION NAME AND ADDRESS North Carolina State University Dept. of Materials Engineering P. O. Box 7907, Raleigh, NC 27695-7907	10. PROGRAM ELEMENT, PROJECT, TASK AREA & WORK UNIT NUMBERS EP 1153.1 EP 021-02-03 NR 043-027	
11. CONTROLLING OFFICE NAME AND ADDRESS OSD-427 Arlington, VA 22217	12. REPORT DATE February 20, 1985	13. NUMBER OF PAGES 153
14. MONITORING AGENCY NAME & ADDRESS (if different from Controlling Office)	16. SECURITY CLASS. (of this report) Unclassified	
15a. DECLASSIFICATION/DOWNGRADING SCHEDULE		
15. DISTRIBUTION STATEMENT (of this Report) Approved for public release; distribution unlimited		
17. DISTRIBUTION STATEMENT (of the abstract entered in Block 20, if different from Report)		
18. SUPPLEMENTARY NOTES NOTES: 1. This report contains information that is not to be released to the public. 2. This report is for internal use only.		
19. KEY WORDS (Continue on reverse side if necessary and identify by block number) silicon carbide ion implantation Raman spectroscopy chemical vapor deposition thermodynamics oxidation electronic materials TEM Schottky diode in situ doping secondary ion mass spectroscopy p-n junction electrical properties MOS device		
20. ABSTRACT (Continue on reverse side if necessary and identify by block number) During this three-year granting period, the growth and characterization of high purity and high quality 3-SiC thin films has reached a highly sophisticated level. This report details the CVD growth and in situ doping and the thermodynamic considerations thereof as well as ion implantation; SIMS, TEM, Auger, Raman and electrical characterization; ohmic contact studies; oxidation experiments and the fabrication of Schottky barrier diodes and p-n junctions.		

TABLE OF CONTENTS

	<u>Page No.</u>
I. INTRODUCTION.	3
II. GROWTH AND IN SITU DOPING OF BETA-SiC	5
A. Introduction.	5
B. Growth of β -SiC Films	5
1. Modifications to CVD Growth System.	5
2. Thin Film Growth.	9
C. In Situ Doping of β -SiC Thin Films Experimental . . .	10
D. In Situ Doping of β -SiC Thin Films - Theoretical Considerations	36
1. Introduction.	36
2. Free Energies of Formation of the Dopant Gases. .	36
3. Free Energy Minimization Calculations and the Determination of the Gas Species Present .	38
4. Equilibrium Solubility Considerations and Measured Concentrations of Dopants in SiC Thin Films	42
5. Dopant Partial Pressures, Resultant Chemical Concentrations and Electronic Carrier Concentrations in β -SiC.	48
III. CROSS-SECTIONAL TRANSMISSION ELECTRON MICROSCOPY OF β -SiC FILMS.	57
IV. OTHER CANDIDATE SUBSTRATE MATERIALS FOR THE GROWTH OF β -SiC	64
V. REMOVAL OF THE Si SUBSTRATE	66
VI. ELECTRICAL AND RAMAN CHARACTERIZATION - EQUIPMENT AND STUDIES ON THE UNDOPED β -SiC FILMS	67
A. Equipment Employed in this Research for Electrical Characterization	67
B. Ohmic Contact Studies	67
C. Studies of the Effect of the Presence of the Buffer Layer and the Si Substrate on Values of the Electrical Measurements.	68
D. Raman Spectroscopy and Hall Effect Measurements and Their Employment in the Study of the Study of the Effects of Annealing on the Electrical Properties of the As-Grown, Undoped β -SiC Films	70
E. Effects of Annealing on the Surface Properties of β -SiC	72
VII. PREPARATION OF β -SiC FILMS FOR IMPLANTATION, OXIDATION AND DEVICE FABRICATION	79

TABLE OF CONTENTS

	<u>Page No.</u>
I. INTRODUCTION.	3
II. GROWTH AND IN SITU DOPING OF BETA-SiC	5
A. Introduction.	5
B. Growth of β -SiC Films	5
1. Modifications to CVD Growth System.	5
2. Thin Film Growth.	9

	<u>Page No.</u>
VIII. ION IMPLANTATION AND ANNEALING.	83
A. Overview.	83
B. Experiments in Ion Implantation and Annealing of β -SiC	83
1. Introduction.	83
2. Results and Discussion.	95
a. Phosphorous and Aluminum Implants	85
b. Nitrogen and Boron Implants	107
IX. OXIDATION STUDIES	115
X. PLASMA ETCHING STUDIES.	137
XI. DEVICE FABRICATION.	141
A. P-N Junction.	141
B. Schottky Diode.	144
C. Future Devices.	144
XII. REFERENCES.	150
APPENDIX I.	151
APPENDIX II	152
APPENDIX III.	153

I. INTRODUCTION

Silicon carbide is the only compound species that exists in the solid state in the Si-C system and can occur in the cubic (C), hexagonal (H) or rhombohedral (R) structures. It is also classified as existing in the beta and alpha modifications. The beta, or cubic,

II. GROWTH AND IN SITU DOPING OF BETA-SiC

A. Introduction

The principal objectives of this aspect of the program during this reporting period were the reproducible growth of semiconductor quality β -SiC thin films on Si by CVD and the development and employment of techniques for the incorporation of electronically active dopants during growth (in situ doping). The various research avenues required to achieve these goals are described in the following subsections.

B. Growth of β -SiC Films

1. Modifications to CVD Growth System

In the area of CVD, high quality films were achieved near the end of the previous grant; however, they were somewhat difficult to reproduce for several reasons. In the original design, flow monitors and control valves for the SiH_4 and C_2H_4 were of a size which controlled only between 2 and 100 sccm and for the H_2 between 20 and 1000 sccm. However, theoretical research by Kingon, Liaw, Lutz and Davis¹ concerning CVD phase diagrams in the Si-C system as a function of total pressure, composition and temperature as well as recent articles concerning the fundamentals of CVD have validated our own recent experience that very low flow rates of SiH_4 and C_2H_4 and a much higher flow rate of H_2 are necessary to make high quality epitaxial thin films. To this end new flow monitors and valves as well as a larger H_2 purifier were installed.

A schematic of the modified CVD system is shown in Figure 1. The labeled parts are denoted on the following page. Major portions of this system have remained the same as that described in detail in a previous ONR document (See Annual Report #243-027-009 [for the period 1 Jan. 1980 - 31 Dec. 1980] for ONR Grant #N00014-79-C-0121); thus, a description of these areas will not be presented in this report. The newly added or modified portions are shown within the dashed lines; only those aspects will be described below.

Major modifications to the chamber and pumping system were made as well as the incorporation of new lines for additional p-type

layer, ion implantation and annealing studies, oxidation studies, electrical measurements and development of simple devices.

This final report provides a summary of the experimental procedures, the results and a discussion of these results derived from research in the aforementioned topic areas for the three-year period February 1, 1982 - January 31, 1985.

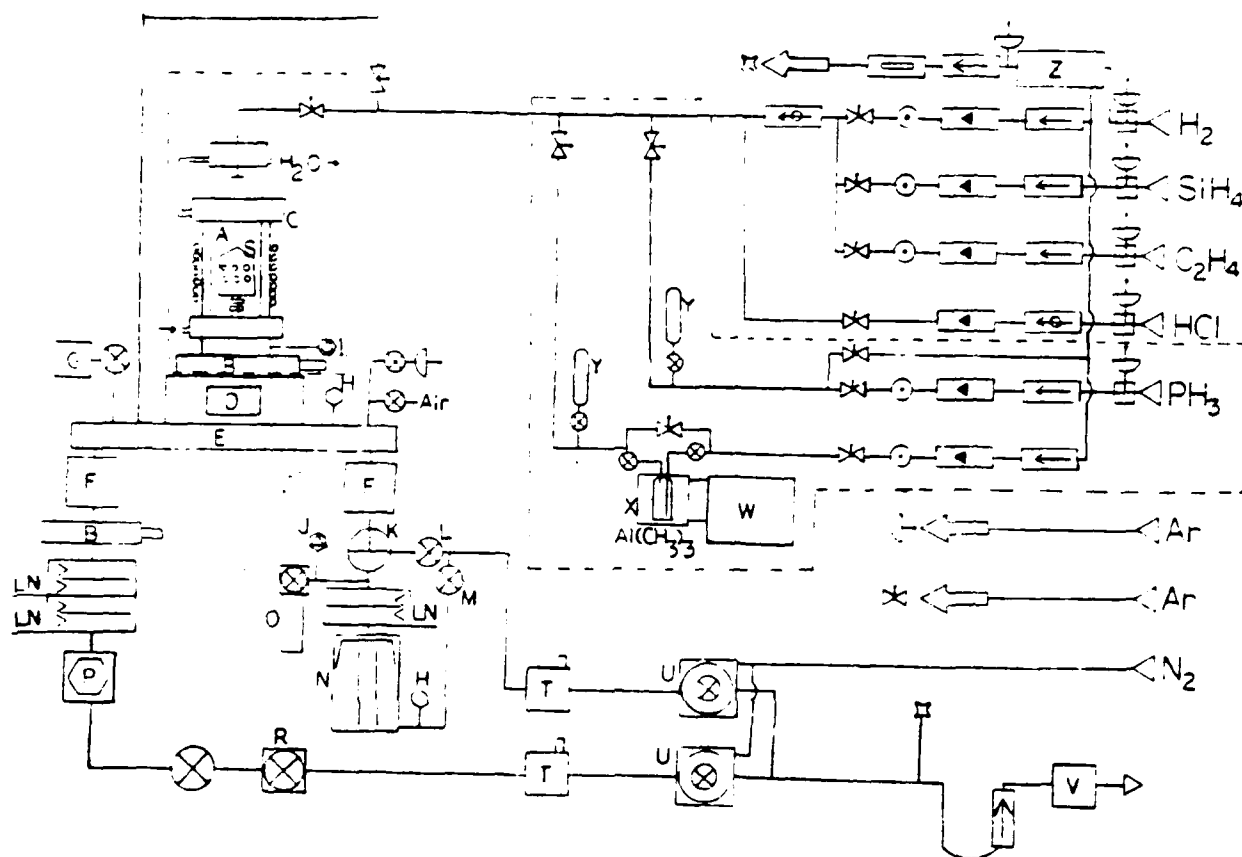


Figure 1. Schematic of NCSU chemical vapor deposition equipment for the growth of β -SiC thin films. Dashed lines denote recently installed portions, as described in the text. Symbols are defined on the following page.

II. GROWTH AND IN SITU DOPING OF BETA-SiC

A. Introduction

The principal objectives of this aspect of the program during this reporting period were the reproducible growth of semiconductor quality β -SiC thin films on Si by CVD and the development and employment of techniques for the incorporation of electronically active dopants during growth (in situ doping). The various research avenues required to achieve these goals are described in the following subsections.

B. Growth of β -SiC Films

1. Modifications to CVD Growth System

In the area of CVD, high quality films were achieved near the end of the previous grant; however, they were somewhat difficult to reproduce for several reasons. In the original design, flow monitors and control valves for the SiH_4 and C_2H_4 were of a size which controlled only between 2 and 100 sccm and for the H_2 between 20 and 1000 sccm. However, theoretical research by Kingon, Liaw, Lutz and Davis¹ concerning CVD phase diagrams in the Si-C system as a function of total pressure, composition and temperature as well as recent articles concerning the fundamentals of CVD have validated our own recent experience that very low flow rates of SiH_4 and C_2H_4 and a much higher flow rate of H_2 are necessary to make high quality epitaxial thin films. To this end new flow monitors and valves as well as a larger H_2 purifier were installed.

A schematic of the modified CVD system is shown in Figure 1. The labeled parts are denoted on the following page. Major portions of this system have remained the same as that described in detail in a previous ONR document (See Annual Report #243-027-009 [for the period 1 Jan. 1980 - 31 Dec. 1980] for ONR Grant #N00014-79-C-0121); thus, a description of these areas will not be presented in this report. The newly added or modified portions are shown within the dashed lines; only those aspects will be described below.

Major modifications to the chamber and pumping system were made as well as the incorporation of new lines for additional p-type

Nomenclature for Symbols on Figure 1.

- A. RF-heated CVD reaction chamber
- F. Automatic valve to chamber
- C. Water cooling jacket
- D. Door for loading chamber
- E. Stainless steel chamber
- F. Particle trap
- G. Baratron pressure sensor
- H. Thermocouple vacuum gage
- I. Convectron vacuum gage
- J. Ionization vacuum gage
- K. Manual gate valve
- L. Roughing valve
- M. Foreline valve
- N. Diffusion pump
- O. Residual gas analyzer chamber
- P. Liquid collection chamber
- R. Automatic butterfly valve
- S. Substrates and susceptor
- T. Molecular shieve trap
- U. Mechanical pump
- V. Bunsen burner
- W. Refrigerated circulating bath
- X. Cooling bath for $\text{Al}(\text{CH}_3)_3$ bottle
- Y. Sampling bottle
- Z. Hydrogen purifier

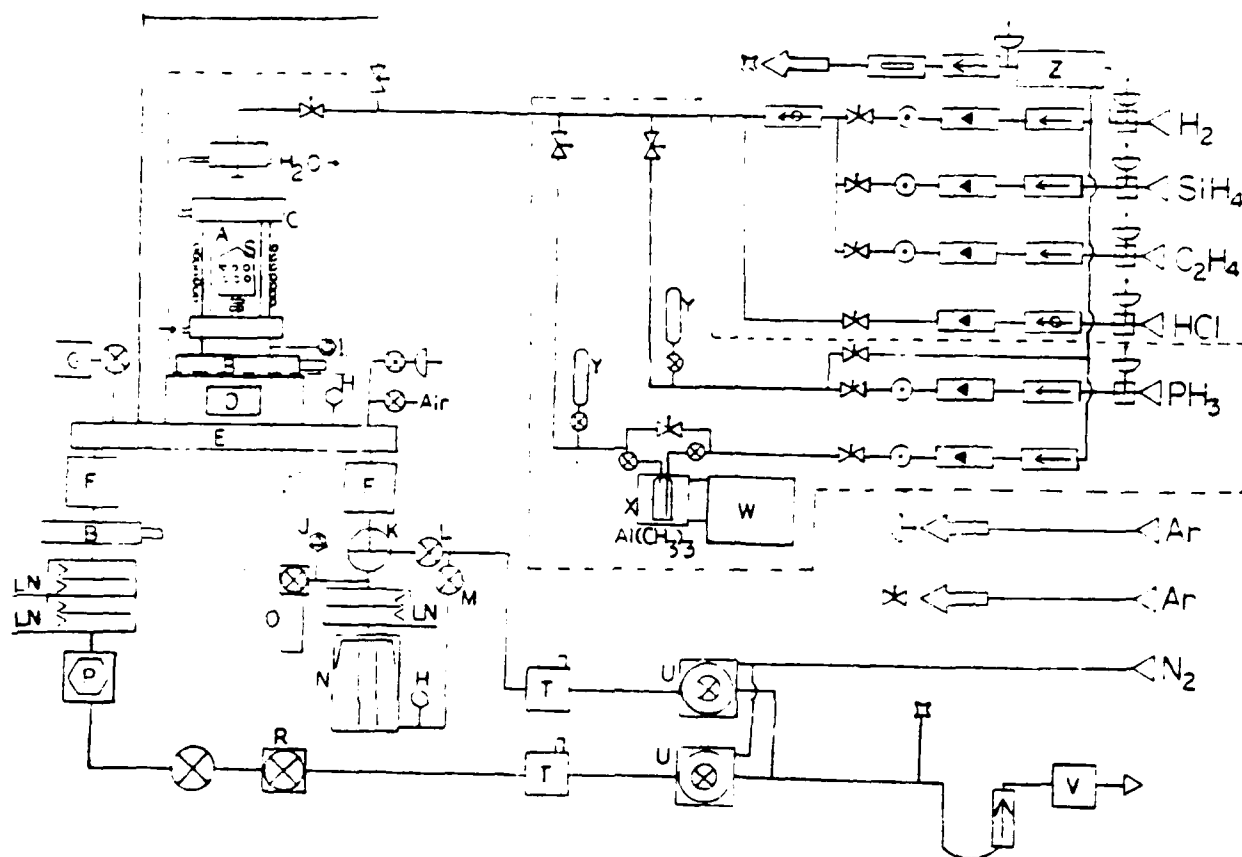


Figure 1. Schematic of NCSU chemical vapor deposition equipment for the growth of β -SiC thin films. Dashed lines denote recently installed portions, as described in the text. Symbols are defined on the following page.

doping with Al (from the vapor of $\text{Al}(\text{CH}_3)_3$ entrained in H_2) and n-type doping with P or N (from a very dilute mixture of PH_3 or NH_3 H_2). In order to maintain a constant vapor pressure of $\text{Al}(\text{CH}_3)_3$, a very accurate (± 0.01 K) "constant" temperature bath was installed. Each type of dopant has a separate line containing the same elements of check valve, flow meter, flow control valve and line shut-off valve as are present in the reactant and carrier gas lines of SiH_4 , C_2H_4 and H_2 . However, an additional gas-collection bottle (part Y in Figure 1) is attached to each of the dopant lines. Each of these bottles can be detached from the line and attached directly to a gas chromatograph mass spectrometer in order to analyze the concentration of the dopant in the line.

The external part of the reactor chamber was also completely modified in order to achieve both more efficient cooling and the ability to vary the distance between the reactant gas entry tube and the SiC-coated graphite susceptor (and thus the Si wafers). Several susceptors of different shapes and sizes were designed and employed in order to determine the optimum configuration for the growth of the best films.

Concerning this last point, because of differences in thickness of the β -SiC films grown in the top portion of the susceptor relative to those in the middle of the susceptor and the formation of an undesirable amount of SiC on the top of the susceptor, several design changes were made, particularly in the length and taper of the very top of this most important item of the reactor system. The final result is both a lengthened susceptor wherein the very upper portion is above the top of the r-f coil in order to more gradually heat and control the dynamics of the flow of the incoming gas stream and a modified entry port on the gas inlet tube so that the gas does not directly impinge on the top cone of the susceptor.

Finally, a residual gas analyzer was connected to the system in order to determine the presence of impurities in the reactant and dopant gases as well as absorbed gases in the chamber, and

Nomenclature for Symbols on Figure 1.

- A. RF-heated CVD reaction chamber
- B. Automatic valve to chamber
- C. Water cooling jacket
- D. Door for loading chamber
- E. Stainless steel chamber
- F. Particle trap
- G. Baratron pressure sensor
- H. Thermocouple vacuum gage
- I. Convectron vacuum gage
- J. Ionization vacuum gage
- K. Manual gate valve
- L. Roughing valve
- M. Foreline valve
- N. Diffusion pump
- O. Residual gas analyzer chamber
- P. Liquid collection chamber
- R. Automatic butterfly valve
- S. Substrates and susceptor
- T. Molecular shieve trap
- U. Mechanical pump
- V. Bunsen burner
- W. Refrigerated circulating bath
- X. Cooling bath for $\text{Al}(\text{CH}_3)_3$ bottle
- Y. Sampling bottle
- Z. Hydrogen purifier

a larger H_2 purifier was placed in operation in order to allow higher flow rates of this gas.

2. Thin Film Growth

Many different deposition conditions, of which three are given in Table I below, were employed to determine the optimum CVD conditions for the growth of semiconductor quality films. An angle lapping technique was also developed for the determination of the thickness of the various films. A broken piece of each analyzed sample is waxed onto a beveled block and lapped on a frosted-glass plate using $0.25 \mu m$ diamond paste. The morphologies of the as-grown final surfaces of the films produced under the conditions noted in Table I varied markedly. The surface of sample #82115 had the appearance of a fine grain size polycrystalline material (although x-ray analysis showed it to be monocrystalline); while, #821029 had a very smooth surface even at 400X. The surface of sample #821028 was mottled in appearance but smooth in texture. It became obvious that the slightly lowered pressure produces the smoothest surface but also the slowest rate of deposition.

Table I. Examples of Deposition Conditions for the CVD Growth of β -SiC Thin Films

Sample #	Substrate	Gas flow Conditions	Deposition Temp. ($^{\circ}C$)	Deposition Time (S)	Deposition Rate ($\mu m/hr$)
821115	(100) Silicon	760 torr 3000 SCCM H_2 2 SCCM SiH_4 1 SCCM C_2H_4	1600K	120	2.0 $\mu m/hr$
821029	(100) Silicon	380 torr 3000 SCCM H_2 2 SCCM SiH_4 1 SCCM C_2H_4	1600K	120	1.65 $\mu m/hr$
821028	(100) Silicon	760 torr 4000 SCCM H_2 2 SCCM SiH_4 1 SCCM C_2H_4	1600K	180	2.63 $\mu m/hr$

The conditions of one atmosphere total pressure coupled with the highest H_2 flow rate allow the most rapid growth rate because more

doping with Al (from the vapor of $\text{Al}(\text{CH}_3)_3$ entrained in H_2) and n-type doping with P or N (from a very dilute mixture of PH_3 or NH_3 H_2). In order to maintain a constant vapor pressure of $\text{Al}(\text{CH}_3)_3$, a very accurate (± 0.01 K) "constant" temperature bath was installed. Each type of dopant has a separate line containing the same elements of check valve, flow meter, flow control valve and line shut-off valve as are present in the reactant and carrier gas lines of SiH_4 , C_2H_4 and H_2 . However, an additional gas-collection bottle (part Y in Figure 1) is attached to each of the dopant lines. Each of these bottles can be detached from the line and attached directly to a gas chromatograph mass spectrometer in order to analyze the concentration of the dopant in the line.

The external part of the reactor chamber was also completely modified in order to achieve both more efficient cooling and the ability to vary the distance between the reactant gas entry tube and the SiC-coated graphite susceptor (and thus the Si wafers). Several susceptors of different shapes and sizes were designed and employed in order to determine the optimum configuration for the growth of the best films.

Concerning this last point, because of differences in thickness of the α -SiC films grown in the top portion of the susceptor relative to those in the middle of the susceptor and the formation of an undesirable amount of SiC on the top of the susceptor, several design changes were made, particularly in the length and taper of the very top of this most important item of the reactor system. The final result is both a lengthened susceptor wherein the very upper portion is above the top of the r-f coil in order to more gradually heat and control the dynamics of the flow of the incoming gas stream and a modified entry port on the gas inlet tube so that the gas does not directly impinge on the top cone of the susceptor.

Finally, a residual gas analyzer was connected to the system in order to determine the presence of impurities in the reactant and dopant gases as well as absorbed gases in the chamber, and

reactant passes the samples per unit time. Additional information on these topics is provided in the March 1983 Annual Letter Report ONR #243-043-0102.

C. In Situ Doping of β -SiC Thin Films Experimental

A limited number of studies have been conducted to investigate the incorporation of electronically active impurities in β -SiC using CVD techniques. Bartlett², Long³ and Nishino⁴ obtained p-type β -SiC by adding B_2H_6 or $AlCl_3$ during the β -SiC growth, while n-type β -SiC was produced without doping. In addition Von Muench⁵ doped polycrystalline β -SiC by adding trimethylaluminum (TMA) to the solution used for bulk crystal growth via the Van Arkel process.

During this reporting period, one of the thrust areas in this growth-related research program has also been the experimental determination of the proper dopant gases, dopant gas/ H_2 ratios and flow rates for the incorporation of B or Al and P or N as p- and n-type dopants, respectively, for the future fabrication of devices. Theoretical considerations of this process are presented in the next subsection.

In this study the dopant substances were incorporated directly in the primary gas stream containing SiH_4 , C_2H_4 and H_2 for the chemical vapor deposition of β -SiC. The dopant hydride gases of PH_3 and B_2H_6 contained in H_2 were employed as sources of P and B, respectively. Nitrogen in H_2 was formerly considered as a potential n-type dopant; however, no incorporation of this element in SiC at or above the $10^{17}/cm^3$ (the minimum detectable limit with the CAMECA ims-3f ion microprobe) was produced even using high flow rates of N_2 . However, ammonia (NH_3) has been recently used as the source of N and found to work very well in this capacity in our process. Finally liquid trimethylaluminum (TEA) used in Japan) because (1) the methyl radical is much more stable to decomposition with the subsequent formation of unwanted C than the ethyl radical and (2) the boiling point of the TMA (293K) is lower than that of the TEA (409K). The concentration in the gas stream is altered by changing the flow rate of H_2 over the TMA. The concentrations in H_2 of all the dopant gases currently being investigated and their respective purities are given in Table II.

a larger H_2 purifier was placed in operation in order to allow higher flow rates of this gas.

2. Thin Film Growth

Many different deposition conditions, of which three are given in Table I below, were employed to determine the optimum CVD conditions for the growth of semiconductor quality films. An angle lapping technique was also developed for the determination of the thickness of the various films. A broken piece of each analyzed sample is waxed onto a beveled block and lapped on a frosted-glass plate using $0.25 \mu m$ diamond paste. The morphologies of the as-grown final surfaces of the films produced under the conditions noted in Table I varied markedly. The surface of sample #82115 had the appearance of a fine grain size polycrystalline material (although x-ray analysis showed it to be monocrystalline); while, #821029 had a very smooth surface even at 400X. The surface of sample #821028 was mottled in appearance but smooth in texture. It became obvious that the slightly lowered pressure produces the smoothest surface but also the slowest rate of deposition.

Table I. Examples of Deposition Conditions for the CVD Growth of β -SiC Thin Films

Sample #	Substrate	Gas flow Conditions	Deposition Temp. ($^{\circ}C$)	Deposition Time (S)	Deposition Rate ($\mu m/hr$)
821115	(100) Silicon	760 torr 3000 SCCM H_2 2 SCCM SiH_4 1 SCCM C_2H_4	1600K	120	2.0 $\mu m/hr$
821029	(100) Silicon	380 torr 3000 SCCM H_2 2 SCCM SiH_4 1 SCCM C_2H_4	1600K	120	1.65 $\mu m/hr$
821028	(100) Silicon	760 torr 4000 SCCM H_2 2 SCCM SiH_4 1 SCCM C_2H_4	1600K	180	2.63 $\mu m/hr$

The conditions of one atmosphere total pressure coupled with the highest H_2 flow rate allow the most rapid growth rate because more

Table II. Concentrations and purities of gases employed as electrically active dopants during the CVD growth of β -SiC.

Dopant Gases	Bottle Concentrations	Purity
Phosphine (PH_3)	4900 ppm (in H_2)	99.9995%(VLSI) Grade
Diborane (B_2H_6)	53.0 ppm (in H_2)	99.9995%(VLSI) Grade
	2500 ppm (in H_2)*	99.9995%(Electronic) Grade
Ammonia (NH_3)	483 ppm (in H_2)	99.9995%(Nitride) Grade
Trimethylaluminum [$(\text{CH}_3)_3\text{Al}$]	Liquid source at room temperature	99.9995%

*The higher concentration B_2H_6 in H_2 has been ordered to increase the boron concentration in β -SiC.

The introduction (or lack of it) of these dopants into the β -SiC films has been analyzed quantitatively as a function of depth using the ion microprobe. Analyses of the dopant/Si ratios of ion implanted standards throughout the concentration range of the asymmetric implant profile results in linear curves of the dopant/Si ratio versus concentration which can be used to quantitatively determine the concentration of a species in the "in-situ" doped films of β -SiC. The depth profiles for Si and N, Si and P, Si and Al and Si and B are given in figures 2-23. The quantitative results from the ion microprobe analyses coupled with use of the aforementioned linear curves to give values of concentration are presented in Table III.

The N^+ SIMS profiles derived from the in situ doping of N_2 in H_2 are shown in Figs. 2 and 3. In both cases, the concentrations in the SiC are not above background ($\sim 10^{17}$ atoms/cc) for this instrument. Even increasing the flow rate to 100 sccm did not move the concentration off background. As such the dopant gas was changed to that of NH_3 in H_2 , the resultant profiles of which are shown in Figs. 4-7. At low flow rates of this gas, the concentration in the β -SiC film remains at or below background as shown in Fig. 4. Increasing the flow rates to 30 and 6 sccm, respectively, showed concomitant increases in the N^+ concentration (See Figs. 5 and 6). However, no further increase occurred in this concentration at the increased flow rate of 9 sccm,

reactant passes the samples per unit time. Additional information on these topics is provided in the March 1983 Annual Letter Report ONR #243-043-0102.

C. In Situ Doping of β -SiC Thin Films Experimental

A limited number of studies have been conducted to investigate the incorporation of electronically active impurities in β -SiC using CVD techniques. Bartlett², Long³ and Nishino⁴ obtained p-type β -SiC by adding B_2H_6 or $AlCl_3$ during the β -SiC growth, while n-type β -SiC was produced without doping. In addition Von Muench⁵ doped polycrystalline β -SiC by adding trimethylaluminum (TMA) to the solution used for bulk crystal growth via the Van Arkel process.

During this reporting period, one of the thrust areas in this growth-related research program has also been the experimental determination of the proper dopant gases, dopant gas/ H_2 ratios and flow rates for the incorporation of B or Al and P or N as p- and n-type dopants, respectively, for the future fabrication of devices. Theoretical considerations of this process are presented in the next subsection.

In this study the dopant substances were incorporated directly in the primary gas stream containing SiH_4 , C_2H_4 and H_2 for the chemical vapor deposition of β -SiC. The dopant hydride gases of PH_3 and B_2H_6 contained in H_2 were employed as sources of P and B, respectively. Nitrogen in H_2 was formerly considered as a potential n-type dopant; however, no incorporation of this element in SiC at or above the $10^{17}/cm^3$ (the minimum detectable limit with the CAMECA ims-3f ion microprobe) was produced even using high flow rates of N_2 . However, ammonia (NH_3) has been recently used as the source of N and found to work very well in this capacity in our process. Finally liquid trimethylaluminum (TEA) used in Japan) because (1) the methyl radical is much more stable to decomposition with the subsequent formation of unwanted C than the ethyl radical and (2) the boiling point of the TMA (293K) is lower than that of the TEA (409K). The concentration in the gas stream is altered by changing the flow rate of H_2 over the TMA. The concentrations in H_2 of all the dopant gases currently being investigated and their respective purities are given in Table II.

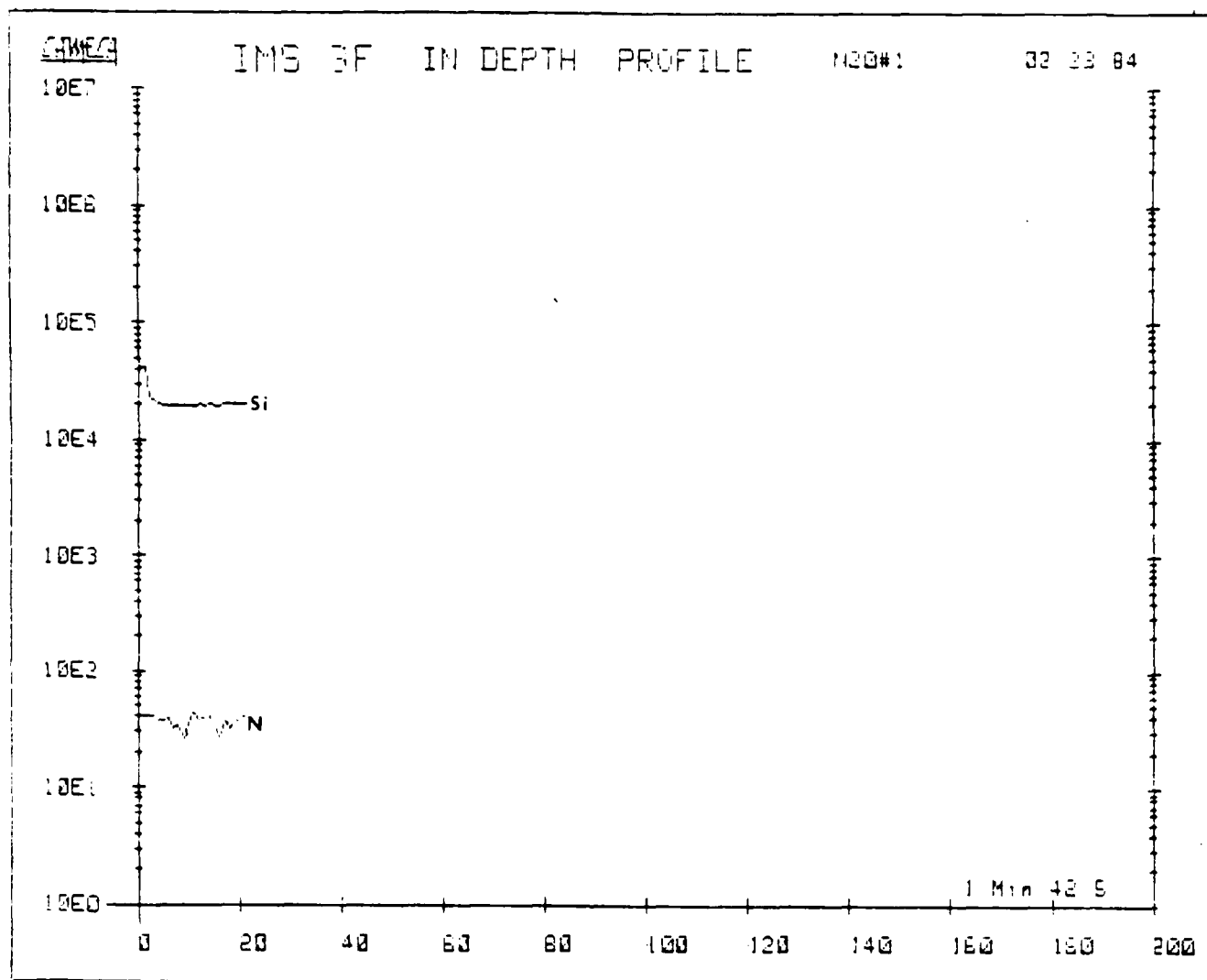


Figure 2. SIMS depth profile of N^+ in situ doped in a β -SiC film using N_2 in H_2 at a flow rate of 20 sccm.

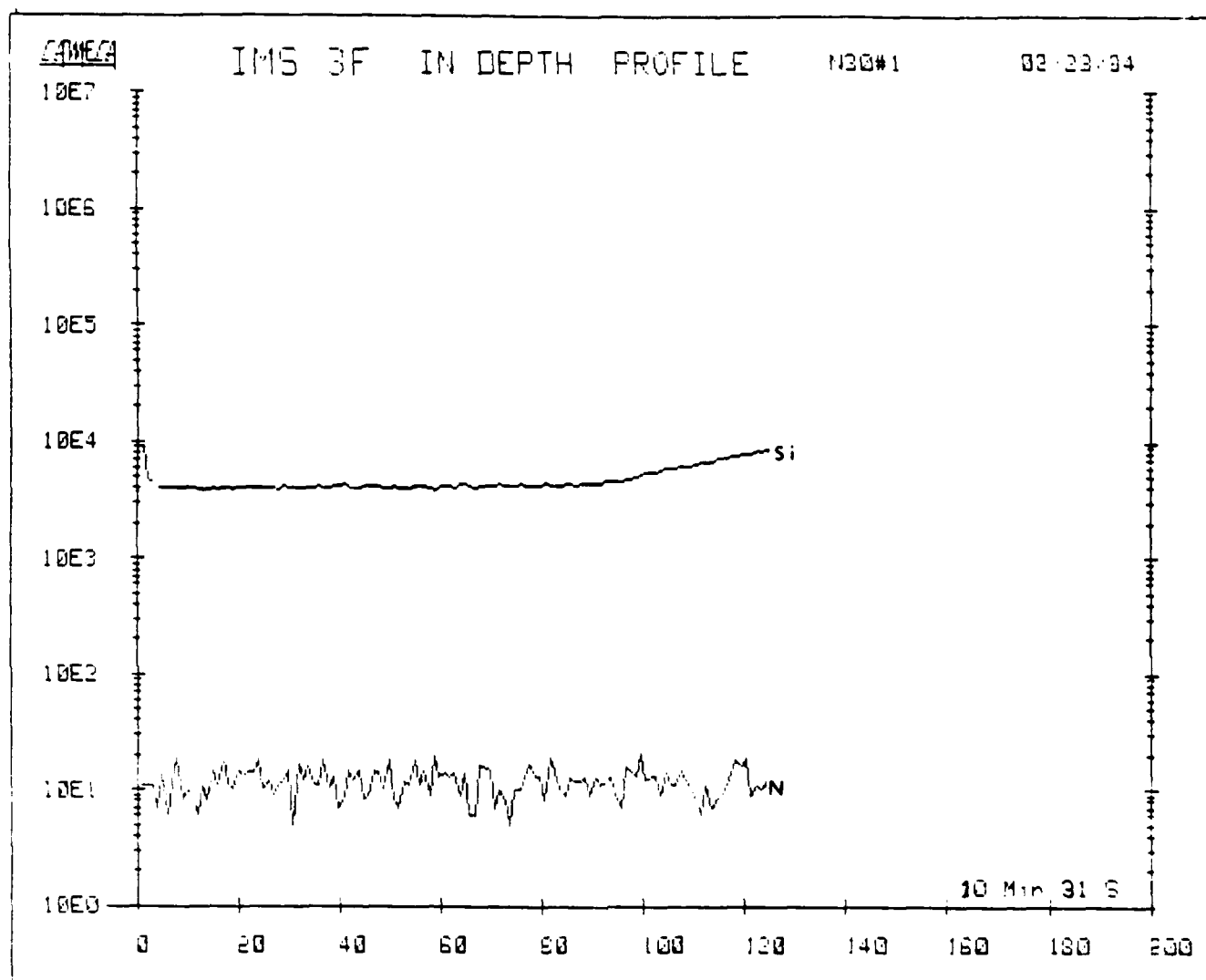


Figure 3. SIMS depth profile of N^+ in situ doped in a β -SiC film using N_2 and H_2 at a flow rate of 30 sccm.

Table II. Concentrations and purities of gases employed as electrically active dopants during the CVD growth of β -SiC.

Dopant Gases	Bottle Concentrations	Purity
Phosphine (PH_3)	4900 ppm (in H_2)	99.9995% (VLSI) Grade

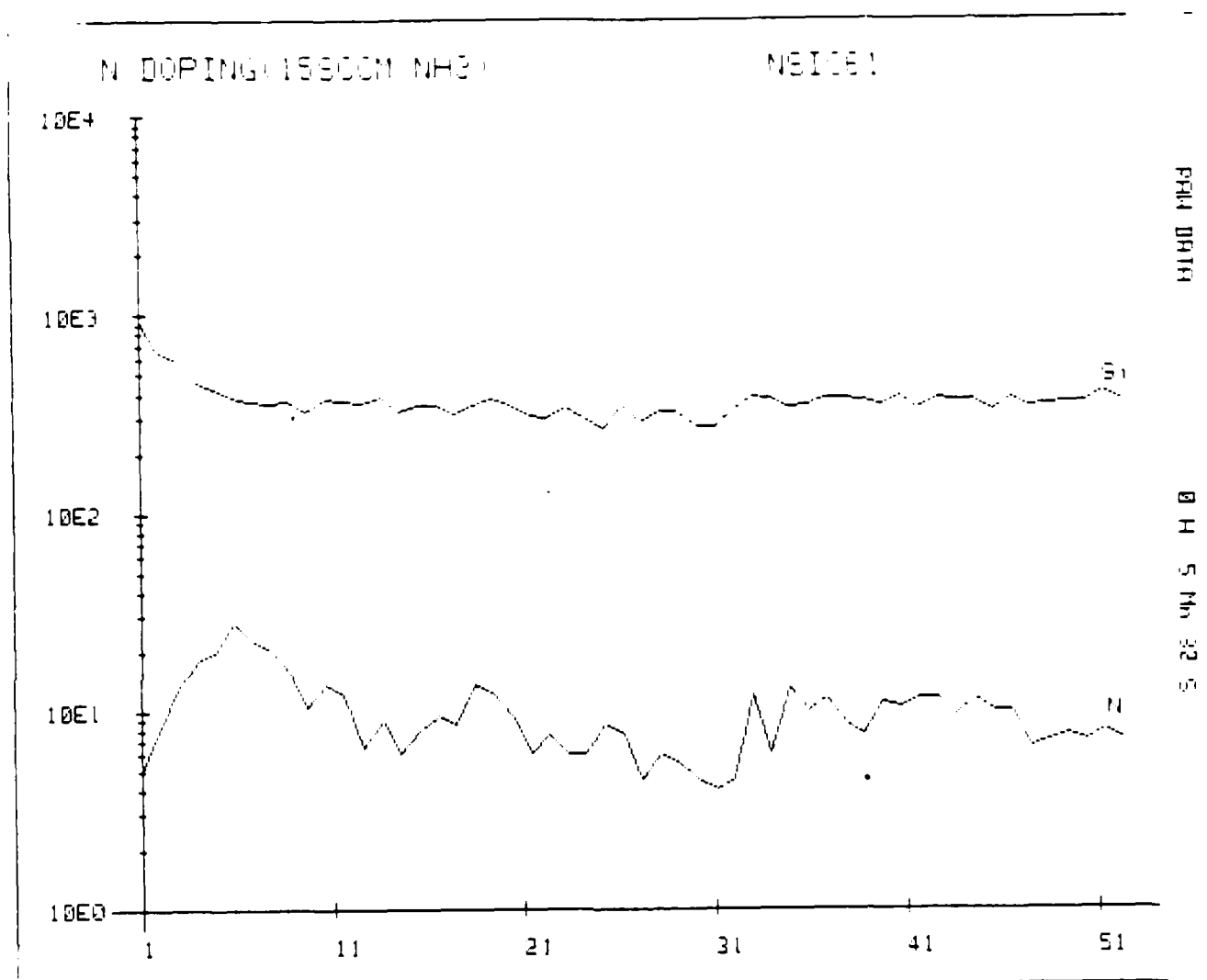


Figure 4. SIMS depth profile of N⁺ in situ doped in a -SiC film using NH₃ in H₂ at a flow rate of 15 sccm.

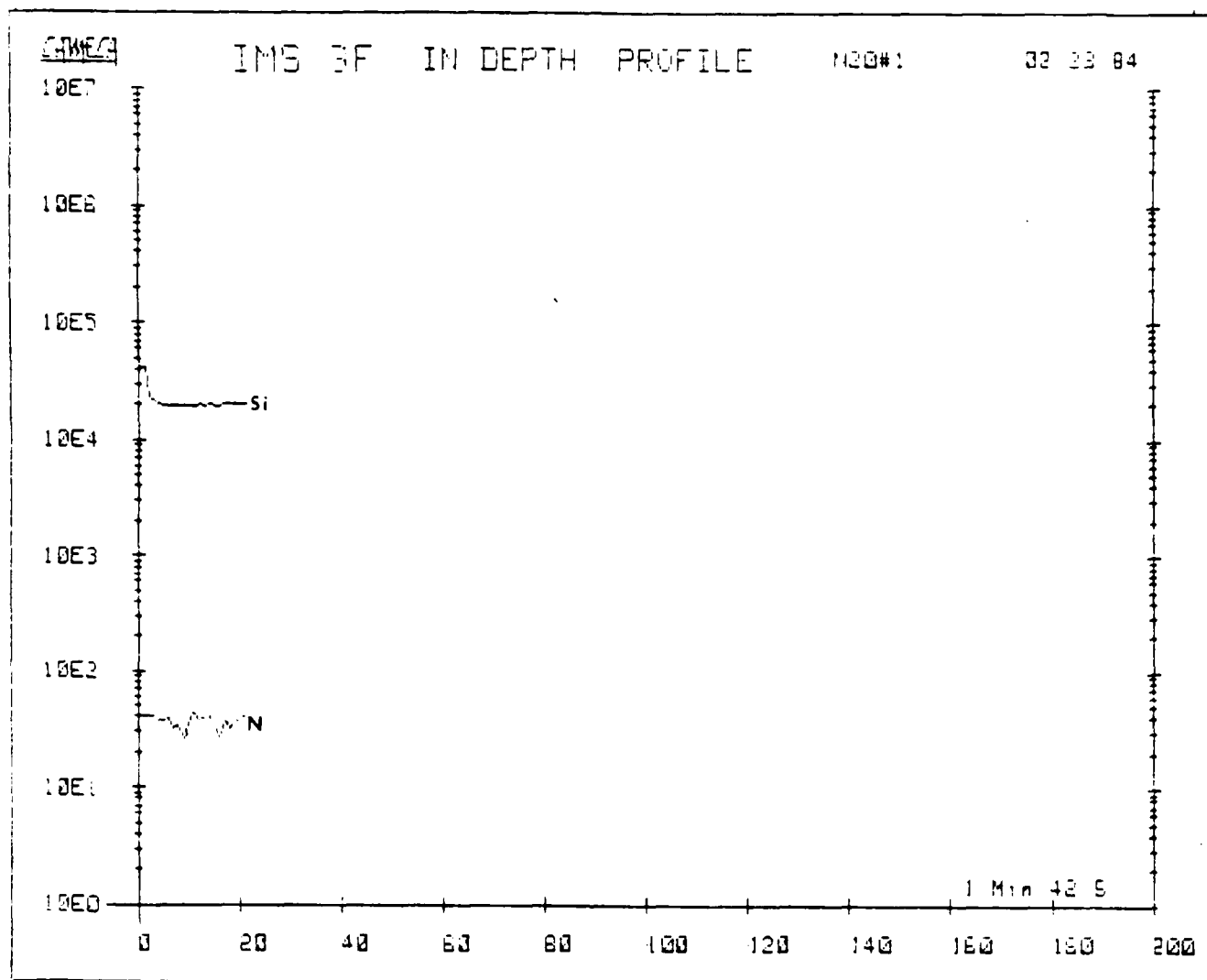


Figure 2. SIMS depth profile of N^+ in situ doped in a β -SiC film using N_2 in H_2 at a flow rate of 20 sccm.

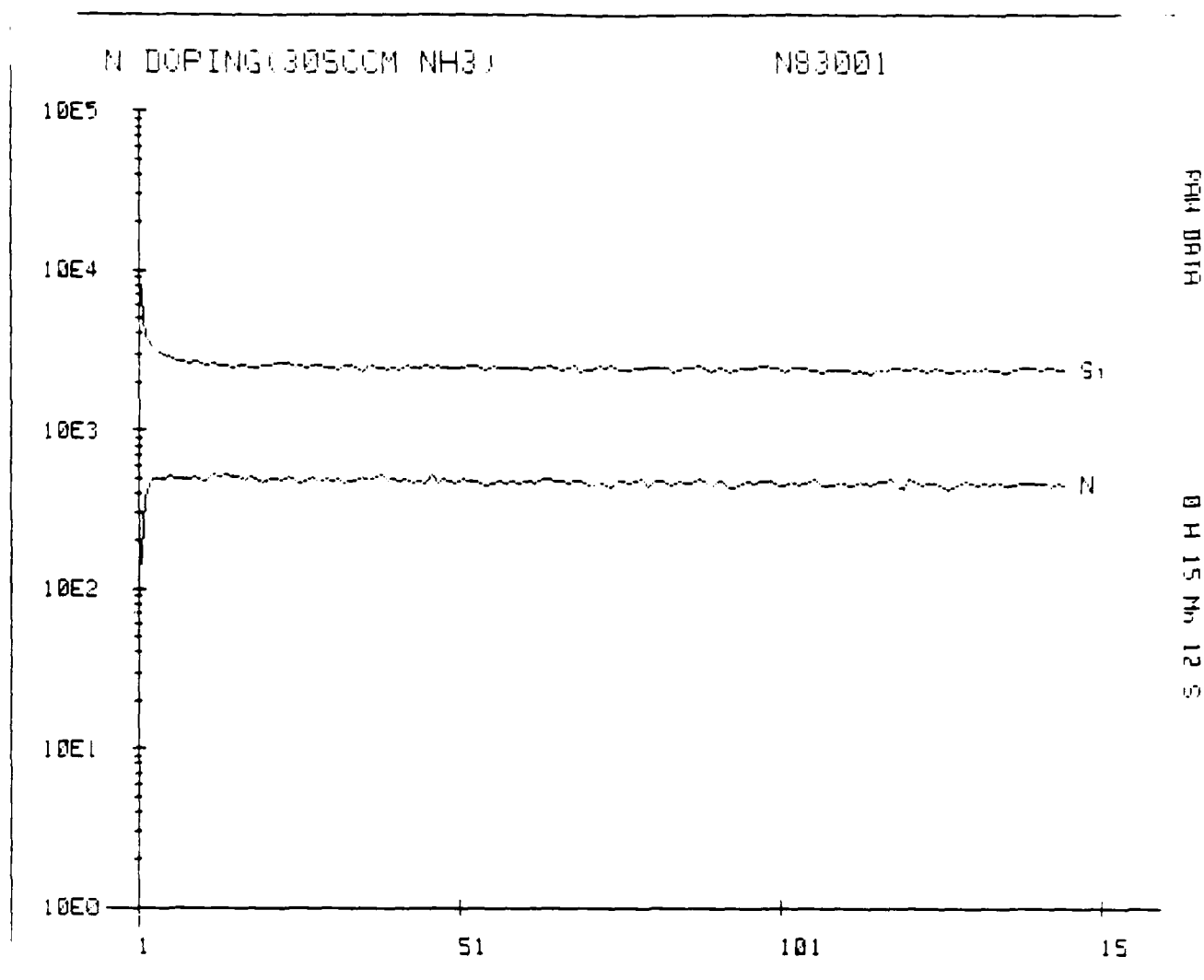


Figure 5. SIMS depth profile of N⁺ in situ doped in a γ -SiC film using NH₃ in H₂ at a flow rate of 30 sccm.

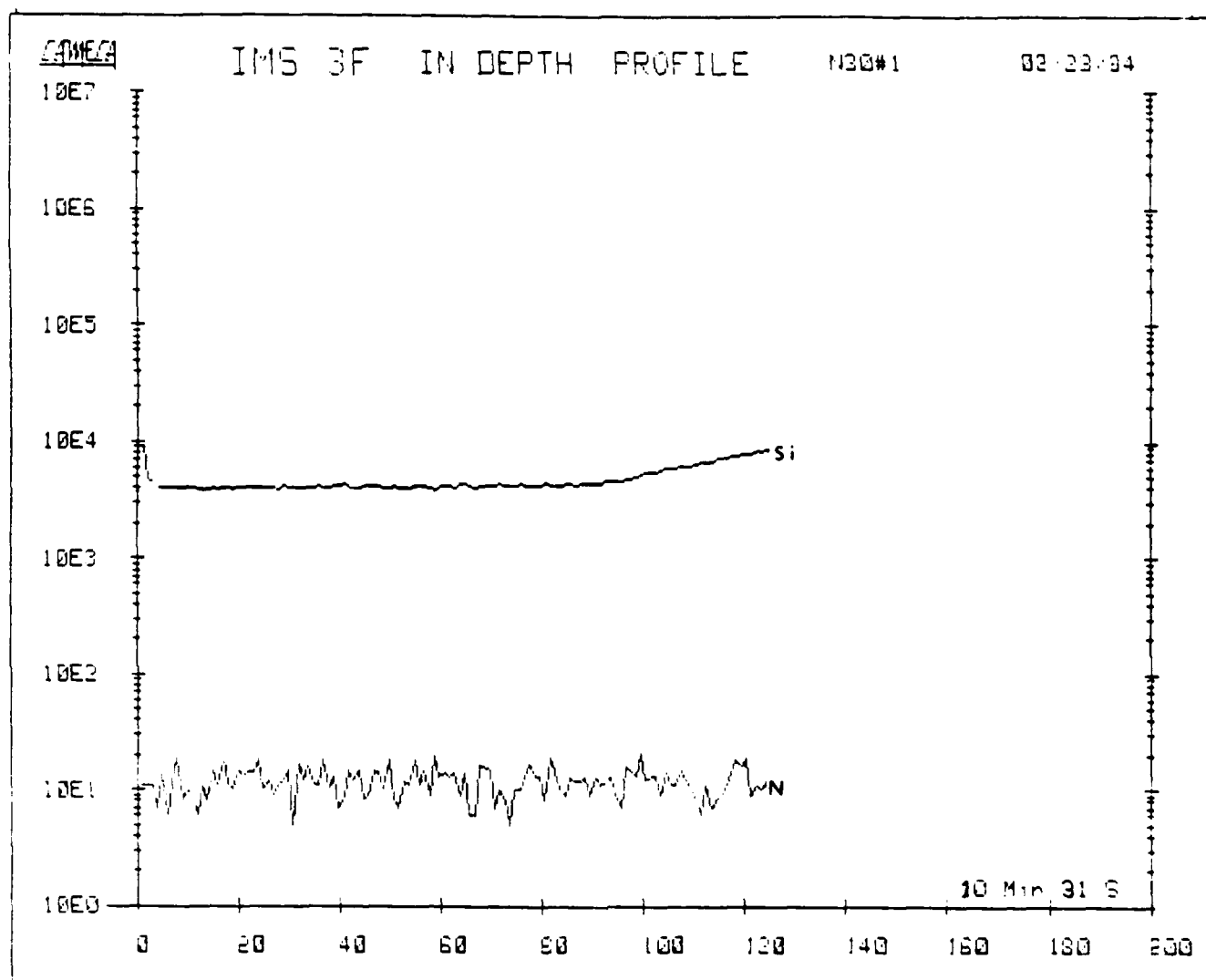


Figure 3. SIMS depth profile of N^+ in situ doped in a β -SiC film using N_2 and H_2 at a flow rate of 30 sccm.

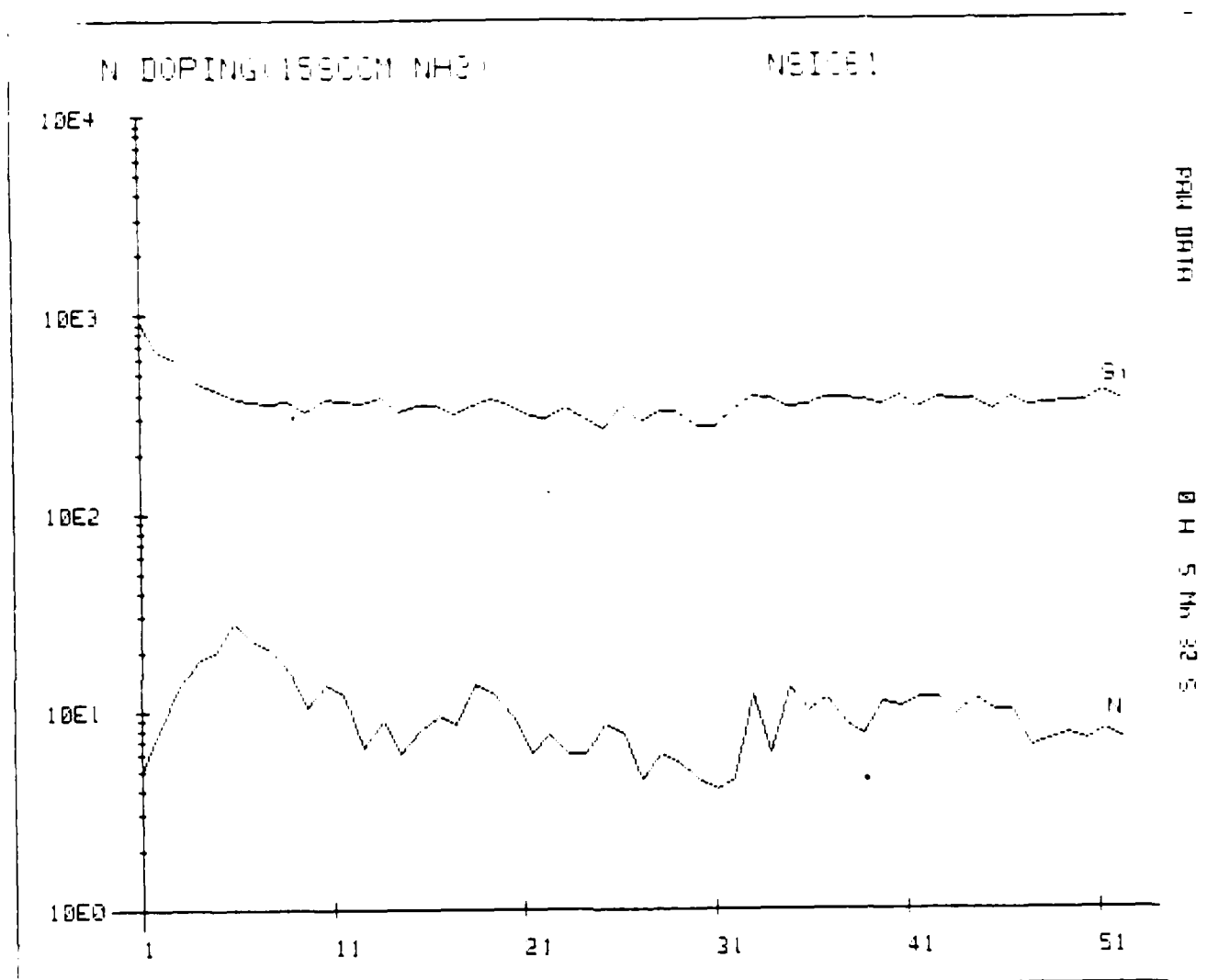


Figure 4. SIMS depth profile of N⁺ in situ doped in a -SiC film using NH₃ in H₂ at a flow rate of 15 sccm.

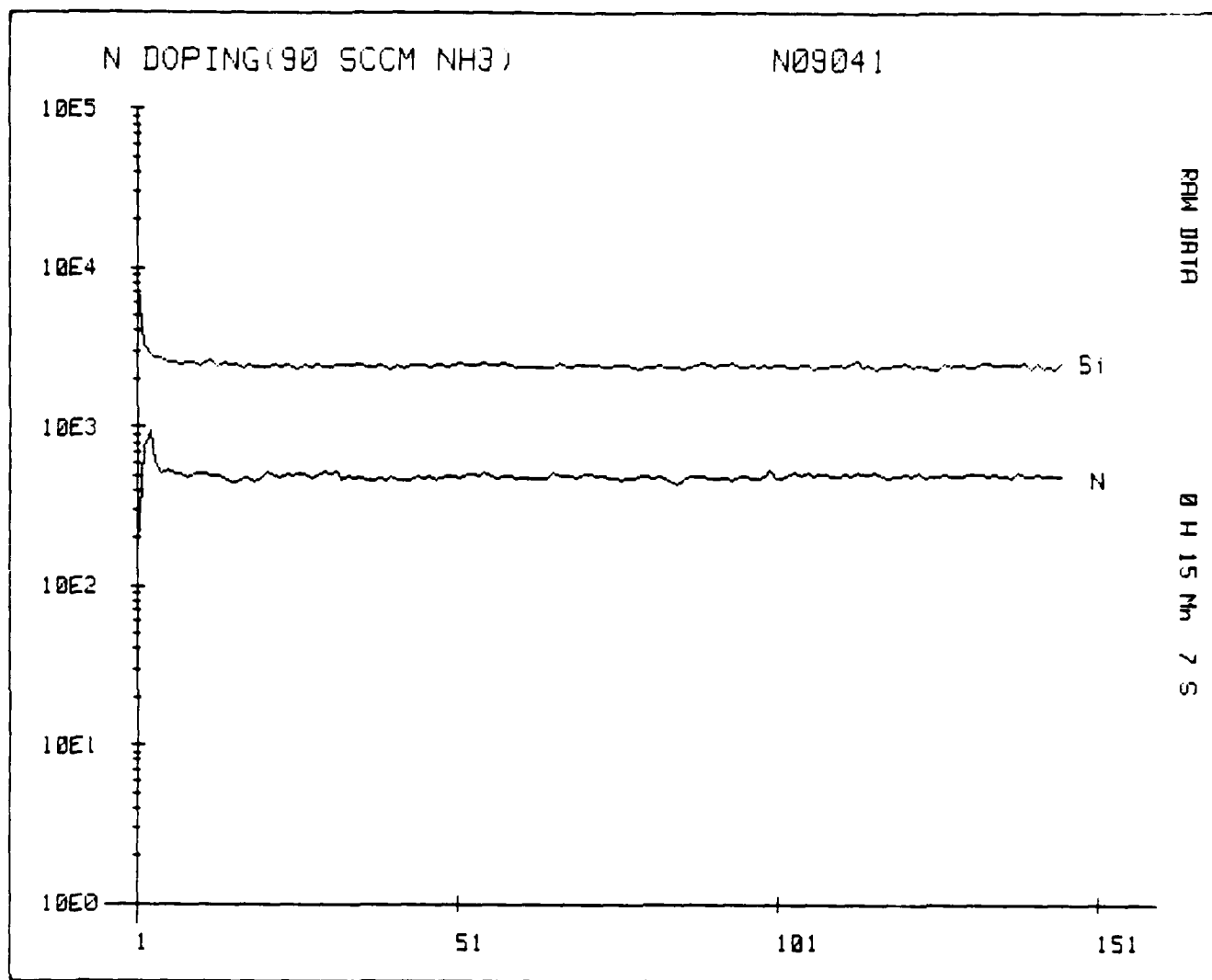


Figure 7. SIMS depth profile of N⁺ in situ doped in a SiC film using NH₃ in H₂ at a flow rate of 90 sccm.

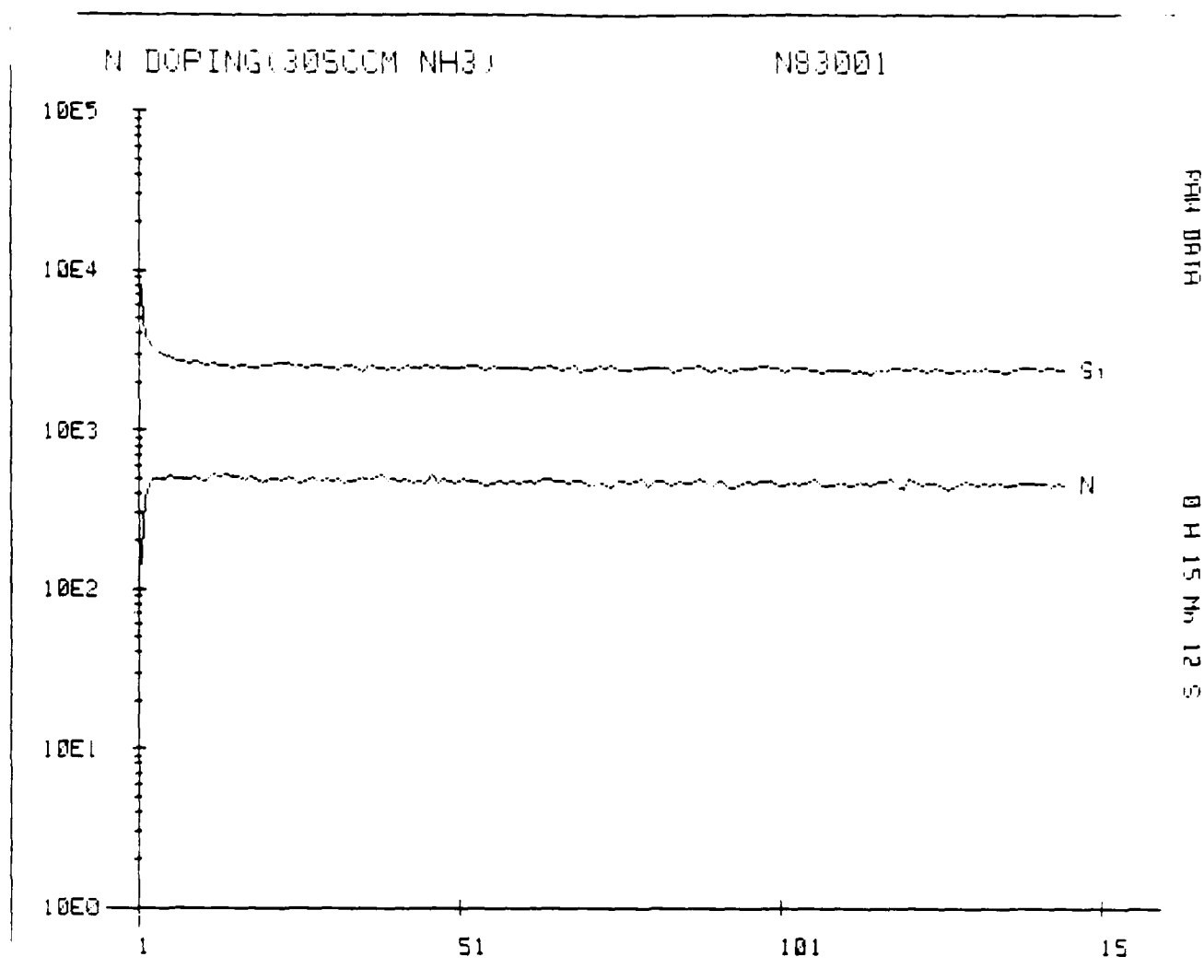


Figure 5. SIMS depth profile of N⁺ in situ doped in a γ -SiC film using NH₃ in H₂ at a flow rate of 30 sccm.

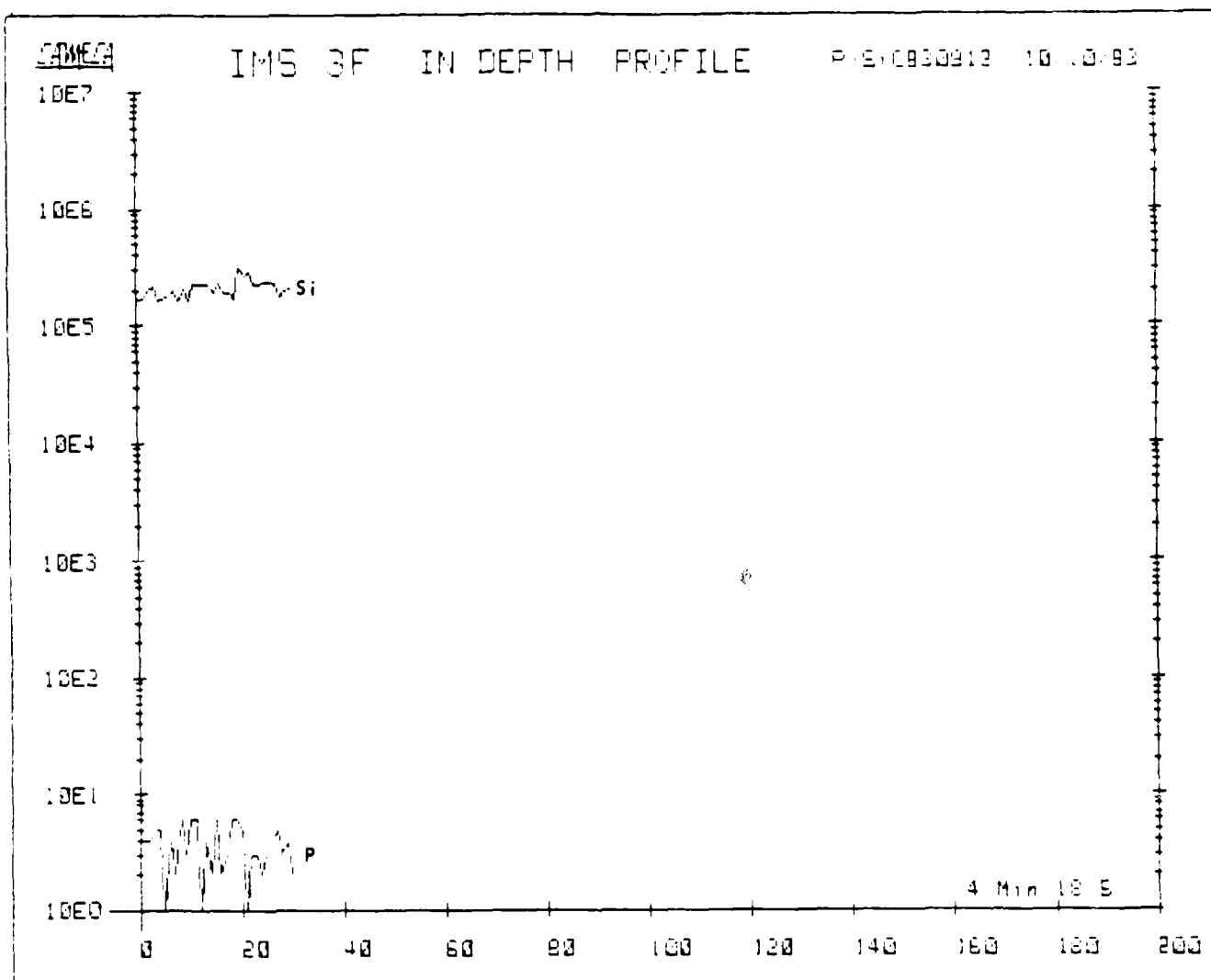
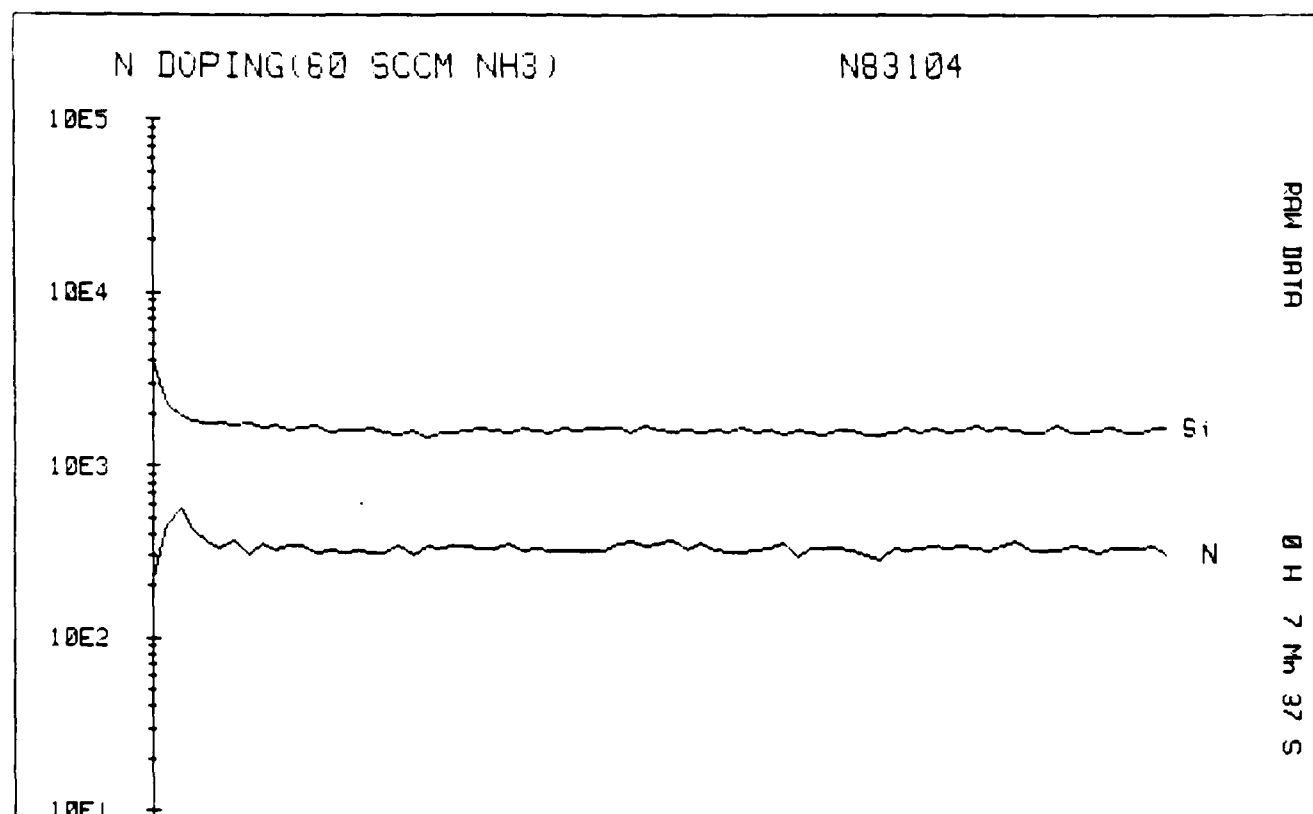


Figure 3. SIMS profile of P^+ in situ doped in a β -SiC thin film using 50 ppm PH_3 in H_2 at a flow rate of 1.6 sccm.



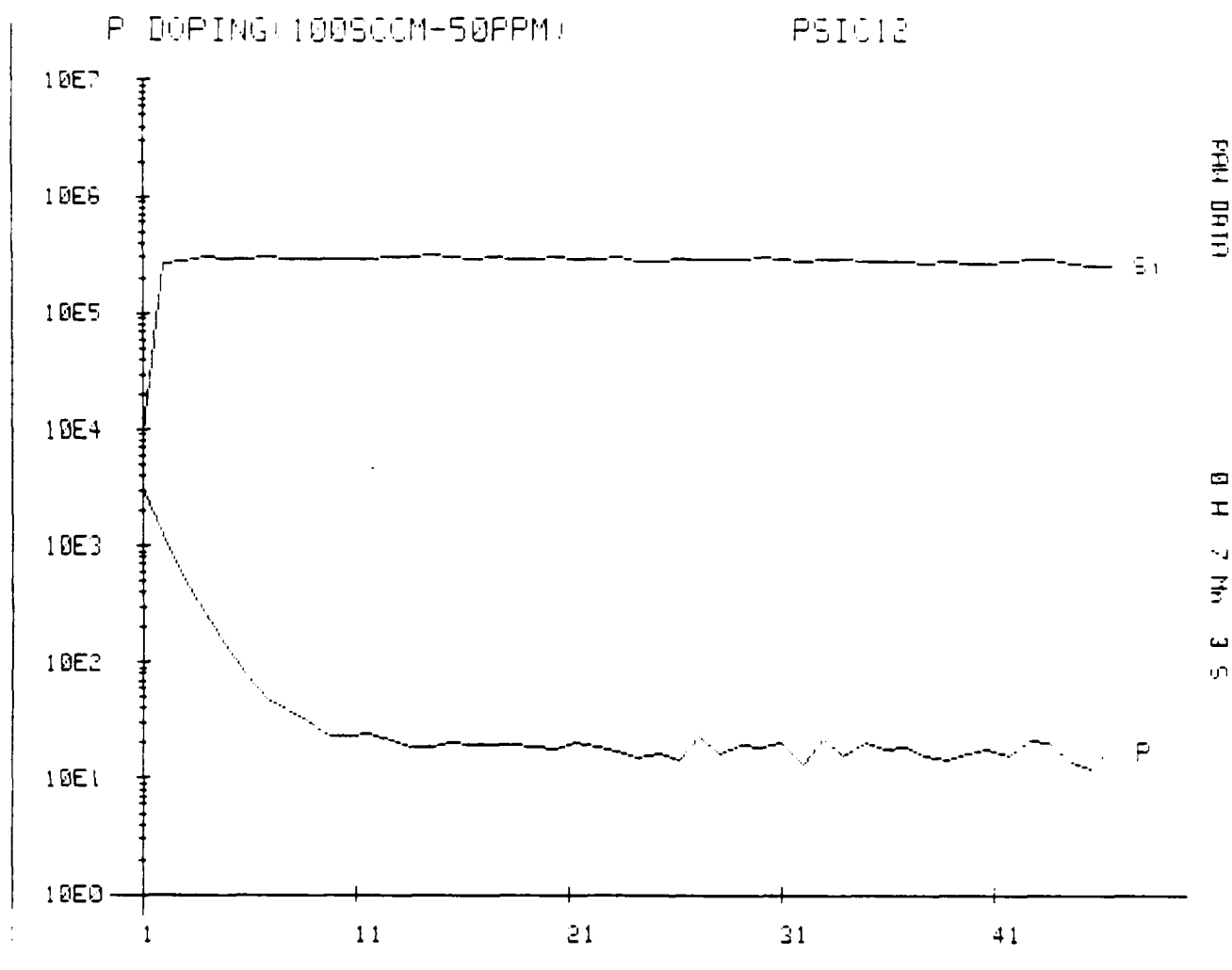


Figure 9. SIMS profile of P^+ in situ doped in a γ -SiC thin film using 50 ppm PH_3 in H_2 at a flow rate of 100 sccm.

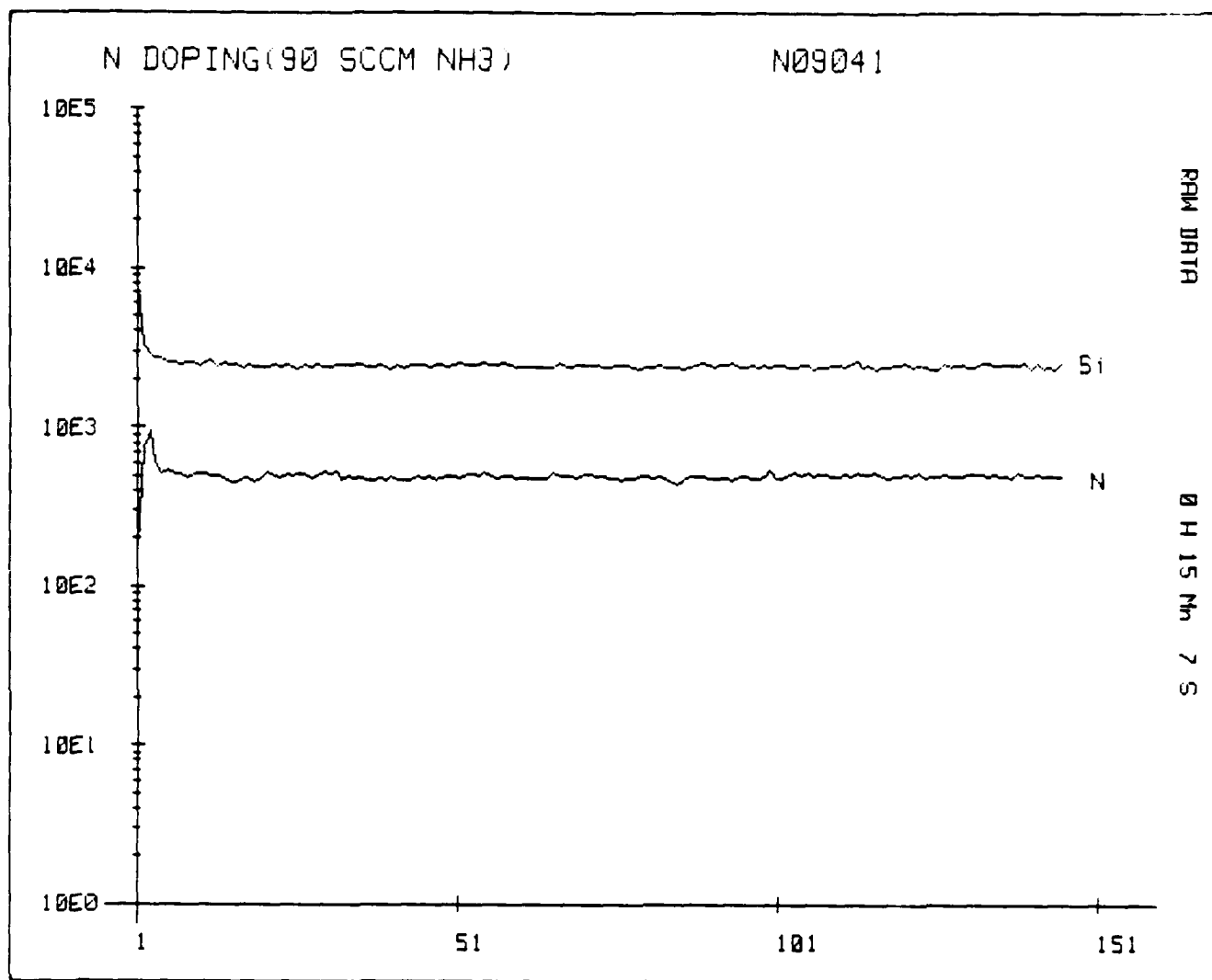


Figure 7. SIMS depth profile of N⁺ in situ doped in a SiC film using NH₃ in H₂ at a flow rate of 90 sccm.

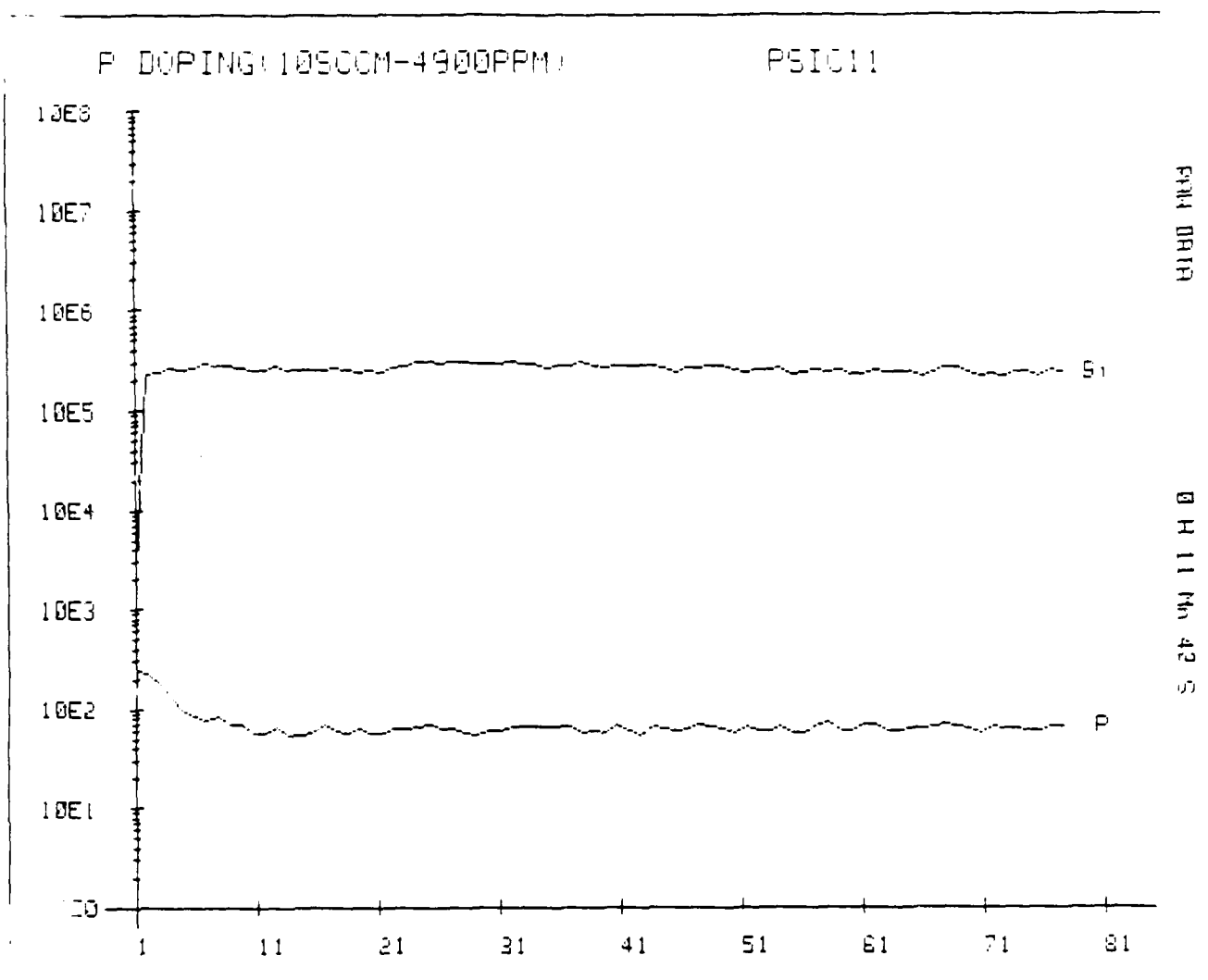


Figure 10. SIMS profile of P^+ in situ doped in a γ -SiC thin film using 4900 ppm PH_3 in H_2 at a flow rate of 10 sccm.

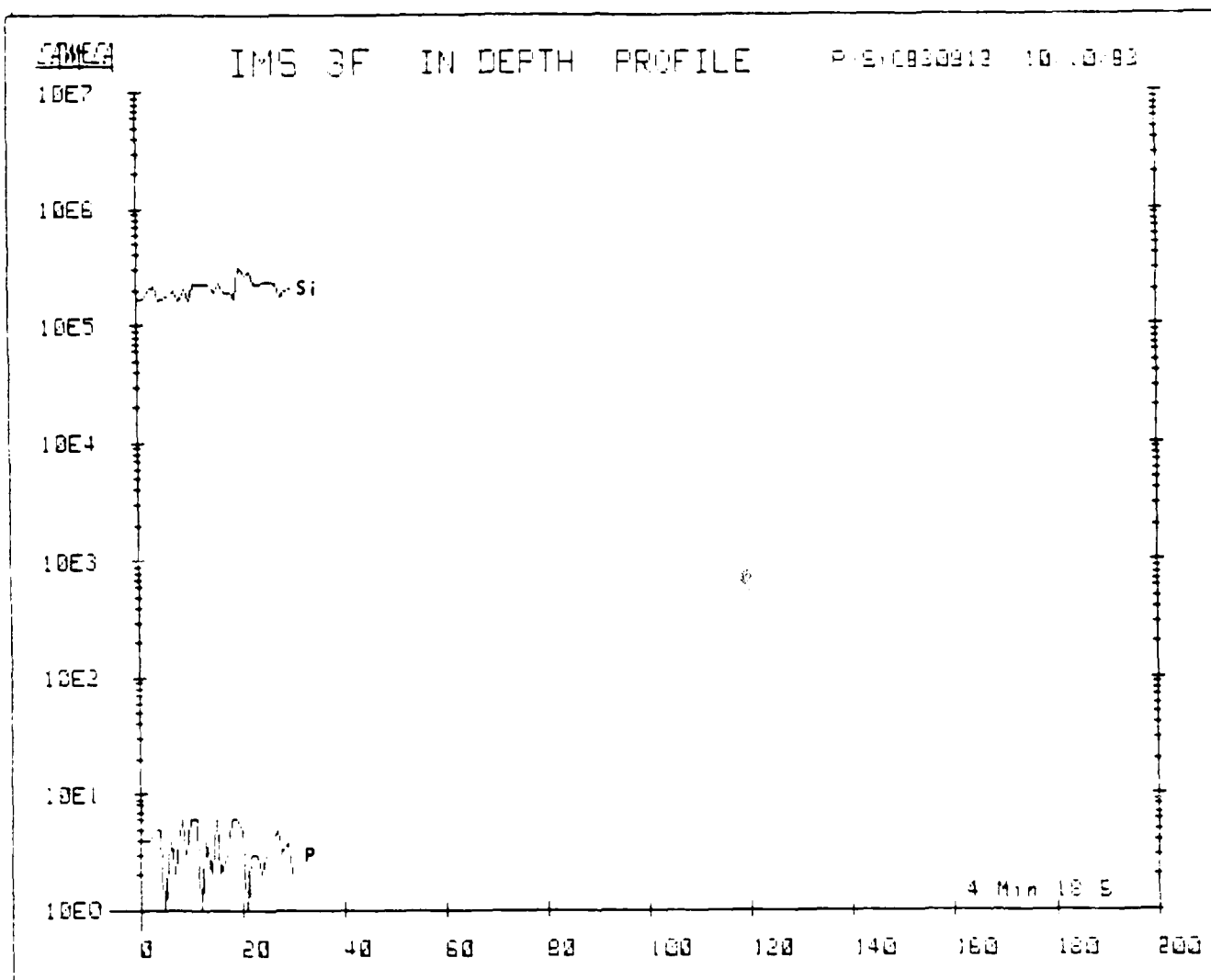


Figure 3. SIMS profile of P^+ in situ doped in a β -SiC thin film using 50 ppm PH_3 in H_2 at a flow rate of 1.6 sccm.

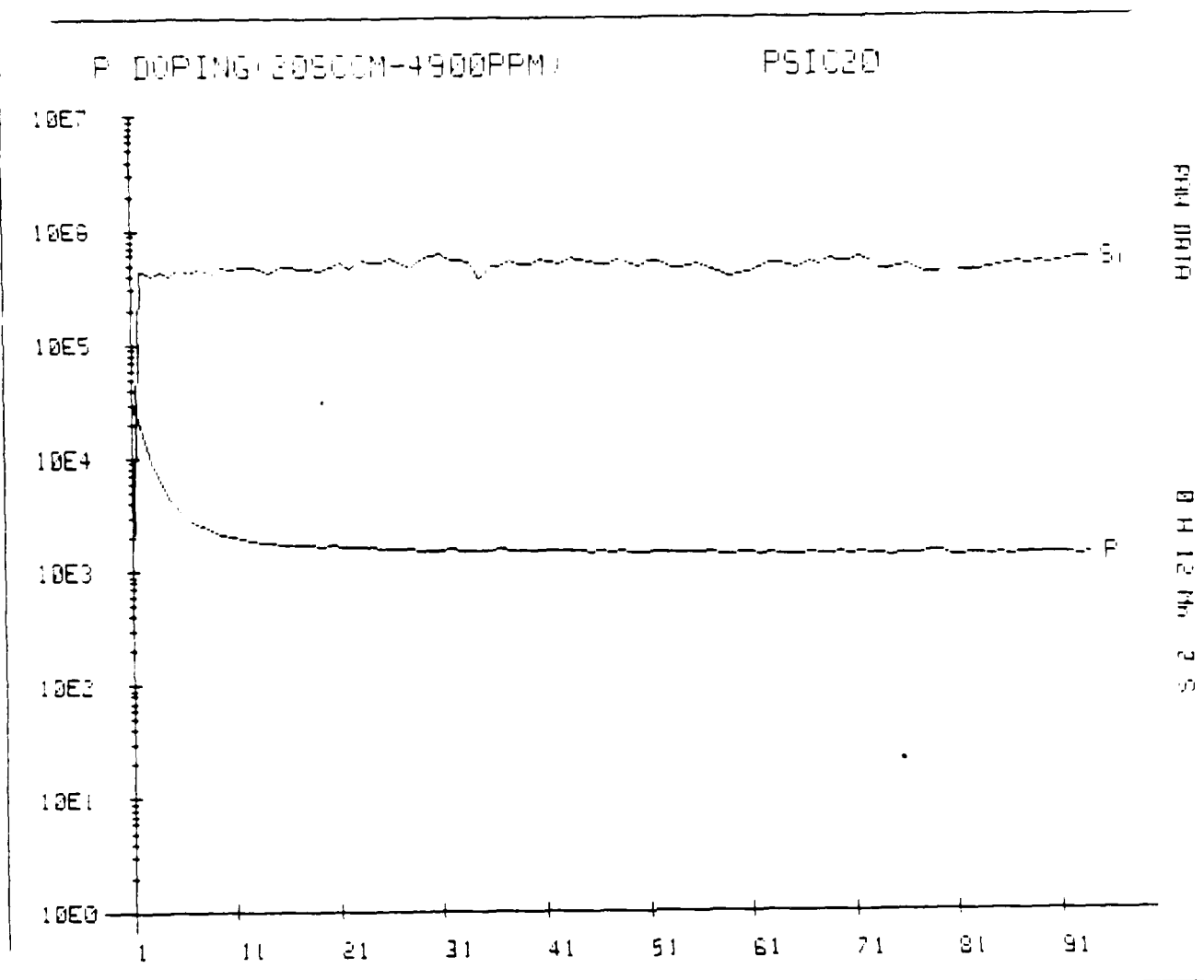


Figure 11. SIMS profile of P^+ in situ doped in a $-SiO$ thin film using 4900 ppm PH_3 in H_2 at a flow rate of 20 sccm.

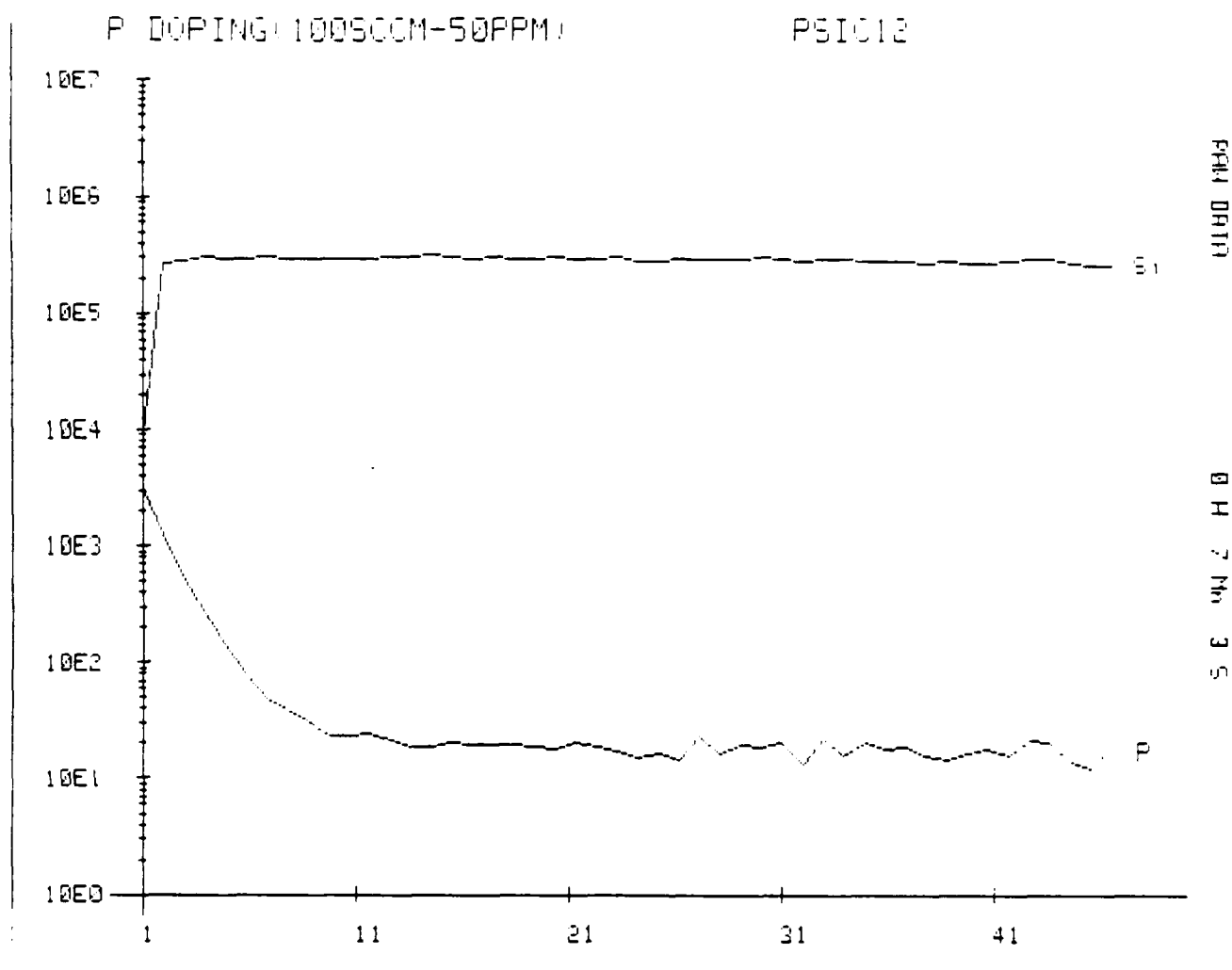


Figure 9. SIMS profile of P^+ in situ doped in a γ -SiC thin film using 50 ppm PH_3 in H_2 at a flow rate of 100 sccm.

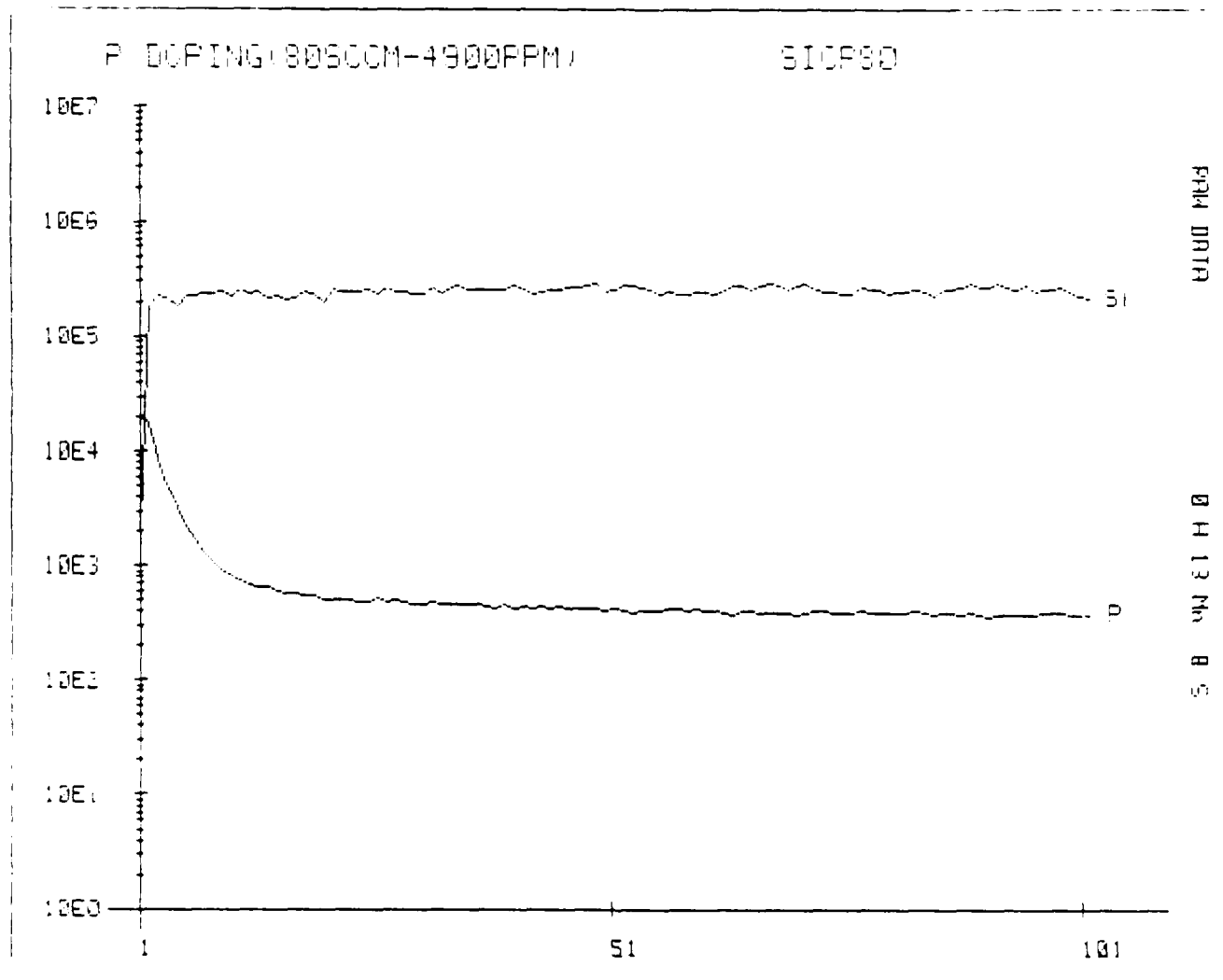


Figure 12. SIMS profile of P^+ in situ doped in a μ -SiC thin film using 4900 ppm PH_3 in H_2 at a flow rate of 80 sccm.

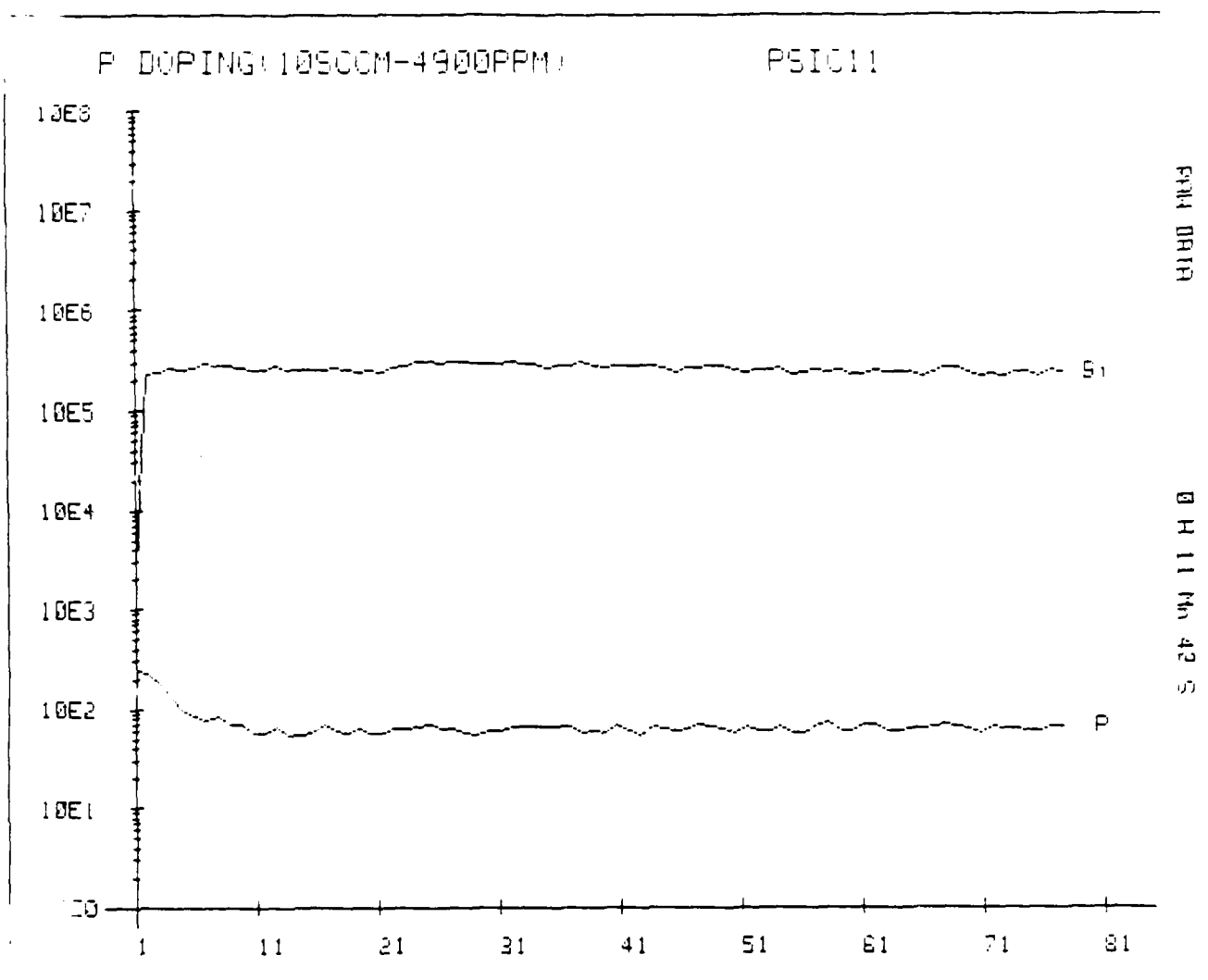


Figure 10. SIMS profile of P^+ in situ doped in a γ -SiC thin film using 4900 ppm PH_3 in H_2 at a flow rate of 10 sccm.

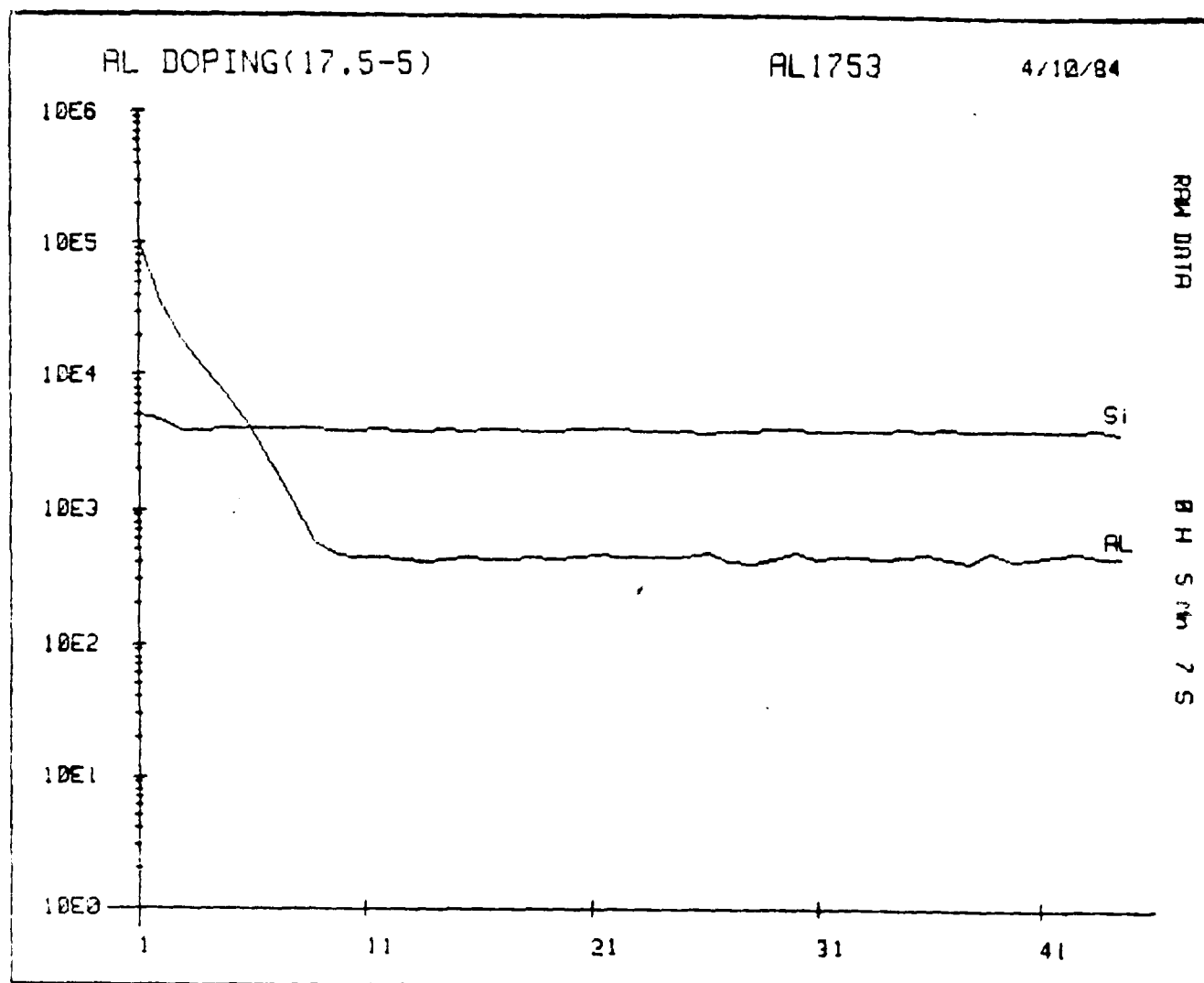


Figure 13. Composition profile of Al^+ which has been "in-situ" doped in a β -SiC thin film using TMA at a temperature of 290.5K and carried in H_2 at a flow rate of 5 sccm. The graph shows ion yield in counts vs data storage channels.

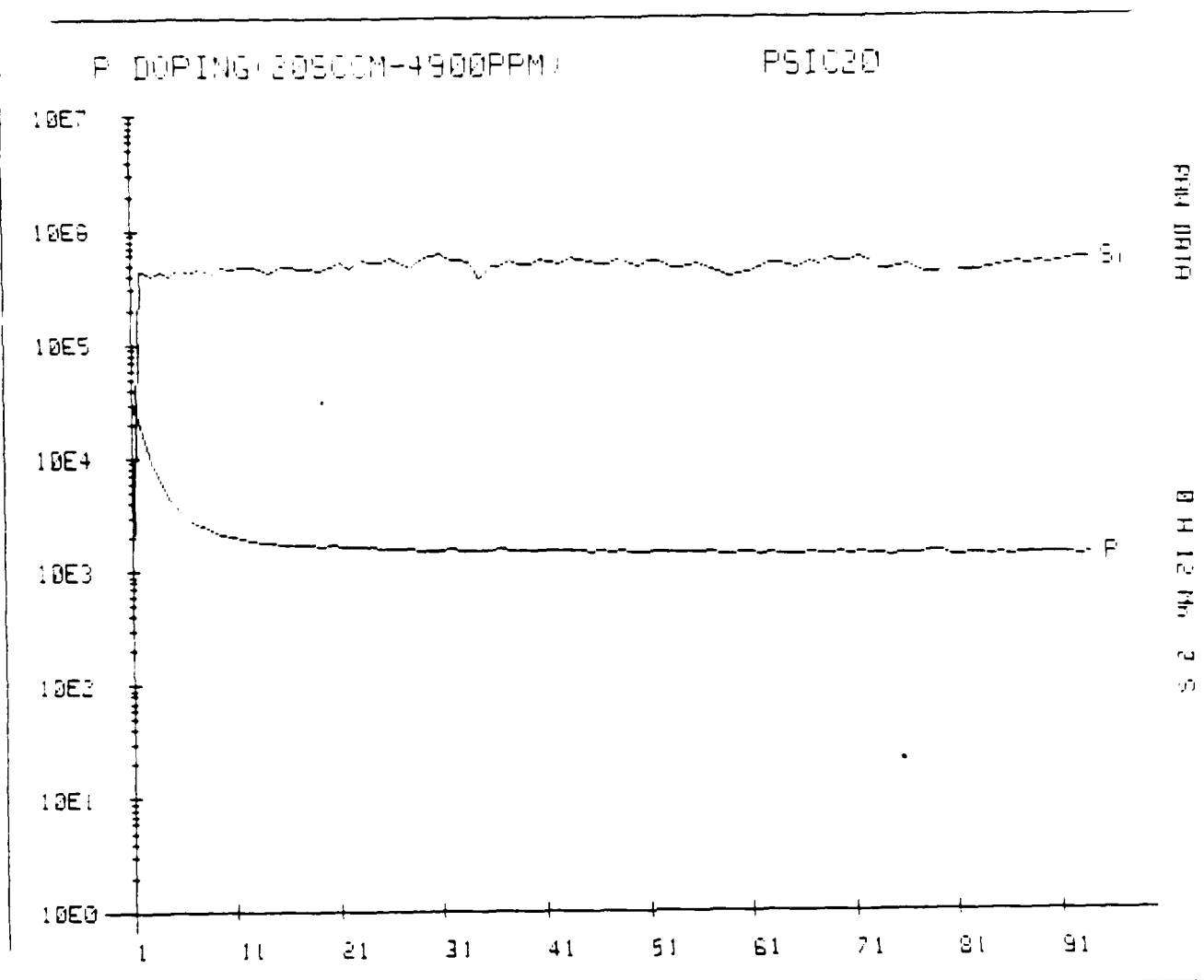


Figure 11. SIMS profile of P^+ in situ doped in a $-SiO$ thin film using 4900 ppm PH_3 in H_2 at a flow rate of 20 sccm.

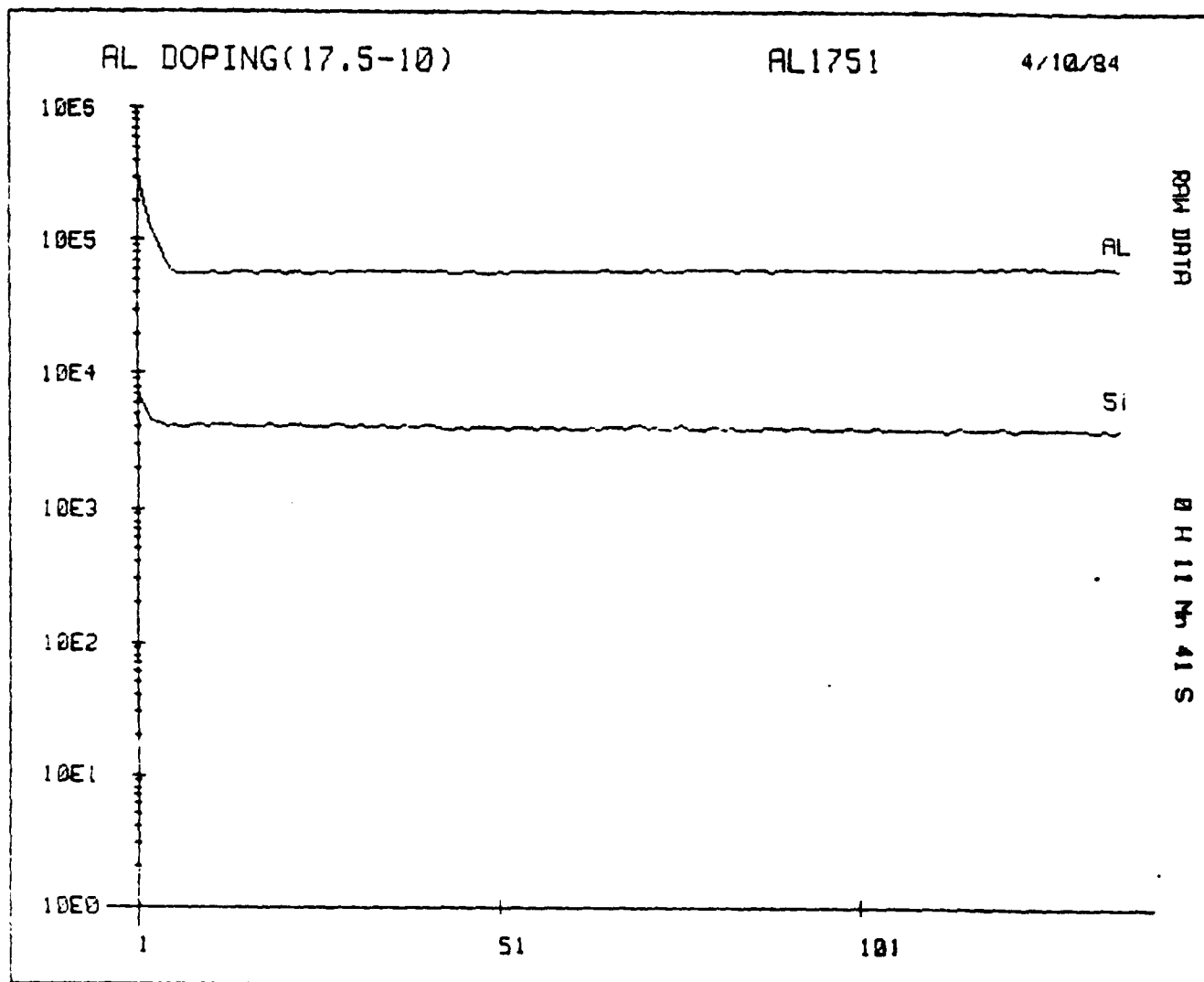


Figure 14. Composition profile of Al^+ which has been "in-situ" doped in a β -SiC thin film using TMA at a temperature of 290.5K and carried in H_2 at a flow rate of 10 sccm. The graph shows ion yield in counts vs data storage channels.

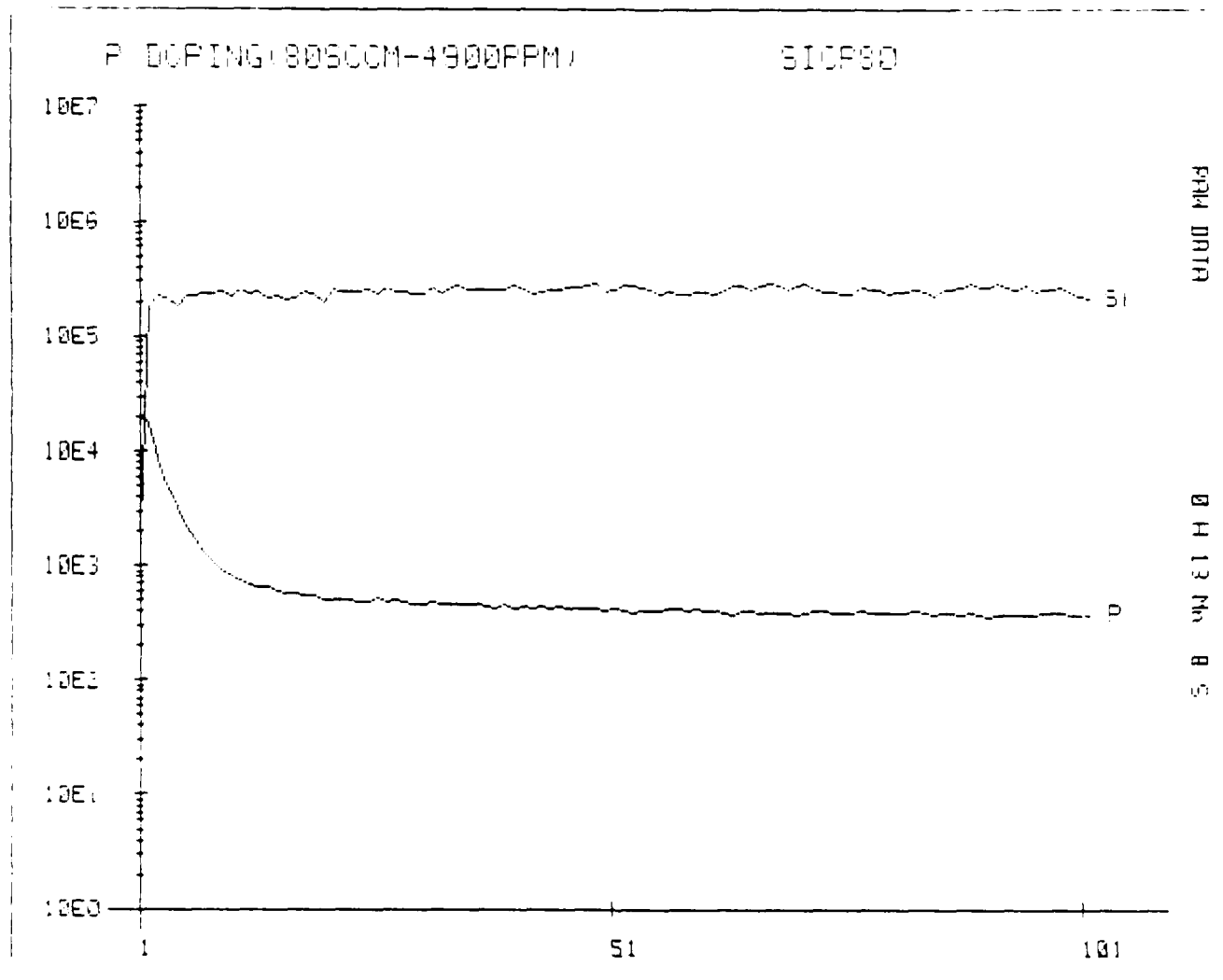


Figure 12. SIMS profile of P^+ in situ doped in a μ -SiC thin film using 4900 ppm PH_3 in H_2 at a flow rate of 80 sccm.

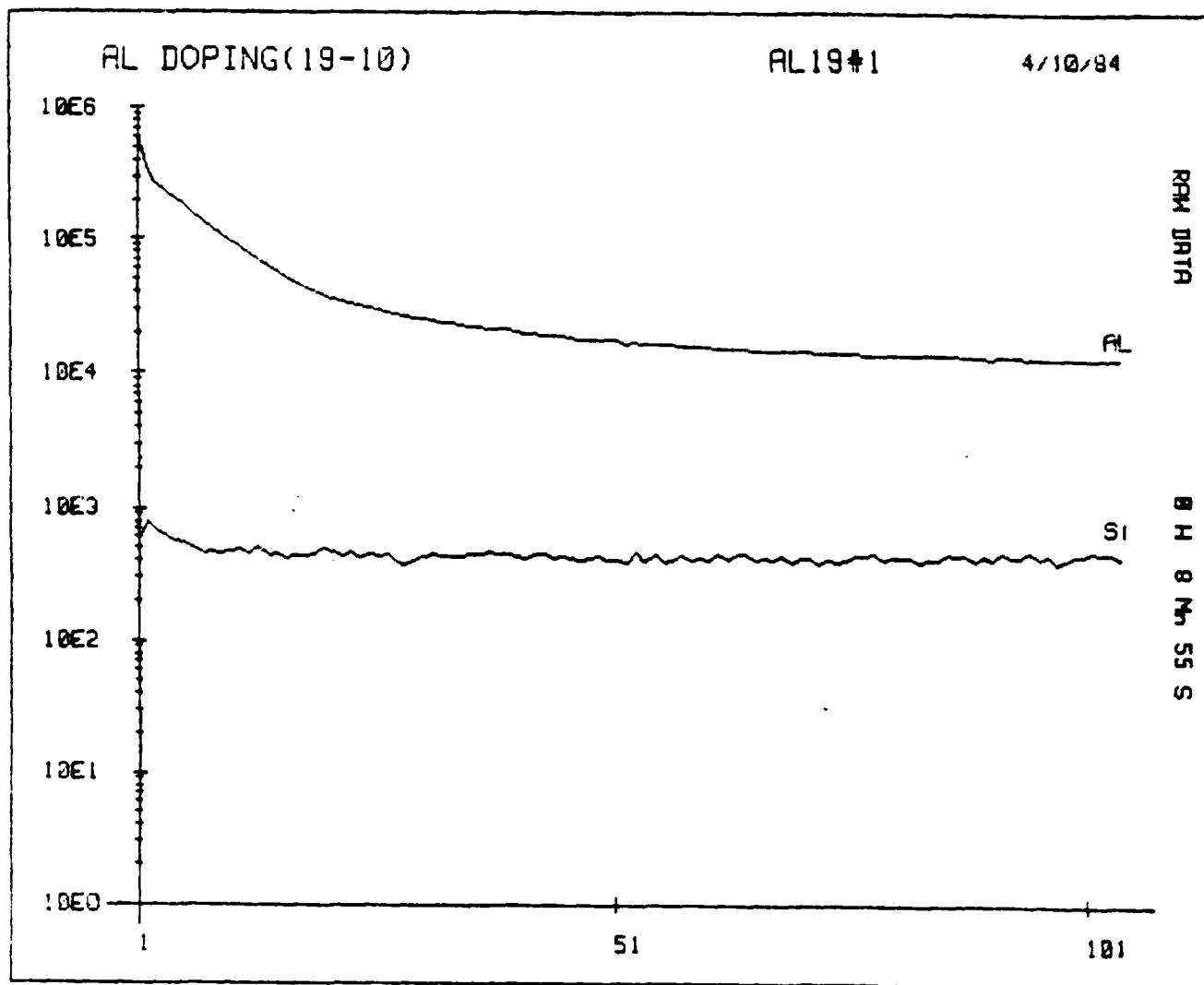


Figure 15. Composition profile of Al^+ which has been "in-situ" doped in a β -SiC thin film using TMA at a temperature of 292K and carried in H_2 at a flow rate of 10 sccm. The graph shows ion yield in counts vs data storage channels.

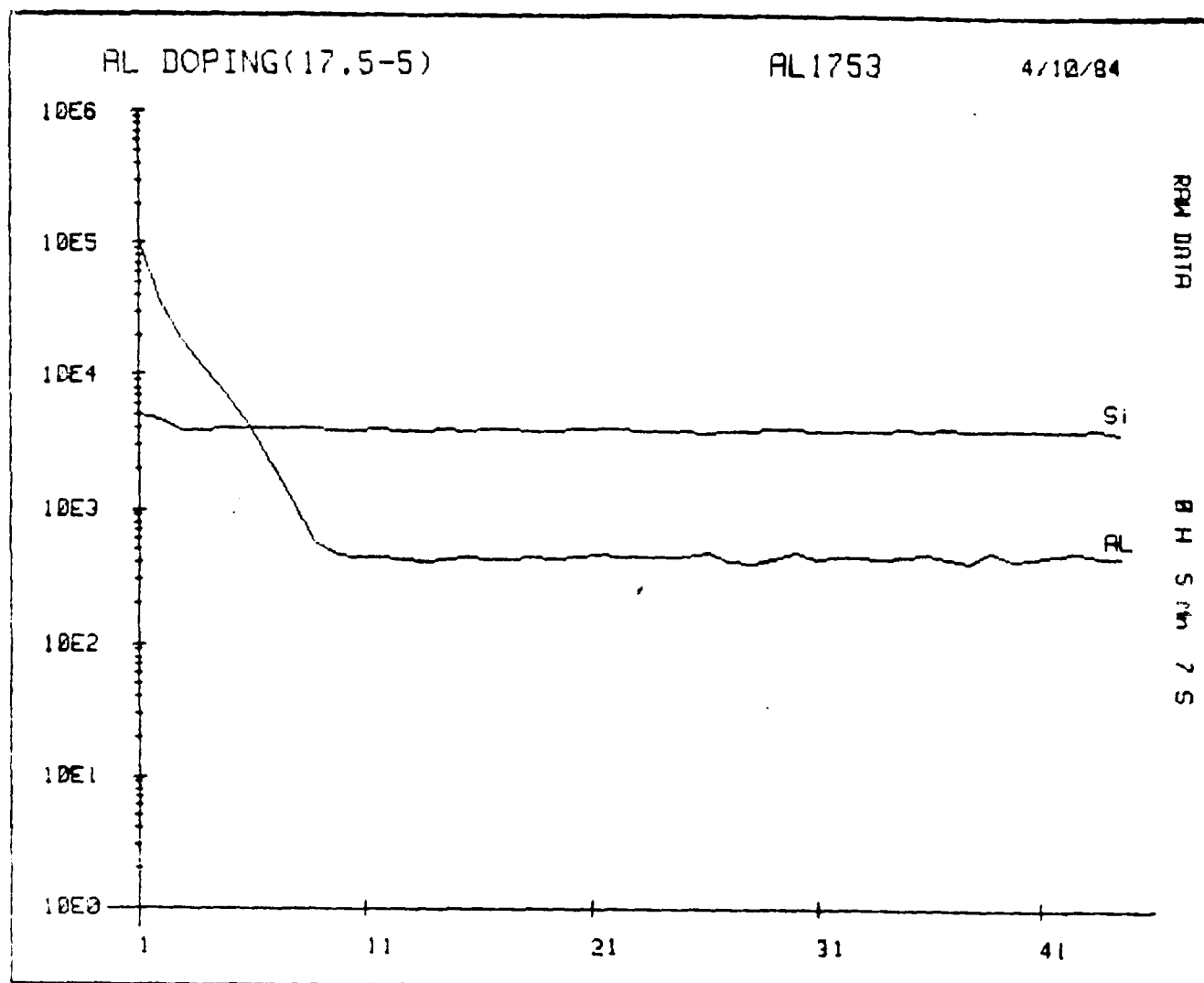


Figure 13. Composition profile of Al^+ which has been "in-situ" doped in a β -SiC thin film using TMA at a temperature of 290.5K and carried in H_2 at a flow rate of 5 sccm. The graph shows ion yield in counts vs data storage channels.

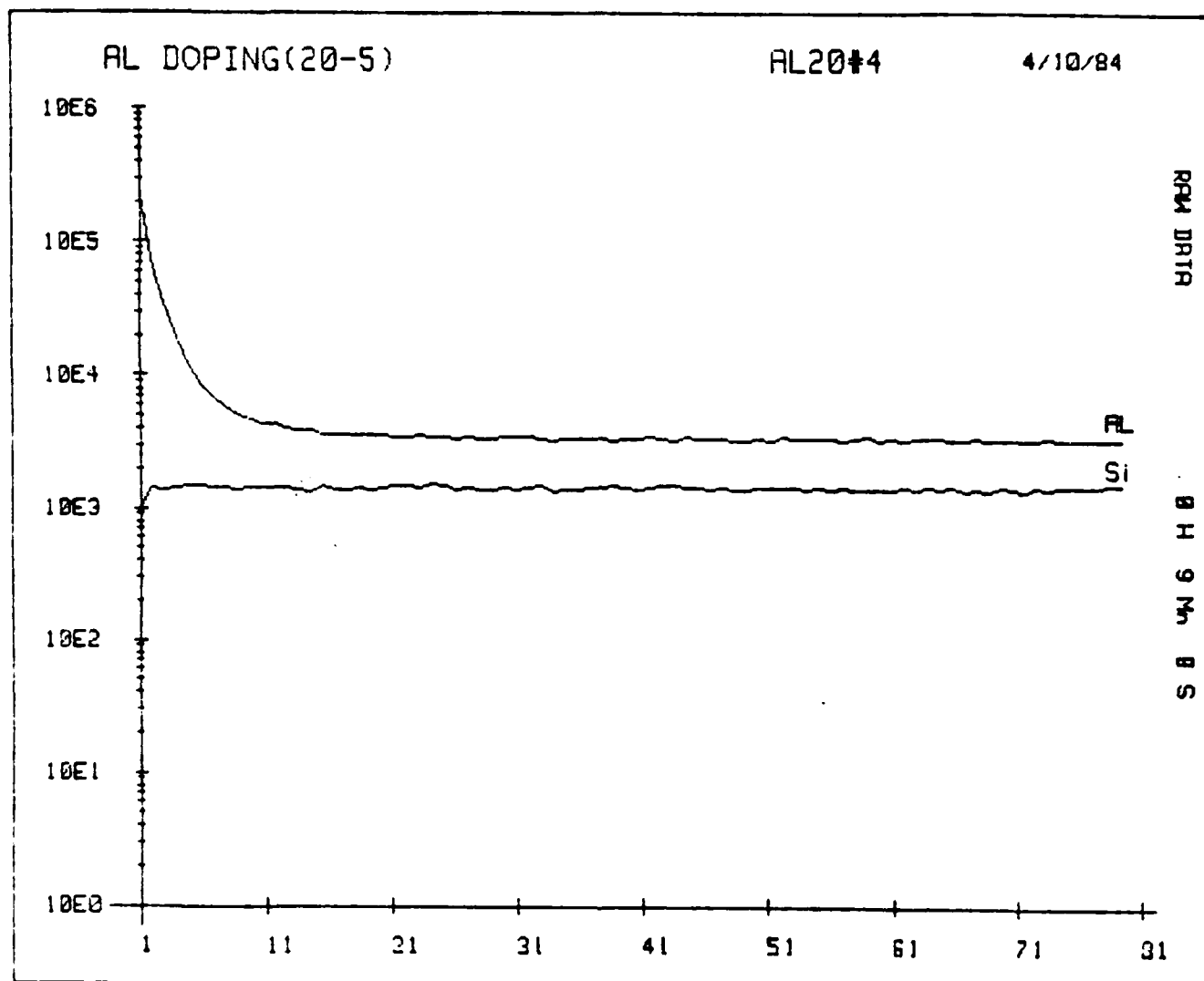


Figure 16. Composition profile of Al⁺ which has been "in-situ" doped in a β -SiC thin film using TMA at a temperature of 293K and carried in H₂ at a flow rate of 5 sccm. The graph shows ion yield in counts vs data storage channels.

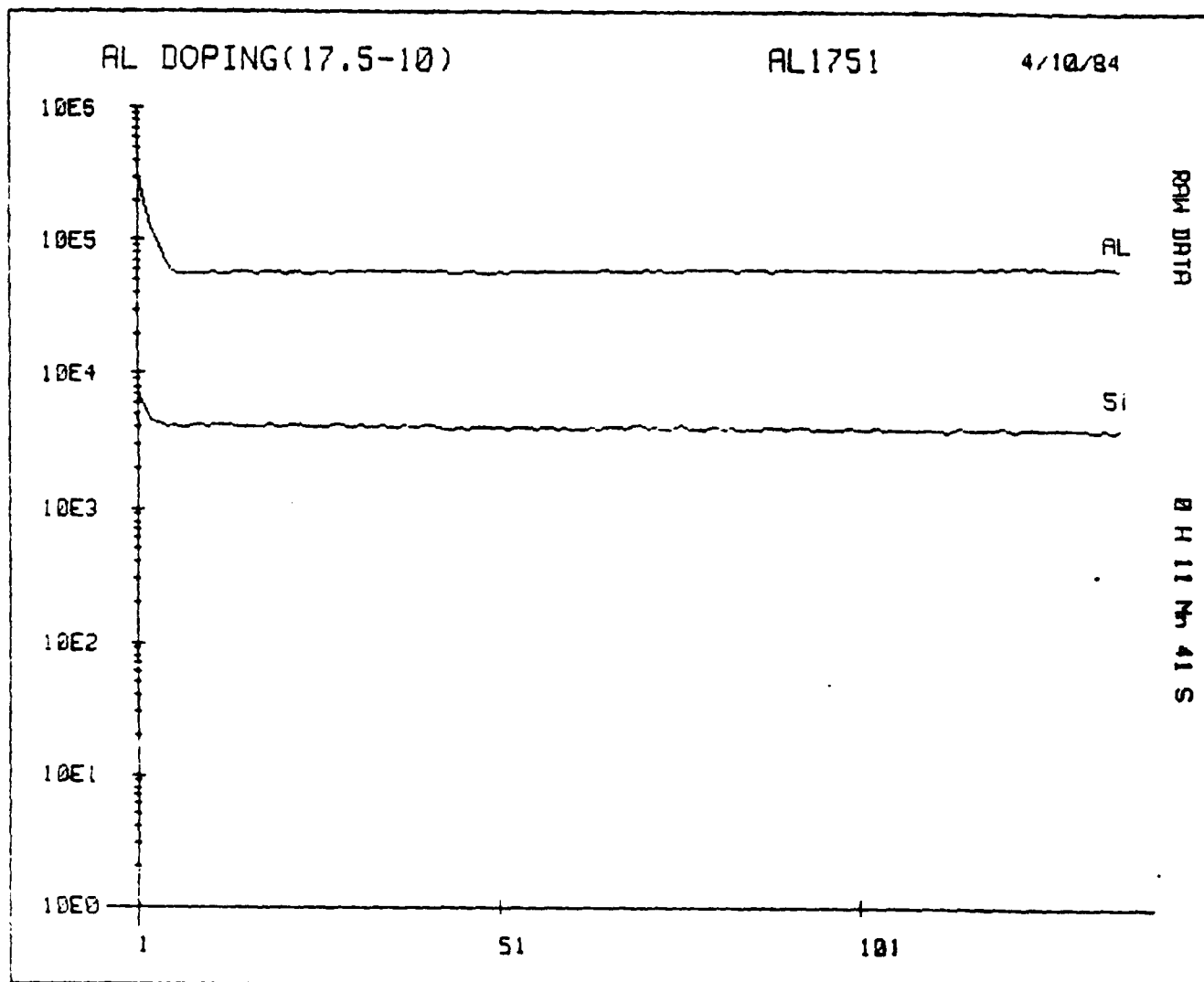


Figure 14. Composition profile of Al^+ which has been "in-situ" doped in a β -SiC thin film using TMA at a temperature of 290.5K and carried in H_2 at a flow rate of 10 sccm. The graph shows ion yield in counts vs data storage channels.

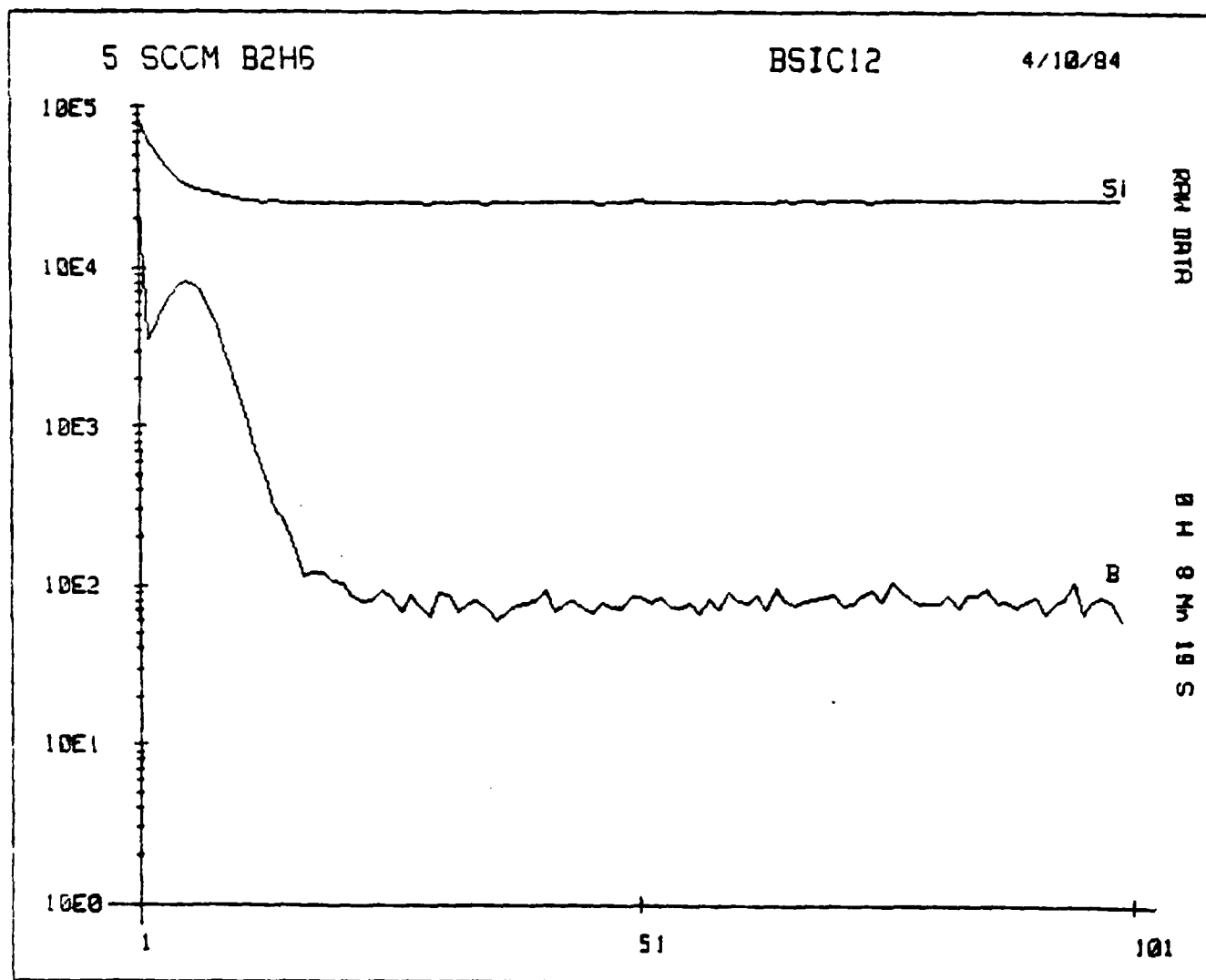


Figure 17. Composition Profile of B⁺ which has been "in-situ" doped in a β-SiC thin film using BH₃ in H₂ at a flow rate of 5 sccm.

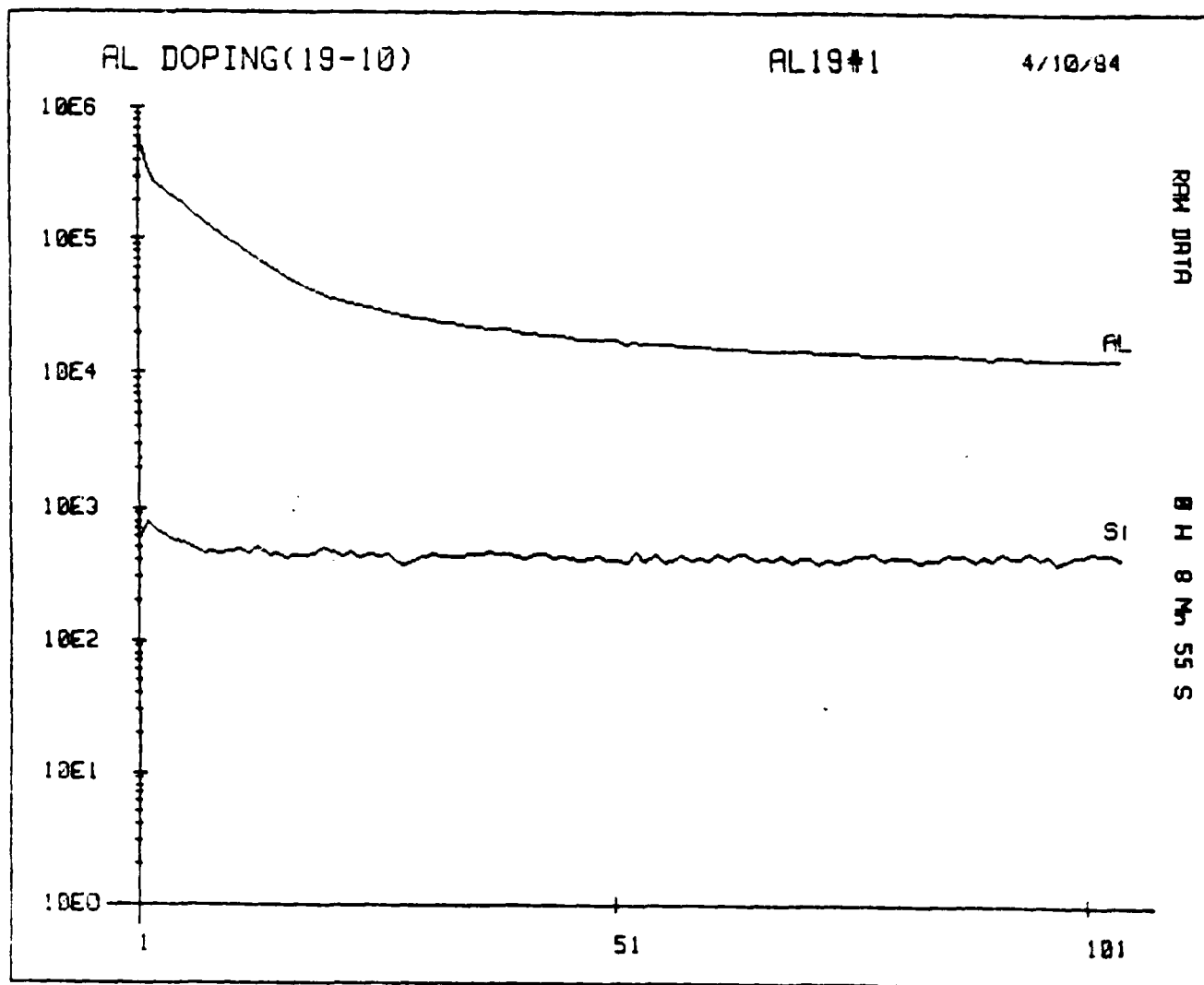


Figure 15. Composition profile of Al^+ which has been "in-situ" doped in a β -SiC thin film using TMA at a temperature of 292K and carried in H_2 at a flow rate of 10 sccm. The graph shows ion yield in counts vs data storage channels.

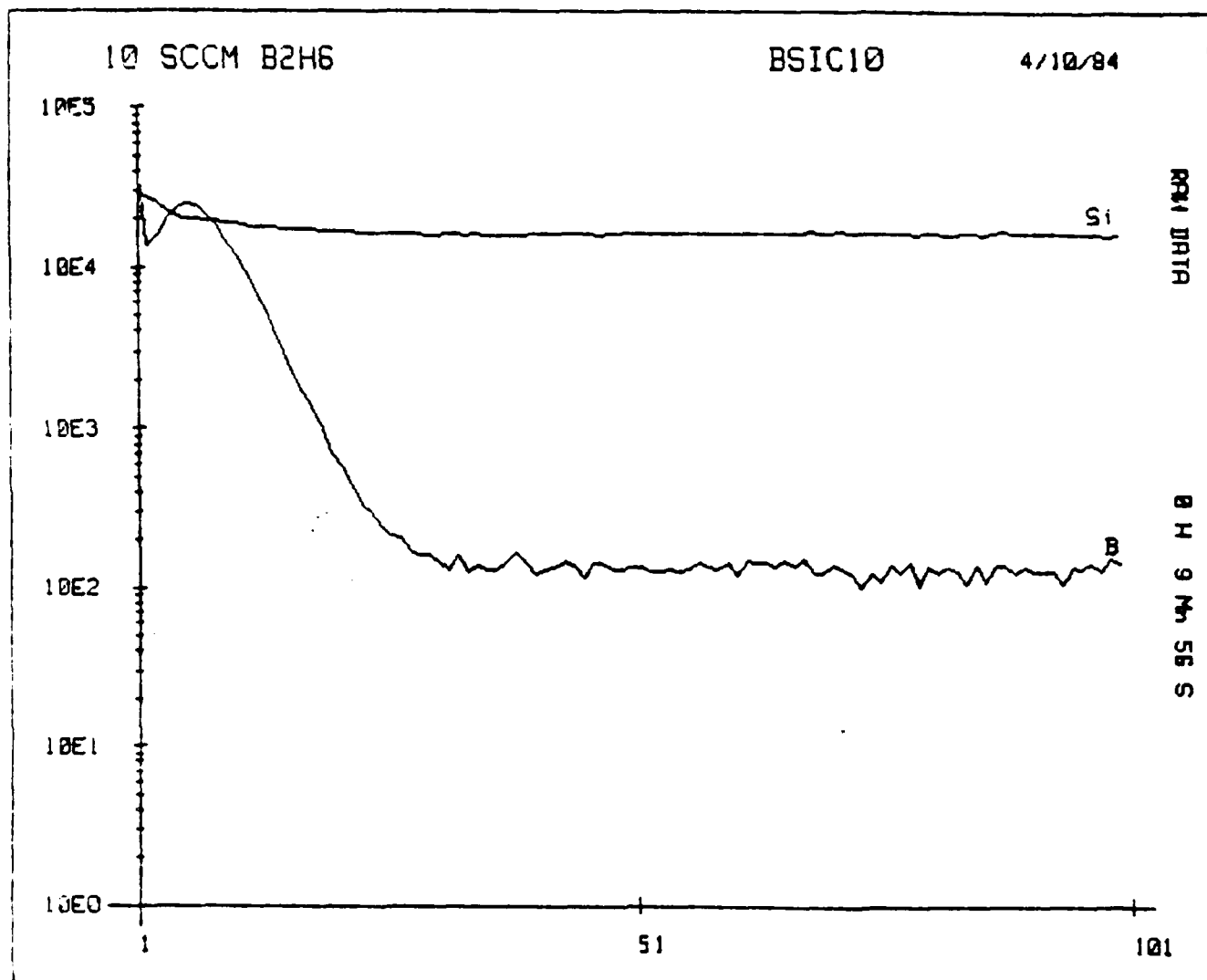


Figure 18. Composition profile of B⁺ which has been "in-situ" doped in a β -SiC thin film using BH₃ and H₂ at a flow rate of 10 sccm.

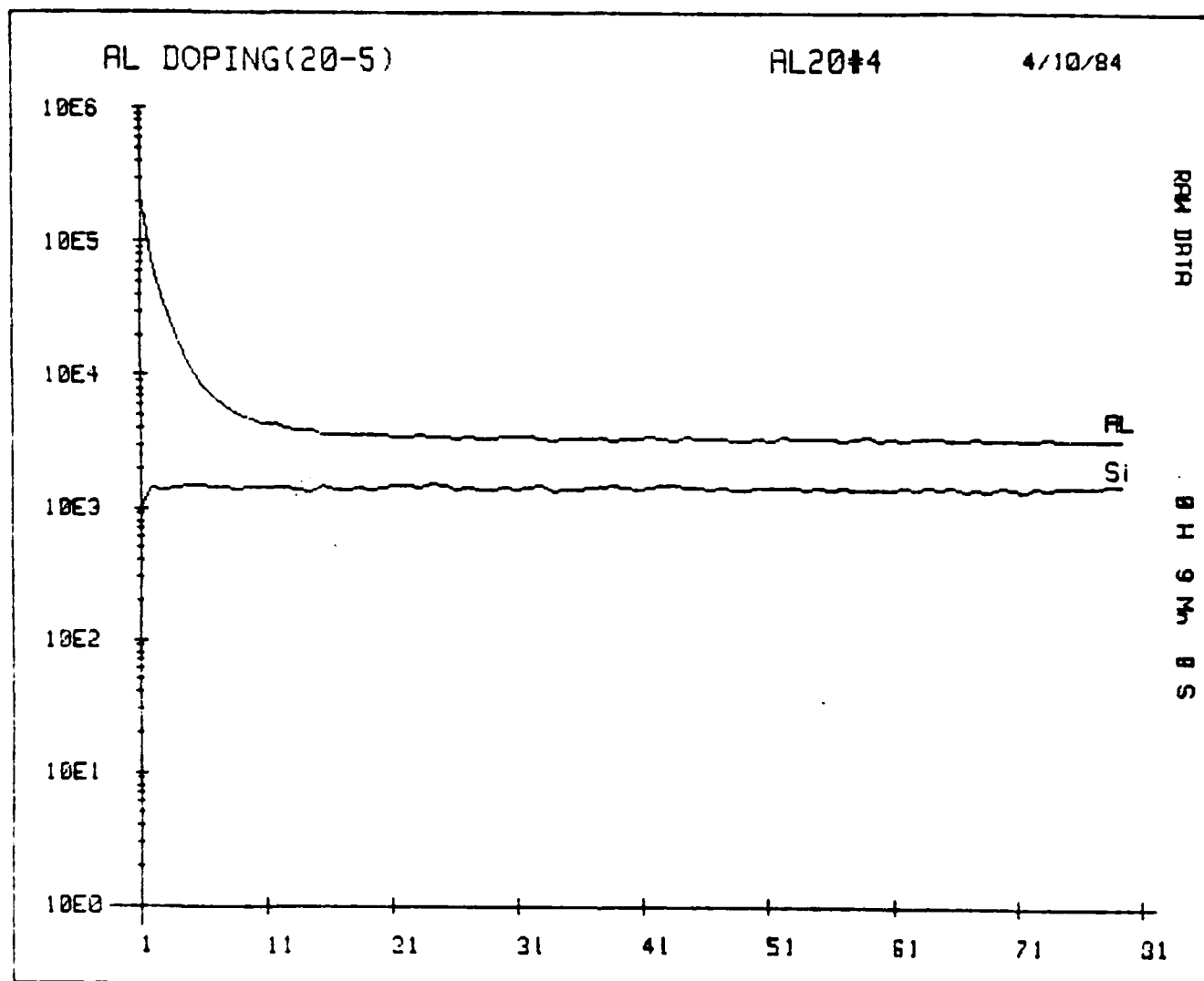


Figure 16. Composition profile of Al⁺ which has been "in-situ" doped in a β -SiC thin film using TMA at a temperature of 293K and carried in H₂ at a flow rate of 5 sccm. The graph shows ion yield in counts vs data storage channels.

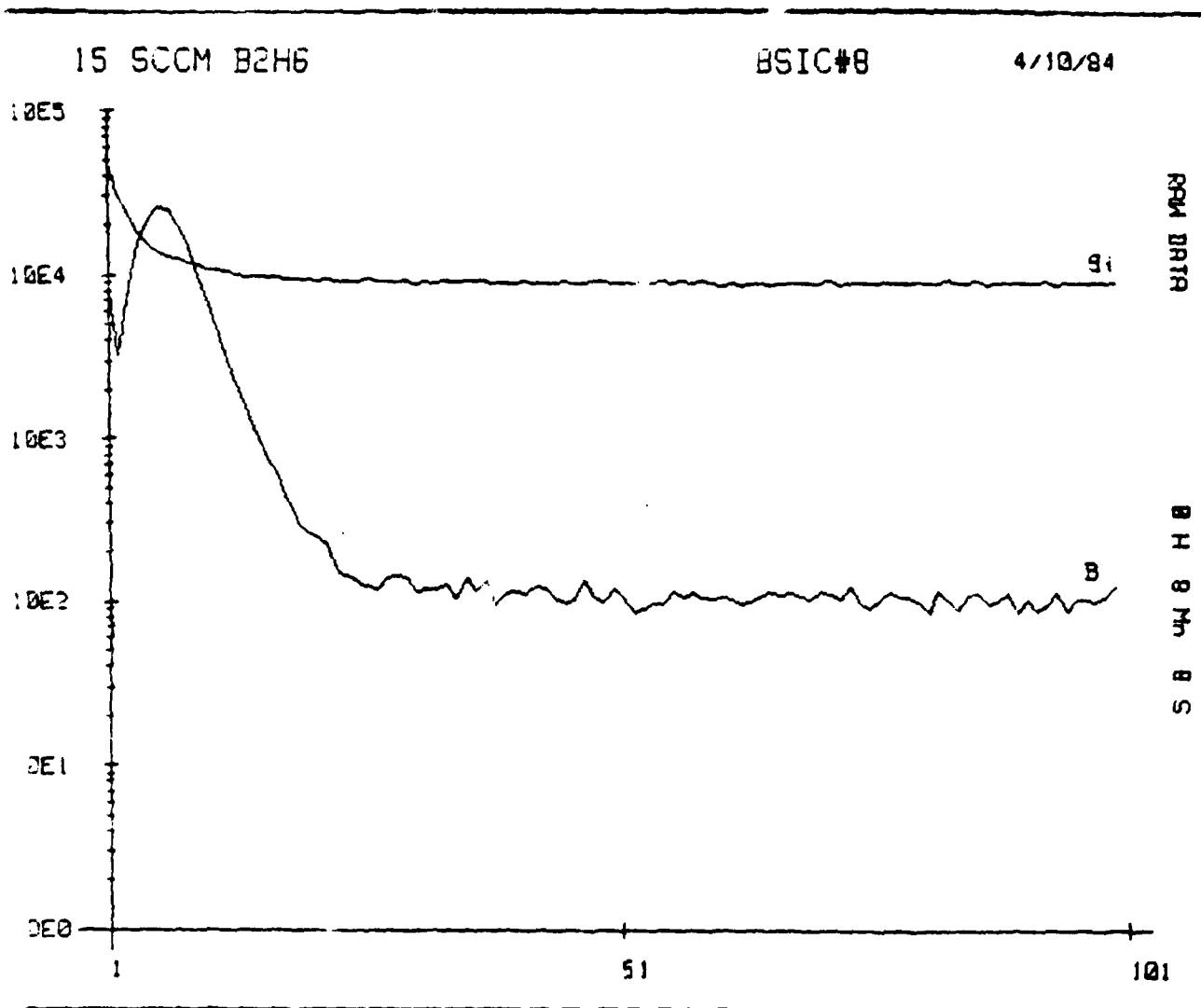


Figure 19. Composition profile of B⁺ which has been "in-situ" doped in a β -SiC thin film using BH₃ and H₂ at a flow rate of 15 sccm.

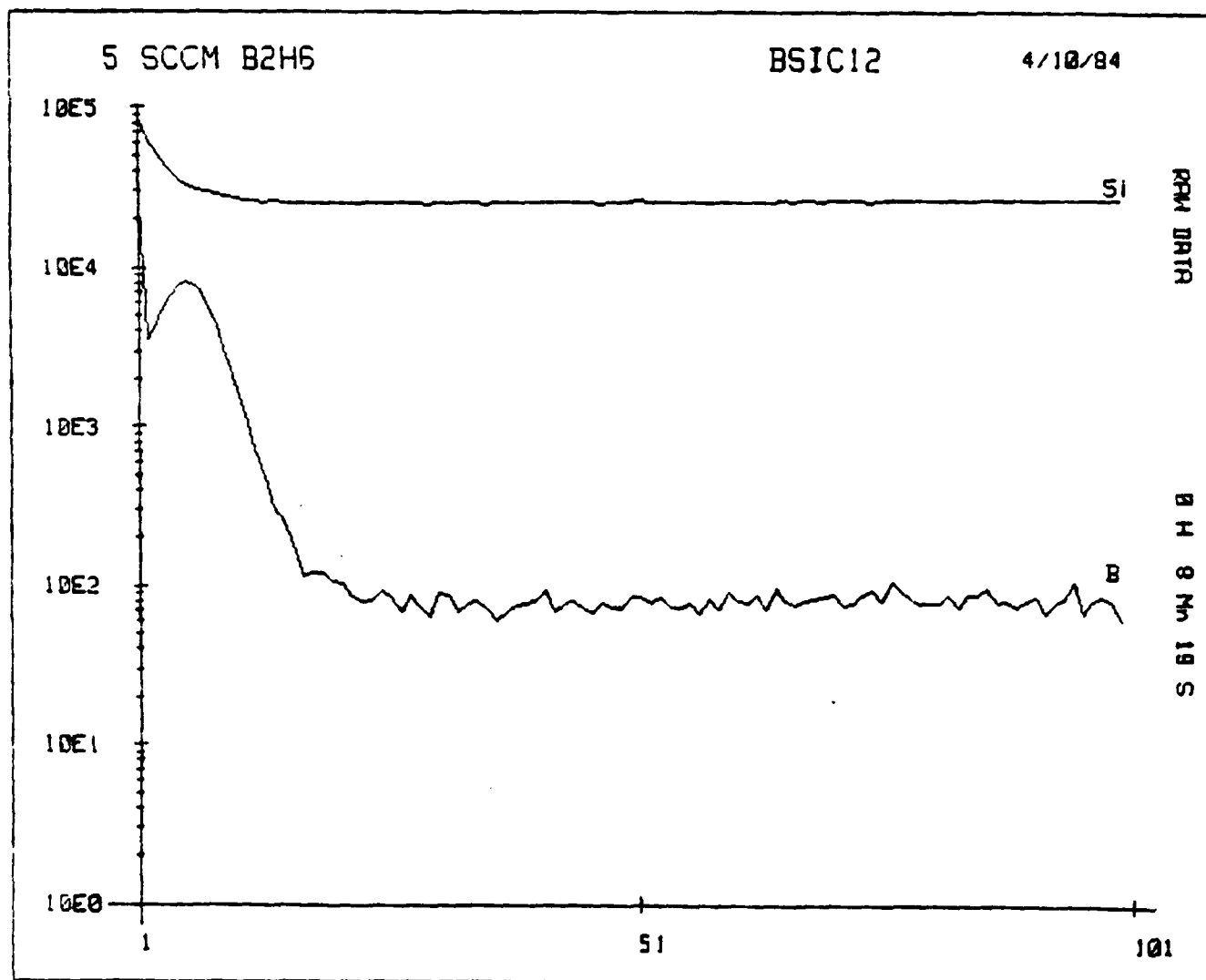


Figure 17. Composition Profile of B⁺ which has been "in-situ" doped in a β-SiC thin film using BH₃ in H₂ at a flow rate of 5 sccm.

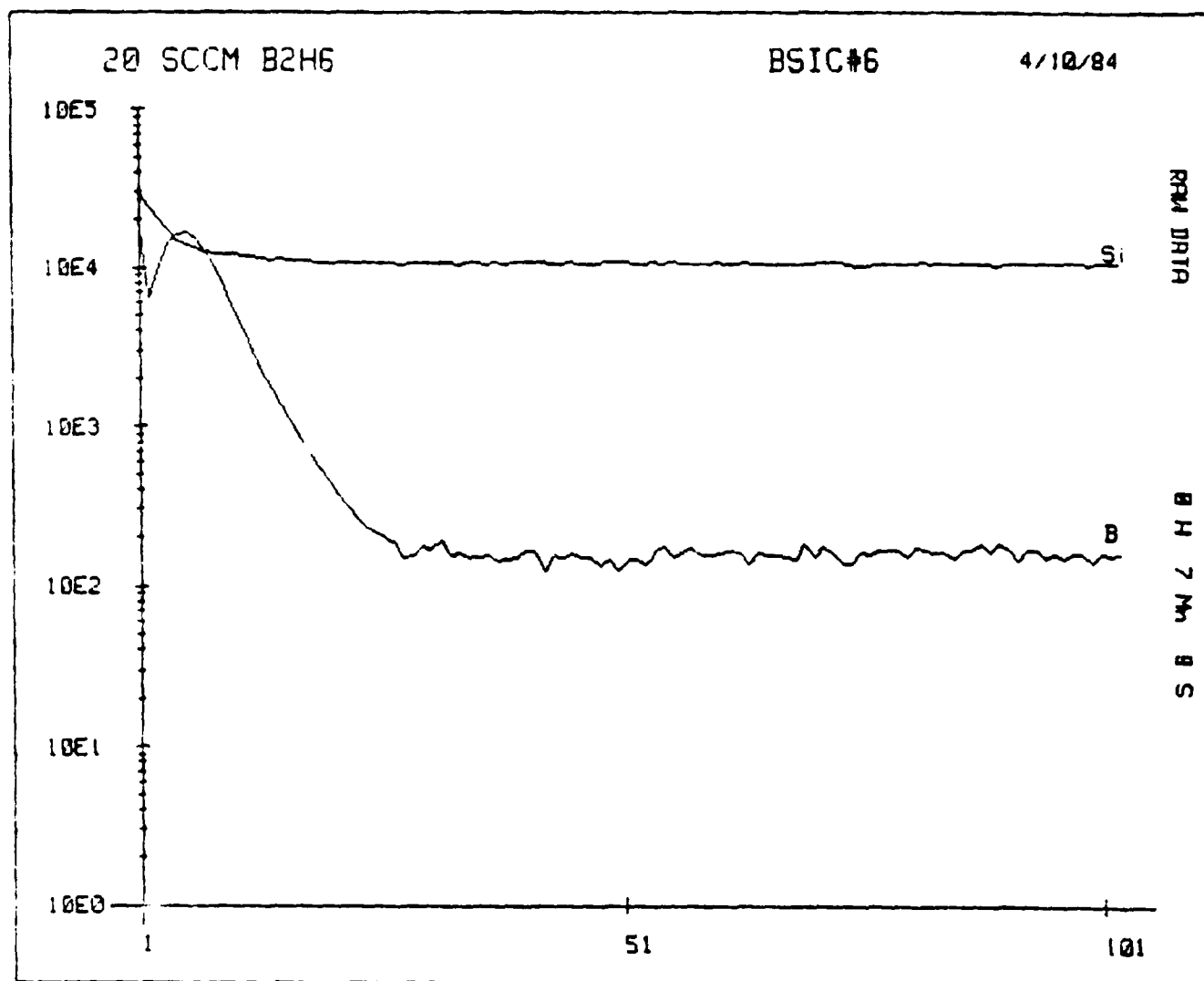
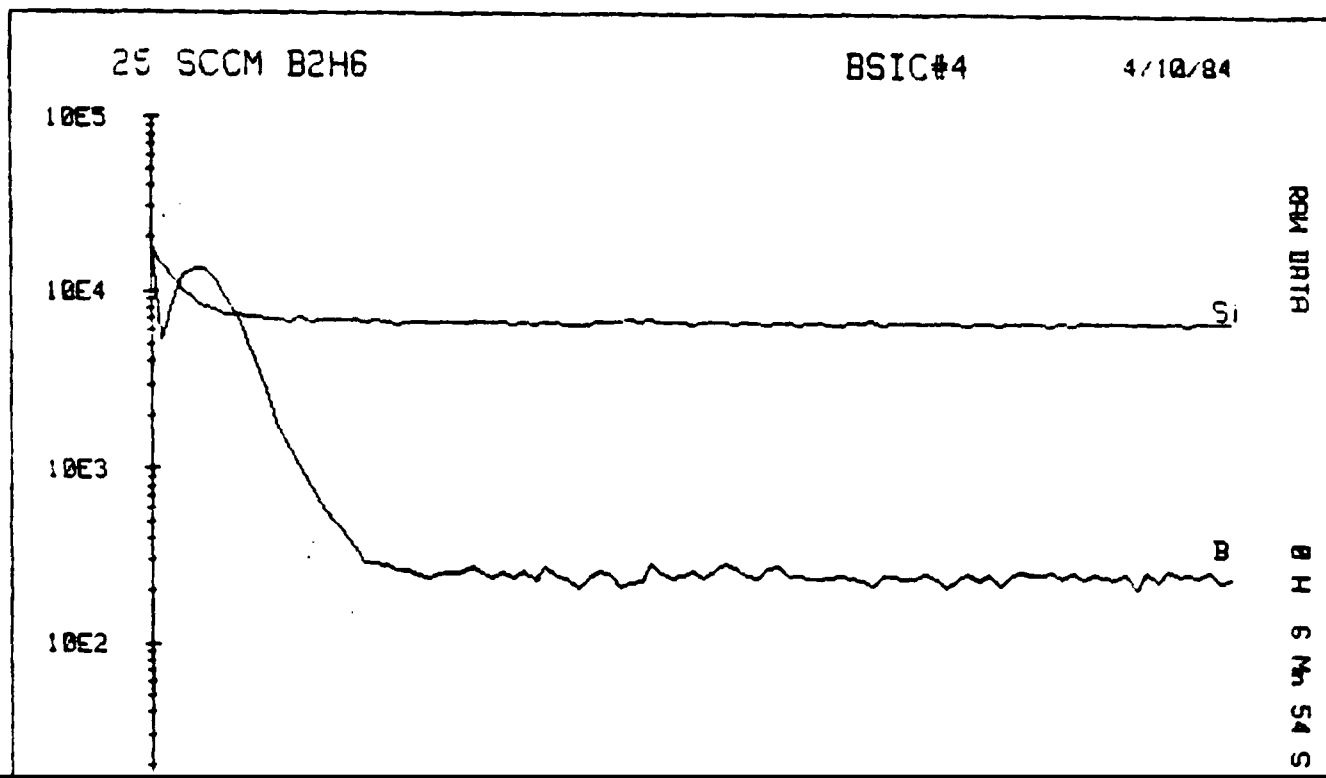


Figure 20. Composition profile of B^+ which has been "in-situ" doped in a 3-SiC thin film using BH_3 and H_2 at a flow rate of 20 sccm.



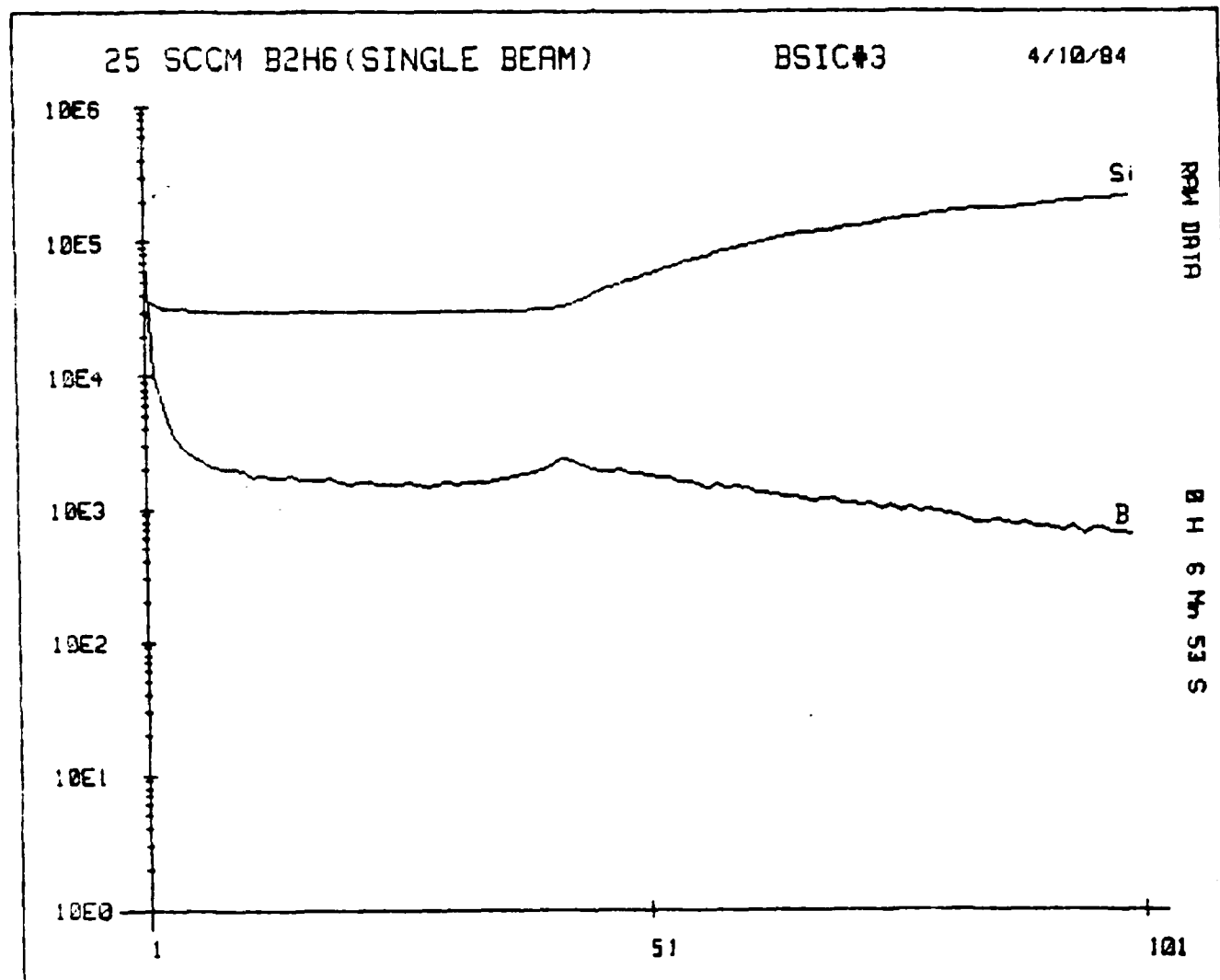


Figure 22. Composition profile of B^+ in 8-SiC films. The film is the same as that described in Figure 21, except the rate of depth profiling is sufficient to penetrate completely the film such that an analysis of the B concentration in the Si substrate is also obtained. The small peak in the middle of the graph represents the 8-SiC/Si interface.

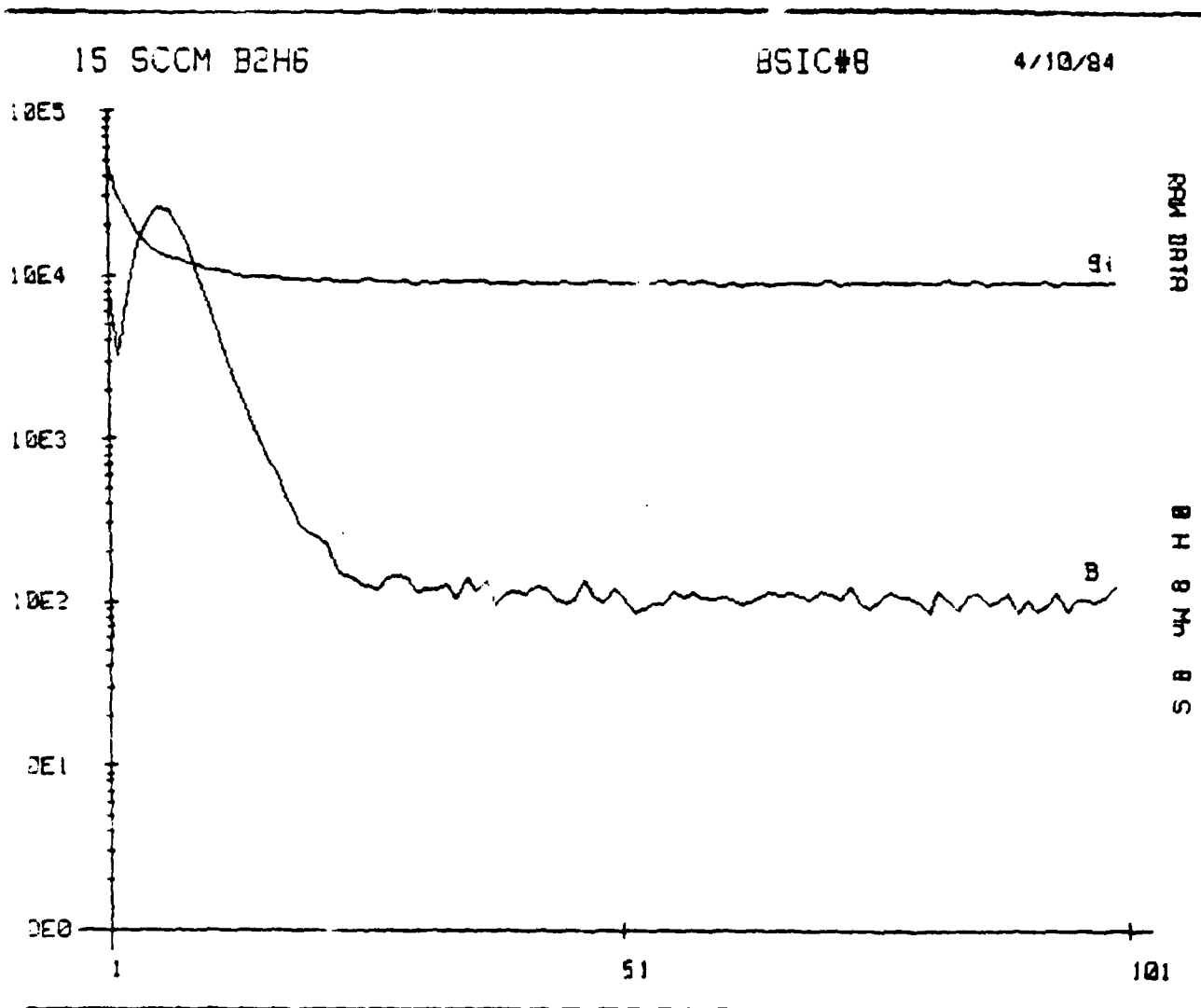


Figure 19. Composition profile of B⁺ which has been "in-situ" doped in a β -SiC thin film using BH₃ and H₂ at a flow rate of 15 sccm.

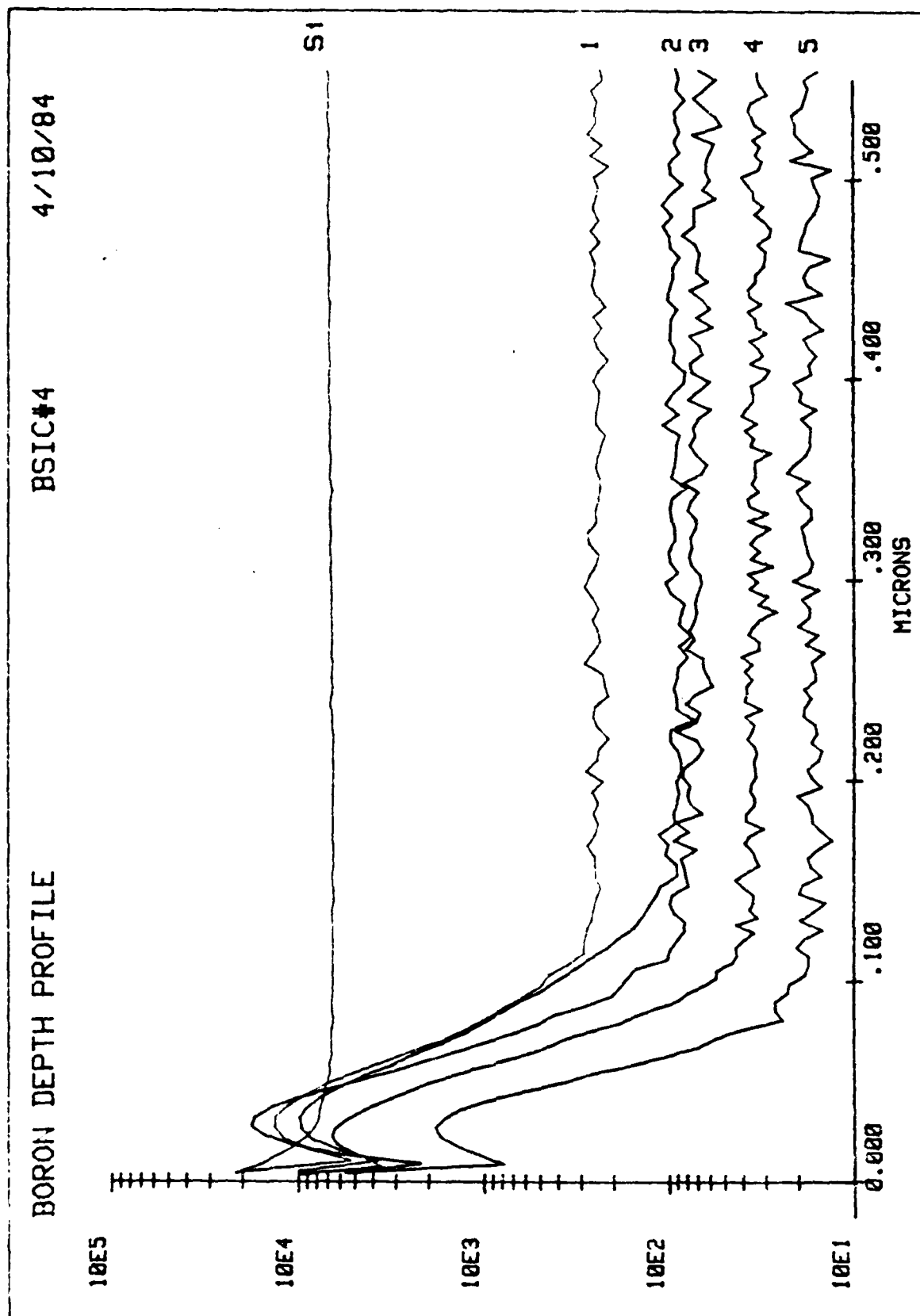


Figure 23. Compilation of figures 17-21 in terms of B⁺ counts vs distance into the film for the various BH₃ in H₂ flow rates. Note that the B count beyond $\approx 0.100 \times 10^{-6}$ m scales with the flow rate with curves #1-5 being the 24, 20, 15, 10 and 5 sccm rates, respectively.

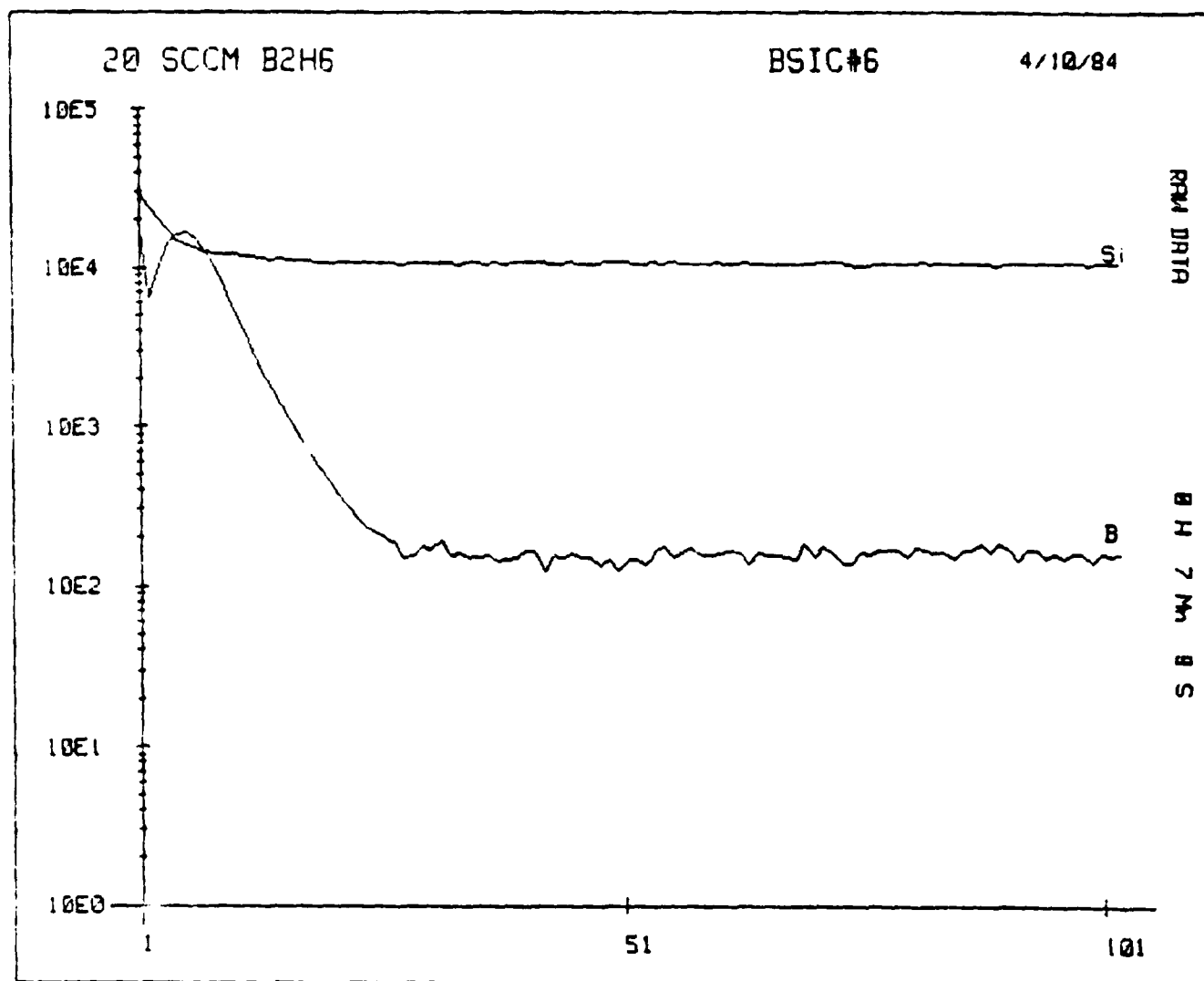


Figure 20. Composition profile of B^+ which has been "in-situ" doped in a 3-SiC thin film using BH_3 and H_2 at a flow rate of 20 sccm.

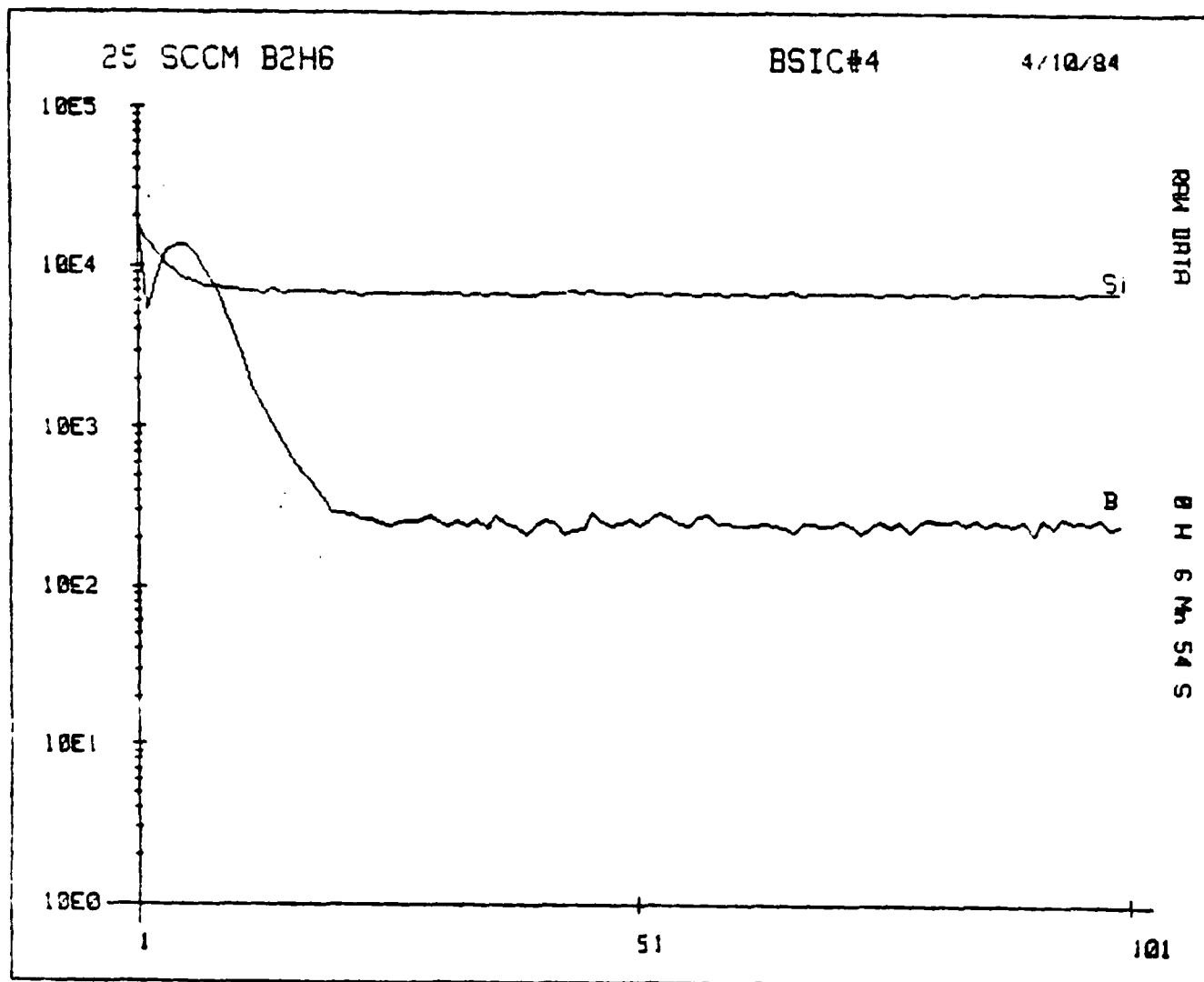


Figure 21. Composition profile of B⁺ which has been "in-situ" doped in a β -SiC thin film using BH₃ and H₂ at a flow rate of 25 sccm.

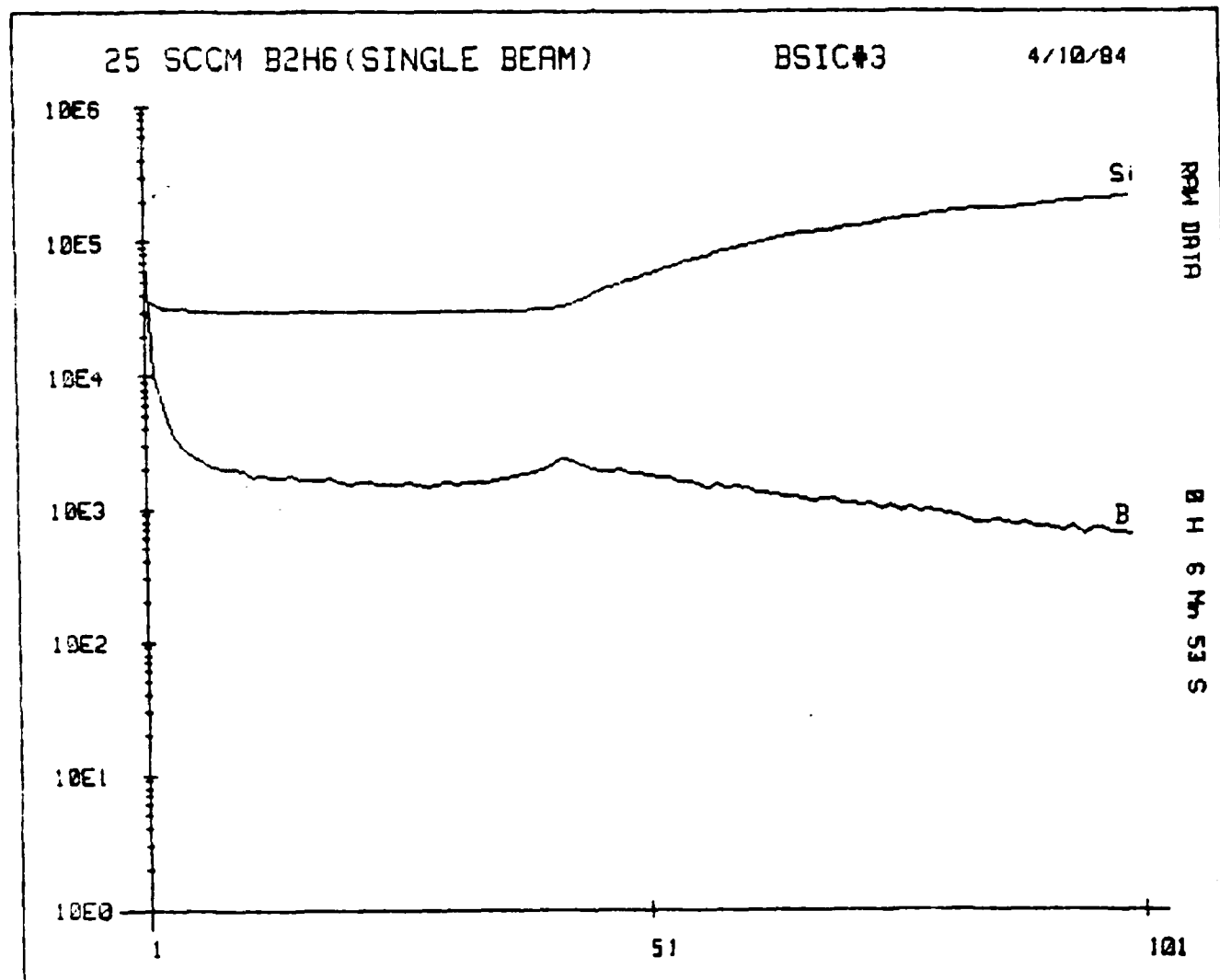


Figure 22. Composition profile of B^+ in 8-SiC films. The film is the same as that described in Figure 21, except the rate of depth profiling is sufficient to penetrate completely the film such that an analysis of the B concentration in the Si substrate is also obtained. The small peak in the middle of the graph represents the 8-SiC/Si interface.

of Fig. 11). Thus $2 - 4 \times 10^{19}$ atoms/cc may represent the P solubility in β -SiC at 1633K.

The increases in the P^+ concentrations in the near surface regions (as well as those of B^+ and Al^+ in Figs. 13-23) is thought to be caused by the fact that during growth the concentrations of SiH_4 and C_2H_4 in the gas stream relative to the concentration of the dopant species are very high. When the valves of the former gases are closed, the concentrations of these species drop considerably in the chamber and the growth slows markedly. However, when the valve to the dopant gases is closed, the relative drop is small and the relative concentration of this gas increases. This leads to the enhanced concentration near the final growth surface.

The concentration of Al as well as B in the regions outside the near surface areas were found to scale in direct proportion to flow rate of the species in H_2 , as shown in Figs. 13-22 and especially Fig. 23. In the case of the Al, the concentration was also directly proportional to the temperature (and, therefore, the vapor pressure) of the TMA, as noted most readily in Table III. Note that the Al profile in Fig. 16 has been mathematically lowered relative to the other Al plots in order to bring it onto the graph.

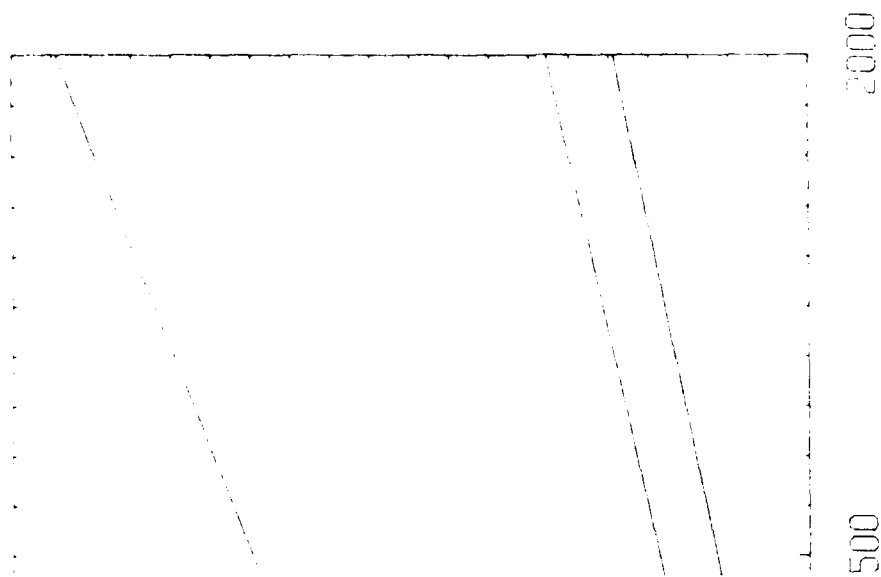
The ion microprobe data noted above was obtained using a $250 \times 10^{-6}m$ sq scanning raster; thus, the rate of profiling was only 0.82 Å/min. However, using a $50 \times 10^{-6}m$ diameter beam allowed a much more rapid rate of profiling and complete penetration of the film and analyses of the dopant in the Si. An example of this is shown in Fig. 22 for B in β -SiC. The small hump in the middle of the graph is the β -SiC/Si interface. As one can see, substantial diffusion of B into Si occurred during growth. Although the 10K ohm-cm resistivity Si contains B at a concentration of $\sim 10^{12}/cm^3$, the level shown in this graph is six orders of magnitude greater than the as-received level. Furthermore, the gradient in concentration is shallow indicating that B diffusion in Si is fast at the temperature of β -SiC growth ($\sim 1593K$). The transport of B is no doubt assisted by pipe diffusion along the misfit dislocations which occur at the Si/ β -SiC interface.

Profiling of the Al^+ composition through the film and into the Si also revealed a hump in Al^+ concentration at the Si/ β -SiC interface of even greater magnitude than in the case of B. No such phenomenon has been observed in the P^+ profiles; however, the total amount of P^+ may be too small to contribute to this increase in composition.

D. In situ Doping of β -SiC Thin Films - Theoretical Considerations

1. Introduction

The technique of in situ doping during thin film growth contrasts with other process technologies which consist of introducing the electronically active impurities from the surface either by diffusion or by ion implantation. The former is subject to the



TEMPERATURE (K)

temperature for B_2H_6 , NH_3 and PH_3 .

of Fig. 11). Thus $2 - 4 \times 10^{19}$ atoms/cc may represent the P solubility in β -SiC at 1633K.

The increases in the P^+ concentrations in the near surface regions (as well as those of B^+ and Al^+ in Figs. 13-23) is thought to be caused by the fact that during growth the concentrations of

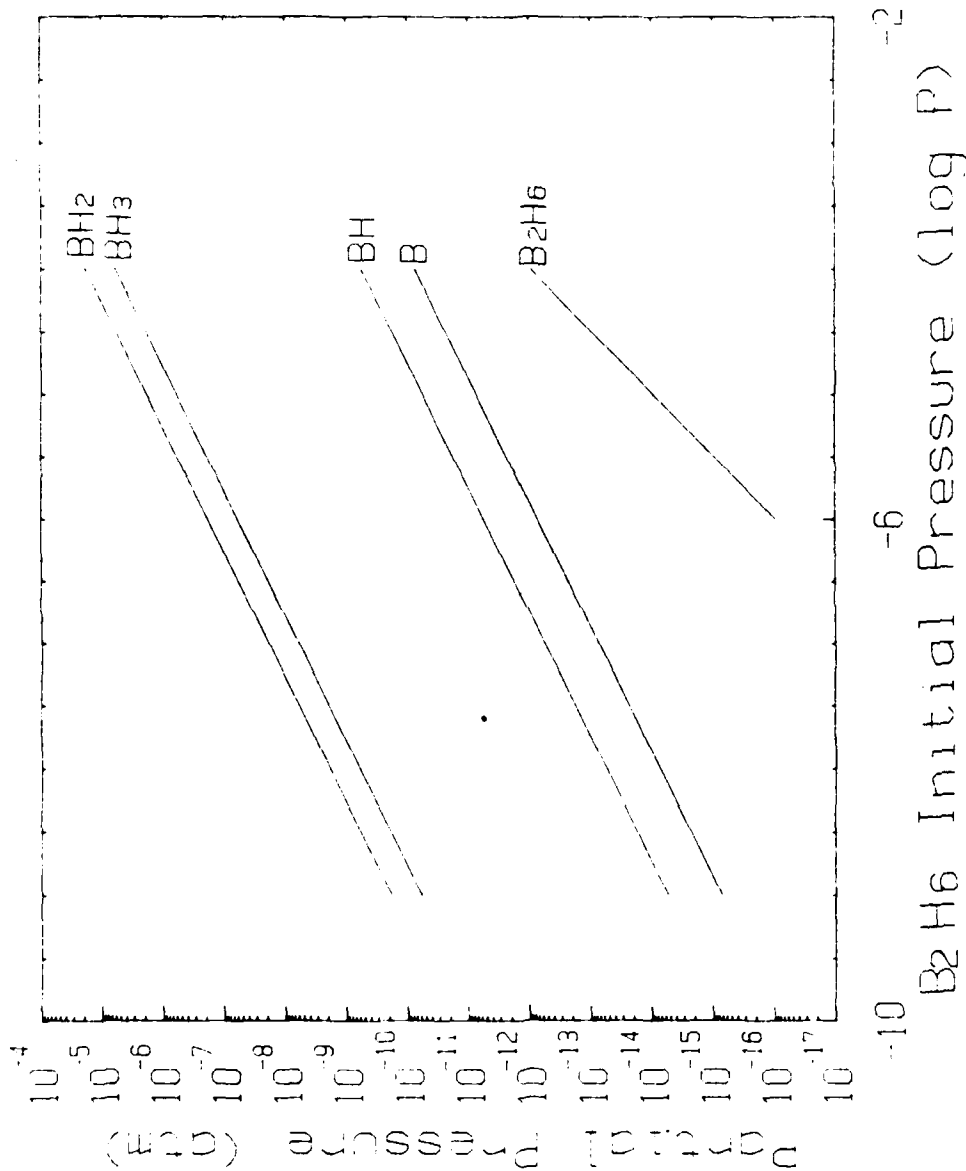


Figure 26. Calculated partial pressures of equilibrium gas species vs initial B_2H_6 gas pressure for the conditions used at NCSU in the CVD deposition of β -SiC. I.e., the gases of C_2H_4 , SiH_4 , and H_2 were also considered present in the mole fractions used experimentally. The total pressure was considered to be one atmosphere.

produced from data given in the JANAF Thermochemical Tables⁷. Data for trimethylaluminum (TMA) is not available. A noteworthy feature of the diagram is that all of the dopant gases have positive free energies of formation at our experimental deposition temperature of 1633K. Therefore, these gases might be expected to completely dissociate at the deposition temperature, if the kinetics for this process are also favorable. However one must consider the effect of the other gases present during CVD on the stability of these dopant sources.

3. Free Energy Minimization Calculations and the Determination of the Gas Species Present During Deposition

Thermodynamic calculations involving all the gases present during deposition provide important information concerning the thermal stability of the dopant gases and allow an educated guess at the molecular and atomic species which are important in determining the kinetics of the CVD reaction.

Calculations of gas phase equilibria for the dopant sources were made by using the computer program "SOLGASMIX-PV" which determines equilibrium compositions by direct minimization of the total free energy of a system at various combinations of temperature, total pressure and gas composition. The necessary thermodynamic values for most of the many species which were considered to possibly exist during deposition were also taken from the JANAF Tables⁹.

The data resulting from these calculations are shown in Figs. 25, 26, and 27. These figures show the calculated equilibrium partial pressures for the various possible gaseous constituents which contain the dopant vs initial reactant gas pressure for P (Fig. 25), B (Fig. 26) and N (Fig. 27) in the Si-C-H system. The calculations were made for the temperature of 1633K and one atmosphere total pressure (the deposition conditions for producing undoped SiC). As implied above all the gases used in the deposition of α -SiC including SiH_4 , C_2H_4 and H_2 as well as the dopant gas in the mole fractions normally employed or under consideration for employment (the dopant gas) were included in the calculations.

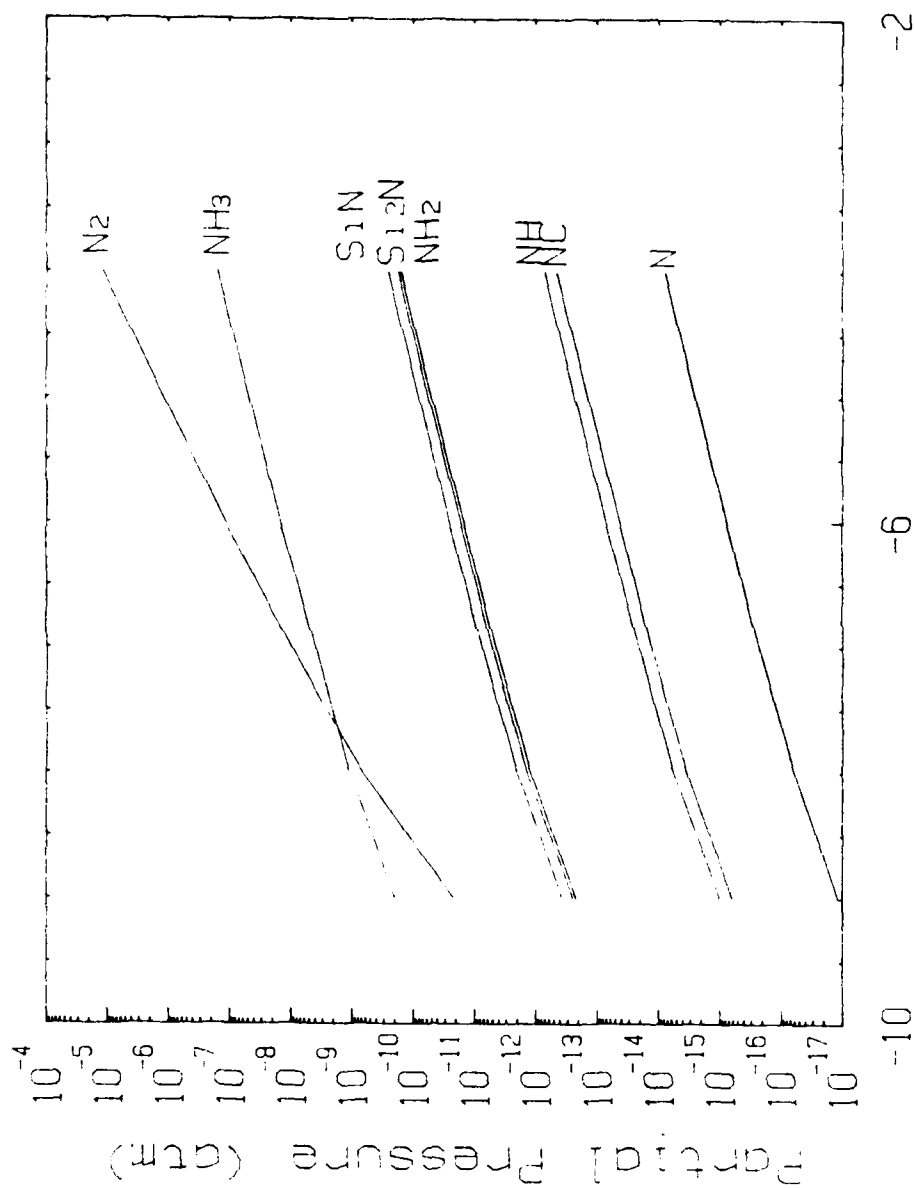
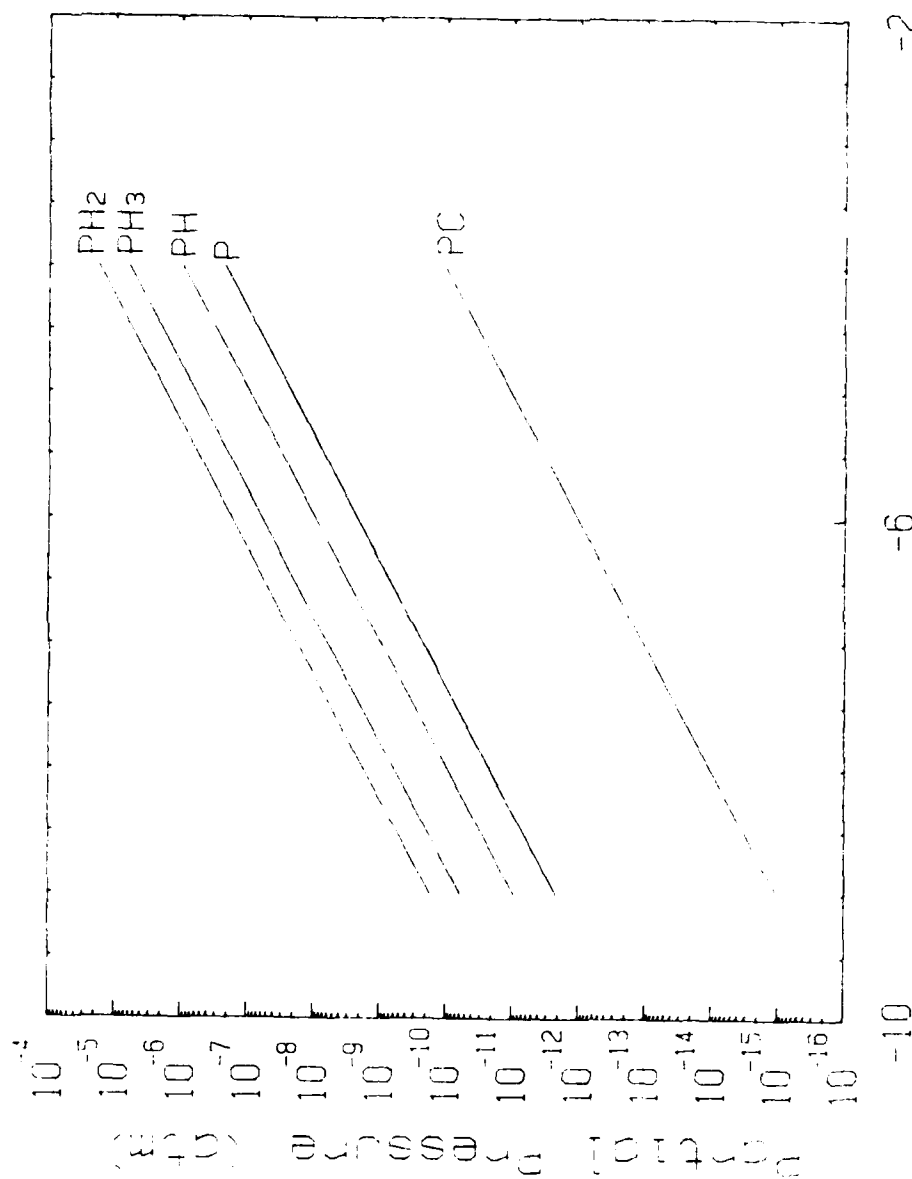


Figure 27. NH_3 Initial Pressure (log P)

Calculated partial pressures of equilibrium gas species vs initial NH_3 gas pressure for the conditions used at NCSU in the CVD deposition of B-SiC. I.e., the gases of C_2H_4 , SiH_4 and H_2 were also considered present in the mole fractions used experimentally. The total pressure was considered to be one atmosphere. NC = nitrogen carbide (gas).



PH₃ Initial Pressure (log P)

Figure 25. Calculated partial pressures of the equilibrium gas species vs the initial PH₃ gas pressure for the conditions used at NCSU in the CVD deposition of β -SiC. I.e., the gases of C₂H₄, SiH₄ and H₂ were also considered present in the mole fractions used experimentally. The total pressure was considered to be one atmosphere. PC = phosphorous carbide (gas).

As noted above, Figs. 25-27 show only the dopant-containing vapor species. The reason for this is that under the conditions used in the present research, no dopant-containing condensed phases were found. An interesting result provided by these calculations is that, with the exception of nitrogen, the species with the highest partial pressure at the deposition temperature are hydrides. The reason for this is the large amount of H_2 carrier gas used in the deposition process which prevents the occurrence of high concentration of the pure elemental species.

4. Equilibrium Solubility Considerations and Measured Concentrations of Dopants in SiC Thin Films

Using the equilibrium solubility considerations of Rai-Choudhury and Salkovitz⁸, the dopant species, when dissolved but not electrically activated (ionized) in the silicon carbide, is presumed to follow Henry's law for a dilute solute, i.e.,

$$P_D^{1/y} = K_D' N_D' \quad (1)$$

where P_D is the gas phase partial pressure of the dopant species in equilibrium with the solid; y is the number of dopant atoms per molecule of the above species; K_D' is the Henry's law constant of the dopant in the solid solution, and N_D' is the concentration of unionized dopant in the solid solution. The activity coefficient, γ_D , may be defined as follows

$$\gamma_D = \frac{N_D' K_D'}{N_D K_D} \quad (2)$$

where γ_D is the ratio of the unionized dopant atom concentration at some actual N_D to that at infinite dilution; N_D is the total chemical concentration of the dopant and K_D is a new Henry's law constant for total dopant concentration.

Combining equations (1) and (2), one gets

$$P_D^{1/y} = K_D \cdot N_D \quad (3)$$

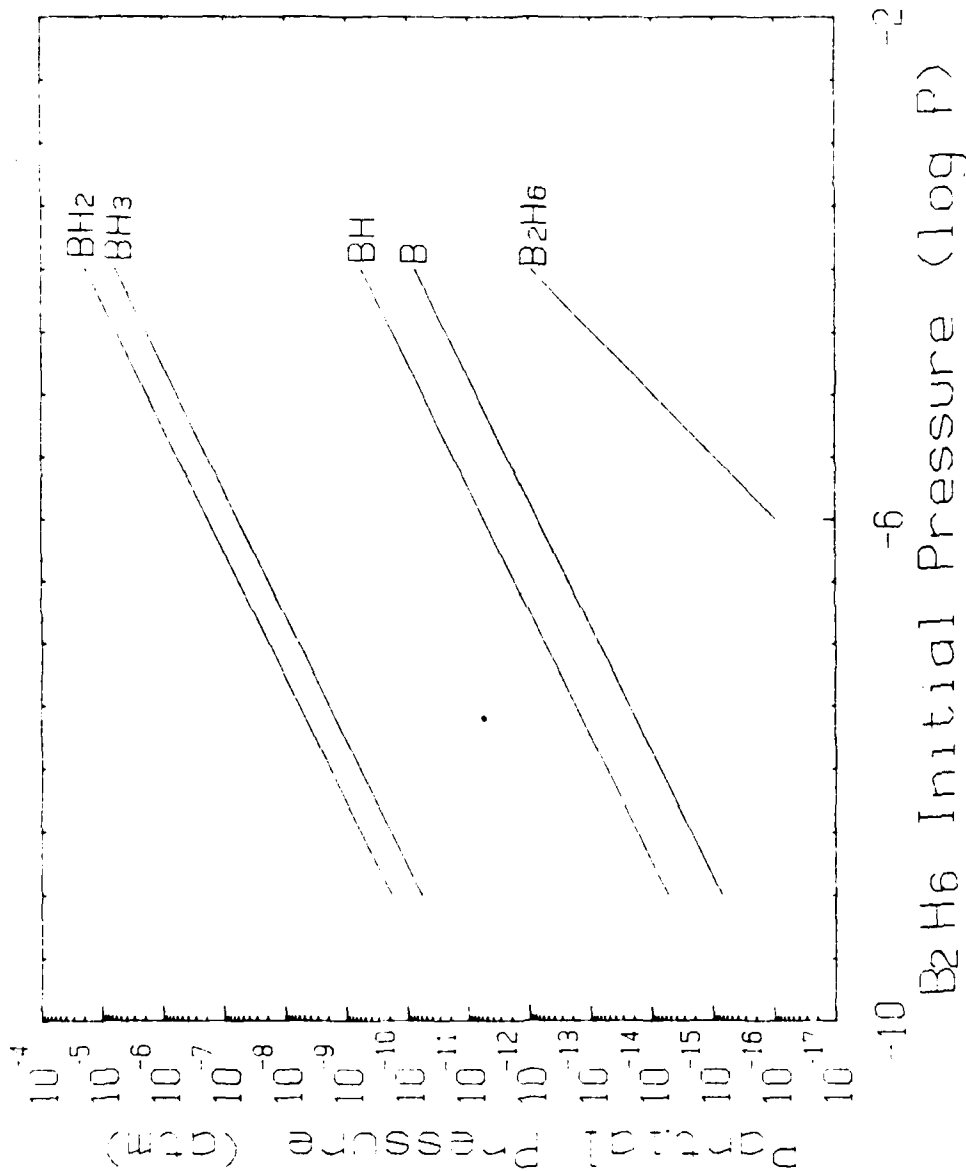


Figure 26. Calculated partial pressures of equilibrium gas species vs initial B_2H_6 gas pressure for the conditions used at NCSU in the CVD deposition of β -SiC. I.e., the gases of C_2H_4 , SiH_4 , and H_2 were also considered present in the mole fractions used experimentally. The total pressure was considered to be one atmosphere.

This last equation predicts that a plot of $\log N_D$ vs $\log P_D$ should be linear with a slope $1/y$, for $N_D < 1 \times 10^{18} \text{ cm}^{-3}$ at typical epitaxial deposition temperatures. At higher concentrations, where a significant fraction of the donor or acceptor atoms in the solid are ionized, the activity coefficient becomes larger than one.

The above procedure allows one to relate the solid dopant partial pressure to the gas phase dopant concentration at equilibrium. Figures 28 and 29 show the results of solid-state dopant concentration vs the initial gas phase dopant partial pressure of B and P, respectively. The solid state dopant concentrations were measured using the ion microprobe. Each figure shows that the log of the solid dopant concentration is linear when plotted as a function of the log of the gas phase dopant concentration. These results are consistent with the Henry's law description of doping.

Figure 30 shows the solid-state Al concentration in SiC as a function of the partial pressure of TMA calculated from the vapor pressure of TMS, the amount of hydrogen flowing over the TMA vessel and the temperature. This result also shows that the Al concentration tracks the partial pressure of TMA as it is altered by changes of the H_2 flow rate through the vessel.

Finally, Fig. 31 shows that N incorporation in β -SiC follows the same linear relationship with partial pressure of NH_3 as shown above for the other dopant species. In this case however, the solubility limit appears to have been reached at $\sim 2 \times 10^{20}$ atoms/cc as noted in the previous subsection.

The results of this latter study are consistent with the results reported by J. Bloem¹⁰ for dopant incorporation in Si in that the rate of dopant incorporation is linearly proportional to the mole fraction (N) of the starting dopant gas in the range of mole fractions between 10^{-9} and 10^{-6} . However, these results do not provide an indication as to which species is in equilibrium with the impurity incorporated in the solid, i.e., which particular single or multiple species provided the dopant atoms which were incorporated in the β -SiC. Furthermore, we are not sure that all of the various

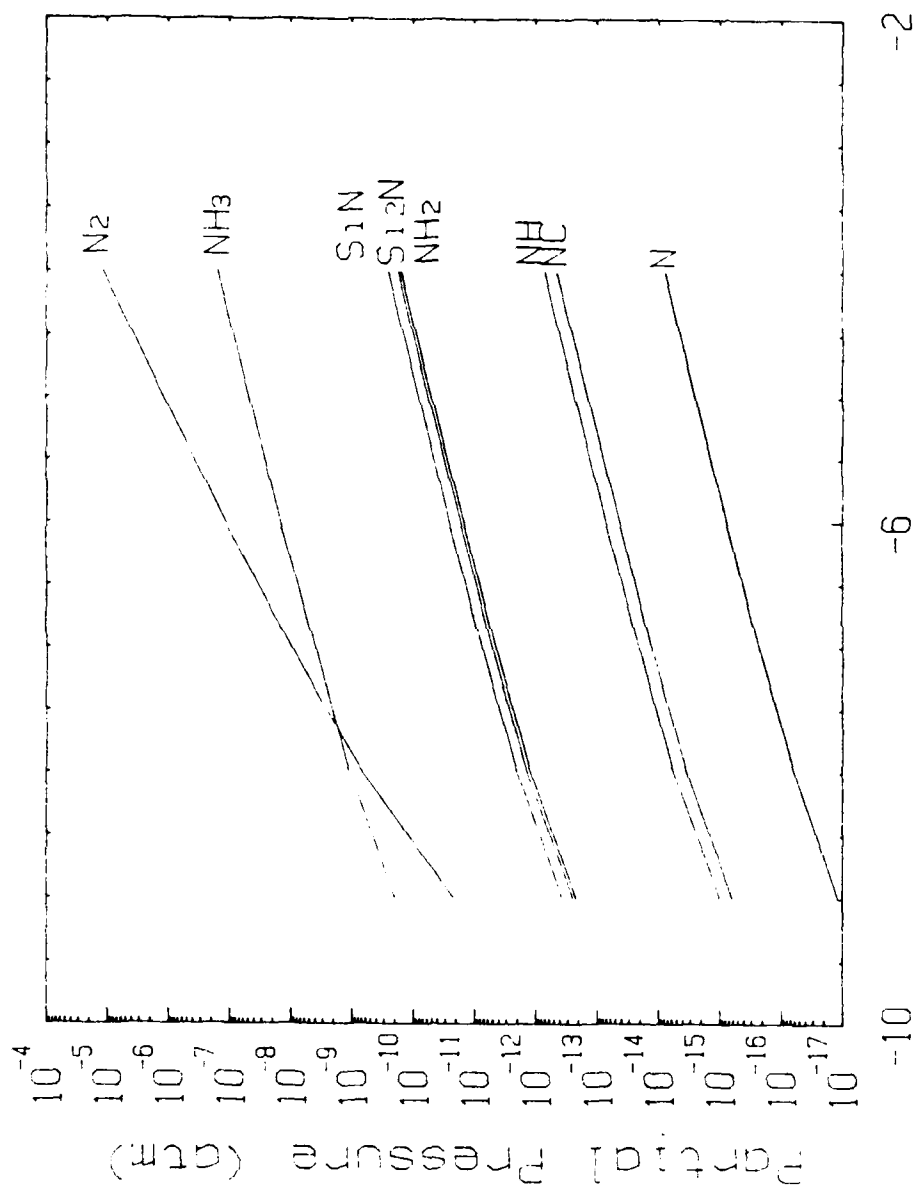


Figure 27. NH_3 Initial Pressure (log P)

Calculated partial pressures of equilibrium gas species vs initial NH_3 gas pressure for the conditions used at NCSU in the CVD deposition of B-SiC. I.e., the gases of C_2H_4 , SiH_4 and H_2 were also considered present in the mole fractions used experimentally. The total pressure was considered to be one atmosphere. NC = nitrogen carbide (gas).

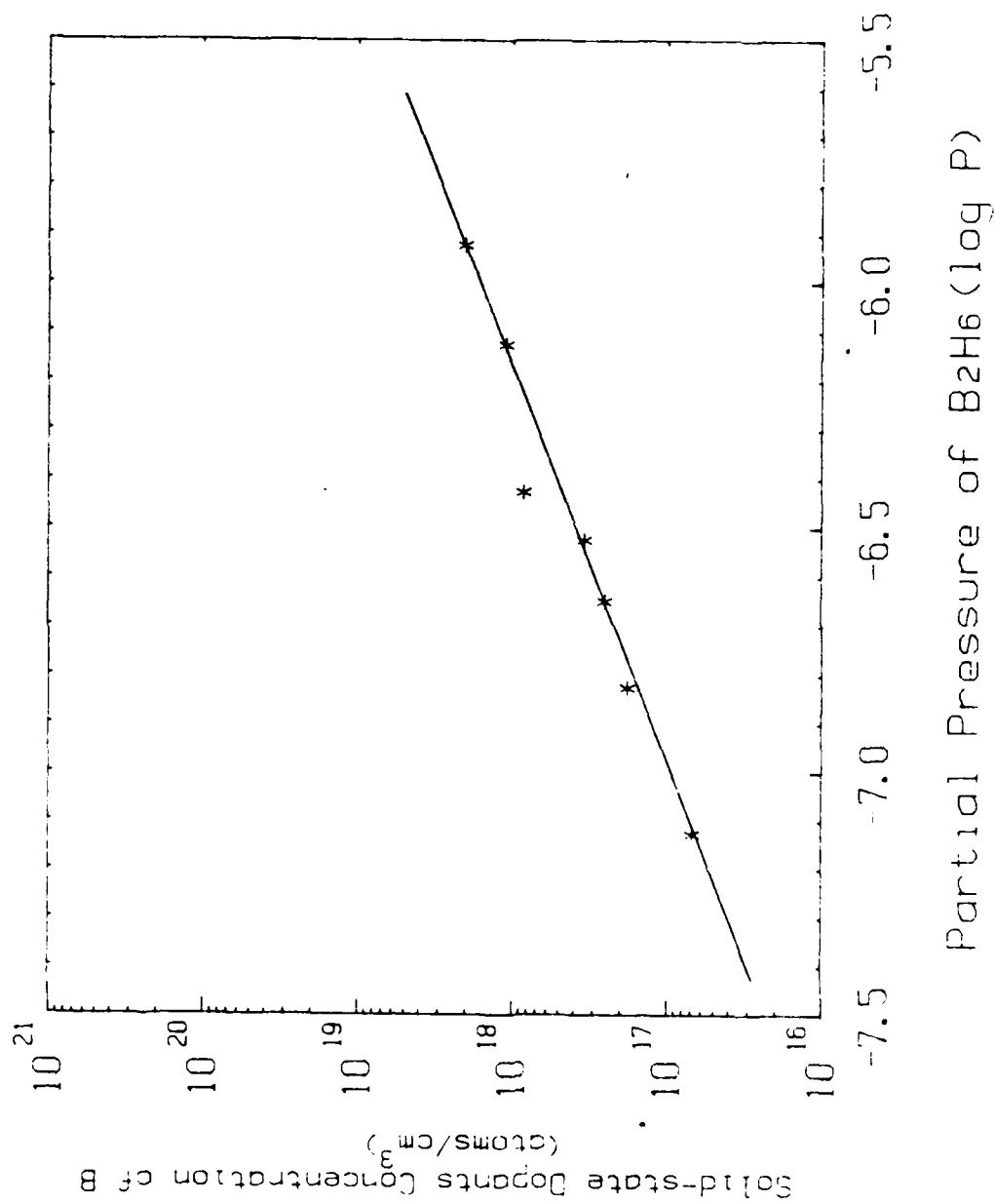


Figure 28. Experimentally measured solid-state dopant concentration of B in CVD grown β -SiC films vs initial partial pressure of B₂H₆ in flowing H₂.

As noted above, Figs. 25-27 show only the dopant-containing vapor species. The reason for this is that under the conditions used in the present research, no dopant-containing condensed phases were found. An interesting result provided by these calculations is that, with the exception of nitrogen, the species with the highest partial pressure at the deposition temperature are hydrides. The reason for this is the large amount of H_2 carrier gas used in the deposition process which prevents the occurrence of high concentration of the pure elemental species.

4. Equilibrium Solubility Considerations and Measured Concentrations of Dopants in SiC Thin Films

Using the equilibrium solubility considerations of Rai-Choudhury and Salkovitz⁸, the dopant species, when dissolved but not electrically activated (ionized) in the silicon carbide, is presumed to follow Henry's law for a dilute solute, i.e.,

$$P_D^{1/y} = K_D' N_D' \quad (1)$$

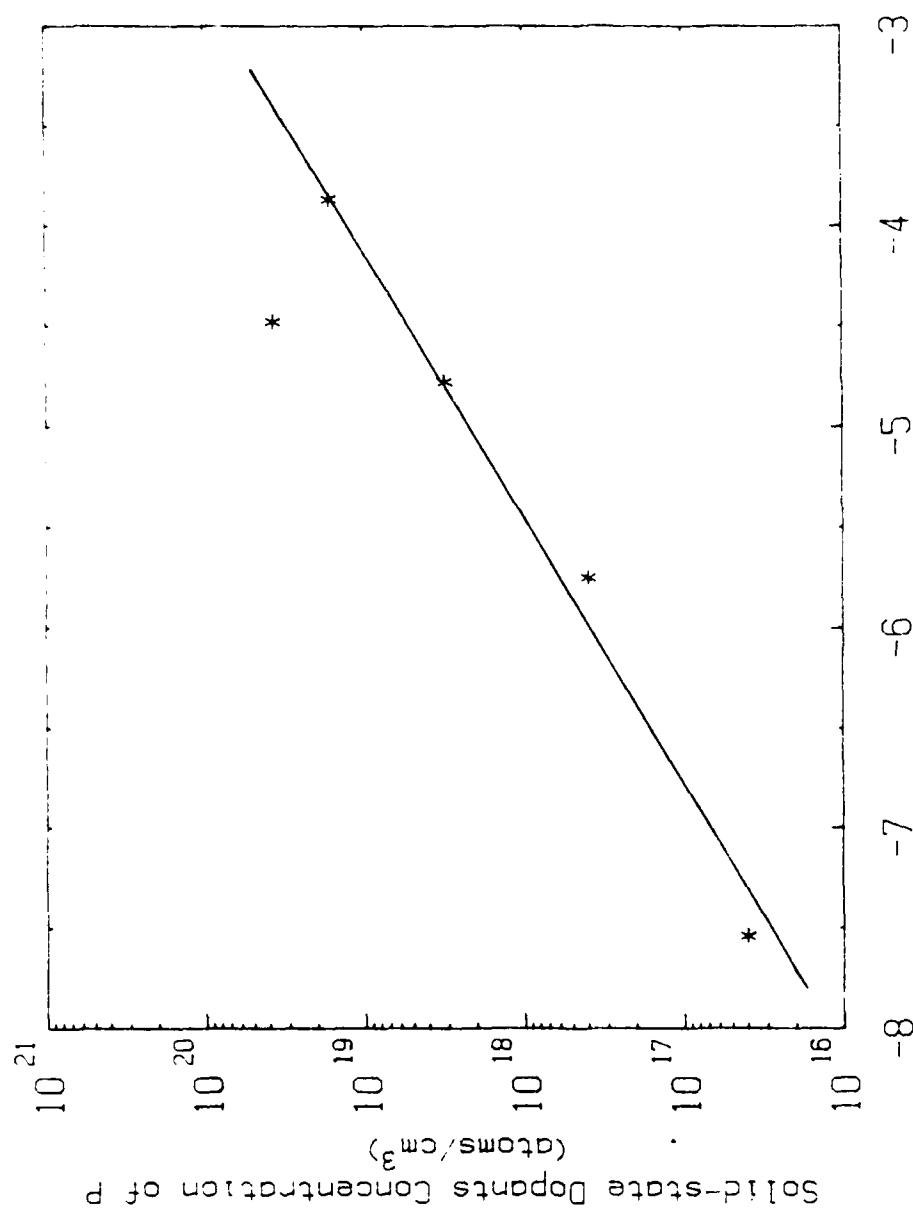
where P_D is the gas phase partial pressure of the dopant species in equilibrium with the solid; y is the number of dopant atoms per molecule of the above species; K_D' is the Henry's law constant of the dopant in the solid solution, and N_D' is the concentration of unionized dopant in the solid solution. The activity coefficient, γ_D , may be defined as follows

$$\gamma_D = \frac{N_D' K_D'}{N_D K_D} \quad (2)$$

where γ_D is the ratio of the unionized dopant atom concentration at some actual N_D to that at infinite dilution; N_D is the total chemical concentration of the dopant and K_D is a new Henry's law constant for total dopant concentration.

Combining equations (1) and (2), one gets

$$P_D^{1/y} = K_D \cdot N_D \quad (3)$$



Partial Pressure of PH₃ (log P)

Figure 29. Experimentally measured solid-state dopant concentration of P in CVD grown β -SiC films vs initial partial pressure of PH₃ in flowing H₂.

This last equation predicts that a plot of $\log N_D$ vs $\log P_D$ should be linear with a slope $1/y$, for $N_D < 1 \times 10^{18} \text{ cm}^{-3}$ at typical epitaxial deposition temperatures. At higher concentrations, where a significant fraction of the donor or acceptor atoms in the solid are ionized, the activity coefficient becomes larger than one.

The above procedure allows one to relate the solid dopant partial pressure to the gas phase dopant concentration at equilibrium. Figures 28 and 29 show the results of solid-state dopant concentration vs the initial gas phase dopant partial pressure of B and P, respectively. The solid state dopant concentrations were measured using the ion microprobe. Each figure shows that the log of the solid dopant concentration is linear when plotted as a function of the log of the gas phase dopant concentration. These results are consistent with the Henry's law description of doping.

Figure 30 shows the solid-state Al concentration in SiC as a function of the partial pressure of TMA calculated from the vapor pressure of TMS, the amount of hydrogen flowing over the TMA vessel and the temperature. This result also shows that the Al concentration tracks the partial pressure of TMA as it is altered by changes of the H_2 flow rate through the vessel.

Finally, Fig. 31 shows that N incorporation in β -SiC follows the same linear relationship with partial pressure of NH_3 as shown above for the other dopant species. In this case however, the solubility limit appears to have been reached at $\sim 2 \times 10^{20}$ atoms/cc as noted in the previous subsection.

The results of this latter study are consistent with the results reported by J. Bloem¹⁰ for dopant incorporation in Si in that the rate of dopant incorporation is linearly proportional to the mole fraction (N) of the starting dopant gas in the range of mole fractions between 10^{-9} and 10^{-6} . However, these results do not provide an indication as to which species is in equilibrium with the impurity incorporated in the solid, i.e., which particular single or multiple species provided the dopant atoms which were incorporated in the β -SiC. Furthermore, we are not sure that all of the various

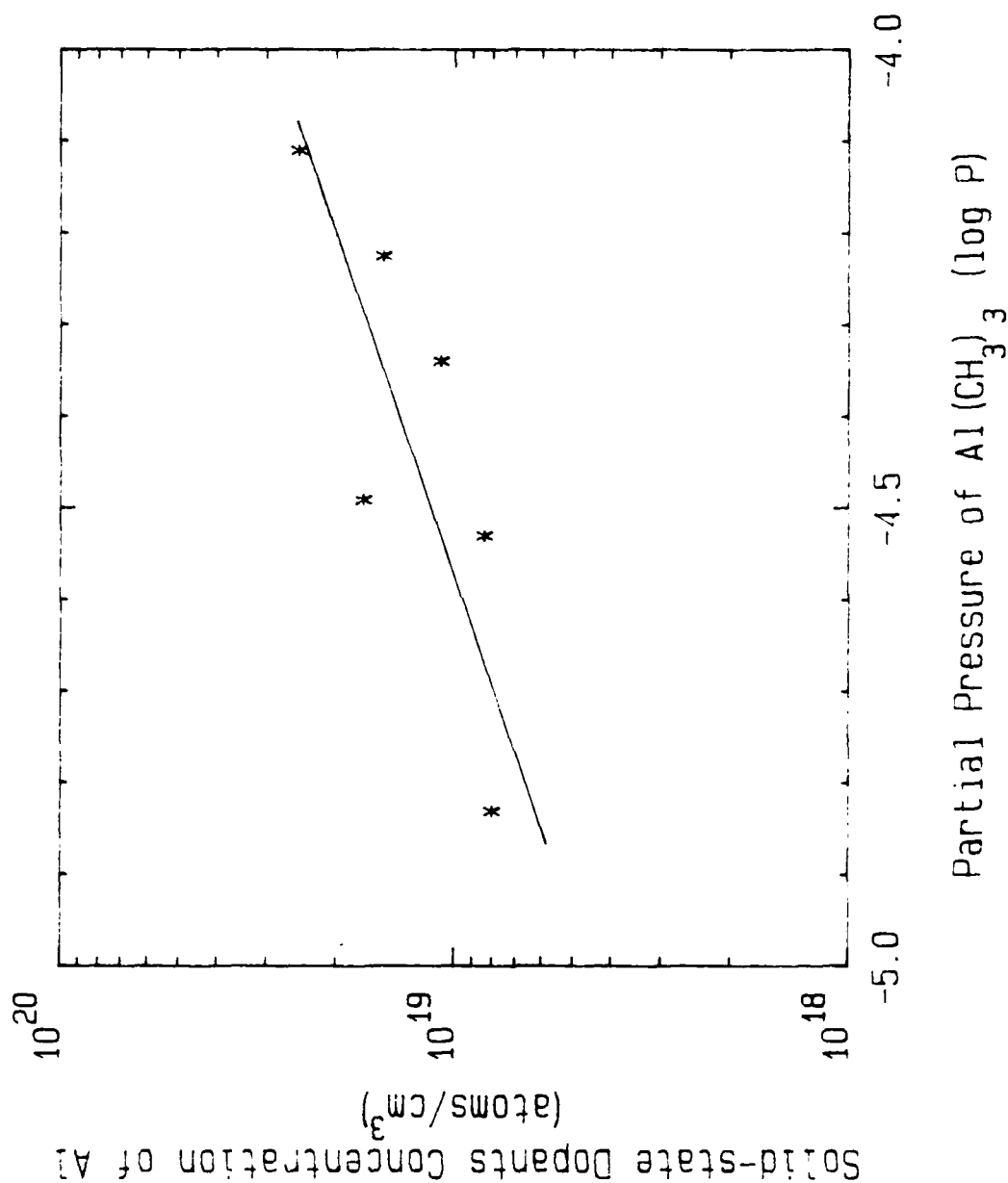
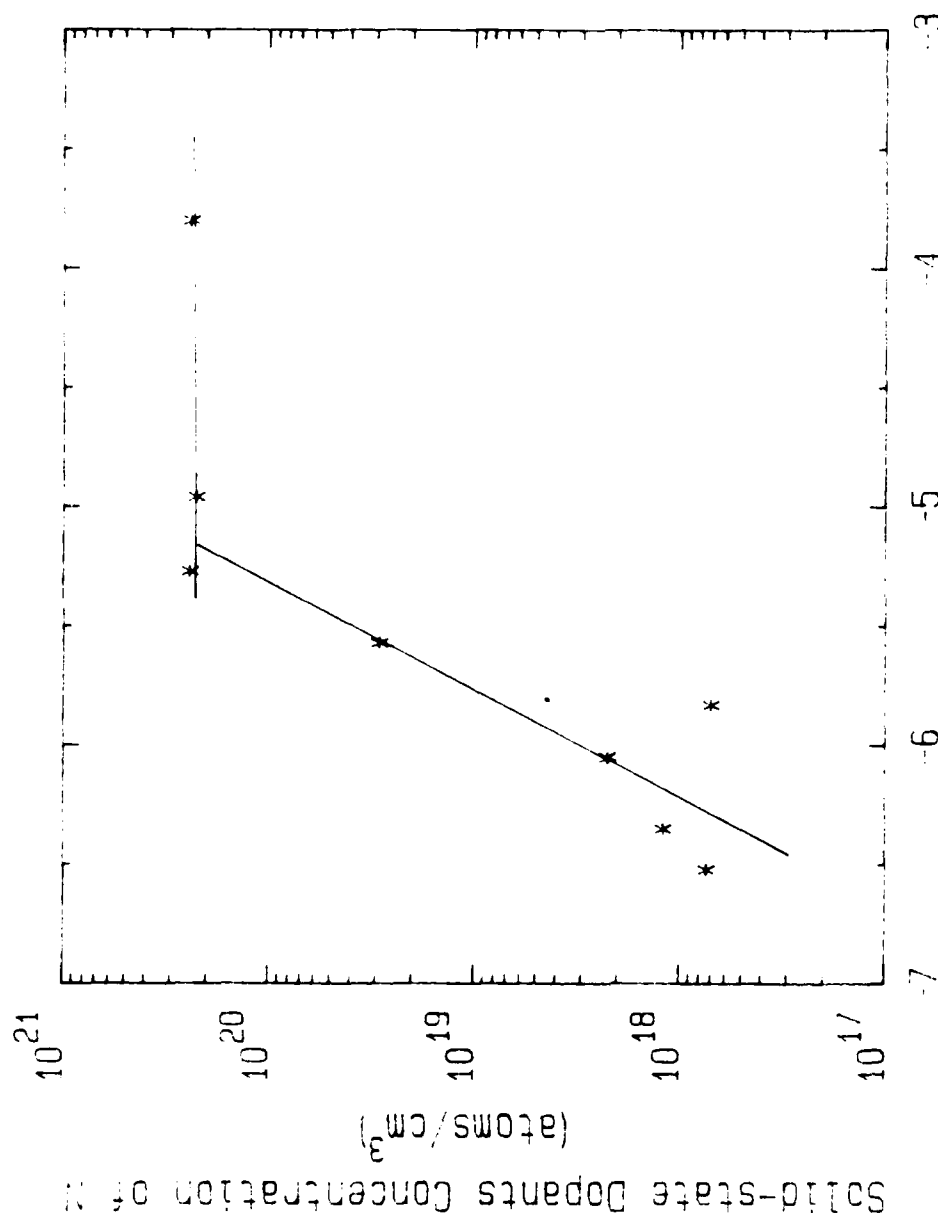


Figure 30. Experimentally measured solid-state dopant concentration of Al in CVD grown n-SiC films vs partial pressure of Al(CH₃)₃ in flowing H₂.



Partial Pressure of N_2 or NH_3 (log P)

Figure 31. Experimentally measured solid-state dopant concentration of N in CVD grown n-SiC films vs partial pressures of N_2 or NH_3 in flowing H_2 .

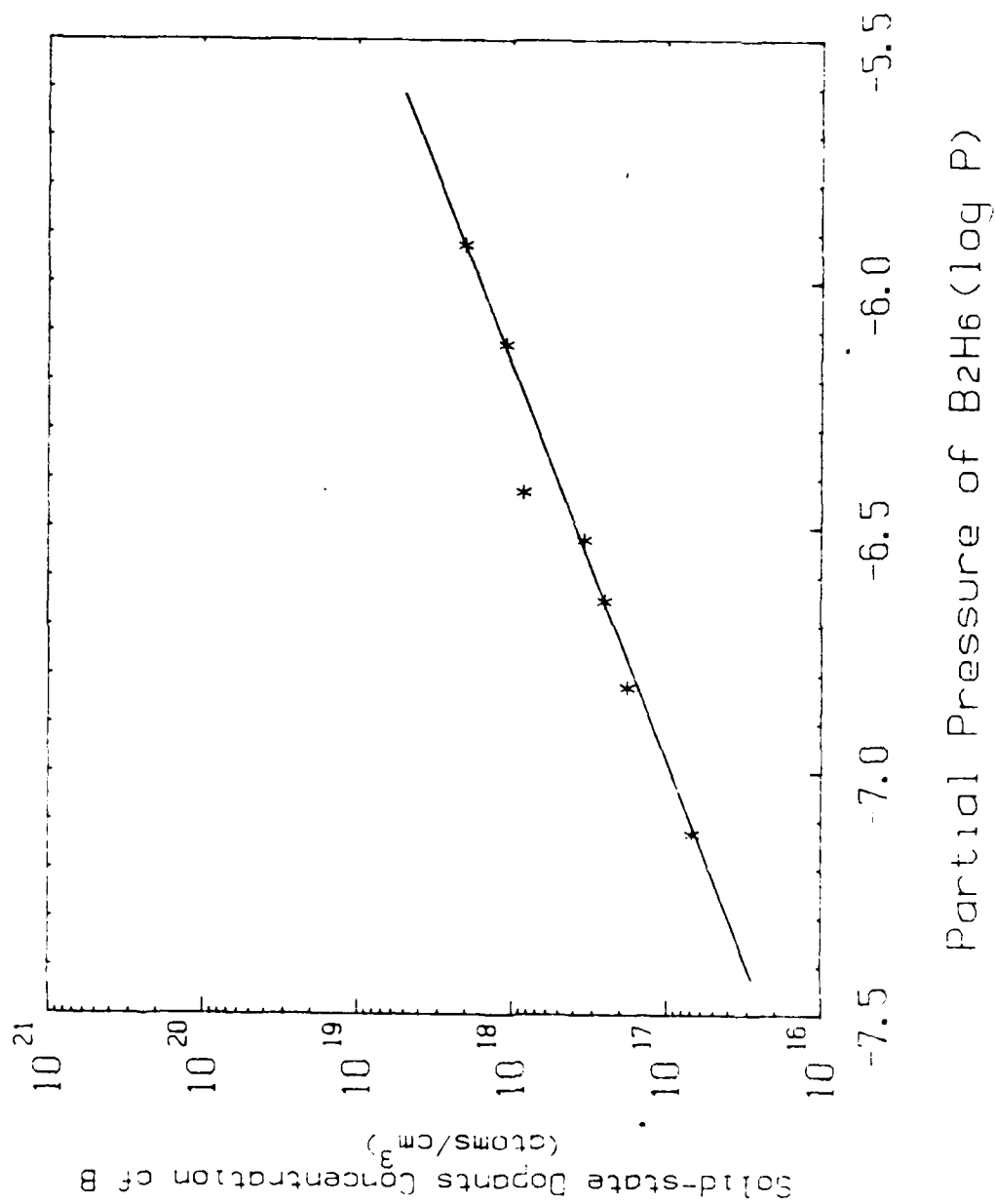


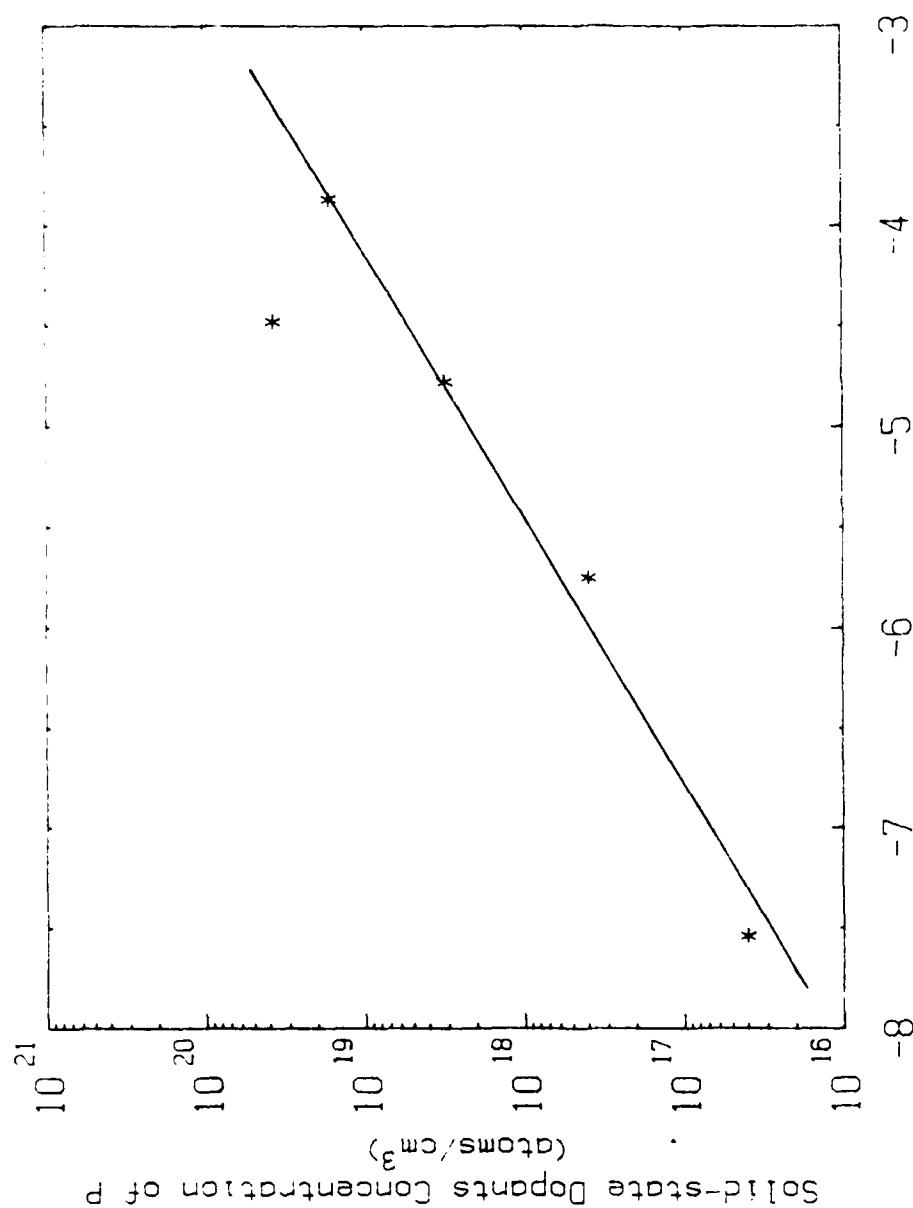
Figure 28. Experimentally measured solid-state dopant concentration of B in CVD grown β -SiC films vs initial partial pressure of B₂H₆ in flowing H₂.

species predicted in Figs. 24-27 would actually be present in our system for it is not necessarily at equilibrium during the growth process. These calculations nevertheless provide useful insight into the dopant gas phase species which are likely to be present in equilibrium with silicon carbide and which may enter into the rate processes determining the elemental doping level in the solid thin film.

5. Dopant Partial Pressures, Resultant Chemical Concentrations and Electronic Carrier Concentrations in β -SiC

As illustrated in Figs. 25-27, the various dopant sources decompose to several species in equilibrium under the conditions used in the NCSU CVD reactor to grow the β -SiC thin films. It is very unlikely that all of these gaseous constituents containing the given dopant species contribute to doping the films in proportion to their equilibrium partial pressure. Some of the constituents must undergo additional decomposition lest H must be incorporated in the sample. Thus, for the purpose of this particular study of chemical and electronic carrier concentrations as a function of dopant partial pressure, only the monoatomic species of N, P, B and Al are considered to be the constituents from which dopant incorporation actually occurs. Figure 32 is a composite diagram taken from Figs. 25-27 for each of the species of N (or N_2), P and B. Although P has the highest partial pressure of the monoatomic species, it has the lowest atomic concentration in the SiC at a given partial pressure of the PH_3 dopant gas as shown in Fig. 33. The reverse is true for N and NH_3 . Thus the incorporation of a particular species into SiC depends strongly on the sticking coefficient of that species which, in turn, depends on the kinetics of diffusion of the gaseous species to and away from the substrate and the rate of reaction, on the availability of a lattice site, the ease of substitution on that site and the ability to chemically bond to the structure at the temperatures of growth. In effect this is essentially a measure of the solubility of the species as discussed below.

Although solubility data from direct measurements such as diffusion or lattice parameter studies are not available for the temperature range of CVD growth (1600-1673K) used in this research, the SIMS



Partial Pressure of PH₃ (log P)

Figure 29. Experimentally measured solid-state dopant concentration of P in CVD grown β -SiC films vs initial partial pressure of PH₃ in flowing H₂.

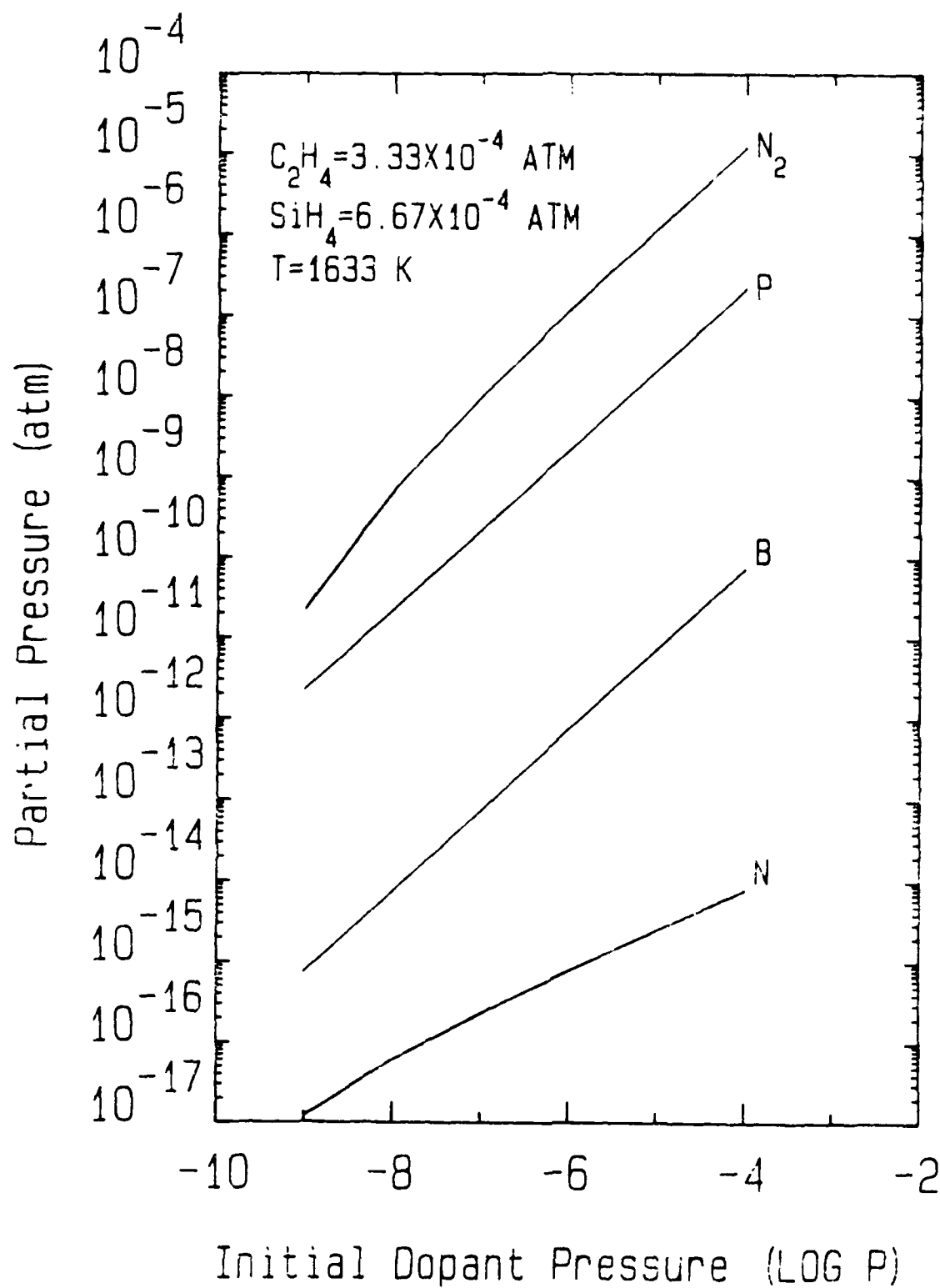


Figure 32. Calculated partial pressure of dopant atoms vs. initial pressure of dopant source gases at the deposition conditions of 1633K, 760 Torr, 1 sccm C_2H_4 , 2 sccm SiH_4 and 3000 sccm H_2 .

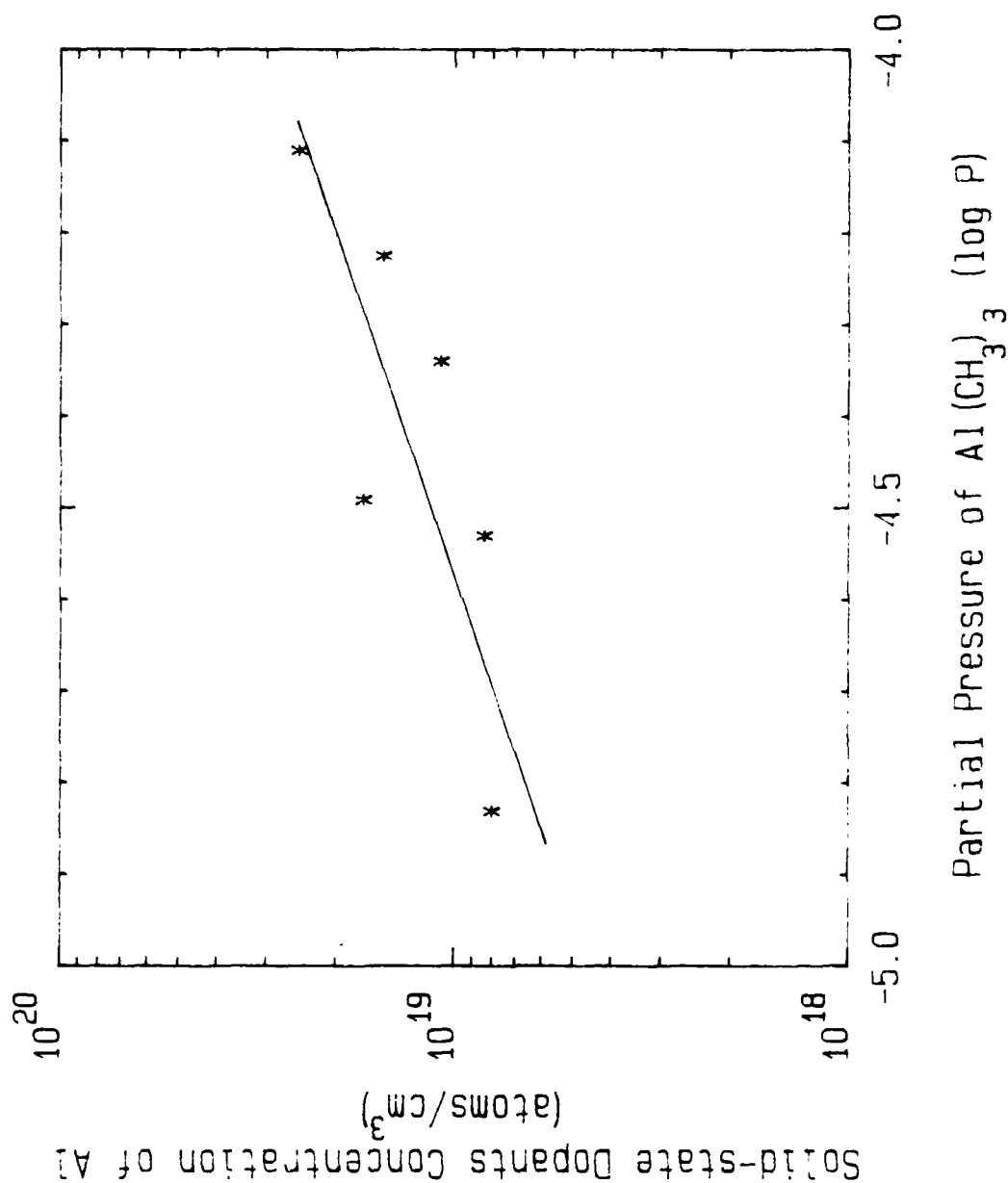


Figure 30. Experimentally measured solid-state dopant concentration of Al in CVD grown n-SiC films vs partial pressure of Al(CH₃)₃ in flowing H₂.

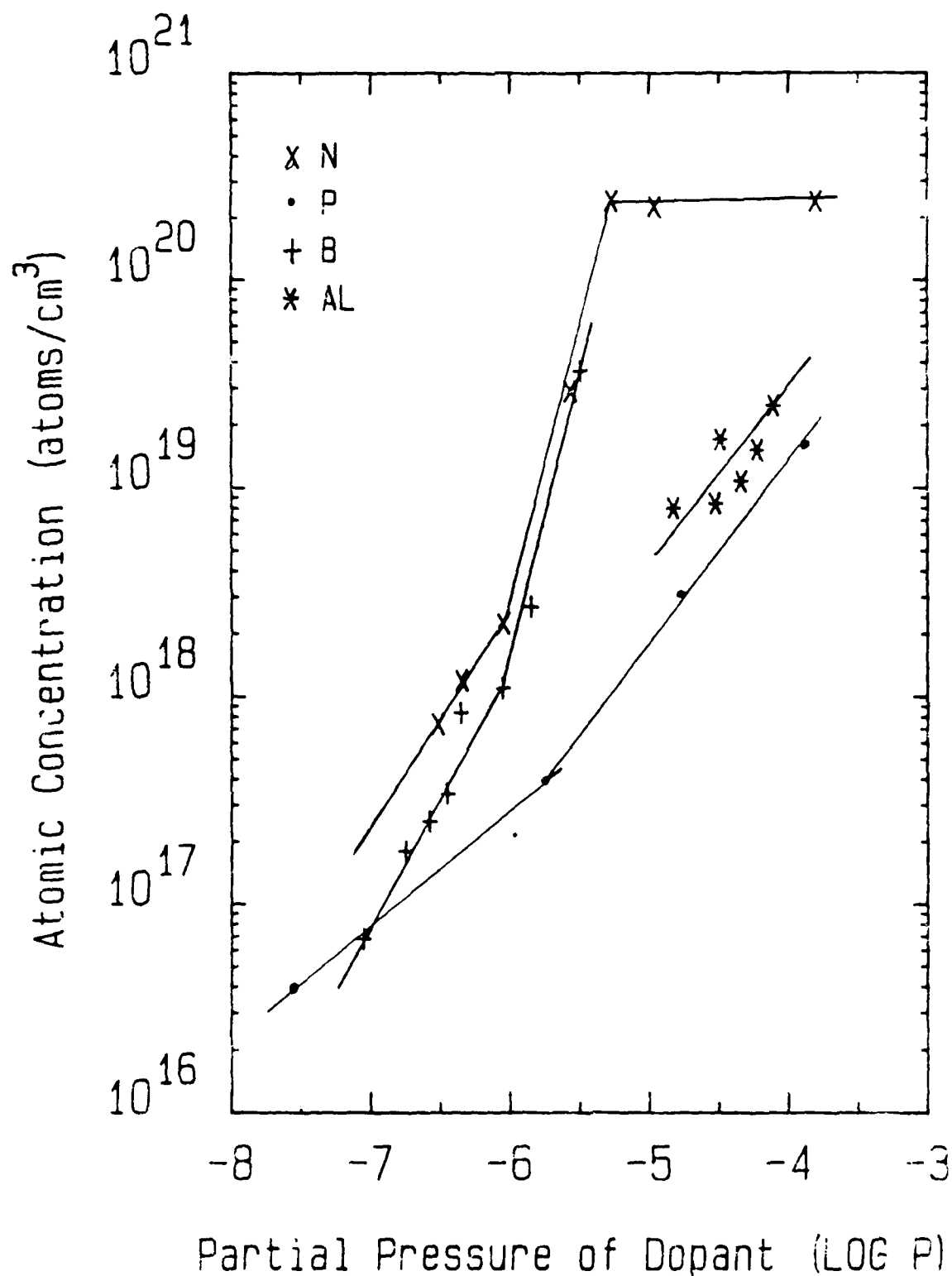
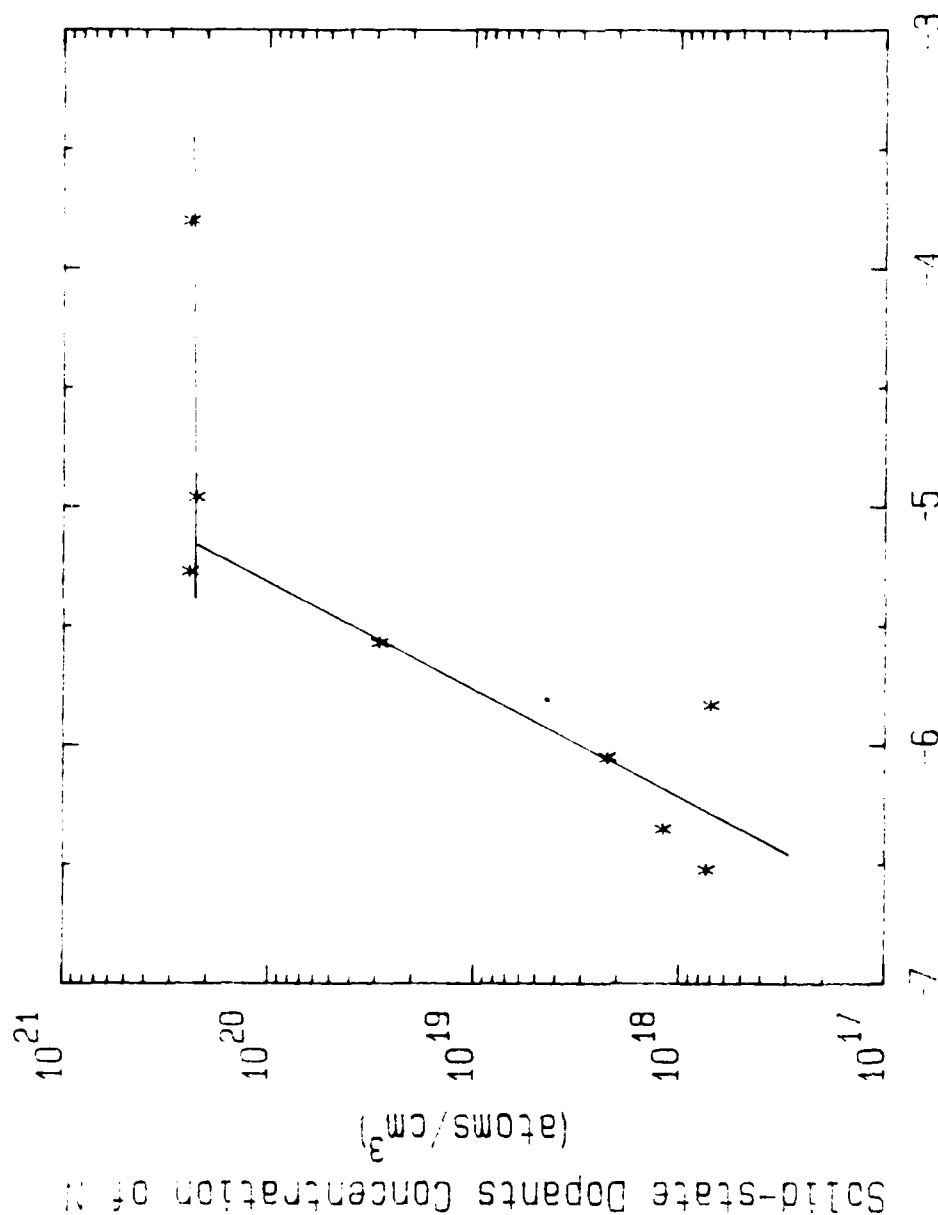


Figure 33. Experimental atomic concentrations of dopants in the CVD doped γ -SiC films vs. partial pressure of dopant source gases in the gas stream or the growth conditions noted in the caption of Figure 32.



Partial Pressure of N_2 or NH_3 (log P)

Figure 31. Experimentally measured solid-state dopant concentration of N in CVD grown n-SiC films vs partial pressures of N_2 or NH_3 in flowing H_2 .

measurements of atomic concentration as a function of partial pressure of the precursor dopant gas in the gas stream gives some idea of the ranges of dopant which can be incorporated. Figure 33 is a compilation of this data; Figs. 34-37 shows this data for the individual gas species as well as the active carrier concentration in some of the same samples, as measured by the capacitance-voltage (C-V). (Miller feed back profiler) technique.

With the exception of B, the atomic concentration of each species has a reasonably linear relationship with the partial pressure of the precursor gas. In the case of N (the only dopant species under consideration which is a gas in the elemental form and the species which forms the most unstable carbide), saturation of this constituent at a concentration of $\sim 2 \times 10^{20}/\text{cm}^3$ appears to occur as shown in Fig. 34. This most likely indicates the solubility limit at the temperature of growth (1633K), as already noted above.

The n-type carrier concentration of the N-doped samples (Fig. 34) was measured for only two samples, as it was difficult to measure a higher carrier concentration with the C-V measurement technique. The ratio of carrier concentration to N concentration is ~ 0.1 .

The chemical concentration of atomic P was also found to be linearly proportional to the partial pressure of PH_3 , but over two different regions of the latter (see Fig. 35). The knee of the curve is located at $\sim 5 \times 10^{17} \text{ P}/\text{cm}^3$. At this concentration, the surface of the β -SiC film changes from smooth to rough as the pressure of PH_3 is increased. This change in surface texture may indicate the onset of some polycrystallinity. The increased incorporation of P above $5 \times 10^{17}/\text{cm}^3$ may be caused by the occupation of these atoms on grain boundary sites. The n-type carrier concentration is also linearly proportional to partial pressure of PH_3 . The ratio of this carrier concentration to the P concentration is again ~ 0.1 .

The incorporation phenomenon found in the case of P is even more pronounced and supported by data in the case of B, as shown in Fig. 36. For this species, the knee of the curve in atomic concentration occurs at $10^{18}/\text{cm}^3$. Again the surface texture changes from smooth to rough at this concentration. The ratio of the carrier concentration to atomic concentration is 0.005-0.01.

species predicted in Figs. 24-27 would actually be present in our system for it is not necessarily at equilibrium during the growth process. These calculations nevertheless provide useful insight into the dopant gas phase species which are likely to be present in equilibrium with silicon carbide and which may enter into the rate processes determining the elemental doping level in the solid thin film.

5. Dopant Partial Pressures, Resultant Chemical Concentrations and Electronic Carrier Concentrations in β -SiC

As illustrated in Figs. 25-27, the various dopant sources decompose to several species in equilibrium under the conditions used in the NCSU CVD reactor to grow the β -SiC thin films. It is very unlikely that all of these gaseous constituents containing the given dopant species contribute to doping the films in proportion to their equilibrium partial pressure. Some of the constituents must undergo additional decomposition lest H must be incorporated in the sample. Thus, for the purpose of this particular study of chemical and electronic carrier concentrations as a function of dopant partial pressure, only the monoatomic species of N, P, B and Al are considered to be the constituents from which dopant incorporation actually occurs. Figure 32 is a composite diagram taken from Figs. 25-27 for each of the species of N (or N_2), P and B. Although P has the highest partial pressure of the monoatomic species, it has the lowest atomic concentration in the SiC at a given partial pressure of the PH_3 dopant gas as shown in Fig. 33. The reverse is true for N and NH_3 . Thus the incorporation of a particular species into SiC depends strongly on the sticking coefficient of that species which, in turn, depends on the kinetics of diffusion of the gaseous species to and away from the substrate and the rate of reaction, on the availability of a lattice site, the ease of substitution on that site and the ability to chemically bond to the structure at the temperatures of growth. In effect this is essentially a measure of the solubility of the species as discussed below.

Although solubility data from direct measurements such as diffusion or lattice parameter studies are not available for the temperature range of CVD growth (1600-1673K) used in this research, the SIMS

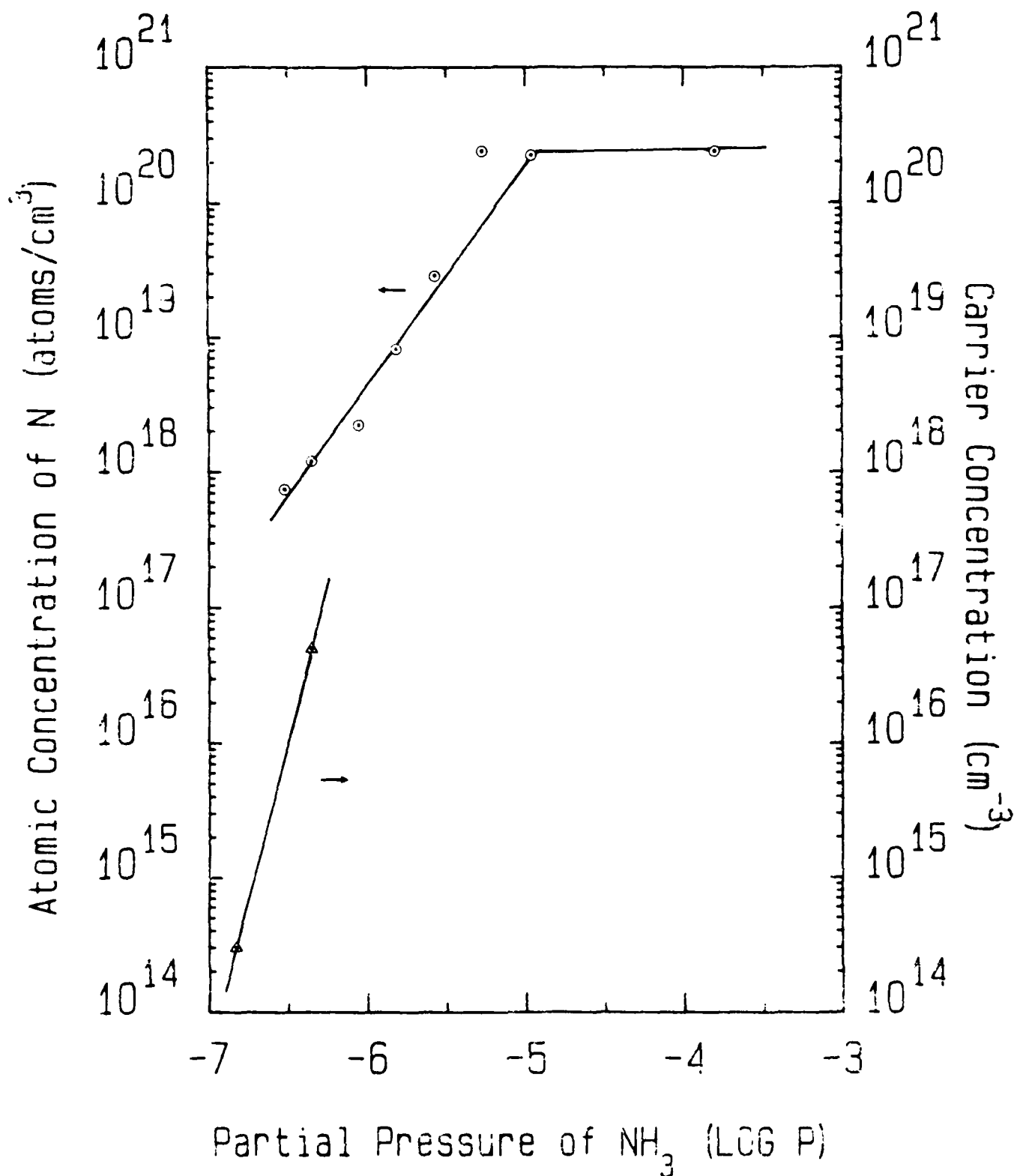


Figure 34. Atomic concentration of N and n-type carrier concentration of the doped SiC films vs. partial pressure of NH₃ in the gas stream. The films were grown under the conditions noted in the caption of Figure 32.

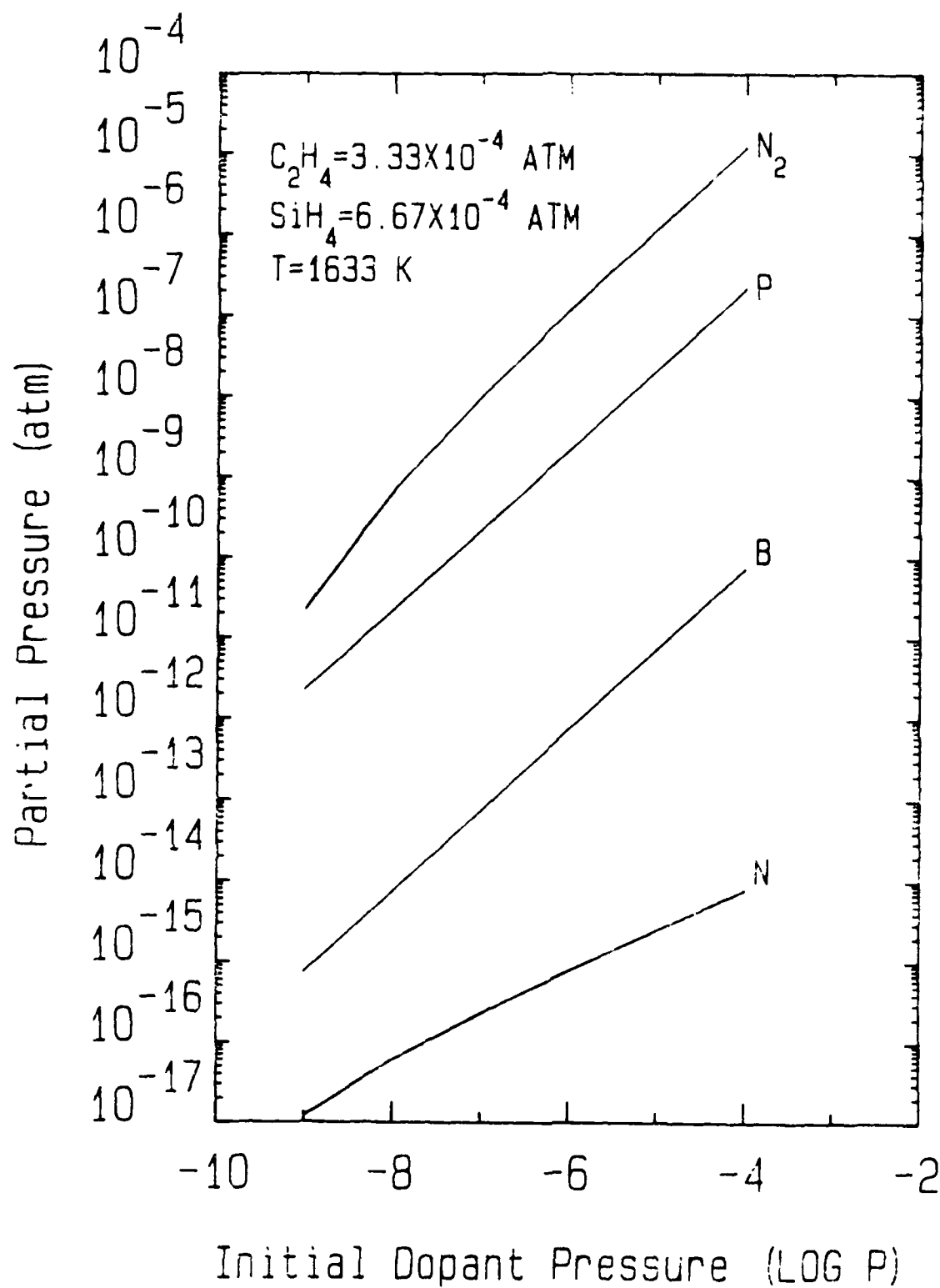


Figure 32. Calculated partial pressure of dopant atoms vs. initial pressure of dopant source gases at the deposition conditions of 1633K, 760 Torr, 1 sccm C_2H_4 , 2 sccm SiH_4 and 3000 sccm H_2 .

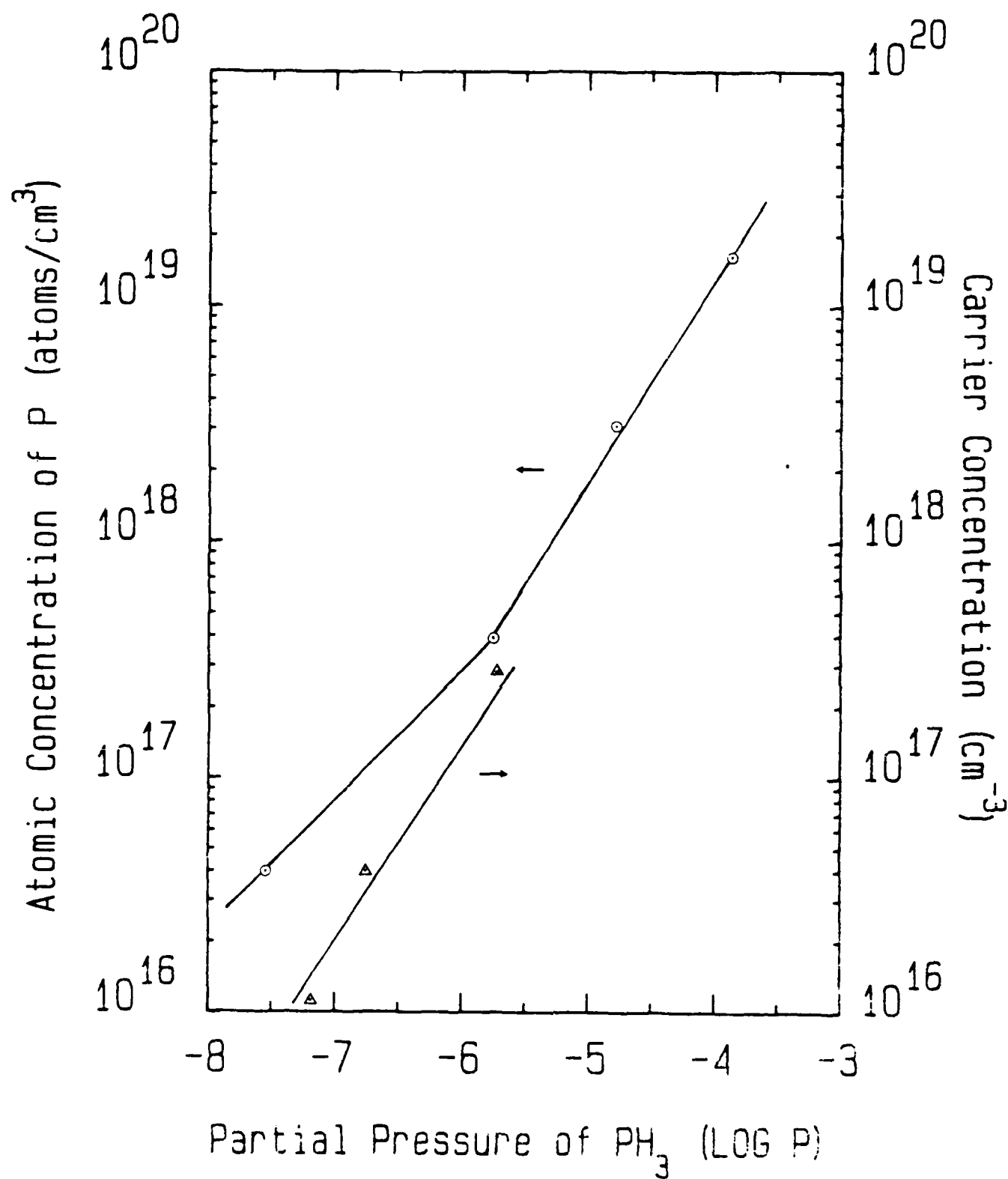


Figure 35. Atomic concentration of P and n-type carrier concentration of the dopant β -SiC films vs. partial pressure of PH₃ in the gas stream. The films were grown under the conditions noted in the caption of Figure 32.

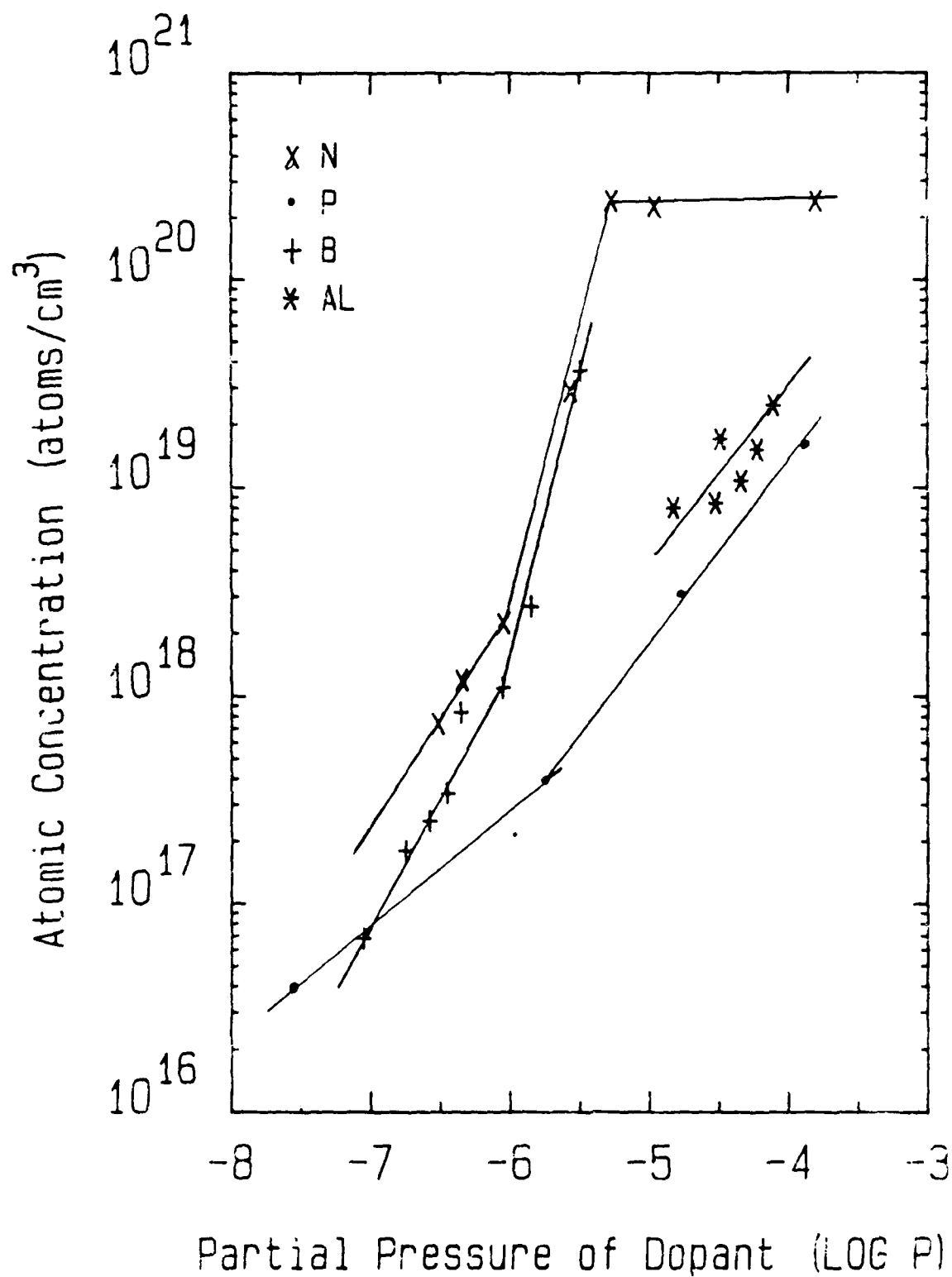


Figure 33. Experimental atomic concentrations of dopants in the CVD doped γ -SiC films vs. partial pressure of dopant source gases in the gas stream or the growth conditions noted in the caption of Figure 32.

measurements of atomic concentration as a function of partial pressure of the precursor dopant gas in the gas stream gives some idea of the ranges of dopant which can be incorporated. Figure 33 is a compilation of this data; Figs. 34-37 shows this data for the individual gas species as well as the active carrier concentration in some of the same samples, as measured by the capacitance-voltage (C-V). (Miller feed back profiler) technique.

With the exception of B, the atomic concentration of each species has a reasonably linear relationship with the partial pressure of the precursor gas. In the case of N (the only dopant species under consideration which is a gas in the elemental form and the species which forms the most unstable carbide), saturation of this constituent at a concentration of $\sim 2 \times 10^{20}/\text{cm}^3$ appears to occur as shown in Fig. 34. This most likely indicates the solubility limit at the temperature of growth (1633K), as already noted above.

The n-type carrier concentration of the N-doped samples (Fig. 34) was measured for only two samples, as it was difficult to measure a higher carrier concentration with the C-V measurement technique. The ratio of carrier concentration to N concentration is ~ 0.1 .

The chemical concentration of atomic P was also found to be linearly proportional to the partial pressure of PH_3 , but over two different regions of the latter (see Fig. 35). The knee of the curve is located at $\sim 5 \times 10^{17} \text{ P}/\text{cm}^3$. At this concentration, the surface of the β -SiC film changes from smooth to rough as the pressure of PH_3 is increased. This change in surface texture may indicate the onset of some polycrystallinity. The increased incorporation of P above $5 \times 10^{17}/\text{cm}^3$ may be caused by the occupation of these atoms on grain boundary sites. The n-type carrier concentration is also linearly proportional to partial pressure of PH_3 . The ratio of this carrier concentration to the P concentration is again ~ 0.1 .

The incorporation phenomenon found in the case of P is even more pronounced and supported by data in the case of B, as shown in Fig. 36. For this species, the knee of the curve in atomic concentration occurs at $10^{18}/\text{cm}^3$. Again the surface texture changes from smooth to rough at this concentration. The ratio of the carrier concentration to atomic concentration is 0.005-0.01.

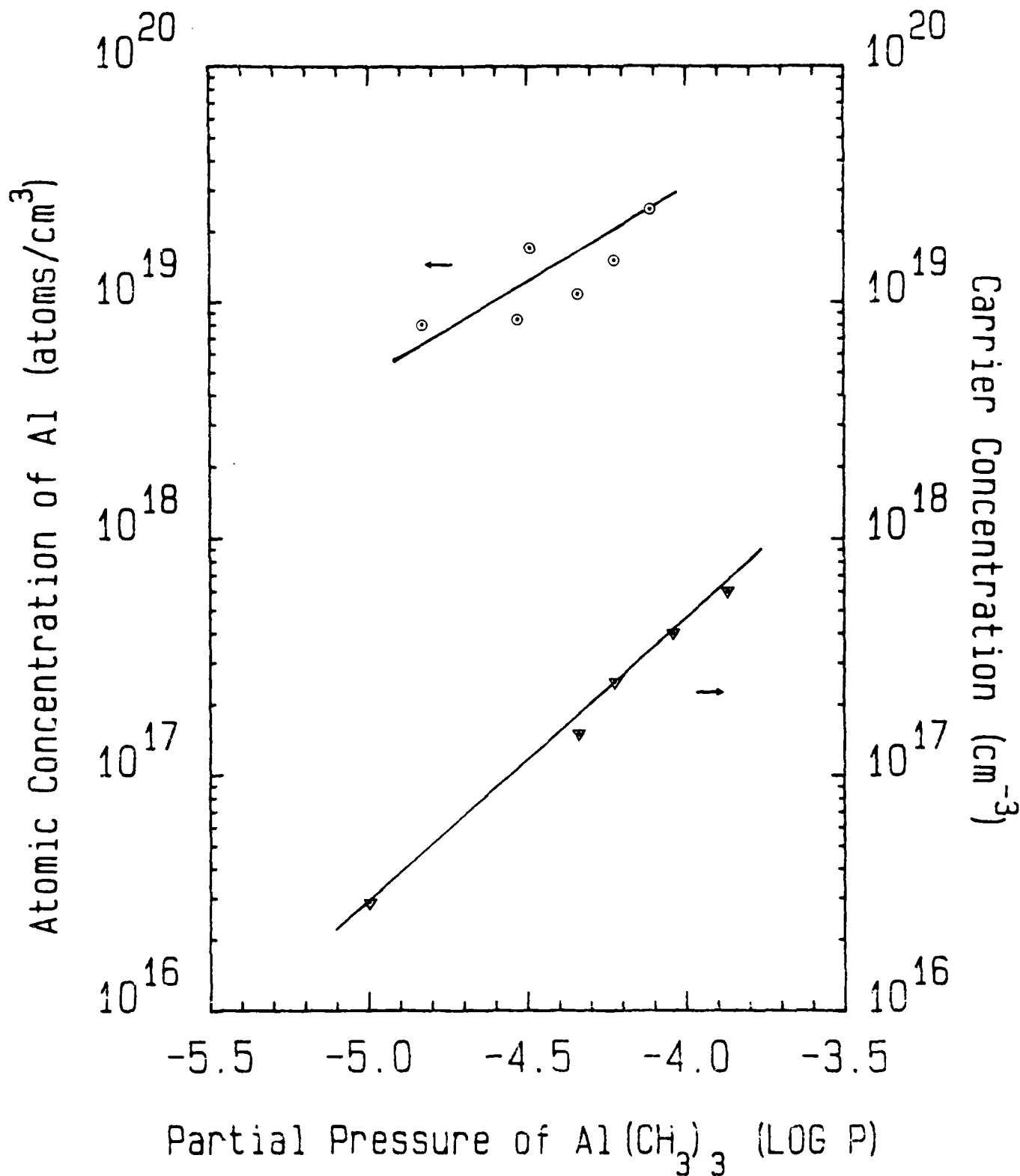


Figure 37. Atomic concentration of Al and p-type carrier concentration of the doped β -SiC films vs. partial pressure of Al(CH₃)₃ in the gas stream. The films were grown under the conditions noted in the caption of Figure 32.

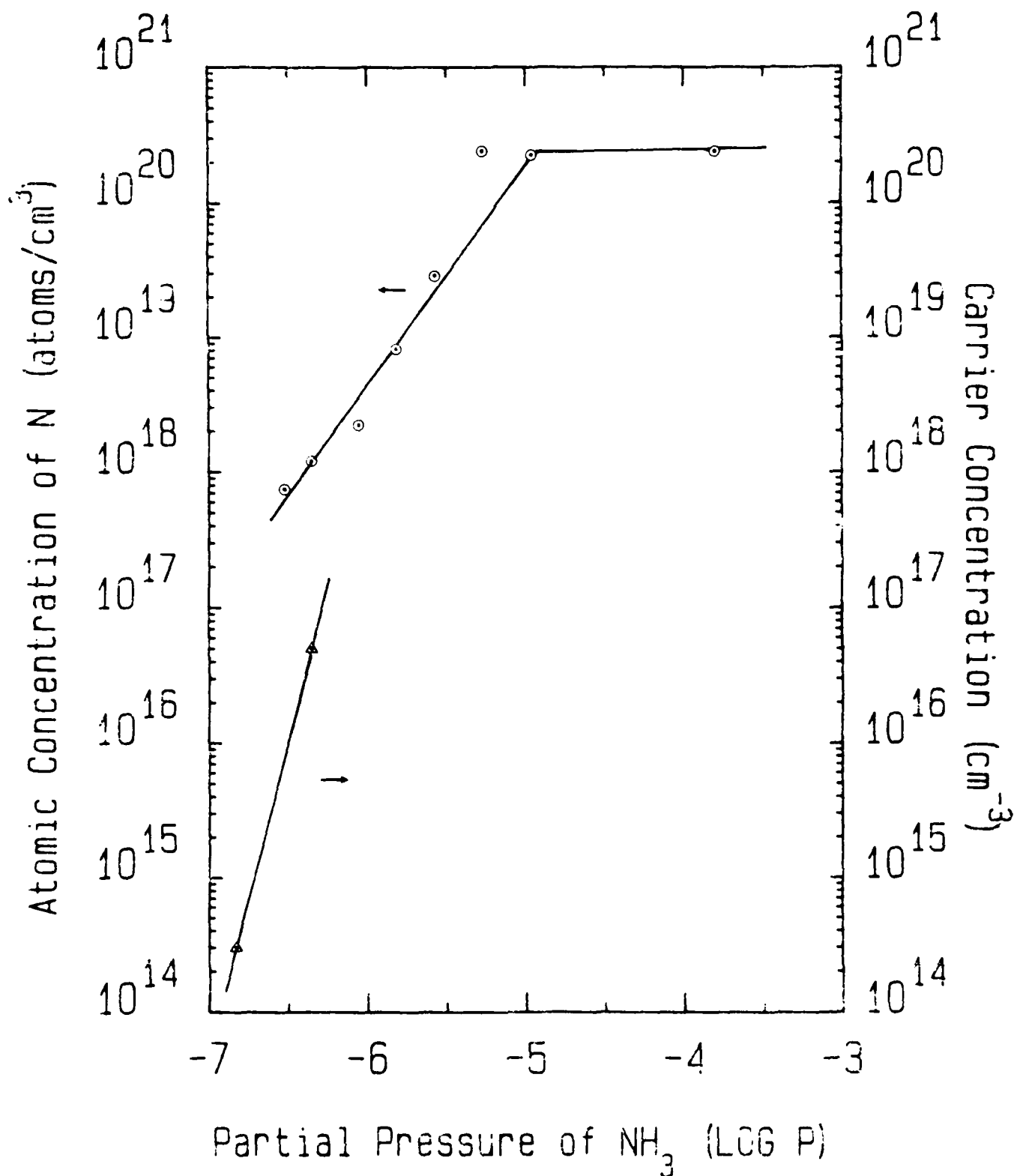


Figure 34. Atomic concentration of N and n-type carrier concentration of the doped $\beta\text{-SiC}$ films vs. partial pressure of NH_3 in the gas stream. The films were grown under the conditions noted in the caption of Figure 32.

Finally, in the case of Al (see Fig. 37) linear relationships between chemical and carrier (p-type) concentrations were measured. As in the case of B, the ratio of carrier concentration to atomic concentration is approximately 0.01.

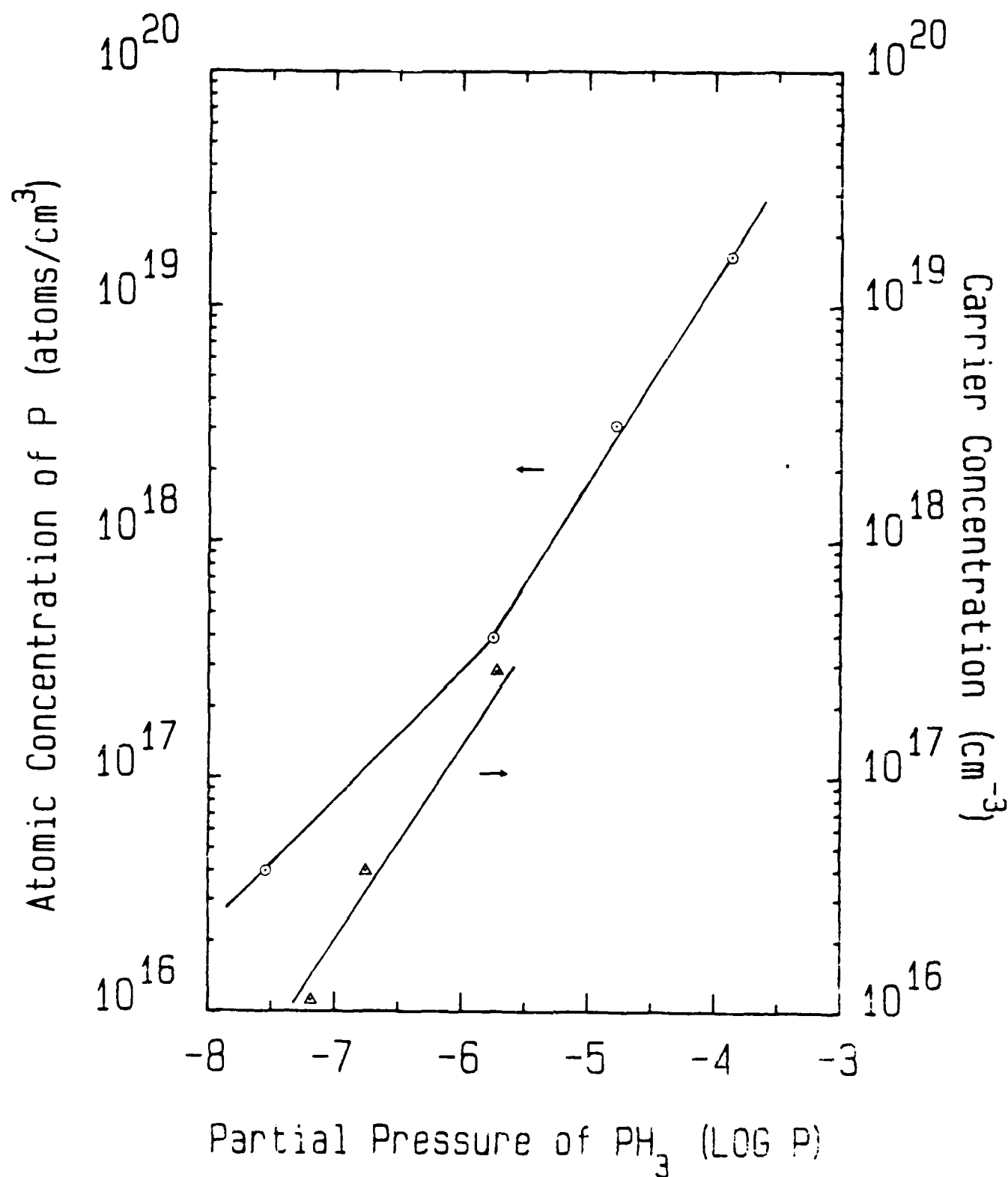


Figure 35. Atomic concentration of P and n-type carrier concentration of the dopant β -SiC films vs. partial pressure of PH_3 in the gas stream. The films were grown under the conditions noted in the caption of Figure 32.

III. CROSS-SECTIONAL TRANSMISSION ELECTRON MICROSCOPY OF β -SiC FILMS

To ascertain the structural quality of the as-grown β -SiC thin films and thereby discern the efficacy of various processing parameters on the growth, we have concluded that cross-sectional transmission electron microscopy (XTEM) is the most important diagnostic tool to accomplish these objectives. This section discusses our findings in this area during this report period as well as provides pictorial evidence of the substructure of several of the films. The β -SiC films studied had a total thickness of approximately 11 μm .

As seen in Figs. 38 ($\vec{g} = [111]$) and 39 ($\vec{g} = [023]$) this particular sample contains stacking faults as the major defect but also a modest concentration of dislocations--located primarily at the ends of the stacking faults (Shockley partials). A set of partials can be seen in Fig. 39 along the edge of a stacking fault between the letters A and B.

At the Si/ β -SiC interface there begins a dense strain region which extends approximately 3 μm into the film. Although this region can be observed at the top of Figs. 38 and 39, its character is more readily seen at high magnification (250,000X) in Fig. 40 ($\vec{g} = [111]$). This micrograph was taken from the same interface region as Fig. 38. Most of the substructure shown in Fig. 40 is elastic strain rather than the stacking faults and dislocations which are encountered further away from the interface.

Figure 41 ($\vec{g} = [011]$) is particularly noteworthy, for here essentially all of the Si layer has been removed during sample preparation. Furthermore, the small band of Si remaining is much thinner than the SiC layer which occupies most of the photograph. Although stacking faults are still evident away from the interface, a large portion of the elastic strain has been relieved by the loss of the Si. Thus, although the converted layer allows one to grow a crack free β -SiC film on (100) Si, it does not alleviate the mismatches in thermal expansion and lattice parameter as much as was initially believed.

As shown in Figs. 41 and 42 ($\vec{g} = [200]$), the defect density decreases dramatically as moves toward the final growth surface

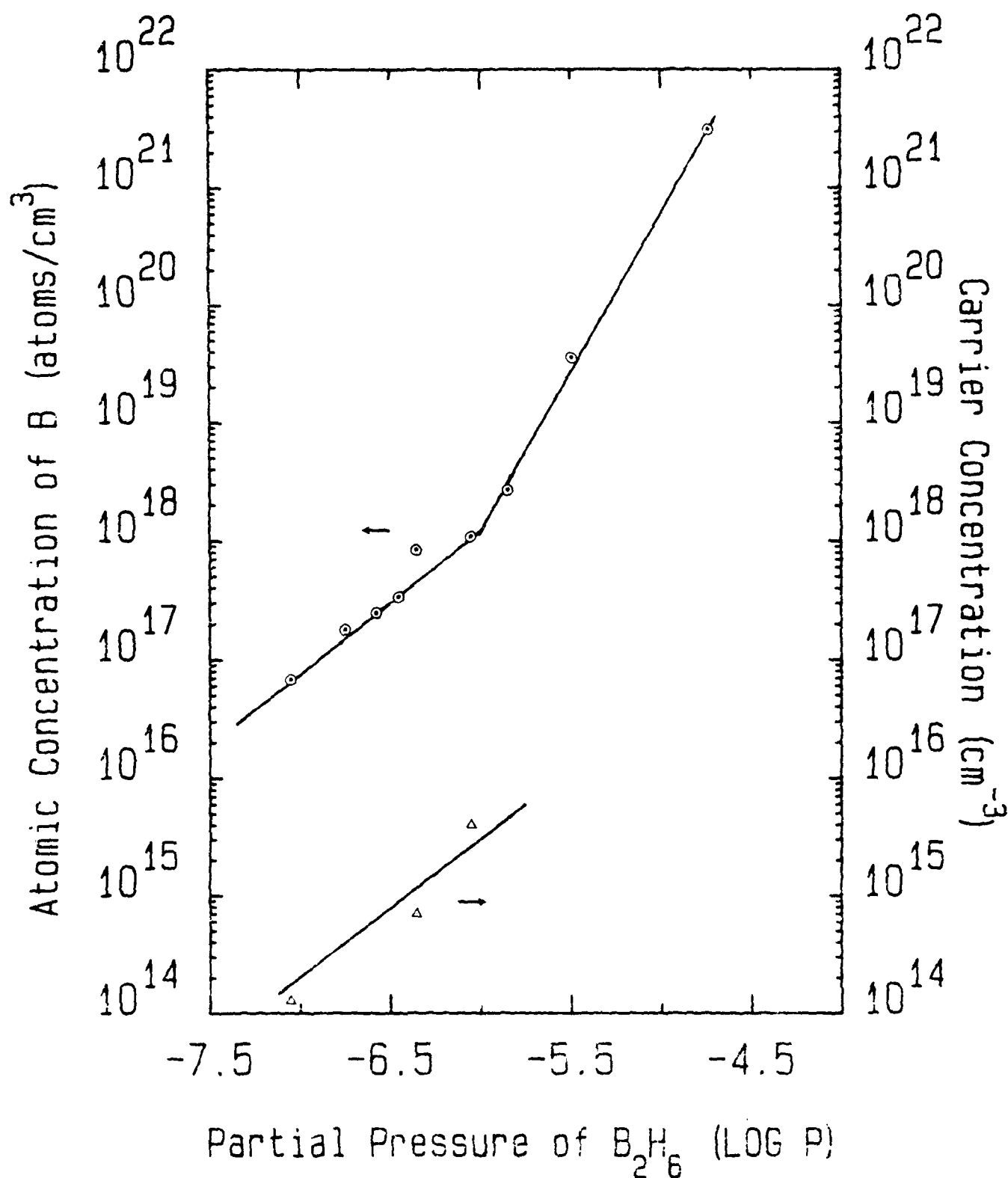


Figure 36. Atomic concentration of B and p-type carrier concentration of the doped α -SiC films vs. partial pressure of B_2H_6 in the gas stream. The films were grown under the conditions noted in the caption of Figure 32.

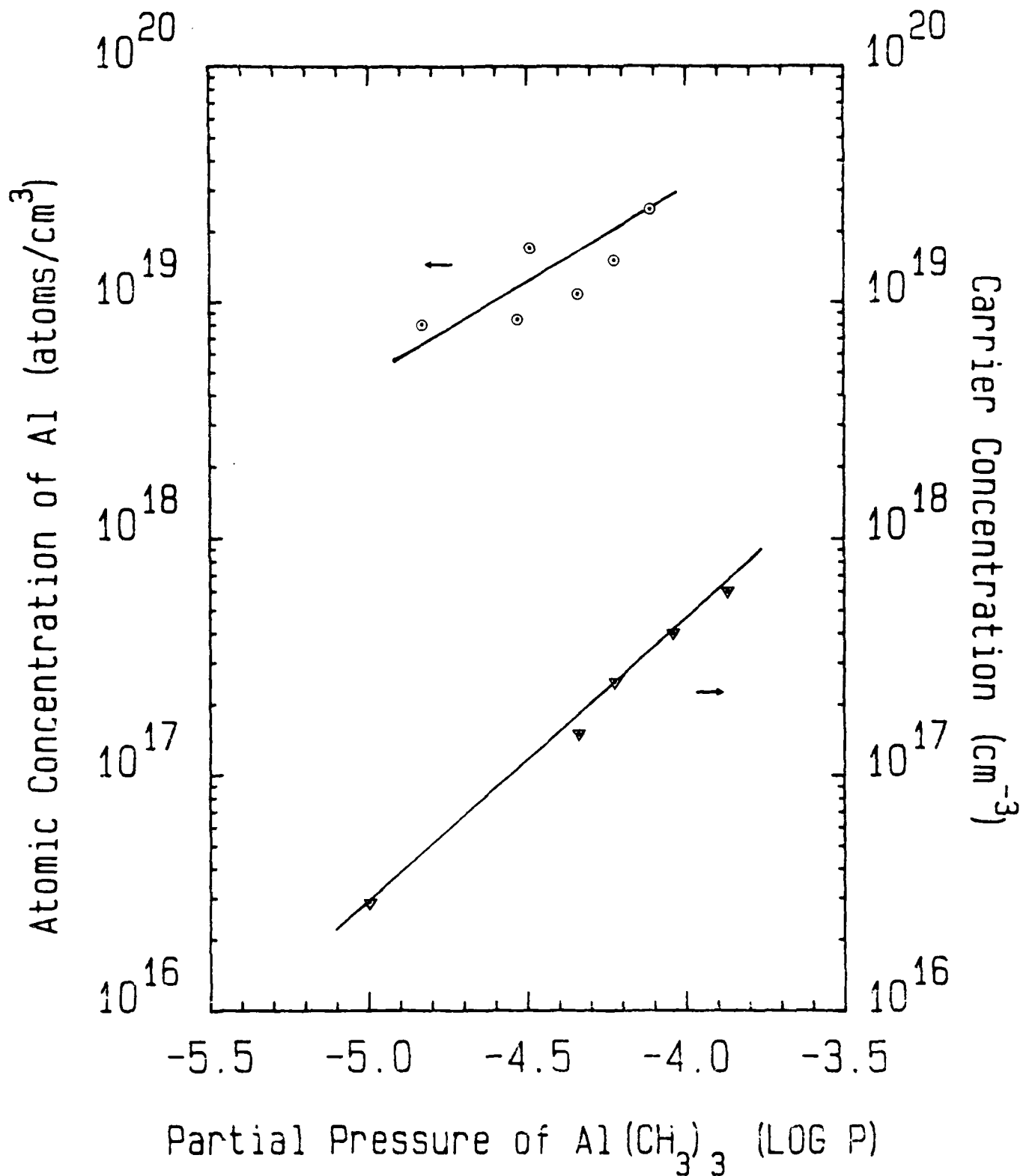


Figure 37. Atomic concentration of Al and p-type carrier concentration of the doped β -SiC films vs. partial pressure of Al(CH₃)₃ in the gas stream. The films were grown under the conditions noted in the caption of Figure 32.



Figure 38. Cross-sectional micrographs of single crystal thin film of undoped CVD β -SiC deposited on single crystal (100) Si at 1630K and 1 atm. using a gas mixture of SiH_4 , C_2H_4 and H_2 . Micrograph shows full range of defects present in the as-grown film including stacking faults, partial and misfit dislocations and interfacial strain contrast. $\vec{q} = [111]$.

Finally, in the case of Al (see Fig. 37) linear relationships between chemical and carrier (p-type) concentrations were measured. As in the case of B, the ratio of carrier concentration to atomic concentration is approximately 0.01.

III. CROSS-SECTIONAL TRANSMISSION ELECTRON MICROSCOPY OF β -SiC FILMS

To ascertain the structural quality of the as-grown β -SiC thin films and thereby discern the efficacy of various processing parameters on the growth, we have concluded that cross-sectional transmission electron microscopy (XTEM) is the most important diagnostic tool to accomplish these objectives. This section discusses our findings in this area during this report period as well as provides pictorial evidence of the substructure of several of the films. The β -SiC films studied had a total thickness of approximately 11 μm .

As seen in Figs. 38 ($\vec{g} = [111]$) and 39 ($\vec{g} = [023]$) this particular sample contains stacking faults as the major defect but also a modest concentration of dislocations--located primarily at the ends of the stacking faults (Shockley partials). A set of partials can be seen in Fig. 39 along the edge of a stacking fault between the letters A and B.

At the Si/ β -SiC interface there begins a dense strain region which extends approximately 3 μm into the film. Although this region can be observed at the top of Figs. 38 and 39, its character is more readily seen at high magnification (250,000X) in Fig. 40 ($\vec{g} = [111]$). This micrograph was taken from the same interface region as Fig. 38. Most of the substructure shown in Fig. 40 is elastic strain rather than the stacking faults and dislocations which are encountered further away from the interface.

Figure 41 ($\vec{g} = [011]$) is particularly noteworthy, for here essentially all of the Si layer has been removed during sample preparation. Furthermore, the small band of Si remaining is much thinner than the SiC layer which occupies most of the photograph. Although stacking faults are still evident away from the interface, a large portion of the elastic strain has been relieved by the loss of the Si. Thus, although the converted layer allows one to grow a crack free β -SiC film on (100) Si, it does not alleviate the mismatches in thermal expansion and lattice parameter as much as was initially believed.

As shown in Figs. 41 and 42 ($\vec{g} = [200]$), the defect density decreases dramatically as moves toward the final growth surface



Figure 39. Cross-sectional TEM micrographs of single crystal thin film of undoped CVD β -SiC deposited on single crystal (100) Si at 1630K and 1 atm. using a gas mixture of SiH_4 , C_2H_4 and H_2 . Micrographs show full range of defects present in the as-grown film including stacking faults, partial and misfit dislocations



Figure 38. Cross-sectional micrographs of single crystal thin film of undoped CVD β -SiC deposited on single crystal (100) Si at 1630K and 1 atm. using a gas mixture of SiH_4 , C_2H_4 and H_2 . Micrograph shows full range of defects present in the as-grown film including stacking faults, partial and misfit dislocations and interfacial strain contrast. $\vec{q} = [111]$.



Figure 40. Same as Figure 8 ($\vec{g} = [111]$), except much higher magnification used to closely observe the strain contrast at the Si/SiC interface.



Figure 39. Cross-sectional TEM micrographs of single crystal thin film of undoped CVD β -SiC deposited on single crystal (100) Si at 1630K and 1 atm. using a gas mixture of SiH_4 , C_2H_4 and H_2 . Micrographs show full range of defects present in the as-grown film including stacking faults, partial and misfit dislocations



Figure 41. Cross-sectional TEM of β -SiC sample grown under the same conditions as noted in the caption of Fig. 38, except doped during growth with P (50 ppm in H_2) at a $2.4 \times 10^{-6} \text{ atm.}$ partial pressure (P concentration of 5×10^{-6}) showing the considerable reduction in strain contrast at the Si/SiC interface with the removal of essentially all of the Si. Electron beam parallel to $[011]$.



Figure 40. Same as Figure 8 ($\vec{g} = [111]$), except much higher magnification used to closely observe the strain contrast at the Si/SiC interface.

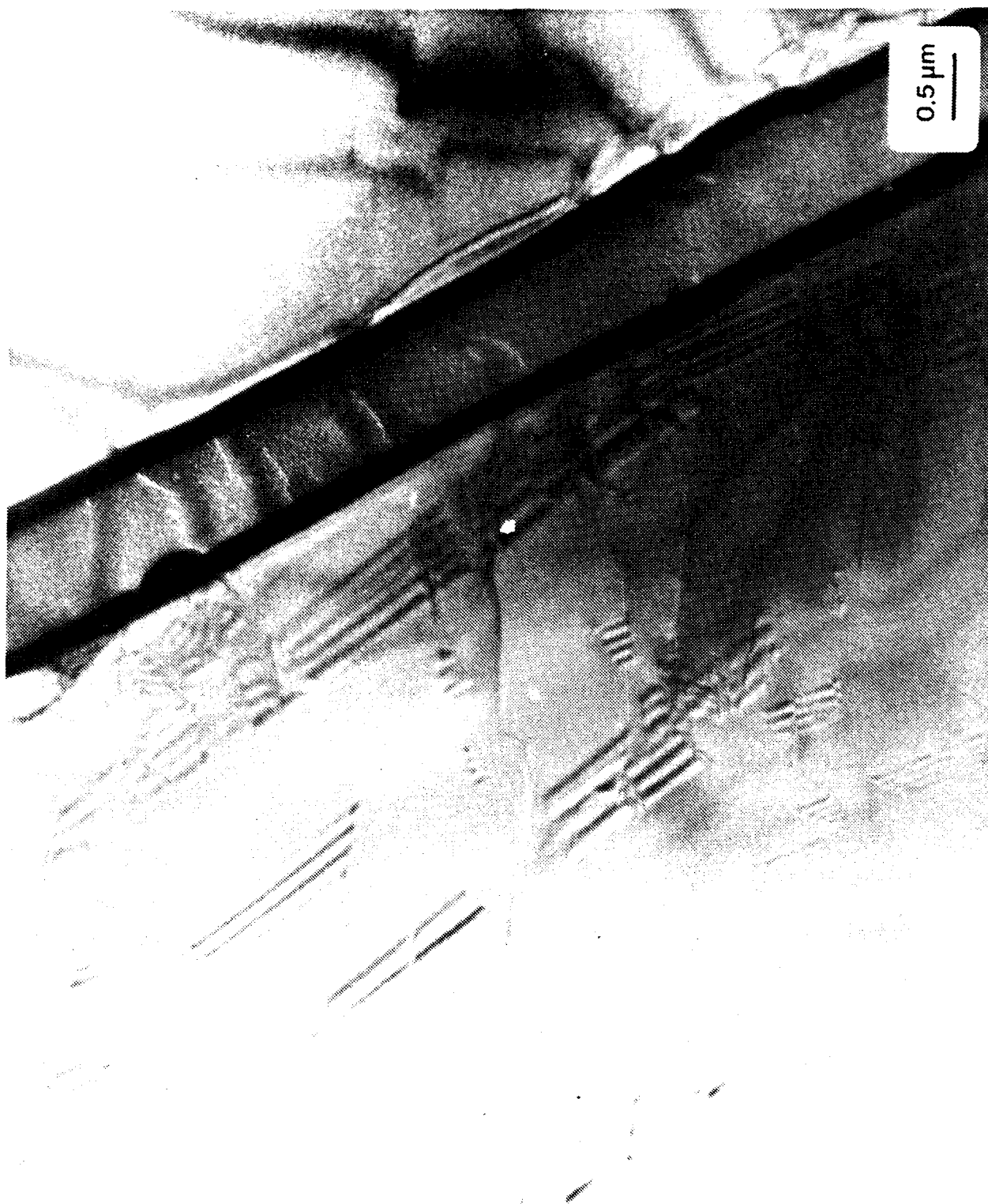


Figure 42. Same as Figure 41, except $\dot{\gamma} = [200]$. Also, in this figure one can observe stacking faults near the final growth surface.

on of
entra-
he

Table IV. Cogent characteristics of particular materials which are candidates for substrates for the heteroepitaxial growth of Beta Silicon Carbide thin films.

Properties	SiC	Si	W	(Al ₂ O ₃) Sapphire	Mullite	TiC	NbC
Structure	Cubic (Zinc-Blende)	Cubic (Zinc-Blende)	Cubic (BCC)	Rhombohedral	Orthorhombic	Cubic (NaCl)	Cubic (NaCl)
Lattice Parameter (Å)	4.3590	5.4307	3.1652	a = 4.758 c = 12.991	a = 7.584 b = 7.693 c = 2.890	4.313	4.457
Thermal Expansion Coefficient	3.8 @ 200°C 4.3 @ 400°C 4.8 @ 600°C 5.2 @ 800°C 5.8 @ 1000°C 5.5 @ 1400-1800°C	2.5 @ 300°K 3.1 @ 400°K 3.5 @ 500°K 3.8 @ 600°K 4.1 @ 700°K 4.3 @ 800°K	2.7 @ 300°K 4.4 @ 400°K 4.6 @ 500°K 4.7 @ 600°K 4.7 @ 700°K 4.8 @ 800°K	8.4 @ 25-800°C (60° to C-axis)	4.5 @ 25-1325°C 5.62 @ 25-1500°C	6.96 @ 298-2273°K 9.5 @ 298-2970°K	6.35 @ 298-2270°K
Melting Point (°C)	2830	1420	3387	2030	1850	3150	3760

V. REMOVAL OF THE Si SUBSTRATE

As noted above and described in the following section, the annealing temperatures for electrical activation of implanted dopants via thermal heating has been found to considerably exceed the melting point of the Si substrate. As such a transfer process on as-grown thin 5 μm films which removed the Si was attempted. Unfortunately as a result of the thinness of the films many of them cracked. As such, the use of these films has been abandoned in favor of thicker samples which are typically 12-17 μm thick.

Initial studies with the removal of the Si from the thick films using the process described in the last report also resulted in cracks in the films. In order to prevent this, a new method of removal has been developed which consists of (1) wax mounting the 12-17 μm film face down on a beryllia substrate and (2) etching at room temperature in 1:1 $\text{HF}:\text{HNO}_3$ to remove the Si. The wax and sample holder must be insoluble in the acid mixture. Once the Si is removed, the wax is dissolved in trichloroethylene. Using this procedure the $\beta\text{-SiC}$ film remains intact.

The resulting thicker films can be used alone if handled with care or may be reinforced by r-f sputtering another material on the surface of initial growth. Tungsten was previously selected as a candidate material because of its refractoriness, very low vapor pressure and the close match in thermal expansion with $\beta\text{-SiC}$. This material is also reported as being a good ohmic contact for n-type SiC. This result will be investigated during device fabrication.

Detailed descriptions of the sample preparation, implantation and annealing procedures, the last of which requires the removal of the Si substrate, are provided in the following sections.

VI. ELECTRICAL AND RAMAN CHARACTERIZATION - EQUIPMENT AND STUDIES ON THE UNDOPED β -SiC FILMS

A. Equipment Employed in this Research for Electrical Characterization

In order to more fully and more accurately electrically characterize the as-grown β -SiC thin films as well as those which had been doped during growth or by ion implantation and the devices subsequently produced in the films, an electrical characterization laboratory has been established. The individual pieces of equipment which have been purchased and their use is as follows:

1. Miller Feedback Profiler
 - a) Measurement of active carrier concentration of planar wafers using an associated Hg probe and the differential C-V method.
 - b) Measurement of junction capacitance of devices using the probe station noted below.
2. Hewlett Packard 4145A Semiconductor Parameter Analyzer
Measurement of the I-V characteristics of thin films and devices and their analyses as well as transport factors and other transistor constants. Used in conjunction with the probe station noted below.
3. Rucker and Kolls Probe Station
 - a) Used with the Miller Feedback Profiler for measurement of junction capacitance.
 - b) Used with HP 4145A for measurement of I-V characteristics of thin films and devices.
 - c) Measurement of various parameters for integrated circuits.
4. Signatone Four Point Probe and associated equipment

which gives the lowest value of this parameter. A list of these materials and their resistivity is given in Table V. Each element or alloy was evaporated onto an as-grown n-type β -SiC film by vacuum evaporation at 10^{-6} torr. Each contact material/thin film combination except that of TaSi₂ was subsequently heated to 1523K for 1.2×10^3 s. The TaSi₂ material was heated only to 1123K for 1.2×10^3 s. As one may see from the data in Table V, the TaSi₂ contact has by far the lowest resistance.

Table V. Contact resistivity of Hg, Cr, Au-Ta and Ta-Si on n-type β -SiC.

Alloy	Contact Resistivity (ohm-cm ²)
Ni	1.4×10^{-1}
Cr	7×10^{-2}
Au-Ta	3×10^{-2}
TaSi ₂	8×10^{-5}

C. Studies of the Effect of the Presence of the Buffer Layer and the Si Substrate on Values of the Electrical Measurements

If current, I , is applied to a SiC film which has not been removed from the Si substrate (and therefore the buffer layer), this current may be considered to be divided into three components: I_1 , I_2 and I_3 where I_1 is the current through the SiC layer, I_2 is the current through the buffer layer and I_3 is the current through the Si substrate. The ratios of these currents, $I_1 : I_2 : I_3$, indicate how much error may be introduced from the buffer and Si layers in actual measurements such as four point probe or Hall effect.

The resistance of each layer can be expressed as $R_i = \rho_i l / A_i$ where ρ_i is the resistivity of each layer, l is the distance between the contacts, and $A_i = t_i w$, where t_i is the thickness of the layer.

Thus

$$R_i = \rho_i l / t_i w$$

(shown as black lines in these figures). Thus since devices are normally fabricated in the near surface regions, the substructure may not be particularly deleterious to device properties. Nevertheless the existence of elastic strain and the stacking faults and dislocations in all the thinner and thicker samples examined provides an impetus to conduct exploratory research using other substrates as described in the next section.

Then,

$$\begin{aligned}
 I_1 : I_2 : I_3 &= V/R_1 : V/R_2 : V/R_3 \\
 &= 1/R_1 : 1/R_2 : 1/R_3 \\
 &= t_1/\rho_1 : t_2/\rho_2 : t_3/\rho_3
 \end{aligned}$$

The resistivity and the thickness of the Si substrate is 10^4 ohm-cm and 500 μm , respectively. The as-grown and undoped β -SiC films produced in this research and removed from the Si substrate normally have a resistivity of $\sim 10^{-2}$ ohm-cm and a thickness of 15 μm . If for the buffer, one assumes the same parameters to have the values of 10^{-3} ohm-cm and 10^{-2} μm , respectively, the ratio $I_1 : I_2 : I_3 = 1 : 6.7 \times 10^{-3} = 3.3 \times 10^{-5}$. Thus, the error introduced by the presence of the buffer layer (assuming the values of ρ and thickness are correct for this layer) can be estimated at less than 1% in the case of undoped SiC. If the dopant is introduced in to the Si (e.g. during in situ doping) the Si must be removed.

Table VI shows the results of Hall effect measurements on 23.6 μm thick samples with and without the Si substrate on the back. There is not much difference in the resistivity or in the carrier concentration, but mobility is markedly increased by the removal of the Si.

Table VI. Results of Hall effect measurements on undoped n-type SiC with and without the Si substrate. The thickness of SiC was 23.6 μm .

	Resistivity (ohm-cm)	Carrier Concn. (cm^{-3})	Mobility ($\text{cm}^2/\text{v-sec}$)
With Si	0.526	4.5×10^{16}	242
Without Si	0.677	2.63×10^{16}	351

D. Raman Spectroscopy and Hall Effect Measurements and Their Employment in the Study of the Effects of Annealing on the Electrical Properties of the As-Grown, Undoped β -SiC Films.

Because Si and SiC have different thermal expansion coefficients, the crystal lattice of each β -SiC film is elastically strained (in tension), especially in the region of the Si/SiC interface. The presence of this strain results in reduced mobility of the majority and minority carriers. To determine the amount of lattice strain in the as-grown, undoped SiC films, and the quantitative effect of this strain on electrical properties, Raman spectroscopy and Hall effect measurements were conducted.

In the Raman technique, an Ar laser tuned to 5145 \AA (green line) was used in this study. The samples for this study were prepared by removing the Si substrate via an etching process in a 1:1 solution of HF and HNO_3 . The β -SiC films were, in turn, sequentially annealed in Ar at 1473K, 1673K, 1773K, 1873K and 2073K for 3.0×10^2 s at each temperature. Following the heating process, the samples were oxidized and etched to remove the thin disturbed surface layer. Fig. 43 shows the increase in the relative intensity of both the TO (translational) and LO (longitudinal) vibration modes of the 2073K annealed films, relative to that of the as-grown. The positions of these peaks have also shifted four wave numbers (i.e. to lower energy positions) as a result of the annealing.

The increases in both sharpness and peak position indicate that relief in the residual strain is accomplished during the annealing process. Olego and Cardona¹¹ have determined the following empirical relationship between the lattice strain ($\frac{\Delta a}{a}$) and the shift (ω_{LO}) in the position of the LO Raman peak.

$$\omega_{LO} = (973 \pm 0.3) + (4532 \pm 30) \left[\frac{\Delta a}{a_0} \right] \quad (1)$$

where ω_{LO} has the units of cm^{-1} and $\left[\frac{\Delta a}{a_0} \right]$ is related to lattice strain. In terms of stress, P,

$$\omega_{LO} = (972.7 \pm 0.3) + (4.75 \pm 0.09)P - [(2.5 \pm 0.4) \times 10^{-2}]P^2 \quad (2)$$

with P having the units of GPa.

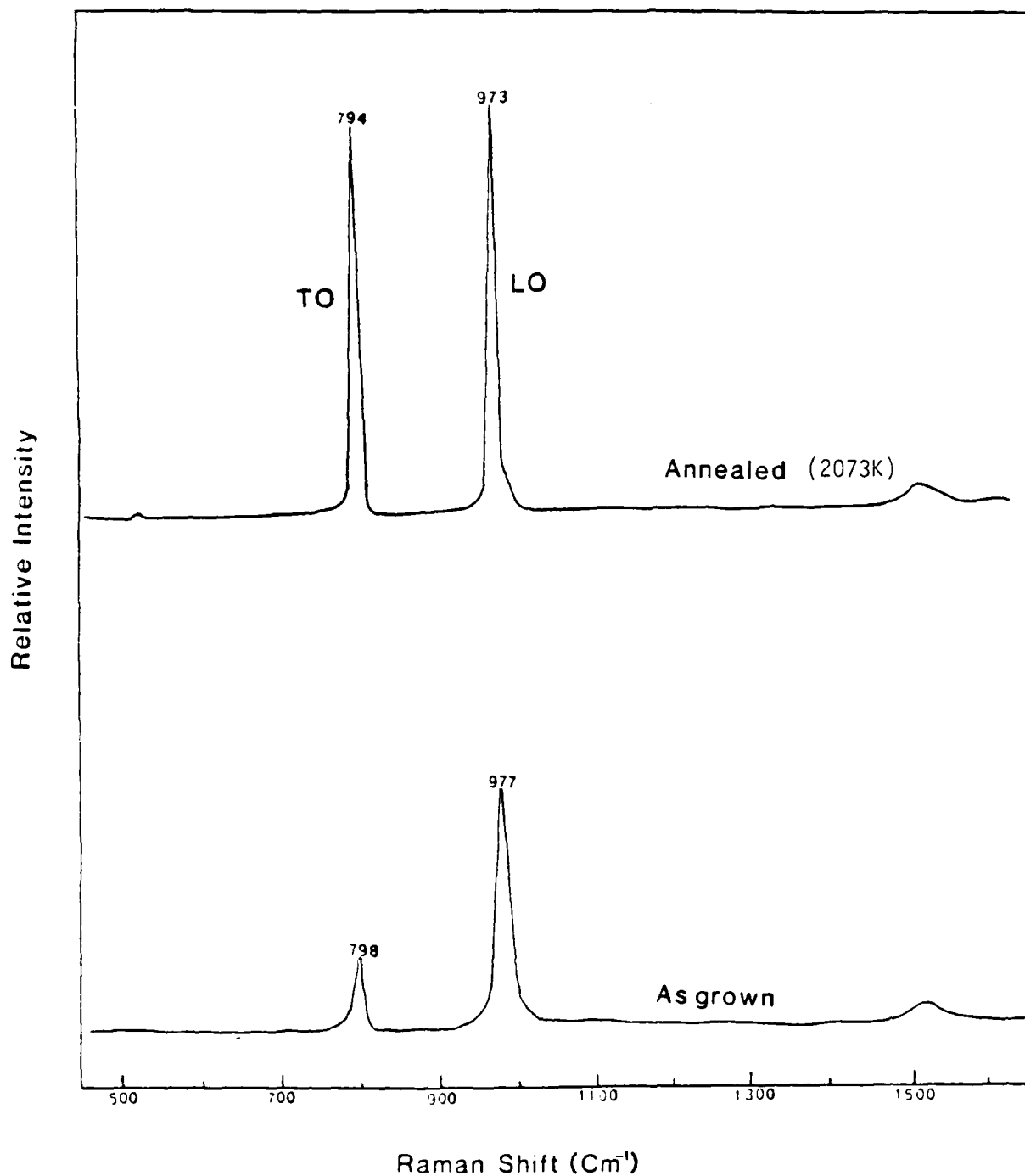


Figure 43. First order Raman spectra of an undoped β -SiC thin film before and after annealing. The Si substrate was etched away prior to the measurements.

V. REMOVAL OF THE Si SUBSTRATE

As noted above and described in the following section, the annealing temperatures for electrical activation of implanted dopants via thermal heating has been found to considerably exceed the melting point of the Si substrate. As such a transfer process on as-grown thin 5 μm films which removed the Si was attempted. Unfortunately as a result of the thinness of the films many of them cracked. As such, the use of these films has been abandoned in favor of thicker samples which are typically 12-17 μm thick.

Initial studies with the removal of the Si from the thick films using the process described in the last report also resulted in cracks in the films. In order to prevent this, a new method of removal has been developed which consists of (1) wax mounting the 12-17 μm film face down on a beryllia substrate and (2) etching at room temperature in 1:1 $\text{HF}:\text{HNO}_3$ to remove the Si. The wax and sample holder must be insoluble in the acid mixture. Once the Si is removed, the wax is dissolved in trichloroethylene. Using this procedure the $\beta\text{-SiC}$ film remains intact.

The resulting thicker films can be used alone if handled with care or may be reinforced by r-f sputtering another material on the surface of initial growth. Tungsten was previously selected as a candidate material because of its refractoriness, very low vapor pressure and the close match in thermal expansion with $\beta\text{-SiC}$. This material is also reported as being a good ohmic contact for n-type SiC. This result will be investigated during device fabrication.

Detailed descriptions of the sample preparation, implantation and annealing procedures, the last of which requires the removal of the Si substrate, are provided in the following sections.

Thus the amount of lattice strain in the β -SiC film is calculated to be 0.0883%; the value of the elastic tensile stress from equation (2) is $0.02 \text{ GPa} = 2 \times 10^8 \text{ dynes/cm}^2$. This latter value is very close to the reported¹² value of tensile strength of $3.5 \times 10^8 \text{ dynes/cm}^2$ for a reaction bonded SiC material containing ~10% by volume of free Si.

Resistivity, active carrier concentration, and Hall mobility were measured on each sample using the van der Pauw method. These samples were also oxidized and etched to remove the disturbed surface layer prior to any measurement. As shown in Fig. 44 the carrier concentration continuously decreases while the mobility increases with an increase in the annealing temperature up to 1873K. These trends are sharply reversed as a result of the 2073 anneal. The increase in mobility of the samples annealed in the 1473K-1873K range is due to the annealing of the residual strain. The reason(s) for the rapid increase in n-type carrier concentration after annealing at 2073K is (are) not known. However it may be postulated to be caused by incorporation of N in the outer near-surface region during heating or by the presence of free C on the surface or by the creation of electrically active defects during heating. However, no N was found in the 2073K annealed samples using SIMS, and any free C is burned off during the oxidation and etching procedure, as noted in Section VI. E below. Thus, only the creation of electrically active defects remains the plausible explanation for the above phenomenon.

E. Effects of Annealing on the Surface Properties of β -SiC

During the annealing study on the undoped SiC films described in VI. D above, it was discovered that the electrical properties of the surface were altered, especially by the 2073K, $3.0 \times 10^2 \text{ s}$ anneal. The I-V characteristics of this sample obtained using a Hg probe are shown in Fig. 45a. Instead of the normal rectifying characteristics, this plot shows the presence of a very good ohmic contact. Further, more the removal of ~100Å of surface via oxidation and etching restores the initial electrical properties as shown in Fig. 45b. This obviously indicates that a conductive layer forms on the SiC surface after the 2073K anneal and that the thickness of this layer is less than 100Å.

VI. ELECTRICAL AND RAMAN CHARACTERIZATION - EQUIPMENT AND STUDIES ON THE UNDOPED β -SiC FILMS

A. Equipment Employed in this Research for Electrical Characterization

In order to more fully and more accurately electrically characterize the as-grown β -SiC thin films as well as those which had been doped during growth or by ion implantation and the devices subsequently produced in the films, an electrical characterization laboratory has been established. The individual pieces of equipment which have been purchased and their use is as follows:

1. Miller Feedback Profiler
 - a) Measurement of active carrier concentration of planar wafers using an associated Hg probe and the differential C-V method.
 - b) Measurement of junction capacitance of devices using the probe station noted below.
2. Hewlett Packard 4145A Semiconductor Parameter Analyzer
Measurement of the I-V characteristics of thin films and devices and their analyses as well as transport factors and other transistor constants. Used in conjunction with the probe station noted below.
3. Rucker and Kolls Probe Station
 - a) Used with the Miller Feedback Profiler for measurement of junction capacitance.
 - b) Used with HP 4145A for measurement of I-V characteristics of thin films and devices.
 - c) Measurement of various parameters for integrated circuits.
4. Signatone Four Point Probe and associated equipment
measurement of sheet resistance
5. Thermocompression bonder for lead wire attachment
6. High Temperature (up to 400°C) Hall effect measurement system

B. Ohmic Contact Studies

The contact resistivity has been measured for several candidate materials for ohmic contact on β -SiC in order to find that material

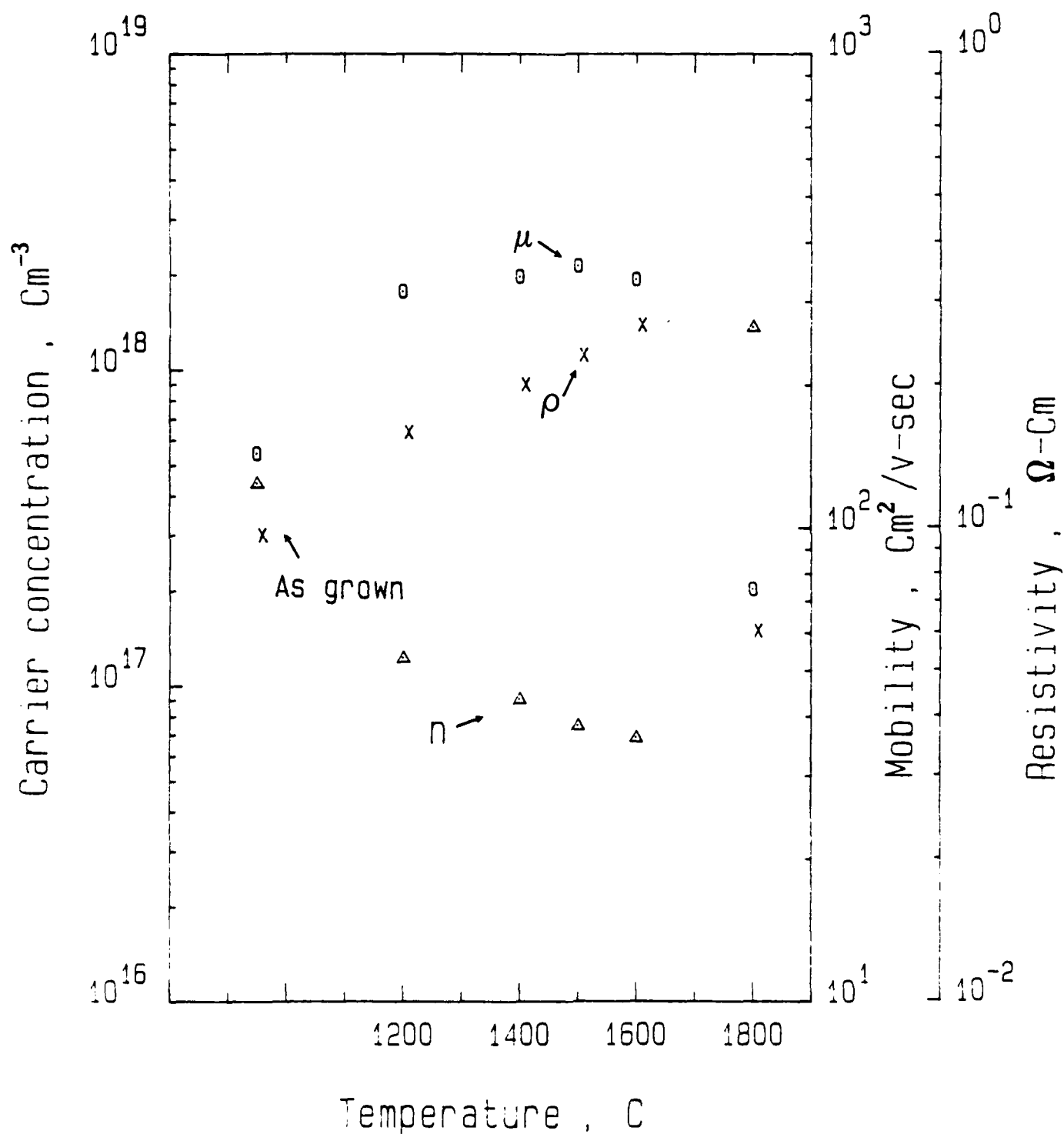


Figure 44. Dependence of annealing temperature on Hall effect parameters in annealed 3-SiC.

which gives the lowest value of this parameter. A list of these materials and their resistivity is given in Table V. Each element or alloy was evaporated onto an as-grown n-type β -SiC film by vacuum evaporation at 10^{-6} torr. Each contact material/thin film combination except that of TaSi₂ was subsequently heated to 1523K for 1.2×10^3 s. The TaSi₂ material was heated only to 1123K for 1.2×10^3 s. As one may see from the data in Table V, the TaSi₂ contact has by far the lowest resistance.

Table V. Contact resistivity of Hg, Cr, Au-Ta and Ta-Si on n-type β -SiC.

Alloy	Contact Resistivity (ohm-cm ²)
Ni	1.4×10^{-1}
Cr	7×10^{-2}
Au-Ta	3×10^{-2}
TaSi ₂	8×10^{-5}

C. Studies of the Effect of the Presence of the Buffer Layer and the Si Substrate on Values of the Electrical Measurements

If current, I , is applied to a SiC film which has not been removed from the Si substrate (and therefore the buffer layer), this current may be considered to be divided into three components: I_1 , I_2 and I_3 where I_1 is the current through the SiC layer, I_2 is the current through the buffer layer and I_3 is the current through the Si substrate. The ratios of these currents, $I_1 : I_2 : I_3$, indicate how much error may be introduced from the buffer and Si layers in actual measurements such as four point probe or Hall effect.

The resistance of each layer can be expressed as $R_i = \rho_i l / A_i$ where ρ_i is the resistivity of each layer, l is the distance between the contacts, and $A_i = t_i w$, where t_i is the thickness of the layer.

Thus

$$R_i = \rho_i l / t_i w$$

***** GRAPHICS PLOT *****
HEATED

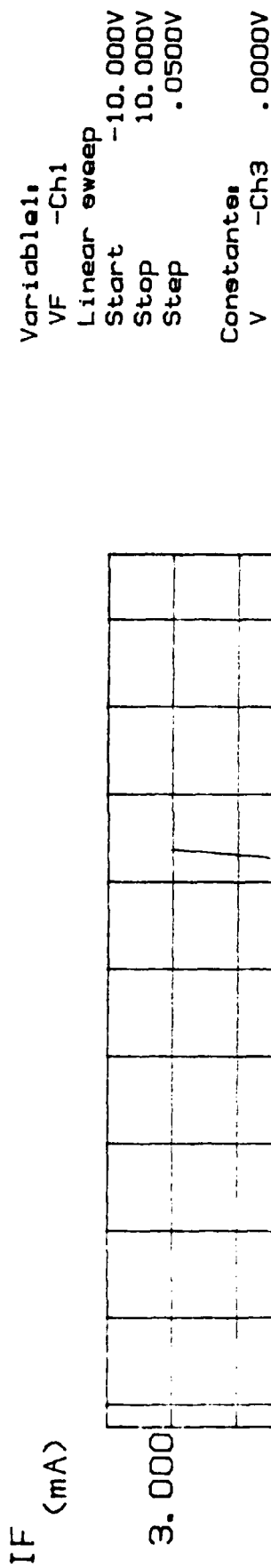


Figure 45a. I-V characteristics of μ -SiC (using a mercury probe) as-received sample.

Then,

$$\begin{aligned}
 I_1 : I_2 : I_3 &= V/R_1 : V/R_2 : V/R_3 \\
 &= 1/R_1 : 1/R_2 : 1/R_3 \\
 &= t_1/\rho_1 : t_2/\rho_2 : t_3/\rho_3
 \end{aligned}$$

The resistivity and the thickness of the Si substrate is 10^4 ohm-cm and 500 μm , respectively. The as-grown and undoped β -SiC films produced in this research and removed from the Si substrate normally have a resistivity of $\sim 10^{-2}$ ohm-cm and a thickness of 15 μm . If for the buffer, one assumes the same parameters to have the values of 10^{-3} ohm-cm and 10^{-2} μm , respectively, the ratio $I_1 : I_2 : I_3 = 1 : 6.7 \times 10^{-3} = 3.3 \times 10^{-5}$. Thus, the error introduced by the presence of the buffer layer (assuming the values of ρ and thickness are correct for this layer) can be estimated at less than 1% in the case of undoped SiC. If the dopant is introduced in to the Si (e.g. during in situ doping) the Si must be removed.

Table VI shows the results of Hall effect measurements on 23.6 μm thick samples with and without the Si substrate on the back. There is not much difference in the resistivity or in the carrier concentration, but mobility is markedly increased by the removal of the Si.

Table VI. Results of Hall effect measurements on undoped n-type SiC with and without the Si substrate. The thickness of SiC was 23.6 μm .

	Resistivity (ohm-cm)	Carrier Concn. (cm^{-3})	Mobility ($\text{cm}^2/\text{v-sec}$)
With Si	0.526	4.5×10^{16}	242
Without Si	0.677	2.63×10^{16}	351

***** GRAPHICS PLOT *****
OXIDIZED

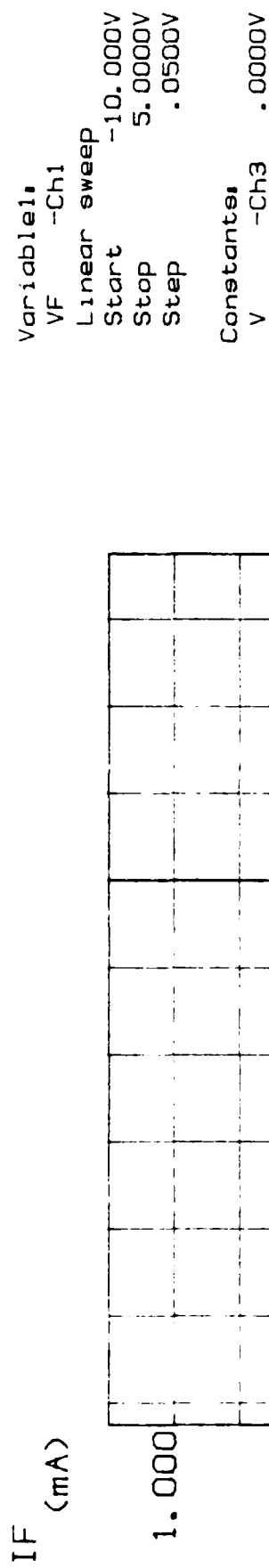


Figure 45b. I-V characteristics of β -SiC (using a mercury probe) after oxidation and etching in HF.

In an attempt to discern the chemistry of this high conductivity layer, Auger electron spectroscopy was conducted on samples prior to and after the 2073 anneal. Only Si, C and O were found in both conditions, as shown in Figs. 46a and b. However, there is a marked increase in the intensity of the C_{KLL} in the annealed sample. The ratio of the peak-to-peak intensity of the C_{KLL} to that of the Si_{LVV} for the sample before heating is 2.1; after heating this ratio increases to 3.5. Thus the presence of an increased amount of surface C as a result of the high temperature anneal is in evidence and explains the high conductivity shown in Fig. 45a.

D. Raman Spectroscopy and Hall Effect Measurements and Their Employment in the Study of the Effects of Annealing on the Electrical Properties of the As-Grown, Undoped β -SiC Films.

Because Si and SiC have different thermal expansion coefficients, the crystal lattice of each β -SiC film is elastically strained (in tension), especially in the region of the Si/SiC interface. The presence of this strain results in reduced mobility of the majority and minority carriers. To determine the amount of lattice strain in the as-grown, undoped SiC films, and the quantitative effect of this strain on electrical properties, Raman spectroscopy and Hall effect measurements were conducted.

In the Raman technique, an Ar laser tuned to 5145 \AA (green line) was used in this study. The samples for this study were prepared by removing the Si substrate via an etching process in a 1:1 solution of HF and HNO_3 . The β -SiC films were, in turn, sequentially annealed in Ar at 1473K, 1673K, 1773K, 1873K and 2073K for 3.0×10^2 s at each temperature. Following the heating process, the samples were oxidized and etched to remove the thin disturbed surface layer. Fig. 43 shows the increase in the relative intensity of both the TO (translational) and LO (longitudinal) vibration modes of the 2073K annealed films, relative to that of the as-grown. The positions of these peaks have also shifted four wave numbers (i.e. to lower energy positions) as a result of the annealing.

The increases in both sharpness and peak position indicate that relief in the residual strain is accomplished during the annealing process. Olego and Cardona¹¹ have determined the following empirical relationship between the lattice strain ($\frac{\Delta a}{a}$) and the shift (ω_{LO}) in the position of the LO Raman peak.

$$\omega_{LO} = (973 \pm 0.3) + (4532 \pm 30) \left[\frac{\Delta a}{a_0} \right] \quad (1)$$

where ω_{LO} has the units of cm^{-1} and $\left[\frac{\Delta a}{a_0} \right]$ is related to lattice strain. In terms of stress, P,

$$\omega_{LO} = (972.7 \pm 0.3) + (4.75 \pm 0.09)P - [(2.5 \pm 0.4) \times 10^{-2}]P^2 \quad (2)$$

with P having the units of GPa.

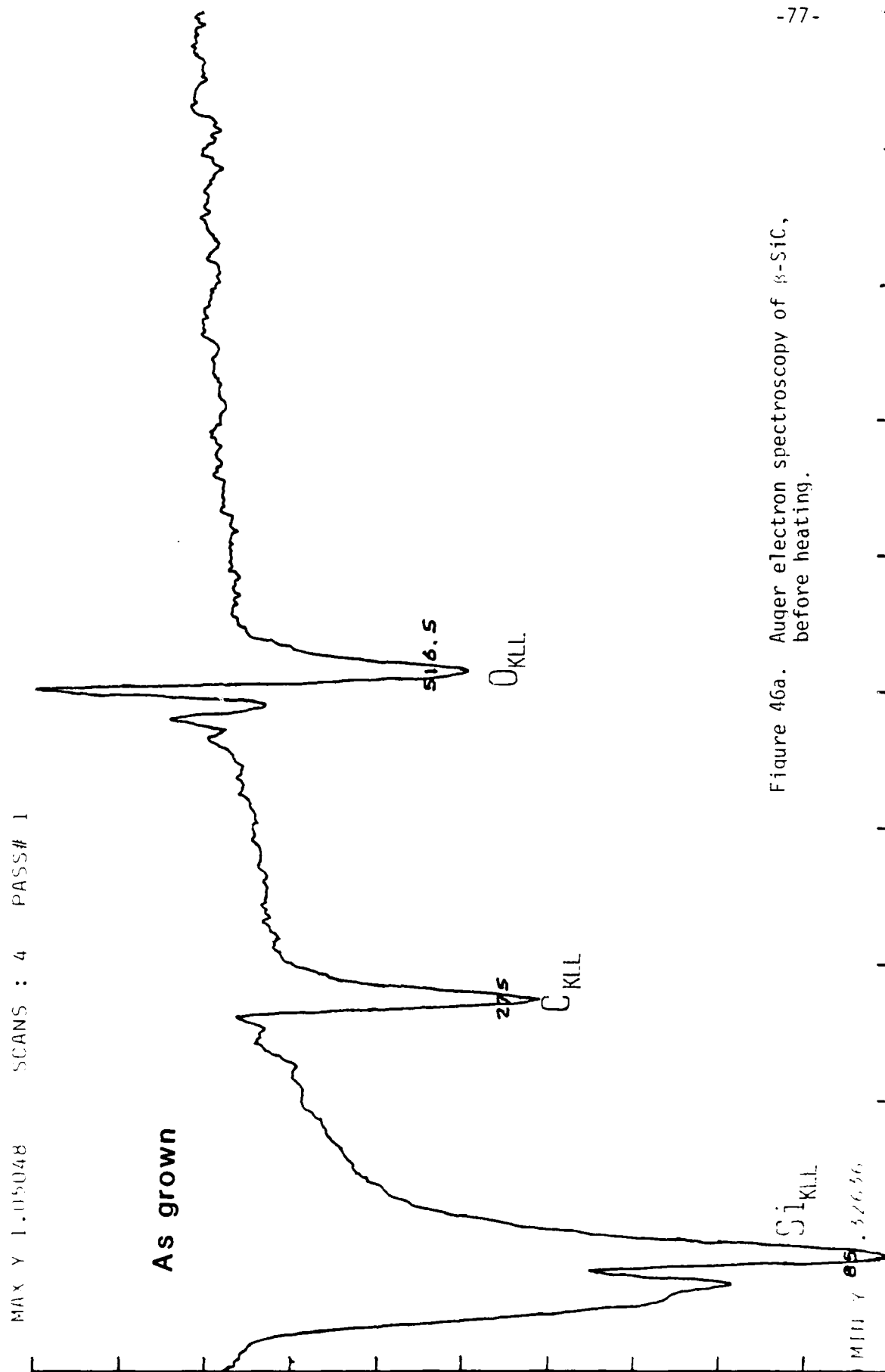


Figure 46a. Auger electron spectroscopy of β -SiC, before heating.

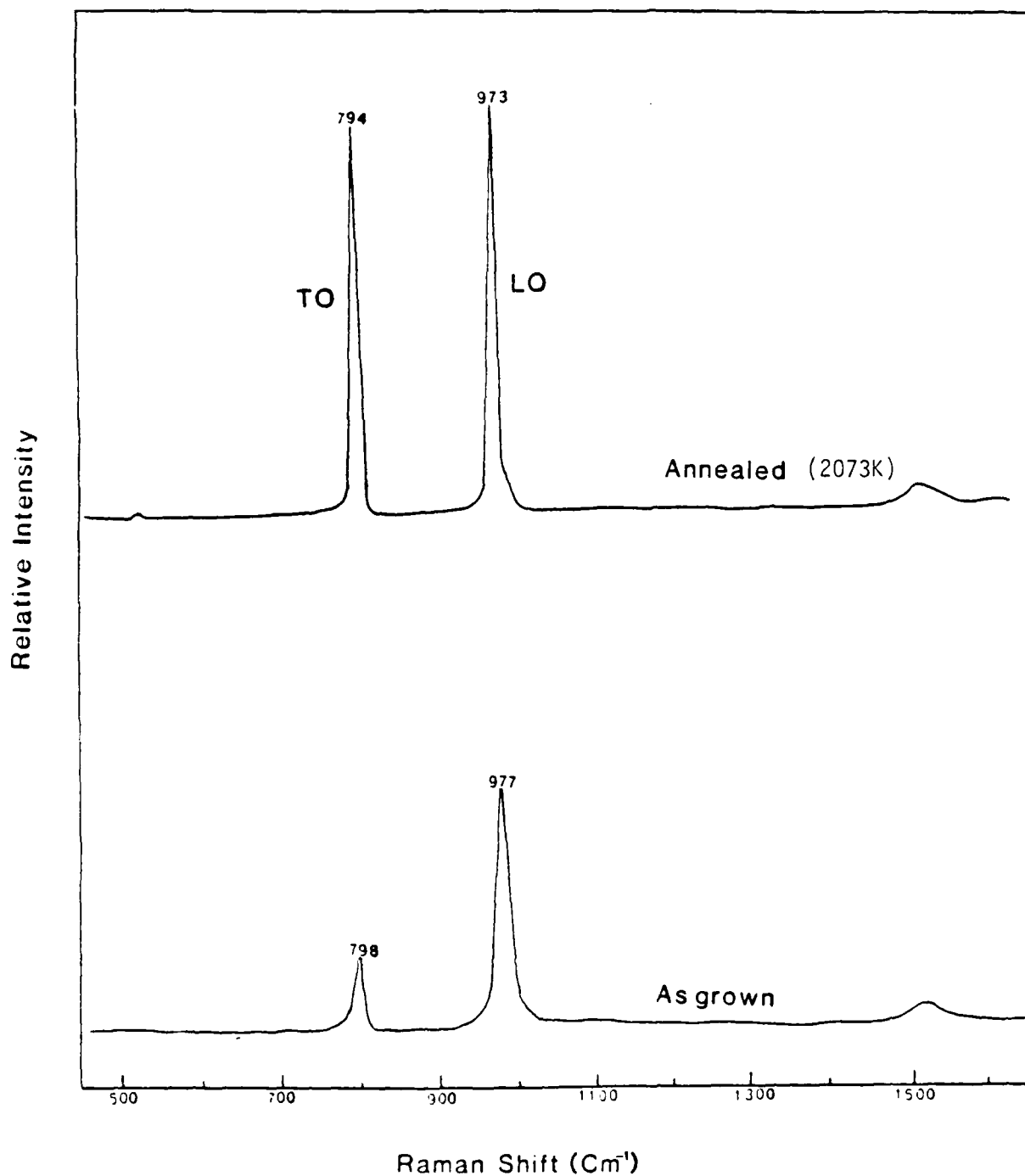


Figure 43. First order Raman spectra of an undoped β -SiC thin film before and after annealing. The Si substrate was etched away prior to the measurements.

MAX Y 1.74E8 SCANS : 5 PAGES # 1

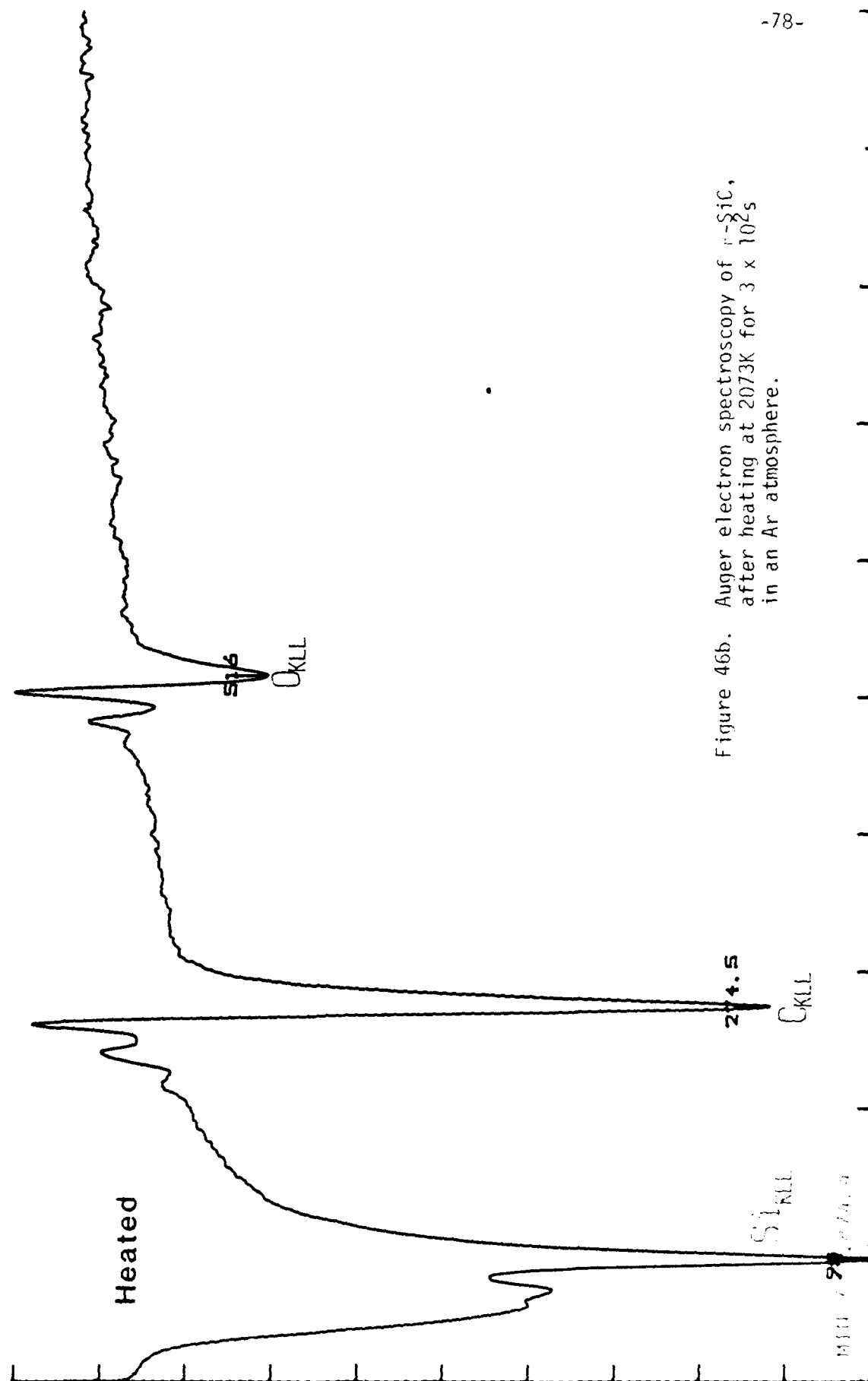


Figure 46b. Auger electron spectroscopy of r-SiC, after heating at 2073K for 3×10^2 s in an Ar atmosphere.

Thus the amount of lattice strain in the β -SiC film is calculated to be 0.0883%; the value of the elastic tensile stress from equation (2) is $0.02 \text{ GPa} = 2 \times 10^8 \text{ dynes/cm}^2$. This latter value is very close to the reported¹² value of tensile strength of $3.5 \times 10^8 \text{ dynes/cm}^2$ for a reaction bonded SiC material containing ~10% by volume of free Si.

Resistivity, active carrier concentration, and Hall mobility were measured on each sample using the van der Pauw method. These samples were also oxidized and etched to remove the disturbed surface layer prior to any measurement. As shown in Fig. 44 the carrier concentration continuously decreases while the mobility increases with an increase in the annealing temperature up to 1873K. These trends are sharply reversed as a result of the 2073 anneal. The increase in mobility of the samples annealed in the 1473K-1873K range is due to the annealing of the residual strain. The reason(s) for the rapid increase in n-type carrier concentration after annealing at 2073K is (are) not known. However it may be postulated to be caused by incorporation of N in the outer near-surface region during heating or by the presence of free C on the surface or by the creation of electrically active defects during heating. However, no N was found in the 2073K annealed samples using SIMS, and any free C is burned off during the oxidation and etching procedure, as noted in Section VI. E below. Thus, only the creation of electrically active defects remains the plausible explanation for the above phenomenon.

E. Effects of Annealing on the Surface Properties of β -SiC

During the annealing study on the undoped SiC films described in VI. D above, it was discovered that the electrical properties of the surface were altered, especially by the 2073K, $3.0 \times 10^2 \text{ s}$ anneal. The I-V characteristics of this sample obtained using a Hg probe are shown in Fig. 45a. Instead of the normal rectifying characteristics, this plot shows the presence of a very good ohmic contact. Further, more the removal of ~100Å of surface via oxidation and etching restores the initial electrical properties as shown in Fig. 45b. This obviously indicates that a conductive layer forms on the SiC surface after the 2073K anneal and that the thickness of this layer is less than 100Å.

VII. PREPARATION OF β -SiC FILMS FOR IMPLANTATION, OXIDATION AND DEVICE FABRICATION

The final surface of as-grown β -SiC is not sufficiently flat (variation of 0.1-0.2 μm) for the fabrication of devices. It is also possible that this uneven surface decreases the measured mobility and increases the leakage current of the film. As such a polishing procedure has been developed to eliminate the wave-like nature of this surface. In this procedure each sample with its Si substrate is wax mounted Si side down on a 2.5 μm precision machined and polished block have a variation in surface flatness within 0.00025 μm across its diameter. The block and sample are then placed in a Syntron polishing/lapping machine containing an oiled nylon cloth work surface. One-tenth micron diamond paste serves as the polishing media.

Typically samples are polished for 48 hours. In that time, approximately 1500 \AA (the amount of as-grown surface roughness) of material is removed. Dektak profilometry results illustrated in Fig. 47, indicates that the surface roughness disappears after the polishing procedure. However any differences in the total thickness of the film from one side to the other remains.

Cross-sectional TEM analyses have also been conducted on polished and polished/oxidized/etched samples to determine the extent of surface damage that results from polishing. Figure 48a shows the surface of a polished sample at a magnification of 200KX ($\vec{g} = [111]$). As indicated by this figure, approximately 200 \AA of surface disorder results during polishing. This damage appeared under many diffracting contrast conditions. No particular type of defect is dominant. To remove polish-induced surface damage, as well as any surface contaminants introduced during growth, oxidation is performed using procedures described below. The standard oxidation presently used involves the growth of 5000 \AA of SiO_2 which removes nearly 1700 \AA of SiC. An STEM micrograph of a polished/oxidized/HF etched SiC sample is shown in Fig. 48b. Again, the magnification was 200KX and diffracting condition $\vec{g} = (111)$. As shown, virtually no surface damage remained after oxidation. In addition, the carrier

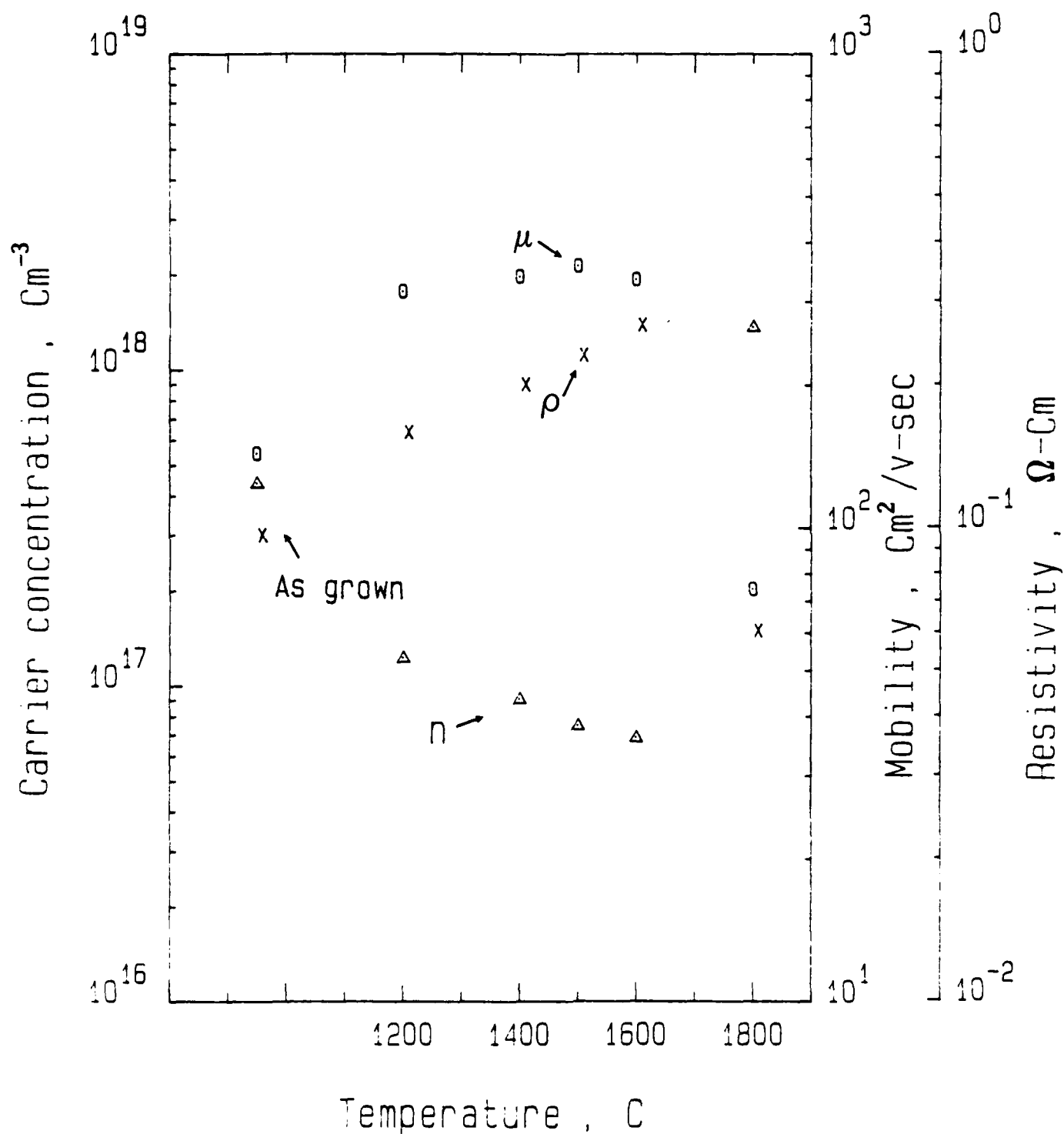


Figure 44. Dependence of annealing temperature on Hall effect parameters in annealed 3-SiC.

*
*
*
*
*

```
Variable:
VF      -Ch1
Linear sweep
Start   -10.000V
Stop    10.000V
Step    .0500V

Constants:
V       -Ch3      .0000V
```

[illegible]

tic (using a mercury

***** GRAPHICS PLOT *****
OXIDIZED

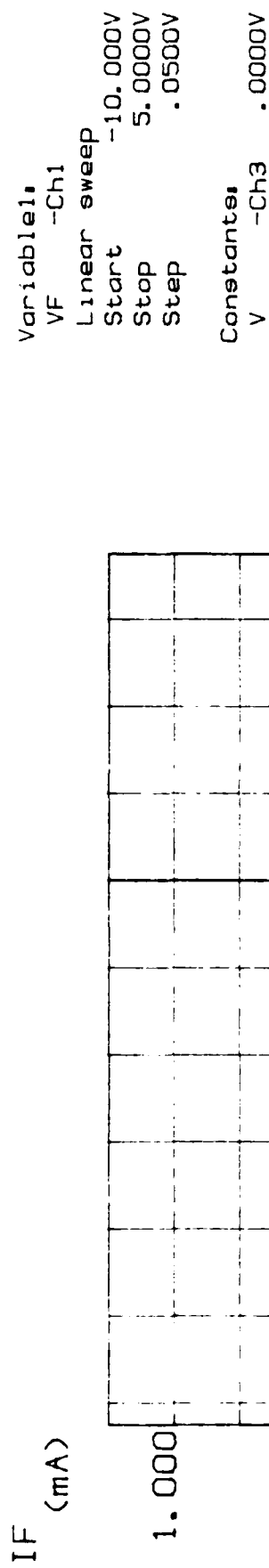


Figure 45b. I-V characteristics of β -SiC (using a mercury probe) after oxidation and etching in HF.

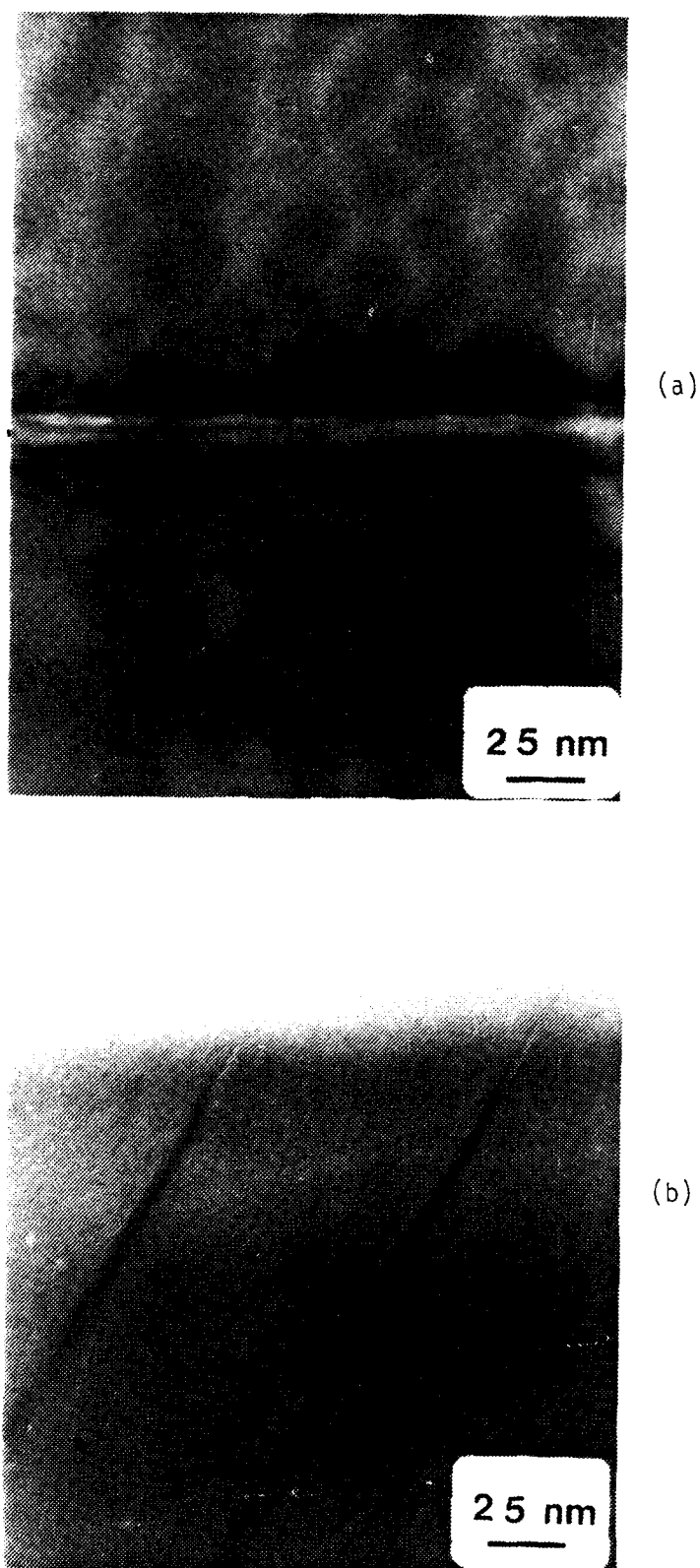


Figure 43. Cross-sectional TEM micrographs of the region at and near the top surface of β -SiC thin films showing (a) subsurface damage after polishing with 0.1 μ m diamond paste and (b) similarly polished sample after oxidation and resultant removal of this damage.

In an attempt to discern the chemistry of this high conductivity layer, Auger electron spectroscopy was conducted on samples prior to and after the 2073 anneal. Only Si, C and O were found in both conditions, as shown in Figs. 46a and b. However, there is a marked increase in the intensity of the C_{KLL} in the annealed sample. The ratio of the peak-to-peak intensity of the C_{KLL} to that of the Si_{LVV} for the sample before heating is 2.1; after heating this ratio increases to 3.5. Thus the presence of an increased amount of surface C as a result of the high temperature anneal is in evidence and explains the high conductivity shown in Fig. 45a.

concentration of $7 \times 10^{16}/\text{cm}^3$ was found to be very constant as a function of depth (up to $0.25 \mu\text{m}$) into the film (see section X for a more complete explanation of this aspect).

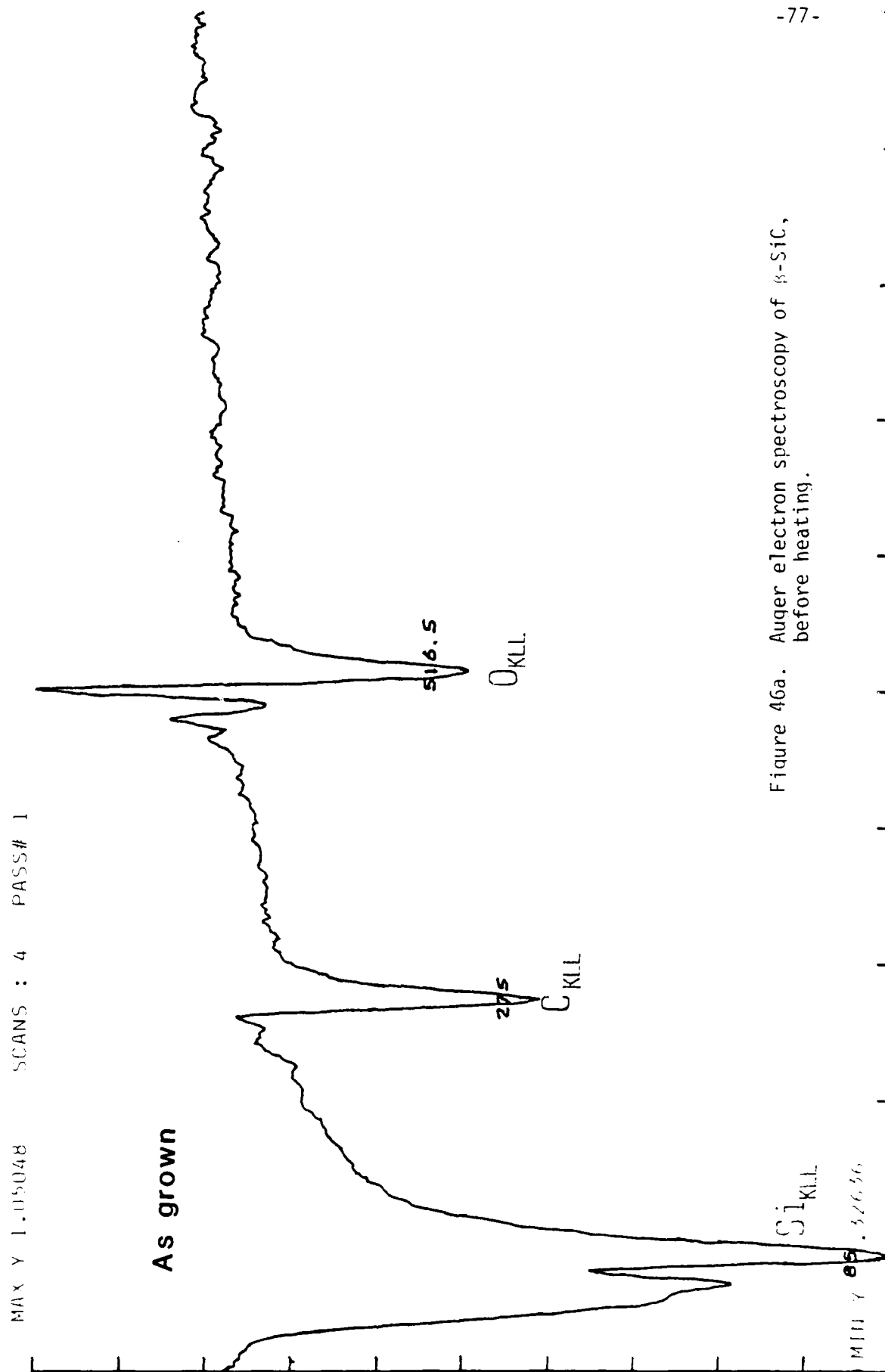


Figure 46a. Auger electron spectroscopy of β -SiC, before heating.

VIII. ION IMPLANTATION AND ANNEALING

A. Overview

In the course of this research program, ions of Al, P, B, and N were implanted into the β -SiC thin films at various dose levels and energies. The films were, in turn annealed at increasingly higher temperatures and measured for the onset of electrical ionization of the implanted species via C-V measurements of the amount (and type) of charge carrier present as a function of temperature. The results for each of these dopants will be discussed in turn in the following paragraphs.

Prior to implantation, each as-grown sample was polished, cleaned using the standard RCA routine and the surface damage removed via oxidation. This provides a clean and flat surface. In addition, sheet resistance, R_s , and the intrinsic effective carrier concentration, N_{eff} , were measured in order to have baseline data with which to compare the annealed samples.

B. Experiments in Ion Implantation and Annealing of β -SiC

1. Introduction

The ion implantation in our β -SiC films conducted during the period of this grant by the NCSU implantation facilities and at NRL is shown in Table VII. All starting films were undoped with n-type character and deposited on 10^4 ohm-cm p-type Si wafers. The Si triple implant samples were produced in conjunction with P and Al implants to determine if the regrowth of the amorphous layer produced by the former implant from a position deeper inside the sample than the latter implant could eliminate the unrecovered damage normally associated with the initial position of regrowth. In other words, dislocation loops and other damage are normally associated with the point of onset of regrowth of a heavily damaged or an amorphous layer produced by the implantation procedure. The Si was implanted to a greater depth than the maximum depth of the subsequent P implant as well as at intermediate and shallow depths by using three different implant schedules (see Table III). Cross sectional electron microscopy coupled with

May 1, 1978 SCANS : 5 PRS, # 1

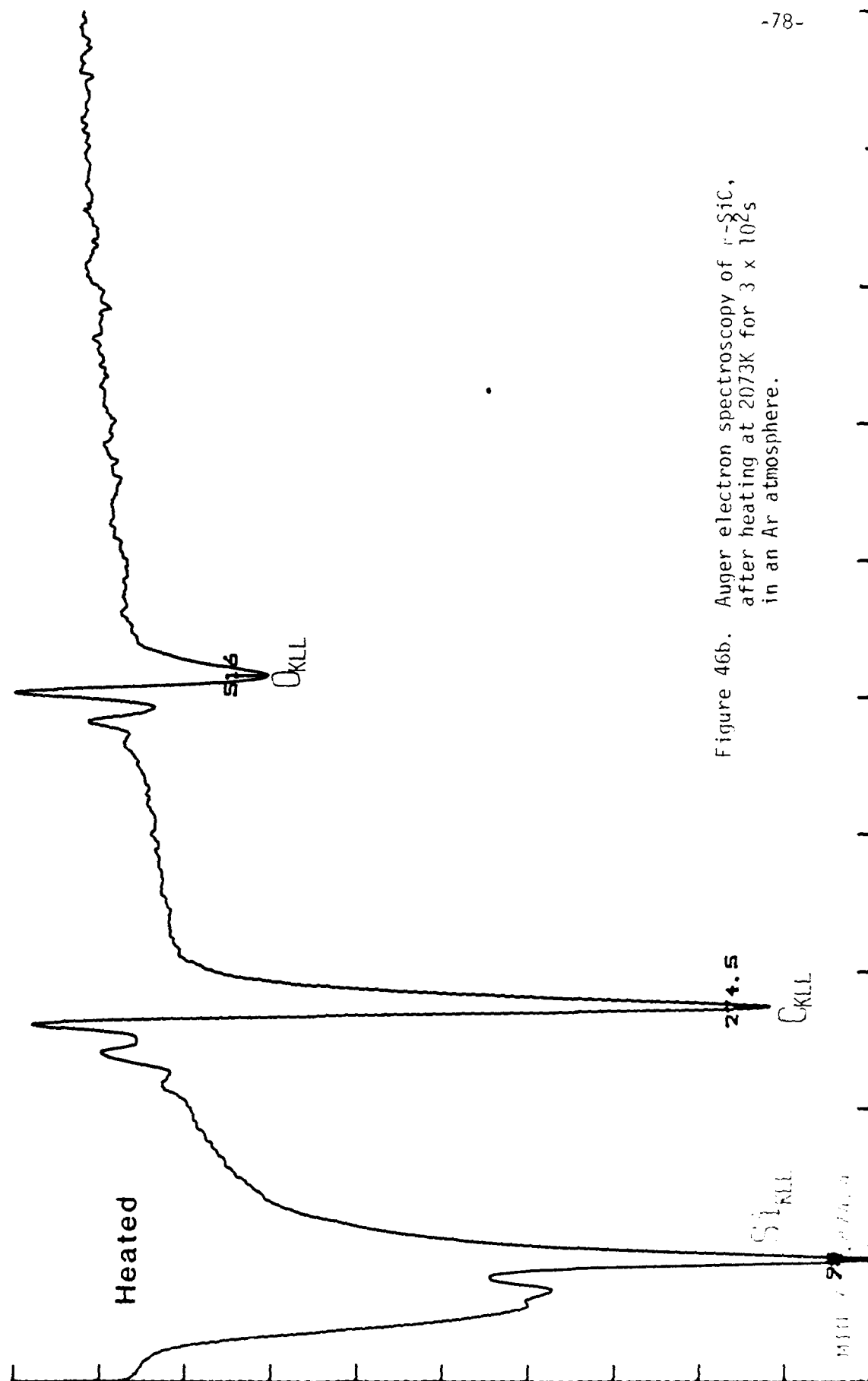


Figure 46b. Auger electron spectroscopy of r-SiC, after heating at 2073K for 3×10^2 s in an Ar atmosphere.

microdiffraction has shown this multiple implant region to be amorphous. However, damage recovery (or, at least, electrical activation of the charge carriers) has been a not unexpected problem.

According to Marsh¹³, recovery of ion implanted structural damage in α -SiC is $\approx 95\%$ complete after 900s at 1473K with any residual disorder being caused by nonequilibrium point and line defects. By contrast, electrical activation of implanted charge carrier species is not complete until a temperature of ≈ 1973 K. Thus, another thrust area in this reporting period has been to ascertain if these results were also true for our β -SiC films.

Table VII. Schedule of Beta SiC Samples and Implant Species and Conditions.
All samples were implanted using a % offset.

Implant Species	No. of Samples	Implant Conditions		Temp.	Utilization Implant Samples (No)
Potential(keV)	Dose(1/cm ²)				
Si	4	320	1.36×10^{15}	Ambient	XTEM after implantation(1)
		160	8.6×10^{15}	Ambient	Annealing/resistivity study(1)
		80	5×10^{15}	Ambient	XTEM after annealing(1) RBS channeling study(1)
P	8	140	4.6×10^{14}	Ambient	(a) without Si triple implant XTEM after implantation(1) Annealing/resistivity study(1) XTEM after annealing(1) RBS channeling study(1) Extra sample(1)
					(b) with Si triple implant Annealing/resistivity study(1) XTEM after annealing(1) RBS channeling study(1)
					(c) without Si triple implant XTEM after implantation(1) Annealing/resistivity study(2) XTEM after annealing(1)
					(d) without Si triple implant XTEM after implantation(1) Annealing/resistivity study(2) XTEM after annealing(1)
	4	110	7.7×10^{13}	Ambient	
	4	220	1.0×10^{15}	LN ₂	
		110	6.0×10^{14}	LN ₂	
		60	3.6×10^{14}	LN ₂	
Al	8	120	4.59×10^{13}	Ambient	(a) without Si triple implant Five samples to be used in the same way as P (a).

VII. PREPARATION OF β -SiC FILMS FOR IMPLANTATION, OXIDATION AND DEVICE FABRICATION

The final surface of as-grown β -SiC is not sufficiently flat (variation of 0.1-0.2 μm) for the fabrication of devices. It is also possible that this uneven surface decreases the measured mobility and increases the leakage current of the film. As such a polishing procedure has been developed to eliminate the wave-like nature of this surface. In this procedure each sample with its Si substrate is wax mounted Si side down on a 2.5 μm precision machined and polished block have a variation in surface flatness within 0.00025 μm across its diameter. The block and sample are then placed in a Syntron polishing/lapping machine containing an oiled nylon cloth work surface. One-tenth micron diamond paste serves as the polishing media.

Typically samples are polished for 48 hours. In that time, approximately 1500 \AA (the amount of as-grown surface roughness) of material is removed. Dektak profilometry results illustrated in Fig. 47, indicates that the surface roughness disappears after the polishing procedure. However any differences in the total thickness of the film from one side to the other remains.

Cross-sectional TEM analyses have also been conducted on polished and polished/oxidized/etched samples to determine the extent of surface damage that results from polishing. Figure 48a shows the surface of a polished sample at a magnification of 200KX ($\vec{g} = [111]$). As indicated by this figure, approximately 200 \AA of surface disorder results during polishing. This damage appeared under many diffracting contrast conditions. No particular type of defect is dominant. To remove polish-induced surface damage, as well as any surface contaminants introduced during growth, oxidation is performed using procedures described below. The standard oxidation presently used involves the growth of 5000 \AA of SiO_2 which removes nearly 1700 \AA of SiC. An STEM micrograph of a polished/oxidized/HF etched SiC sample is shown in Fig. 48b. Again, the magnification was 200KX and diffracting condition $\vec{g} = (111)$. As shown, virtually no surface damage remained after oxidation. In addition, the carrier

Table VII. Continued

Implant Species	No. of Samples	Implant Conditions		Temp.	Utilization Implant Samples (No)
		Potential(keV)	Dose($1/\text{cm}^2$)		
					(b) with Si triple implant Three samples to be used in the same way as P (b).
	4	190 110	9×10^{14} 6×10^{14}	Ambient Ambient	(c) without Si triple implant XTEM after implantation(1) Annealing/resistivity study(2)
	4	200 130 70	4.3×10^{16} 3.3×10^{16} 2.0×10^{16}	LN_2 LN_2 LN_2	(d) XTEM after implantation(1) Annealing/resistivity study(2) XTEM after annealing(1)
N	3	120	1.4×10^{14}	Ambient	Annealing/resistivity study(1) XTEM(1) RBS channeling(1)
	4	200 100	1.5×10^{14} 1.1×10^{14}	Ambient Ambient	XTEM after implantation(1) Annealing/resistivity study(2) XTEM after annealing(1)
B	4	200	7.6×10^{13}	Ambient	XTEM after implantation(1) Annealing/resistivity study(2) XTEM after annealing(1)
	4	200 100	2×10^{15} 1.5×10^{15}	Ambient Ambient	XTEM after implantation(1) Annealing/resistivity study(2) XTEM after annealing(1)

2. Results and Discussion

a. Phosphorous and Aluminum Implants

Attempts to achieve electrical activation initially involved the Si triple implant samples containing P or Al as well as implants containing only P or Al as the introduced species and the employment of rapid thermal annealing using a Heatpulse^R 210 with a maximum temperature capability of 1525K within 10s. Four samples were annealed in Ar at 50K intervals from 1073-1525K. The sheet resistance measurements given in Table VIII provided information on the relative extent of activation. The data in this table shows that no activation of either P^+ or Al^+ in the Si^+ triple implant was observed. Furthermore only a slight drop in resistivity was recorded for the P^+ implant alone from 1423-1523K.

POLISHING RESULTS - PROFILOMETRY



as-grown surface

(a)



after polish

(b)

Figure 47. Dektak surface profile of SiC thin film deposited on Si (a) before polishing--sample has surface roughness of 0.1-0.2 μm, (b) after polishing using 0.1 μm diamond paste--surface roughness negligible.

Table VIII. Effect of Rapid Thermal Annealing at Various Temperatures up to 1523K of Triple Si Ion Implants as Well as Implants of Al^+ (120 keV, $4.59 \times 10^{13}/\text{cm}^2$) and P^+ (140 keV, $4.6 \times 10^{14}/\text{cm}^2$) on Sheet Resistance (ohms/cm^2) in β -SiC Films. Annealing Time was 10s at Each Temperature.

Anneal Temp. (K)/ Resistivity (ohms/cm^2)	Si^+ Triple Imp. plus Al^+	Si^+ Triple Imp. plus P^+	Al^+ in SiC	P^+ in SiC
Initial	>3000	>3000	770	1250
1073	unchanged	unchanged	unchanged	unchanged
1123				
1173				
1223				
1273				
1323	unchanged	unchanged	unchanged	1150
1373				1100
1423				920
1473				
1523				

To increase the temperature further while maintaining the rapidity of heating, a special vacuum evaporation system capable of heating two samples simultaneously to temperatures in excess of 2275K was retrofitted for our annealing studies. To maintain purity, very high purity SiC-coated graphite strip heaters containing a sample cavity were employed for supplying heat to the samples. The maximum use temperature was initially limited by the 1688K melting point of the Si substrate. However, as a result of this, techniques to grow thicker (up to 20 μm) β -SiC films were developed so that the films could be removed before annealing as well as annealed at much higher temperatures. The remainder of this section is concerned only with the results from these thicker samples.

The low dose (7.7×10^{13}) P implant shown in Table VII has, from LSS theory, a projected range, R_p in SiC of 0.0921 μm . The fluctuation or straggle in R_p is $\Delta R_p = 0.0303$. Figure 49 shows the profile of the concentration vs the depth determined with the ion microprobe for this P-implanted SiC as well as the theoretical implant curve from LSS calculations using the same conditions noted above. These calculations assume the implant is made into an amorphous SiC. The experimental peak concentration appears at 0.0940 μm which deviates only 1.9% from the LSS value of 0.0902 μm .

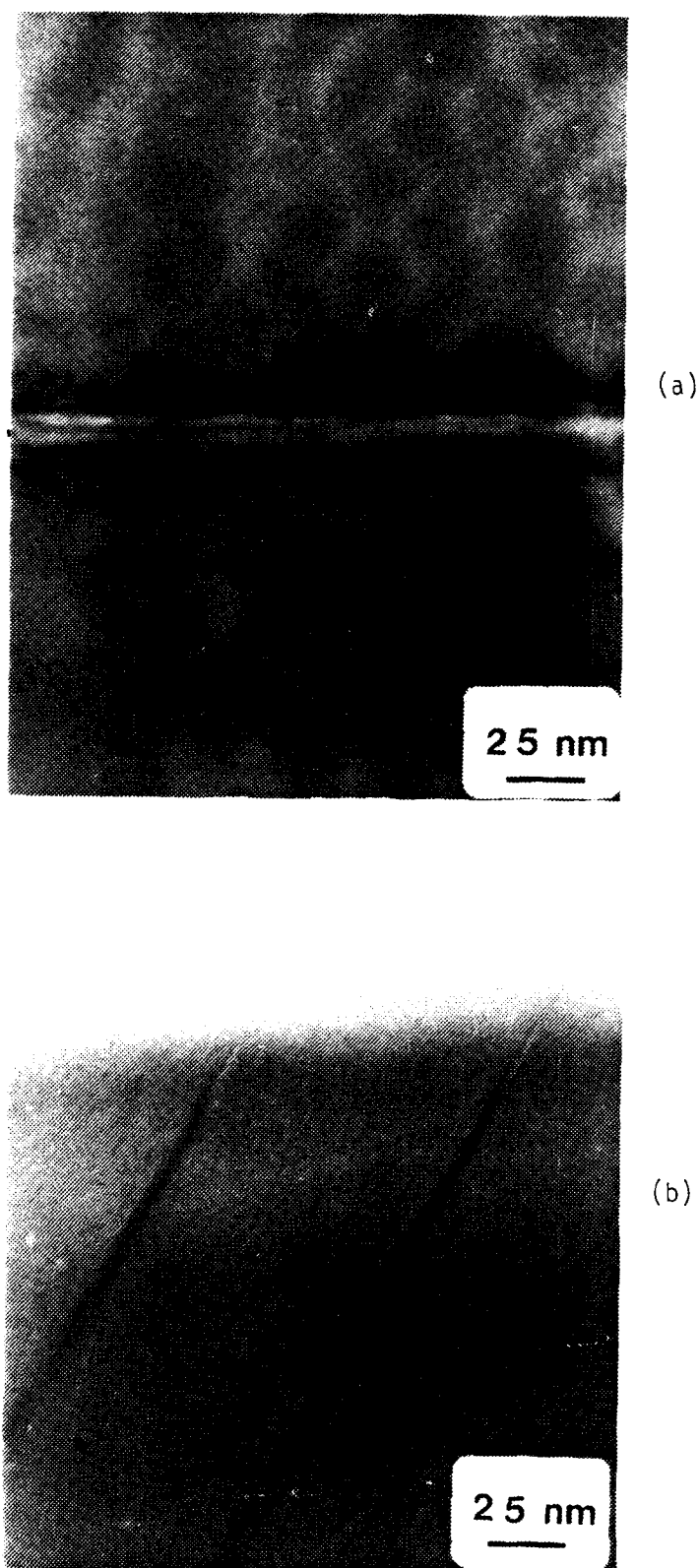


Figure 43. Cross-sectional TEM micrographs of the region at and near the top surface of β -SiC thin films showing (a) subsurface damage after polishing with 0.1 μ m diamond paste and (b) similarly polished sample after oxidation and resultant removal of this damage.

P IN B-SIC
AT/CM3

PSICE2

08/30/84

10E20

10E19

10E18

10E17

10E16

RATIO PLOT

LSS

0.000

.100

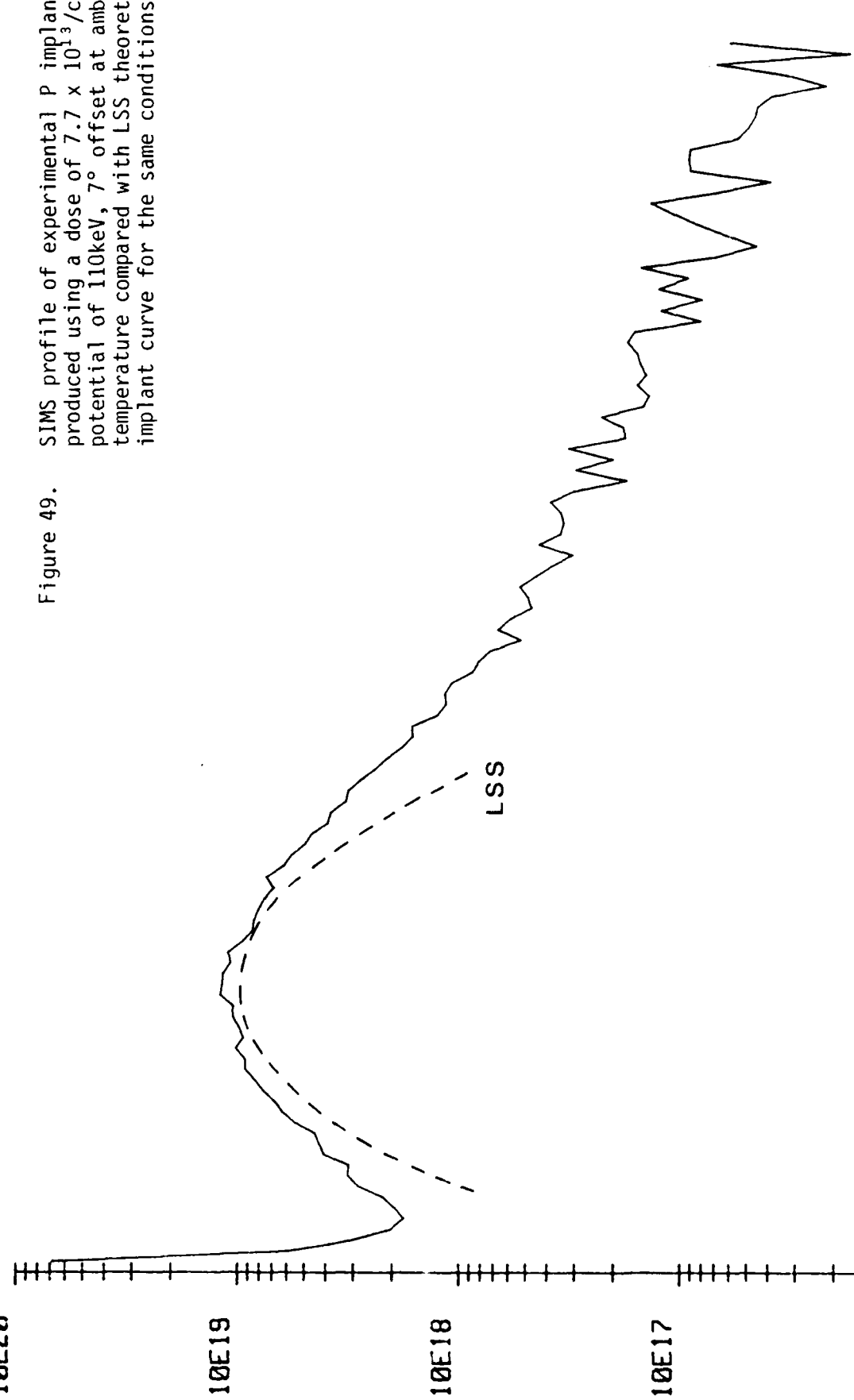
.200

.300

.400

MICRONS

Figure 49. SIMS profile of experimental P implant produced using a dose of $7.7 \times 10^{13}/\text{cm}^2$ potential of 110keV, 7° offset at ambient temperature compared with LSS theoretical implant curve for the same conditions.



concentration of $7 \times 10^{16}/\text{cm}^3$ was found to be very constant as a function of depth (up to $0.25 \mu\text{m}$) into the film (see section X for a more complete explanation of this aspect).

To observe the structural surface damage caused by ion implantation, XTEM was again utilized. As shown in Fig. 50a (mag. = 100KX $g = [111]$), a 1600Å surface layer best characterized as point defect rich is evident. The first 200-300Å appears to be fairly defect free as the higher energy electronic scattering events dominate the incident ion displacement. The center of the adjacent darker band is approximately 900Å from the sample surface. This coincides very well with the R_p value of 904Å obtained from SIMS analyses. No amorphization occurred as indicated by the extension of stacking faults from the unimplanted region through the implanted region to the surface.

As shown in Table IX, the intrinsic electron carrier concentration of the pre-implanted sample was $4 \times 10^{17}/\text{cm}^3$. The C-V profile is given in Fig. 51. At a reverse bias value of 3.2 V, the leakage current increased quickly to 200 μA . No further voltage was applied.

Table IX. Summary of annealing results for P implanted into β -SiC.
Implant conditions: dose = 7.71×10^{13} , energy = 110 keV.

Anneal Temp (K)	Anneal Time (min)	R_s (Ω/\square)	N_{eff} (cm^{-3})	Anneal Atmosph.
Preimplant	NA	40	4×10^{17}	NA
RT	NA	40	9×10^{17} (?)	NA
1273	10	40	NR	Argon
1373	10	40		
1473	10	40		
1573	10	40		
1673	10	39		
1713	5	38		
1773	5	37		
1823	5	37		
1873	5	34		
1973	3.5	25		
2013	3.5	23		
2073	3.5	18	$\sim 10^{18}$	
2173	2.5	18	NR	

Following implantation a C-V measurement was conducted (i.e., this constitutes a sample which has received a room temperature anneal).

VIII. ION IMPLANTATION AND ANNEALING

A. Overview

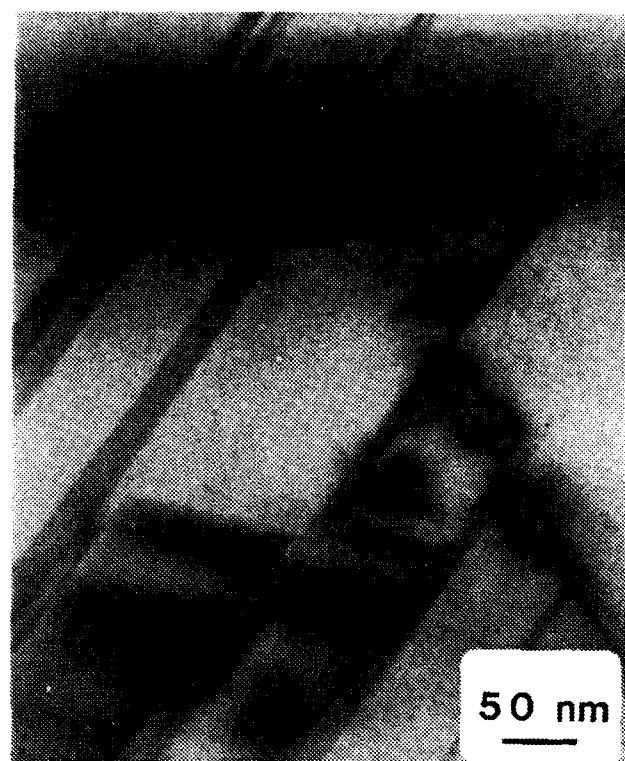
In the course of this research program, ions of Al, P, B, and N were implanted into the β -SiC thin films at various dose levels and energies. The films were, in turn annealed at increasingly higher temperatures and measured for the onset of electrical ionization of the implanted species via C-V measurements of the amount (and type) of charge carrier present as a function of temperature. The results for each of these dopants will be discussed in turn in the following paragraphs.

Prior to implantation, each as-grown sample was polished, cleaned using the standard RCA routine and the surface damage removed via oxidation. This provides a clean and flat surface. In addition, sheet resistance, R_s , and the intrinsic effective carrier concentration, N_{eff} , were measured in order to have baseline data with which to compare the annealed samples.

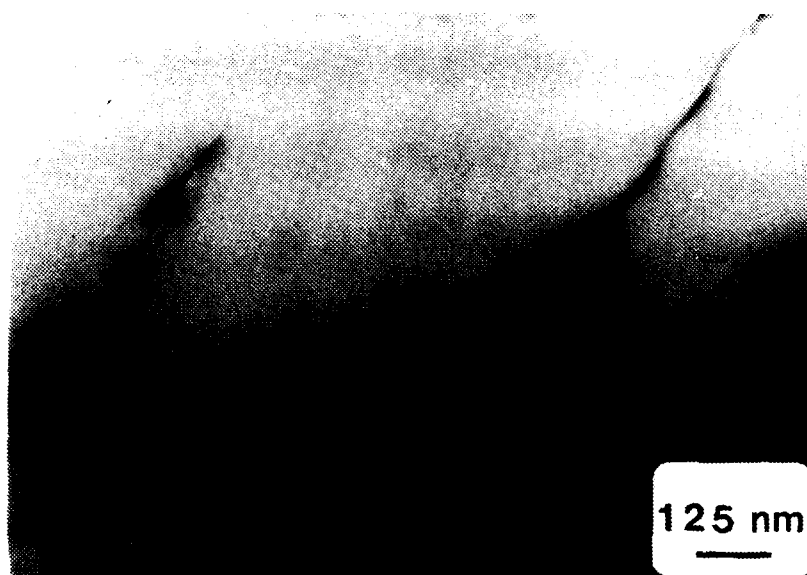
B. Experiments in Ion Implantation and Annealing of β -SiC

1. Introduction

The ion implantation in our β -SiC films conducted during the period of this grant by the NCSU implantation facilities and at NRL is shown in Table VII. All starting films were undoped with n-type character and deposited on 10^4 ohm-cm p-type Si wafers. The Si triple implant samples were produced in conjunction with P and Al implants to determine if the regrowth of the amorphous layer produced by the former implant from a position deeper inside the sample than the latter implant could eliminate the unrecovered damage normally associated with the initial position of regrowth. In other words, dislocation loops and other damage are normally associated with the point of onset of regrowth of a heavily damaged or an amorphous layer produced by the implantation procedure. The Si was implanted to a greater depth than the maximum depth of the subsequent P implant as well as at intermediate and shallow depths by using three different implant schedules (see Table III). Cross sectional electron microscopy coupled with



(a)



(b)

Figure 50. Cross-sectional TEM micrographs of a P implanted (dose = $7.7 \times 10^{13}/\text{cm}^2$, potential = 110 keV) β -SiC single crystal thin film showing (a) the as-implanted region (top one third of micrograph) with intersecting stacking faults and (b) same region after annealing at 2073K for 210s.

microdiffraction has shown this multiple implant region to be amorphous. However, damage recovery (or, at least, electrical activation of the charge carriers) has been a not unexpected problem.

According to Marsh¹³, recovery of ion implanted structural damage in α -SiC is $\approx 95\%$ complete after 900s at 1473K with any residual disorder being caused by nonequilibrium point and line defects. By contrast, electrical activation of implanted charge carrier species is not complete until a temperature of ≈ 1973 K. Thus, another thrust area in this reporting period has been to ascertain if these results were also true for our β -SiC films.

Table VII. Schedule of Beta SiC Samples and Implant Species and Conditions.
All samples were implanted using a % offset.

Implant Species	No. of Samples	Implant Conditions		Temp.	Utilization Implant Samples (No)
Potential(keV)	Dose(1/cm ²)				
Si	4	320	1.36×10^{15}	Ambient	XTEM after implantation(1)
		160	8.6×10^{15}	Ambient	Annealing/resistivity study(1)
		80	5×10^{15}	Ambient	XTEM after annealing(1) RBS channeling study(1)
P	8	140	4.6×10^{14}	Ambient	(a) without Si triple implant XTEM after implantation(1) Annealing/resistivity study(1) XTEM after annealing(1) RBS channeling study(1) Extra sample(1)
					(b) with Si triple implant Annealing/resistivity study(1) XTEM after annealing(1) RBS channeling study(1)
					(c) without Si triple implant XTEM after implantation(1) Annealing/resistivity study(2) XTEM after annealing(1)
					(d) without Si triple implant XTEM after implantation(1) Annealing/resistivity study(2) XTEM after annealing(1)
	4	110	7.7×10^{13}	Ambient	
	4	220	1.0×10^{15}	LN ₂	
		110	6.0×10^{14}	LN ₂	
		60	3.6×10^{14}	LN ₂	
Al	8	120	4.59×10^{13}	Ambient	(a) without Si triple implant Five samples to be used in the same way as P (a).

Table VII. Continued

Implant Species	No. of Samples	Implant Conditions		Temp.	Utilization Implant Samples (No)
		Potential(keV)	Dose($1/\text{cm}^2$)		
					(b) with Si triple implant Three samples to be used in the same way as P (b).
	4	100	0.1014		

As indicated in Figure 51, the leakage current was very high at -0.2 V. For that reason the N_{eff} value for the RT anneal is not credible. After each anneal, C-V measurements were attempted. However, no response was recorded until the 2073K, 3.5-minute anneal temperature was reached. The result is also shown in Figure 51. Quite clearly the profile shape closely mimicks the SIMS profile with the peak being near the $0.09 \mu\text{m}$ value previously determined. The effective carrier concentration value at this peak is, however, one order of magnitude lower than the implanted concentration of phosphorous atoms which is the same ratio of concentrations found in the in situ doped samples. The only conclusion to derive from this result is that at room temperature the activation combined with ionization of P is $\sim 10\%$ of the maximum 10^{19} value.

During the 2173K -2.5-minute anneal the sample began to decompose. As indicated in Table IX, R_s did not change from the value at 2073K and N_{eff} could not be measured. A plot of annealing temperature vs R_s is shown in Figure 52.

To observe the extent of P impurity diffusion of the 2073K annealed sample, ion microprobe analysis was conducted. Figure 53 compares the concentration vs depth profiles of the as-implanted (preannealed) and annealed samples. As expected, the annealed profile peak became marginally depressed and widened. It seems fair to conclude that, as far as devices are concerned, diffusion of P

Table VIII. Effect of Rapid Thermal Annealing at Various Temperatures up to 1523K of Triple Si Ion Implants as Well as Implants of Al⁺ (120 keV, $4.59 \times 10^{13}/\text{cm}^2$) and P⁺ (140 keV, $4.6 \times 10^{14}/\text{cm}^2$) on Sheet Resistance (ohms/cm²) in β -SiC Films. Annealing Time was 10s at Each Temperature.

Anneal Temp. (K)/ Resistivity (ohms/cm ²)	Si ⁺ Triple Imp. plus Al ⁺	Si ⁺ Triple Imp. plus P ⁺	Al ⁺ in SiC	P ⁺ in SiC
Initial	>3000	>3000	770	1250
1073	unchanged	unchanged	unchanged	unchanged
1123				
1173				
1223				
1273				
1323	unchanged	unchanged	unchanged	unchanged
1373				
1423				
1473				
1523				
				1150
				1100
				920

To increase the temperature further while maintaining the rapidity of heating, a special vacuum evaporation system capable of heating two samples simultaneously to temperatures in excess of 2275K was retrofitted for our annealing studies. To maintain purity, very high purity SiC-coated graphite strip heaters containing a sample cavity were employed for supplying heat to the samples. The maximum use temperature was initially limited by the 1688K melting point of the Si substrate. However, as a result of this, techniques to grow thicker (up to 20 μm) β -SiC films were developed so that the films could be removed before annealing as well as annealed at much higher temperatures. The remainder of this section is concerned only with the results from these thicker samples.

The low dose (7.7×10^{13}) P implant shown in Table VII has, from LSS theory, a projected range, R_p in SiC of 0.0921 μm . The fluctuation or straggle in R_p is $\Delta R_p = 0.0303$. Figure 49 shows the profile of the concentration vs the depth determined with the ion microprobe for this P-implanted SiC as well as the theoretical implant curve from LSS calculations using the same conditions noted above. These calculations assume the implant is made into an amorphous SiC. The experimental peak concentration appears at 0.0940 μm which deviates only 1.9% from the LSS value of 0.0902 μm .

LOW DOSE P ANNEAL

$$D = 7.7 \times 10^{13} \text{ cm}^{-2}$$

$$E = 110 \text{ keV}$$

SHEET RESISTANCE Ω/\square

100

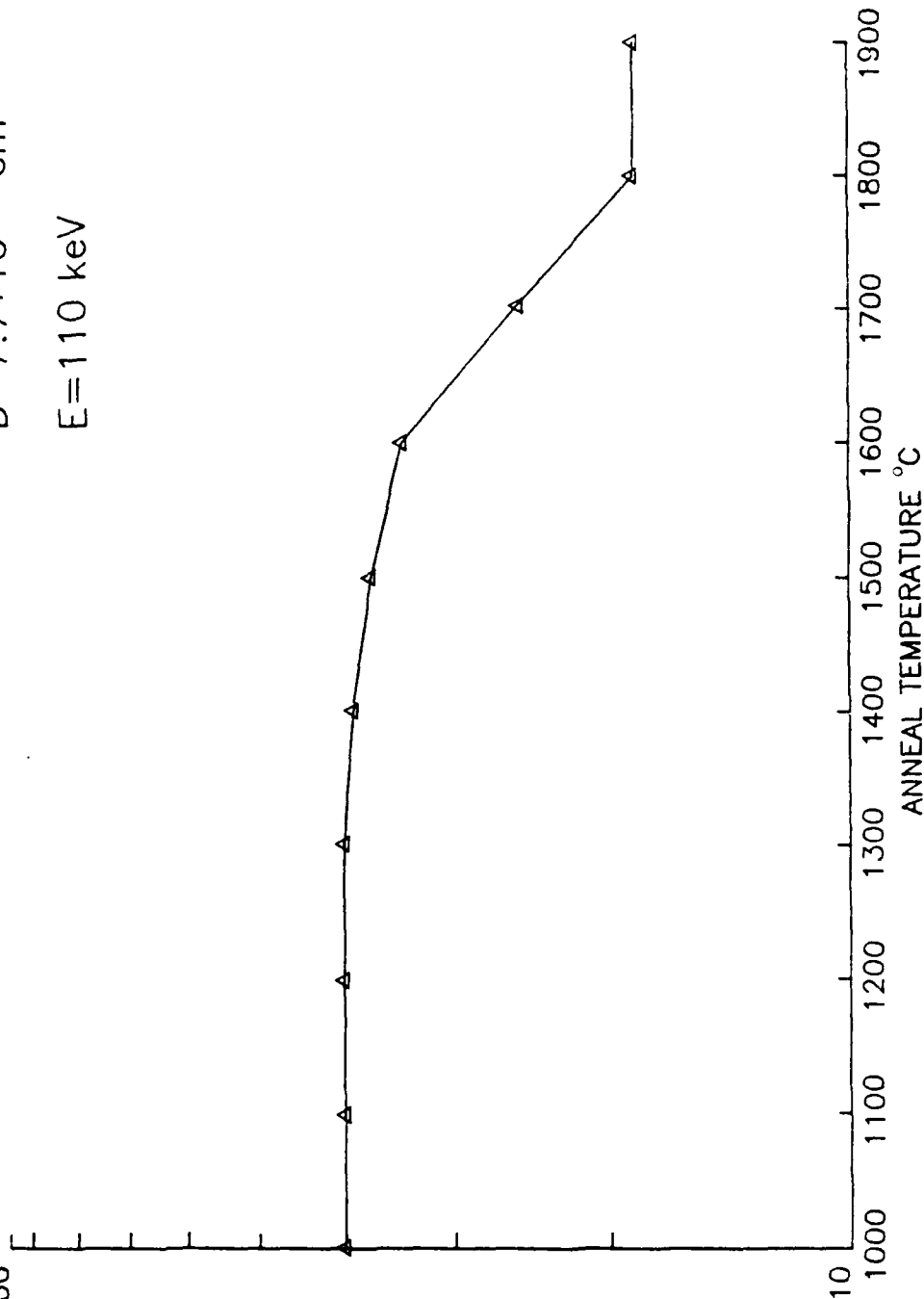


Figure 52. Sheet resistance as a function of annealing temperature for a P-implanted β -SiC (dose = $7.7 \times 10^{13} \text{ cm}^{-2}$ at 110 keV) thin film.

P IN B-SIC
AT/CM3

PSICE2

08/30/84

10E20

10E19

10E18

10E17

10E16

RATIO PLOT

LSS

0.000

.100

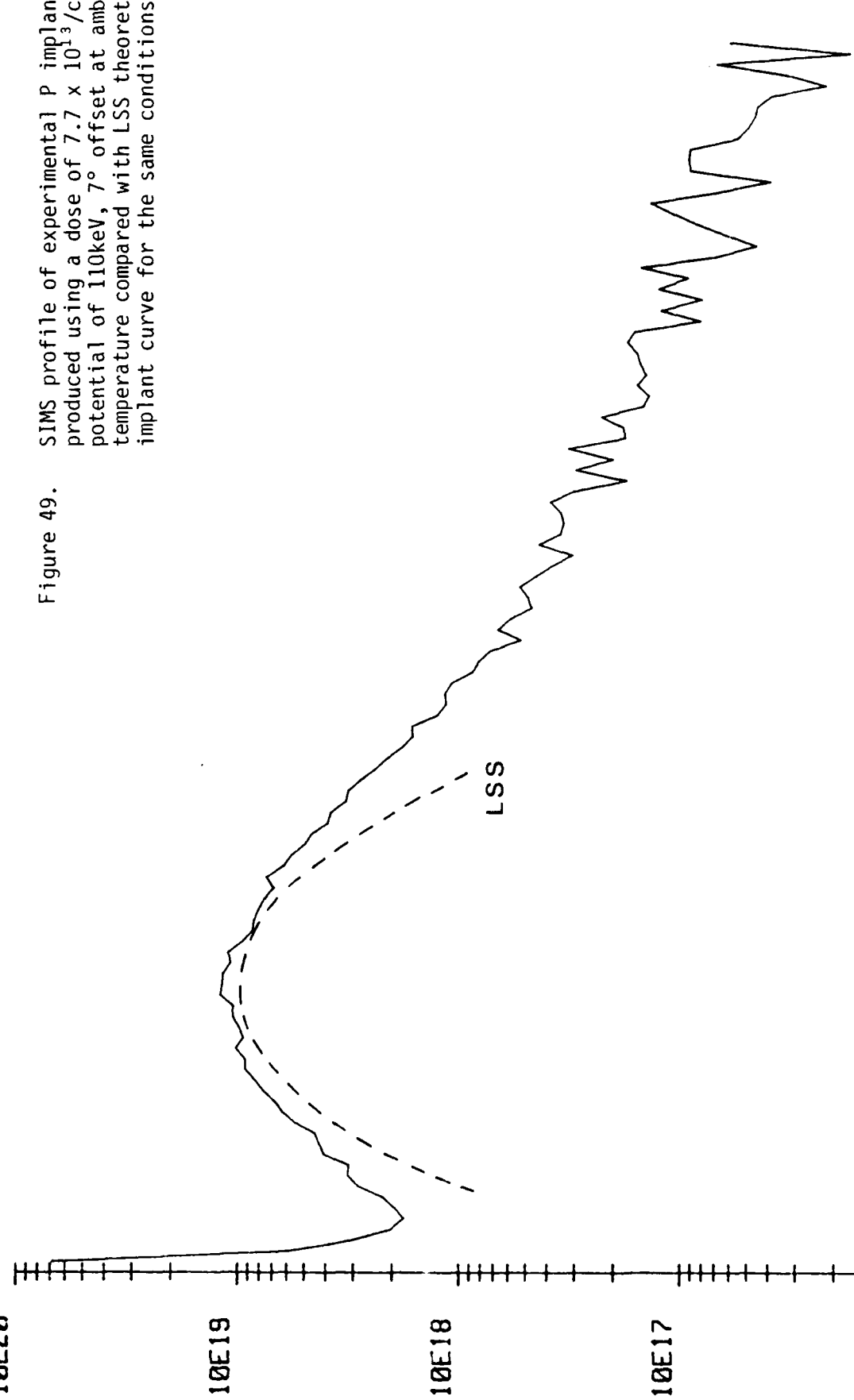
.200

.300

.400

MICRONS

Figure 49. SIMS profile of experimental P implant produced using a dose of $7.7 \times 10^{13}/\text{cm}^2$ potential of 110keV, 7° offset at ambient temperature compared with LSS theoretical implant curve for the same conditions.



P IN B-SIC
AT/CM3

SCALE FACTOR=3.21E+21

PSICE3

08/30/84

10E21

10E20

10E19

10E18

10E17

10E16

RATIO PLOT

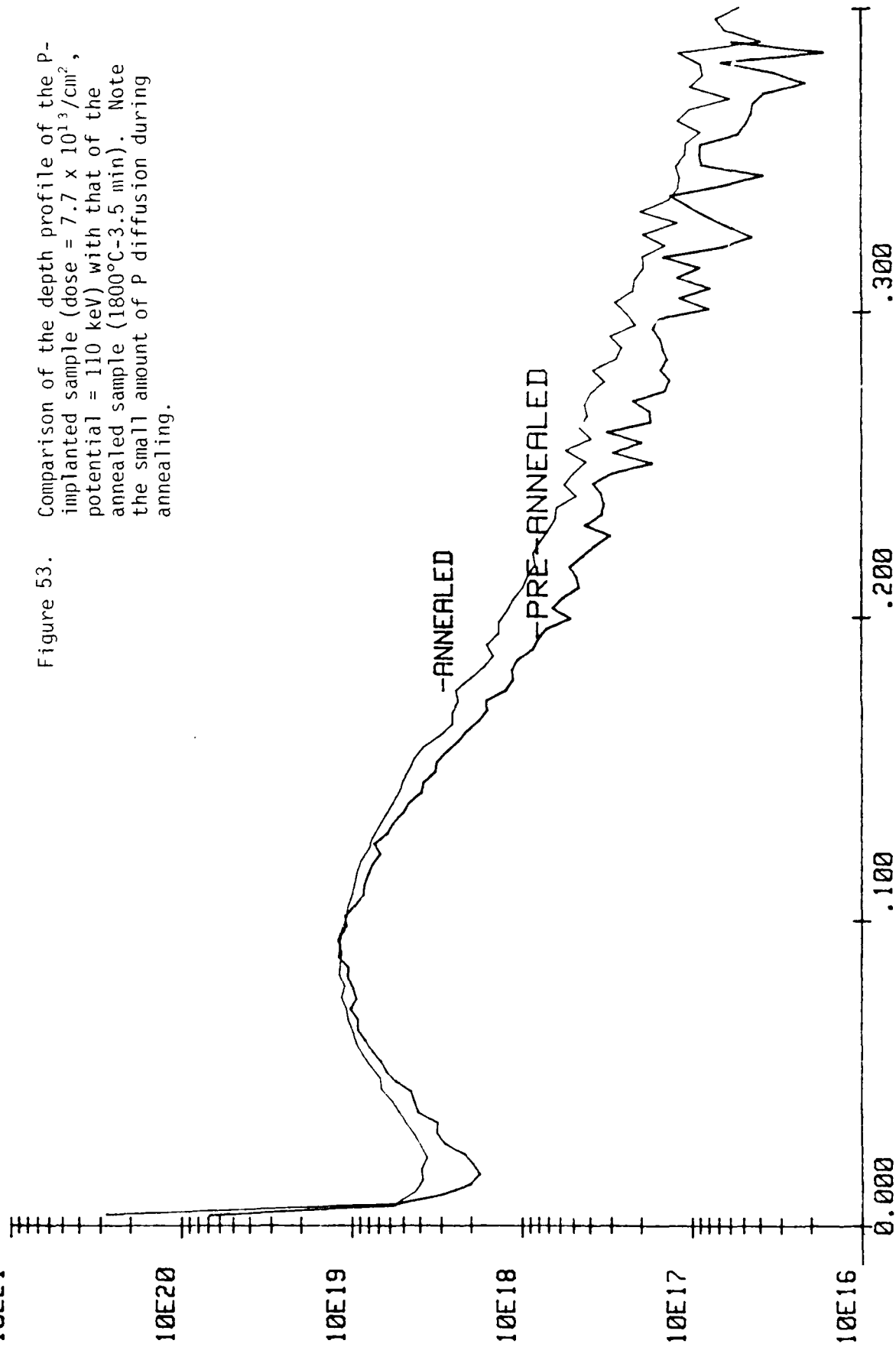


Figure 53. Comparison of the depth profile of the P-implanted sample (dose = $7.7 \times 10^{13}/\text{cm}^2$, potential = 110 keV) with that of the annealed sample (1800°C-3.5 min). Note the small amount of P diffusion during annealing.

To observe the structural surface damage caused by ion implantation, XTEM was again utilized. As shown in Fig. 50a (mag. = 100KX $g = [111]$), a 1600Å surface layer best characterized as point defect rich is evident. The first 200-300Å appears to be fairly defect free as the higher energy electronic scattering events dominate the incident ion displacement. The center of the adjacent darker band is approximately 900Å from the sample surface. This coincides very well with the R_p value of 904Å obtained from SIMS analyses. No amorphization occurred as indicated by the extension of stacking faults from the unimplanted region through the implanted region to the surface.

As shown in Table IX, the intrinsic electron carrier concentration of the pre-implanted sample was $4 \times 10^{17}/\text{cm}^3$. The C-V profile is given in Fig. 51. At a reverse bias value of 3.2 V, the leakage current increased quickly to 200 μA . No further voltage was applied.

Table IX. Summary of annealing results for P implanted into β -SiC.
Implant conditions: dose = 7.71×10^{13} , energy = 110 keV.

Anneal Temp (K)	Anneal Time (min)	R_s (Ω/\square)	N_{eff} (cm^{-3})	Anneal Atmosph.
Preimplant	NA	40	4×10^{17}	NA
RT	NA	40	9×10^{17} (?)	NA
1273	10	40	NR	Argon
1373	10	40		
1473	10	40		
1573	10	40		
1673	10	39		
1713	5	38		
1773	5	37		
1823	5	37		
1873	5	34		
1973	3.5	25		
2013	3.5	23		
2073	3.5	18	$\sim 10^{18}$	
2173	2.5	18	NR	

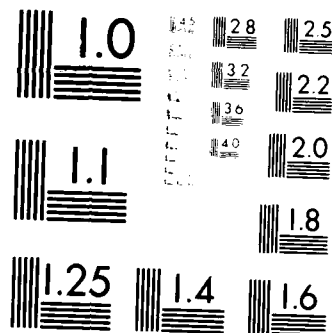
Following implantation a C-V measurement was conducted (i.e., this constitutes a sample which has received a room temperature anneal).

AD-A152 047 FUNDAMENTAL STUDIES OF GROWTH DOPING AND TRANSFORMATION 2/2
IN BETA SILICON C. (U) NORTH CAROLINA STATE UNIV AT
RALEIGH DEPT OF MATERIALS ENGINE. R F DAVIS ET AL.
UNCLASSIFIED 20 FEB 85 NCSU-243-043-006 N00014-84-K-0182 F/G 20/12 NL

END

FILED

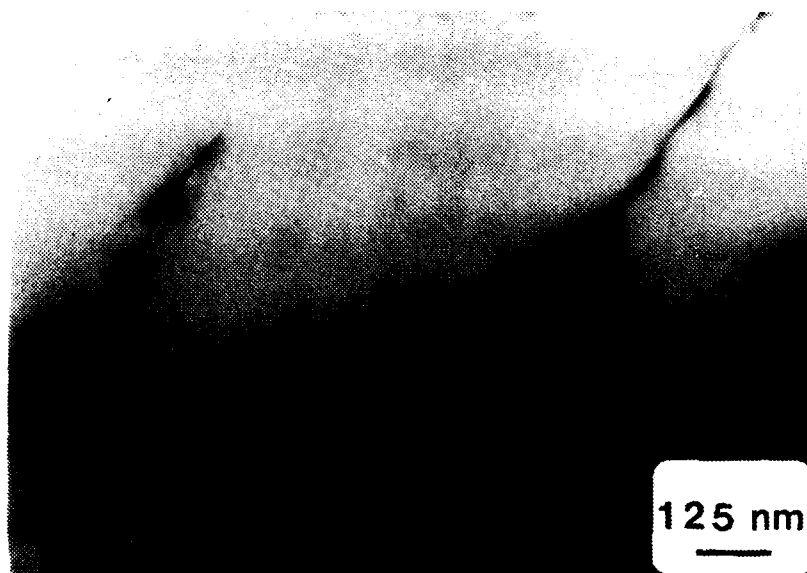
DATA



MICROCOPY RESOLUTION TEST CHART
NATIONAL BUREAU OF STANDARDS-1963-A



(a)



(b)

Figure 50. Cross-sectional TEM micrographs of a P implanted (dose = $7.7 \times 10^{13}/\text{cm}^2$, potential = 110 keV) β -SiC single crystal thin film showing (a) the as-implanted region (top one third of micrograph) with intersecting stacking faults and (b) same region after annealing at 2073K for 210s.

P TRIPLE IN B-SiC
AT/G13

PSTDE3

12/11/84

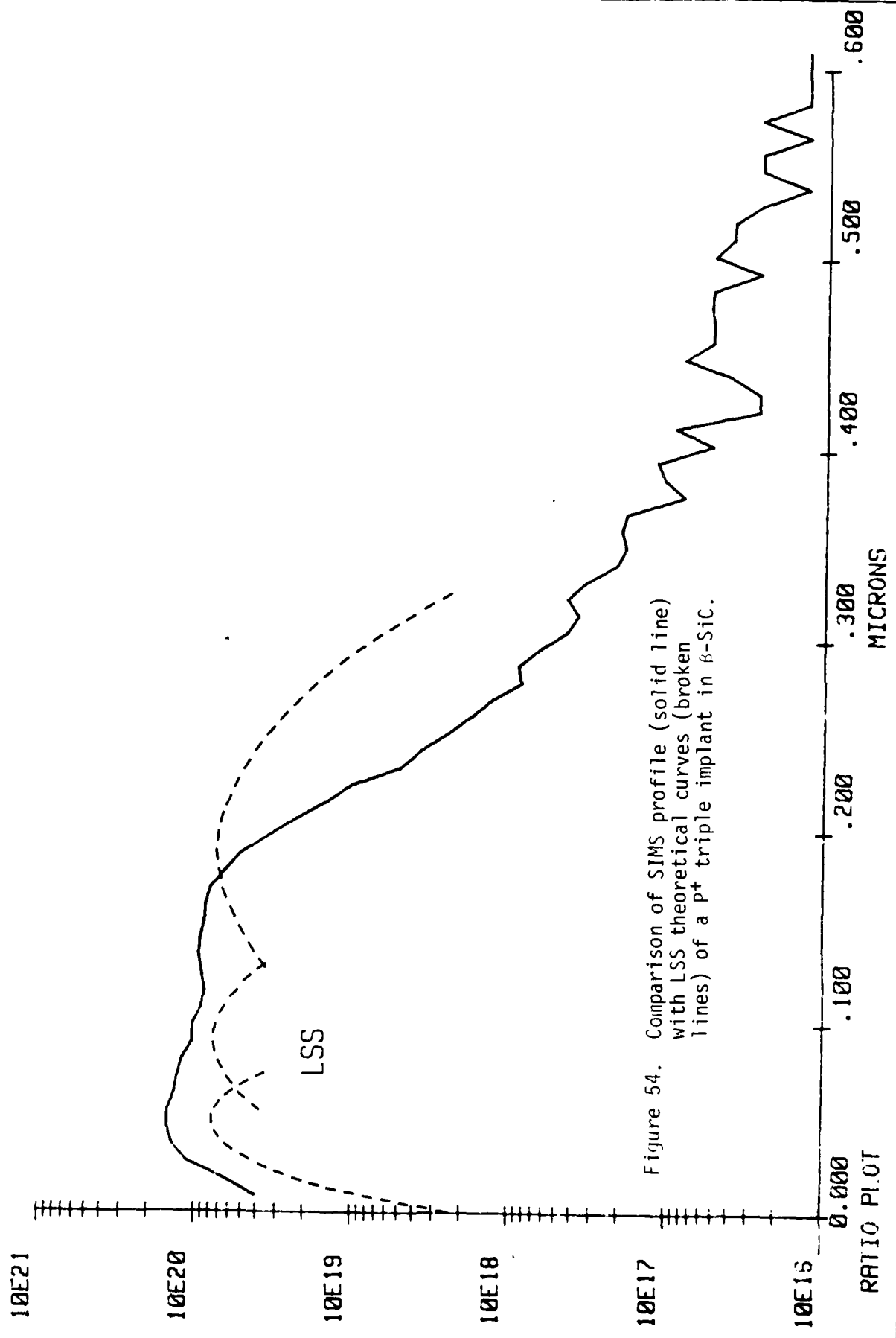


Figure 54. Comparison of SIMS profile (solid line) with LSS theoretical curves (broken lines) of a p⁺ triple implant in B-SiC.

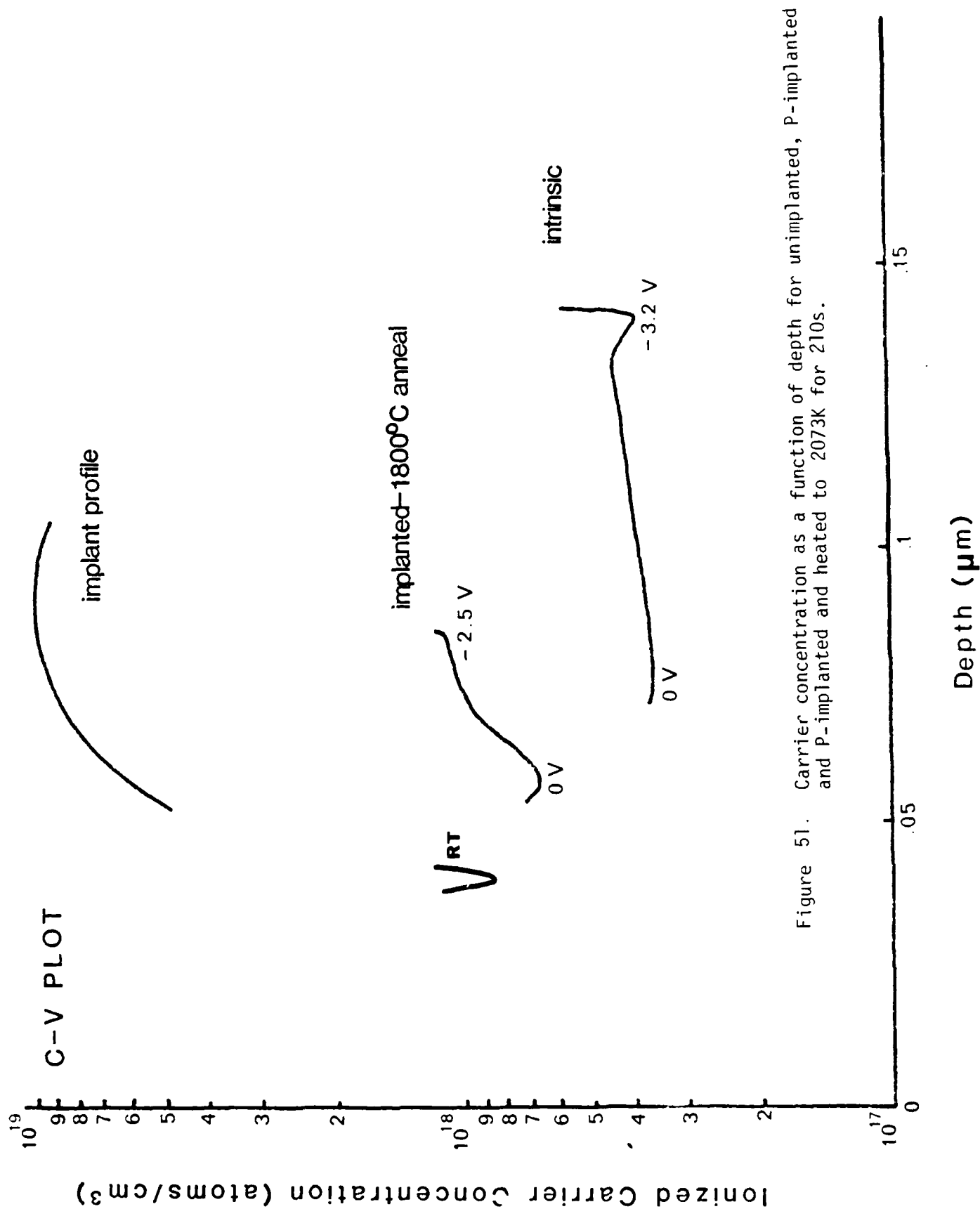


Figure 51. Carrier concentration as a function of depth for unimplanted, P-implanted and P-implanted and heated to 2073K for 210s.

vary considerably in the third implant. This deviation is believed to be caused by error in the implantation procedure. An identical implant sequence will be produced to compare these results.

Figure 55 shows an XTEM micrograph of the P^+ triple implant region. This region (Figure 55a) became amorphous to a depth of $\sim 0.3 \mu m$. A 3.0×10^{22} anneal at 2073K caused solid phase epitaxy as shown in Figure 55b. No straggling ion damage or microtwins resulted. These surprising results were also confirmed in similar research on Al^+ implants described below.

The initial Al^+ implanted samples were used for low temperature annealing studies, as described in Section VII. B.2. They were also very thin ($\leq 5.0 \mu m$) and were easily broken. As such additional samples having both dual and triple Al^+ implants were produced as noted in Table VII. Figure 56 shows the SIMS concentration vs depth profile for the two dose levels. The two LSS profiles are plotted as a comparison. Quite clearly the two implants are additive resulting in a nearly flat peak at a concentration value twice the value of either implant. It is evident that with the use of this multiple implant, a flat profile and sharp junction can be obtained.

Examination by XTEM of the Al implanted near surface region at a magnification of 100KX also revealed an amorphous layer. Closer observation shows that the immediate surface is fairly defect-free. Again, this is caused by the domination of the electronic scattering rather than nuclear scattering. The most clear amorphous region appears near $0.15 \mu m$ corresponding to the median in the SIMS profile. As one continues further away from the implant center, microcrystallinity appears to increase to the amorphous/crystalline interface. The overall degree of amorphization appears to be low. As such XTEM of the annealed sample was not conducted.

In order to monitor the extent of dopant activation as a function of annealing temperature, the sheet resistance of these dual Al implants was determined. As shown in Figure 57, the sheet resistance of the sample remained constant up to 1873K. Between 1873K and 2113K, the sheet resistance decreased from 42 ohms/ \square to 10 ohms/ \square . Annealing the sample at 2173K resulted in excessive SiC decomposition which

As indicated in Figure 51, the leakage current was very high at -0.2 V. For that reason the N_{eff} value for the RT anneal is not credible. After each anneal, C-V measurements were attempted. However, no response was recorded until the 2073K, 3.5-minute anneal temperature was reached. The result is also shown in Figure 51. Quite clearly the profile shape closely mimicks the SIMS profile with the peak being near the $0.09 \mu\text{m}$ value previously determined. The effective carrier concentration value at this peak is, however, one order of magnitude lower than the implanted concentration of phosphorous atoms which is the same ratio of concentrations found in the in situ doped samples. The only conclusion to derive from this result is that at room temperature the activation combined with ionization of P is $\sim 10\%$ of the maximum 10^{19} value.

During the 2173K -2.5-minute anneal the sample began to decompose. As indicated in Table IX, R_s did not change from the value at 2073K and N_{eff} could not be measured. A plot of annealing temperature vs R_s is shown in Figure 52.

To observe the extent of P impurity diffusion of the 2073K annealed sample, ion microprobe analysis was conducted. Figure 53 compares the concentration vs depth profiles of the as-implanted (preannealed) and annealed samples. As expected, the annealed profile peak became marginally depressed and widened. It seems fair to conclude that, as far as devices are concerned, diffusion of P during annealing is insignificant.

Cross-sectional TEM was also utilized to observe the extent of damage recovery in the low dose P implant sample shown in Figure 50a. As shown in Figure 50b, the defect-rich surface appears to have structurally recovered to a large degree after the 2073K anneal. However, the intrinsic defect density of the sample as a whole does not appear to have decreased.

A phosphorous triple implant has also been produced near the end of this grant period. The energy and dose levels are given in Table VII. As above, a comparison between the LSS theoretical dopant concentration and the actual concentration determined by SIMS was made. As shown in Figure 54, there is close agreement in these two results for the first and second implants; however, theory and experiment

LOW DOSE P ANNEAL

$$D = 7.7 \times 10^{13} \text{ cm}^{-2}$$

$$E = 110 \text{ keV}$$

SHEET RESISTANCE Ω/\square

100

10

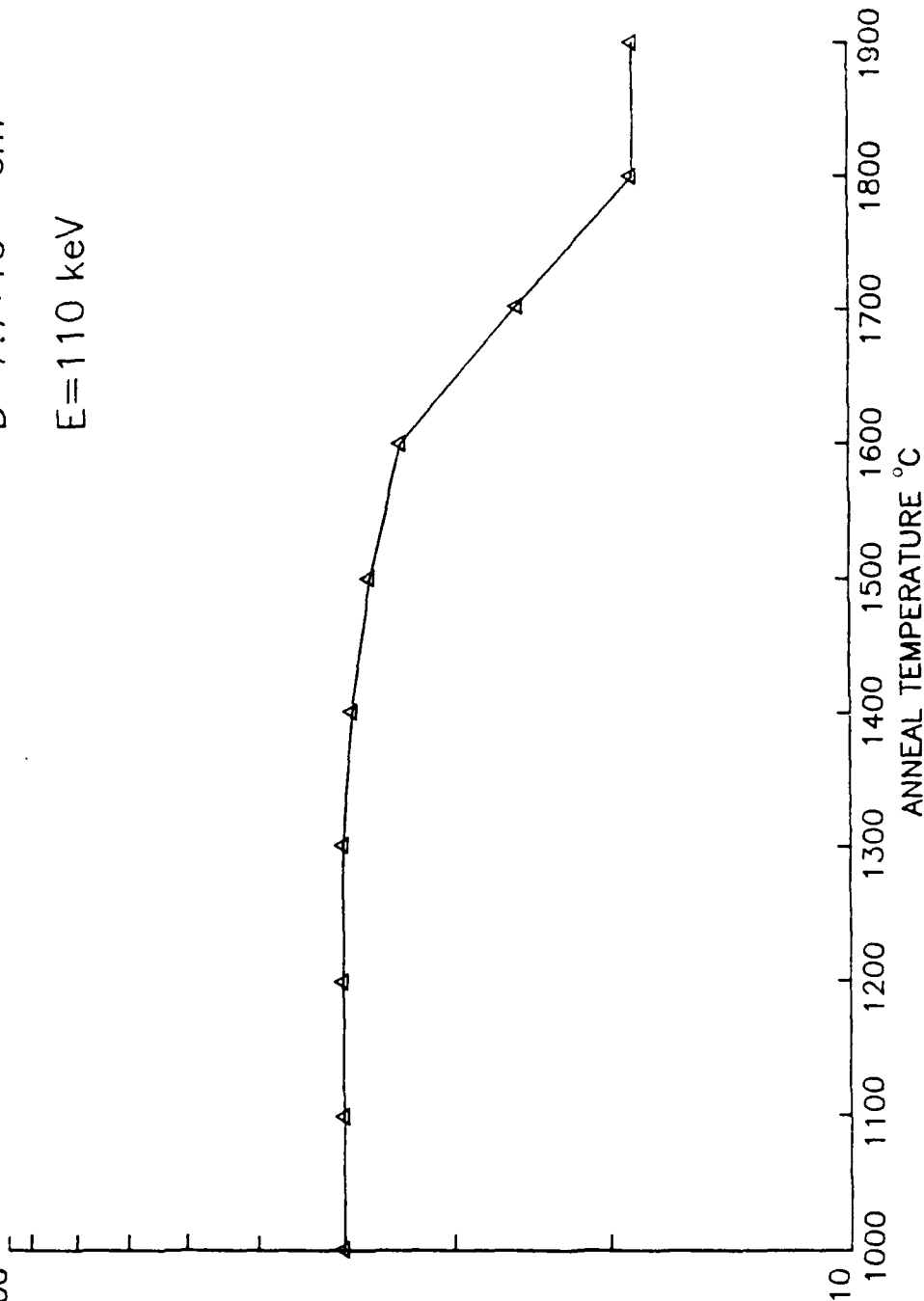


Figure 52. Sheet resistance as a function of annealing temperature for a P-implanted β -SiC (dose = $7.7 \times 10^{13} \text{ cm}^{-2}$ at 110 keV) thin film.



AD-A152 047 FUNDAMENTAL STUDIES OF GROWTH DOPING AND TRANSFORMATION 2/2
IN BETA SILICON C. (U) NORTH CAROLINA STATE UNIV AT
RALEIGH DEPT OF MATERIALS ENGINE. R F DAVIS ET AL.
UNCLASSIFIED 20 FEB 85 NCSU-243-043-006 N00014-84-K-0182 F/G 20/12 NL

END

FILED

DATA

AL DUAL IN B-SIC
AT/CM3

ALSTD2

08/30/84

10E21

10E20

10E19

10E18

10E17

0.000
RATIO PLOT

LSS

.200

.100

.300

.400

.500

.600

MICRONS

Figure 56.

SIMS profile of a dual Al implant (doses and potentials equal to $9 \times 10^{14}/\text{cm}^2$, 190 keV and $6 \times 10^{14}/\text{cm}^2$, 110 keV) into β -SiC film compared with the LSS calculated profiles for each condition.

97

P TRIPLE IN B-SiC
AT/G13

PSTDE3

12/11/84

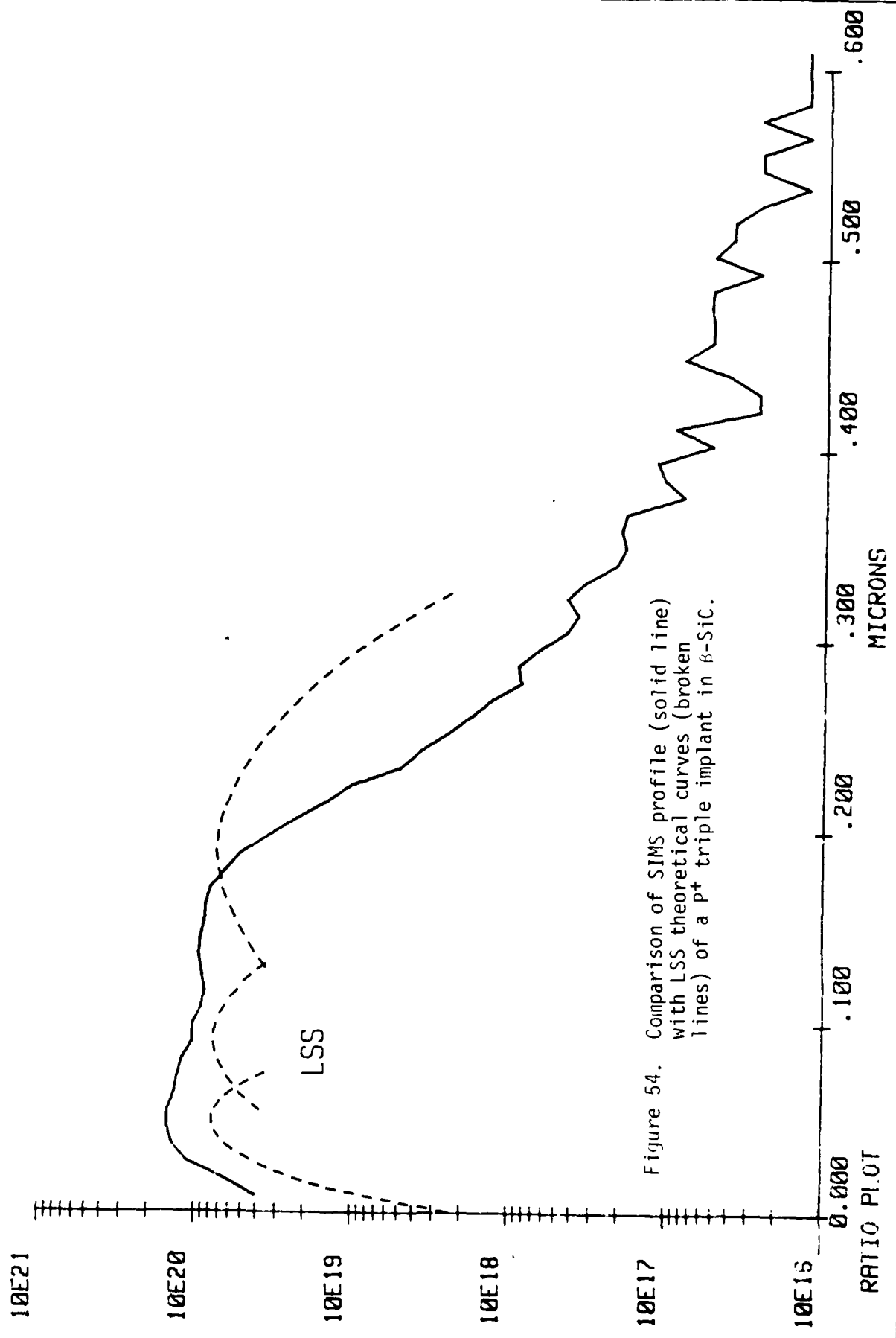


Figure 54. Comparison of SIMS profile (solid line) with LSS theoretical curves (broken lines) of a p⁺ triple implant in B-SiC.

caused degradation in the electrical characteristics of the material by increasing the leakage current.

Following the onset of the activation of the aluminum dopant, capacitance-voltage measurements were serially conducted at room temperature for each annealing temperature to determine the concentration of ionized p-type carriers as a function of depth. As indicated in Figure 58, the intrinsic donor concentration of the sample was $2.5 \times 10^{17}/\text{cm}^3$. After implantation and annealing at 2098K for 3.0×10^2 s in Ar, a p-type signal was detected from 0 to -1.0 volt. The resulting p-type peak concentration was $\sim 3 \times 10^{17}/\text{cm}^3$. When compared to the aluminum atomic concentration, an ionized activation of $\sim 0.1\%$ is realized at room temperature, which is an order of magnitude lower than that measured in the in situ doped samples.

In addition, the spreading resistance as a function of depth was determined for a sample having this aluminum dual implant (Figure 59). This sample was also annealed at 2098K for 5 minutes in argon. Sample preparation involved beveling at a 17 minute angle using a $0.25 \mu\text{m}$ diamond polishing medium contained on a glass plate. As shown in Figure 59, a p-type surface of $\sim 0.2 \mu\text{m}$ depth exhibited a spreading resistance of 10^7 ohms. The n-type background of the remaining SiC showed a spreading resistance of $3 \times 10^4 \Omega$. These spreading resistance values correspond to carrier concentrations of $(p) = 3 \times 10^{17}/\text{cm}^3$ and $(n) = 2.5 \times 10^{17}/\text{cm}^3$, respectively, as determined by capacitance-voltage measurements. Calibration curves of spreading resistance versus ionized carrier concentration for each dopant type are presently being determined.

To observe the extent of aluminum diffusion upon annealing, SIMS was utilized. Figure 60 shows the atomic concentration of aluminum versus depth for an unannealed and a 2098K annealed sample. There is a decrease in aluminum concentration by a factor of two-to-three throughout most of the profile depth as a result of annealing. The surface aluminum concentration slightly increased. This may imply that some aluminum out diffusion occurs at the surface.

A triple Al^+ implant was also produced using the conditions noted in Table VII. The LN_2 was used to suppress any possible dynamic

vary considerably in the third implant. This deviation is believed to be caused by error in the implantation procedure. An identical implant sequence will be produced to compare these results.

Figure 55 shows an XTEM micrograph of the P^+ triple implant region. This region (Figure 55a) became amorphous to a depth of $\sim 0.3 \mu m$. A 3.0×10^{22} anneal at 2073K caused solid phase epitaxy as shown in Figure 55b. No straggling ion damage or microtwins resulted. These surprising results were also confirmed in similar research on Al^+ implants described below.

The initial Al^+ implanted samples were used for low temperature annealing studies, as described in Section VII. B.2. They were also very thin ($\leq 5.0 \mu m$) and were easily broken. As such additional samples having both dual and triple Al^+ implants were produced as noted in Table VII. Figure 56 shows the SIMS concentration vs depth profile for the two dose levels. The two LSS profiles are plotted as a comparison. Quite clearly the two implants are additive resulting in a nearly flat peak at a concentration value twice the value of either implant. It is evident that with the use of this multiple implant, a flat profile and sharp junction can be obtained.

Examination by XTEM of the Al implanted near surface region at a magnification of 100KX also revealed an amorphous layer. Closer observation shows that the immediate surface is fairly defect-free. Again, this is caused by the domination of the electronic scattering rather than nuclear scattering. The most clear amorphous region appears near $0.15 \mu m$ corresponding to the median in the SIMS profile. As one continues further away from the implant center, microcrystallinity appears to increase to the amorphous/crystalline interface. The overall degree of amorphization appears to be low. As such XTEM of the annealed sample was not conducted.

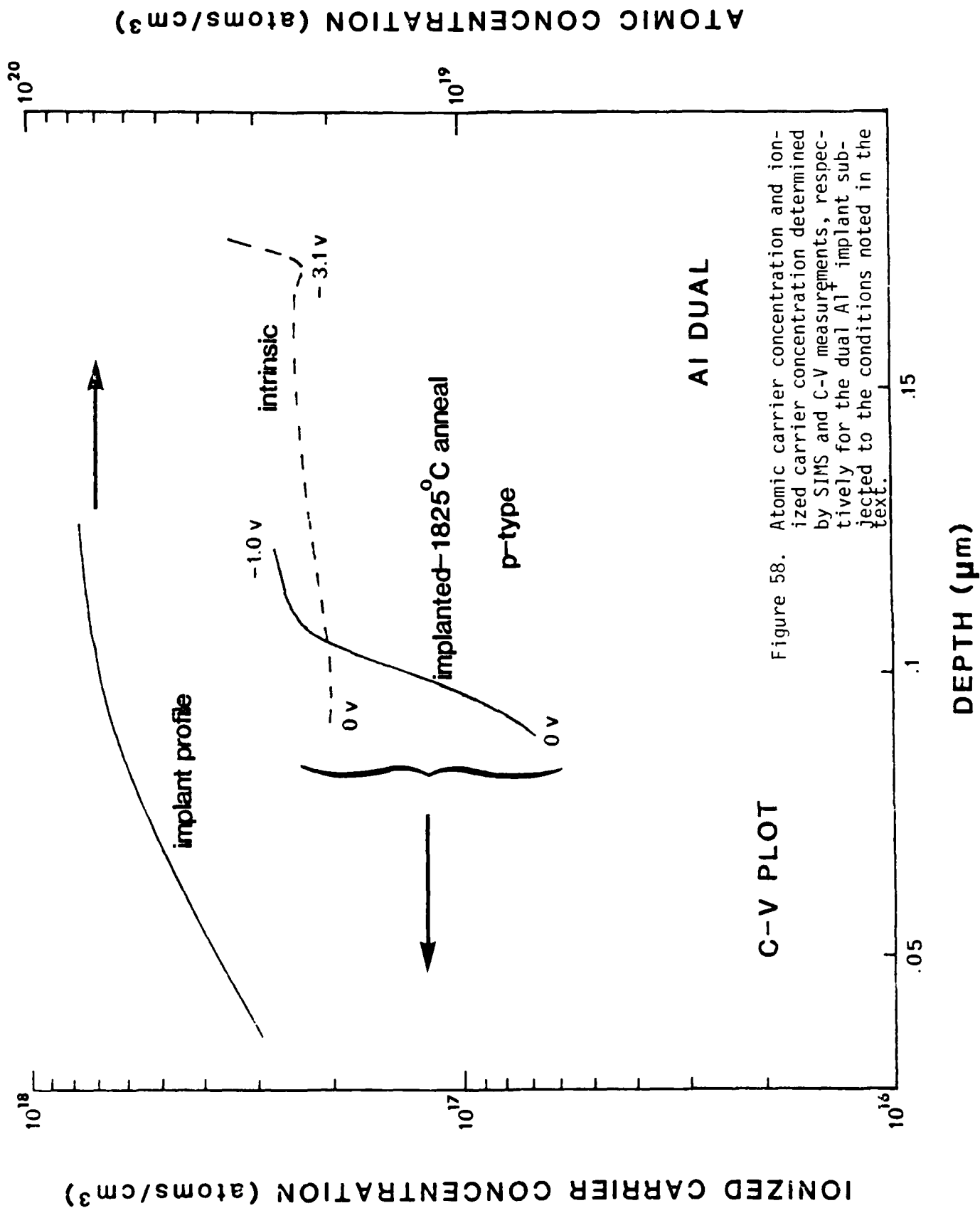


Figure 58. Atomic carrier concentration and ionized carrier concentration determined by SIMS and C-V measurements, respectively for the dual Al⁺ implant subjected to the conditions noted in the text.

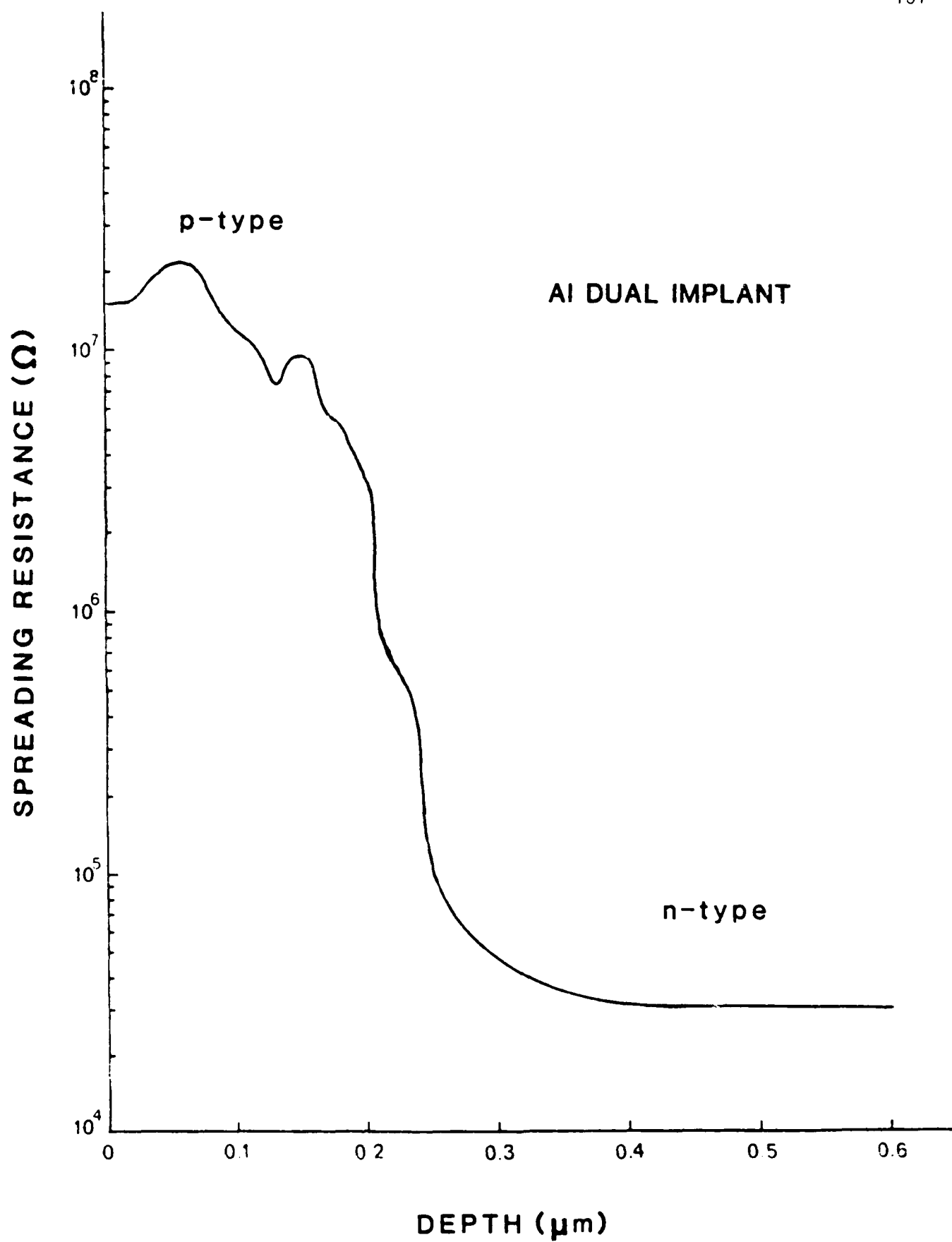


Figure 59. Spreading resistance as a function of depth from the sample surface of an annealed (2073K, 3.0×10^2 s) Al^+ dual implant region in p-SiC.

annealing. Using the dose and energy values noted in Table VII, the theoretical LSS dopant profiles were superimposed on the SIMS profile of concentration as a function of depth as shown in Figure 61. As one may note, there is excellent correspondence between the theoretical and experimental curves.

Spreading resistance measurements were also conducted on these implanted samples which had been annealed at 2073K. As shown in Figure 62, a surface p-type layer with a peak spreading resistance of $\sim 10^7$ ohms was determined. This value of spreading resistance equals that achieved with the aluminum dual implant (see Figure 59). Note that the peak atomic concentration in the dual implant was $\sim 1 \times 10^{20}/\text{cm}^3$ while that in the triple implant was $\sim 5 \times 10^{21}/\text{cm}^3$. At first an equal spreading resistance between the two implants may appear contradictory. However, a solubility of ~ 1.0 atomic % aluminum in SiC at 2173K limits the amount of dopant that can be accommodated in the crystal lattice. In turn, the concentration of dopant that can be activated is also limited.

The spreading resistance of the remaining n-type SiC was $\sim 2 \times 10^5$ ohms, as is also indicated in Figure 62. This is nearly an order of magnitude higher than that of the n-type SiC used for the aluminum double implant case (see Figure 59). However, this is expected; since, the carrier concentration in the undoped SiC used for the triple implant was measured at $n = 6 \times 10^{15}/\text{cm}^3$.

A cross-section TEM micrograph of the as implanted surface is shown in Figure 63a. As shown, dislocations and stacking faults terminate at the crystalline-implanted interface. In this instance a 0.47 μm deep amorphous layer resulted.

Figure 63b shows an XTEM micrograph of the implanted surface after annealing at 2073K for 3.0×10^2 s in argon. Quite clearly the amorphous layer has regrown by solid phase epitaxy. However, unlike GaAs and other compound semiconductors, no dislocation loops formed at the regrown interface nor microtwins in the regrown bulk. This may result from the already high defect density of the intrinsic material whereby new defects are in some way getterred. Nevertheless, these results are very promising.

AL DUAL IN B-SIC
AT/CM3

ALSTD2

08/30/84

10E21

10E20

10E19

10E18

10E17

0.000
RATIO PLOT

LSS

.200

.100

.300

.400

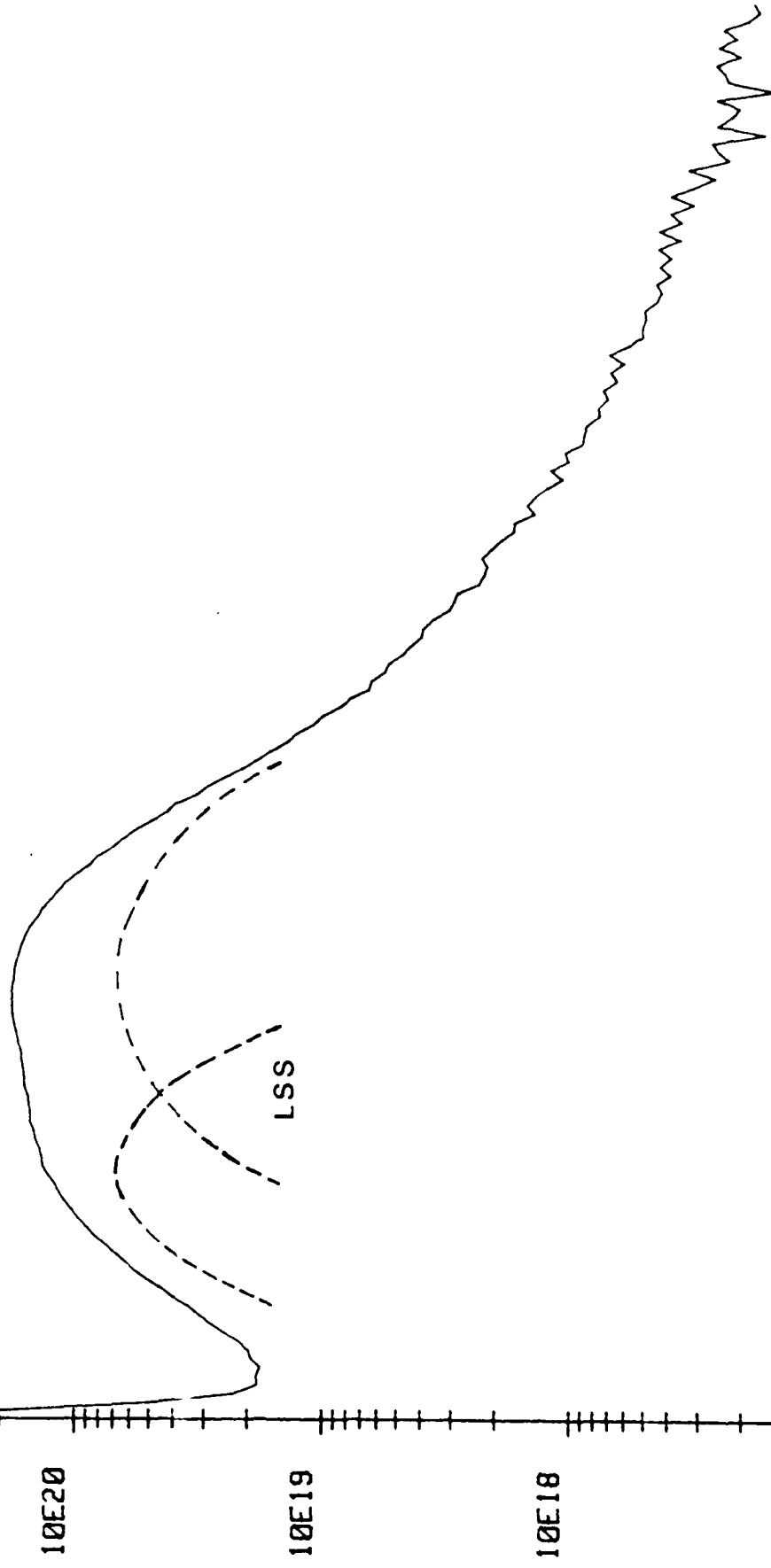
.500

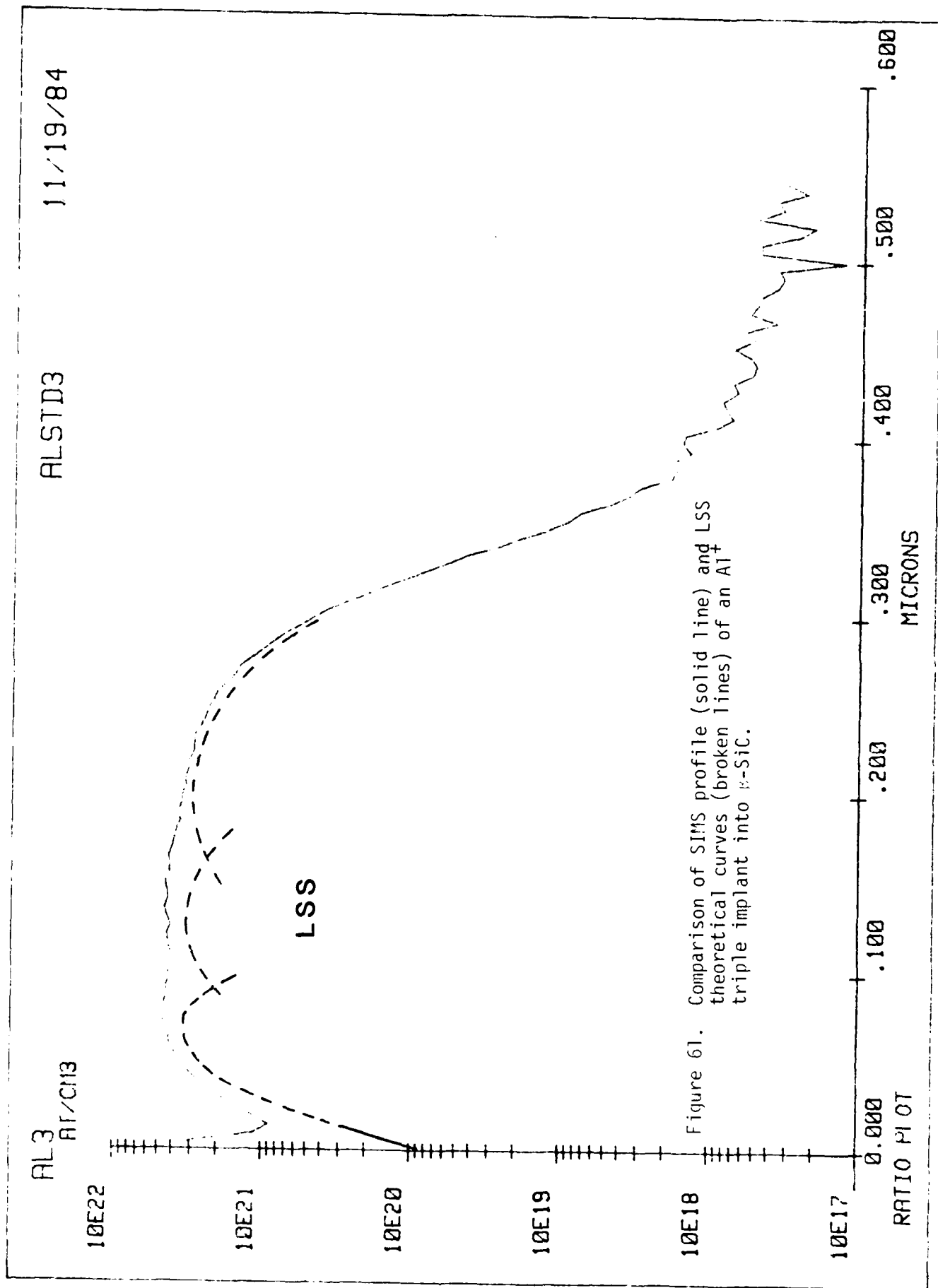
.600

MICRONS

Figure 56.

SIMS profile of a dual Al implant (doses and potentials equal to $9 \times 10^{14}/\text{cm}^2$, 190 keV and $6 \times 10^{14}/\text{cm}^2$, 110 keV) into β -SiC film compared with the LSS calculated profiles for each condition.





DUAL AL ANNEAL

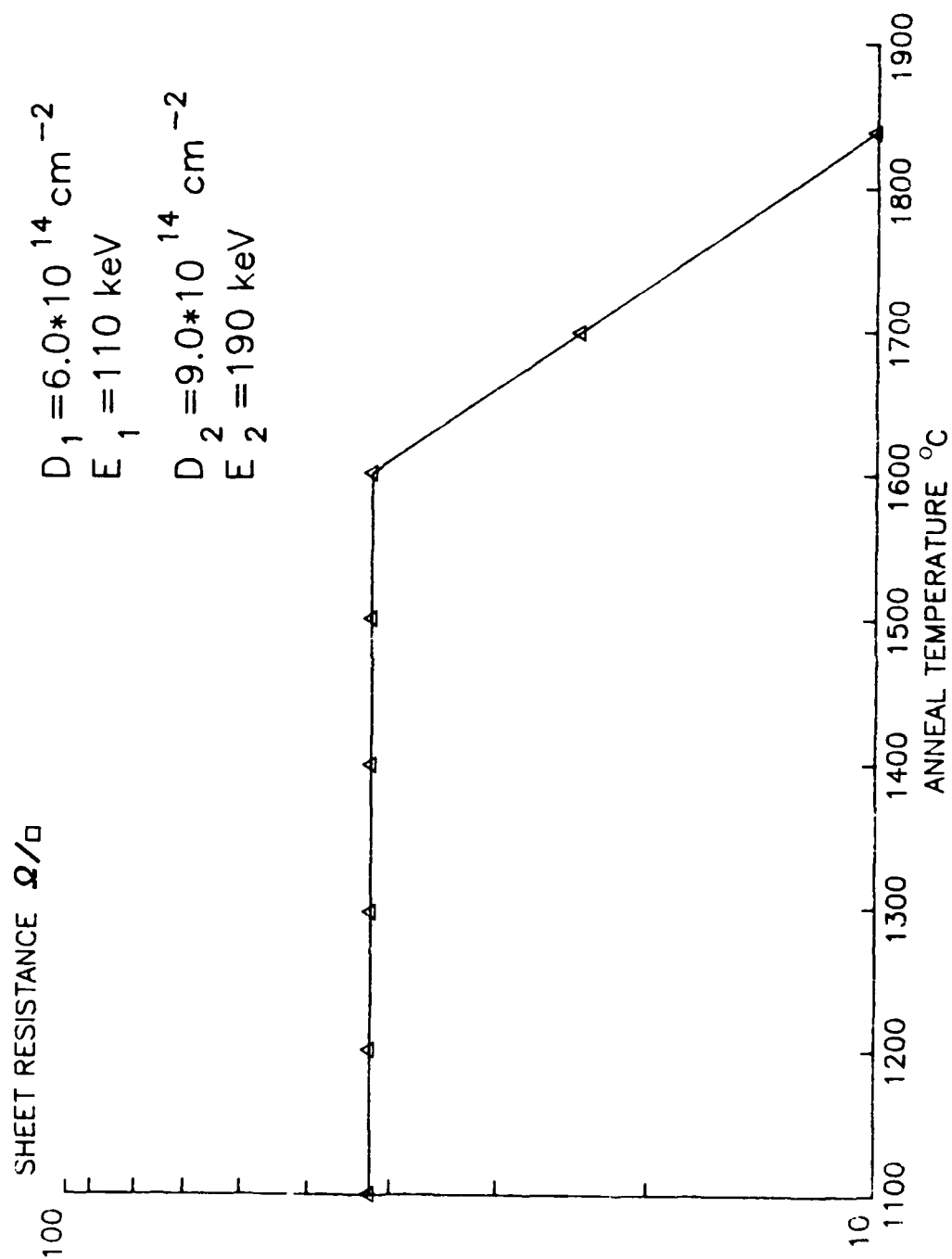


Figure 57. Sheet resistance as a function of annealing temperature (measured at room temperature) for a double Al⁺ implant.

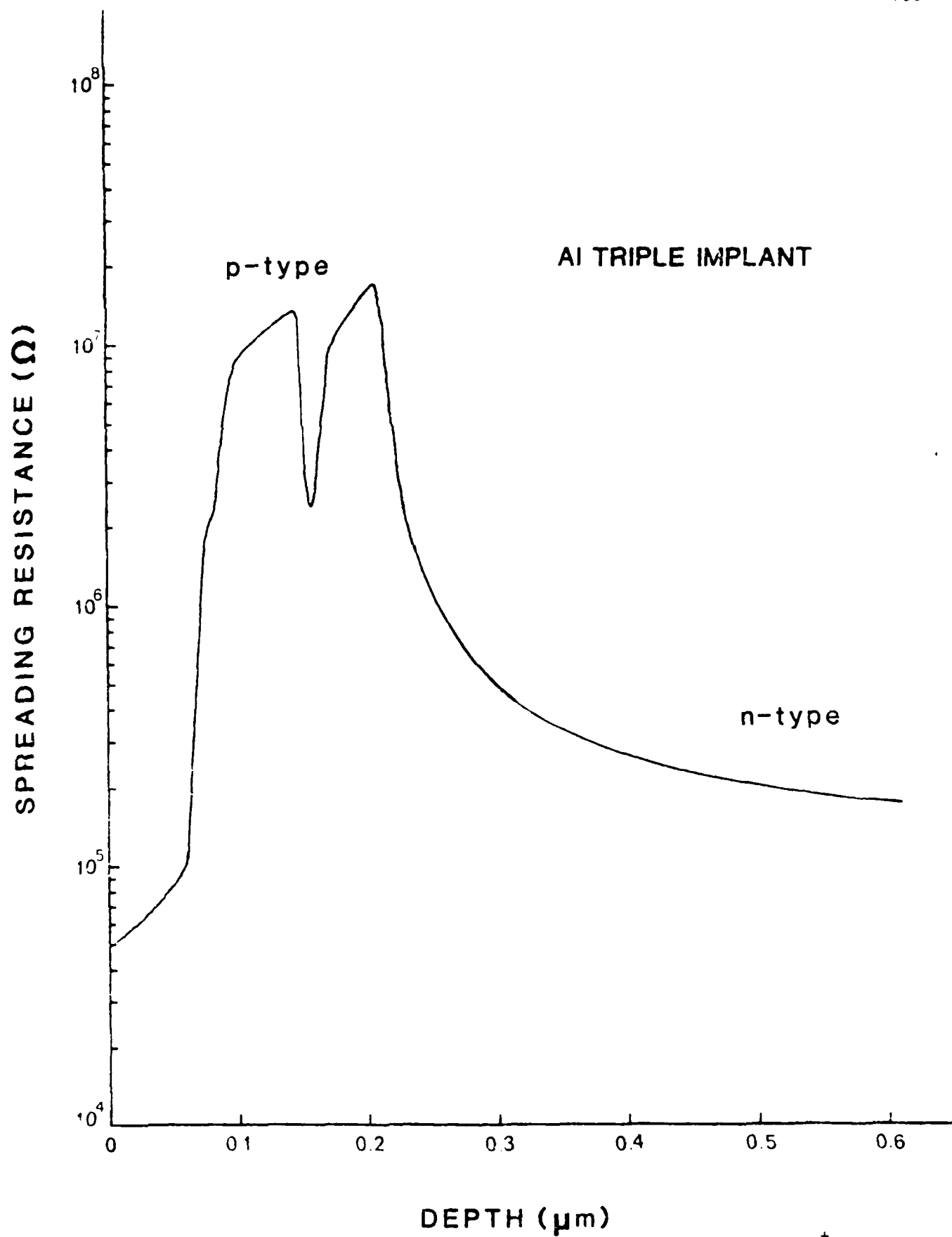


Figure 62. Spreading resistance as a function of depth for an Al^+ triple implant into $\beta\text{-SiC}$.

caused degradation in the electrical characteristics of the material by increasing the leakage current.

Following the onset of the activation of the aluminum dopant, capacitance-voltage measurements were serially conducted at room temperature for each annealing temperature to determine the concentration of ionized p-type carriers as a function of depth. As indicated in Figure 58, the intrinsic donor concentration of the sample was $2.5 \times 10^{17}/\text{cm}^3$. After implantation and annealing at 2098K for 3.0×10^2 s in Ar, a p-type signal was detected from 0 to -1.0 volt. The resulting p-type peak concentration was $\sim 3 \times 10^{17}/\text{cm}^3$. When compared to the aluminum atomic concentration, an ionized activation of ~0.1% is realized at room temperature, which is an order of magnitude lower than that measured in the in situ doped samples.

In addition, the spreading resistance as a function of depth was determined for a sample having this aluminum dual implant (Figure 59). This sample was also annealed at 2098K for 5 minutes in argon. Sample preparation involved beveling at a 17 minute angle using a

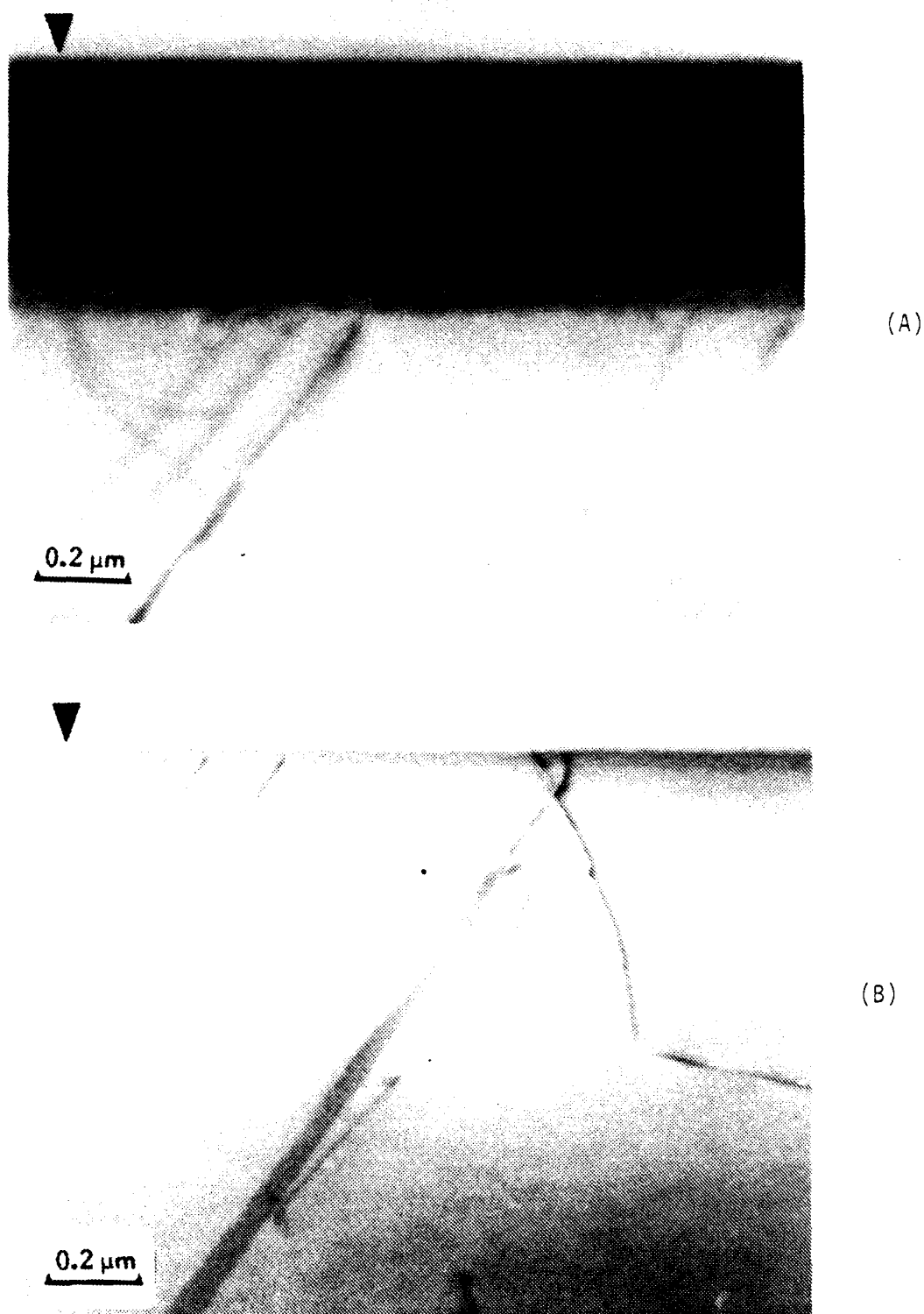


Figure 63. XTEM micrographs of an Al^+ triple implant region produced using the conditions of 200 keV- $4.3 \times 10^{16}/\text{cm}^2$, 130 keV- $4.3 \times 10^{16}/\text{cm}^2$, 70 keV- $2.0 \times 10^{16}/\text{cm}^2$. These micrographs show (A) that a 0.47 μm deep amorphous layer resulted and (b) that solid phase epitaxy occurred as a result of a 2073K- $3.0 \times 10^2\text{s}$ anneal in argon.

b. Nitrogen and Boron Implants

The initial N^+ and B^+ implants were in thin ($\leq 5.0 \mu m$) SiC films which were broken when they were removed from their Si substrates. Subsequent implants described below were made into much thicker samples

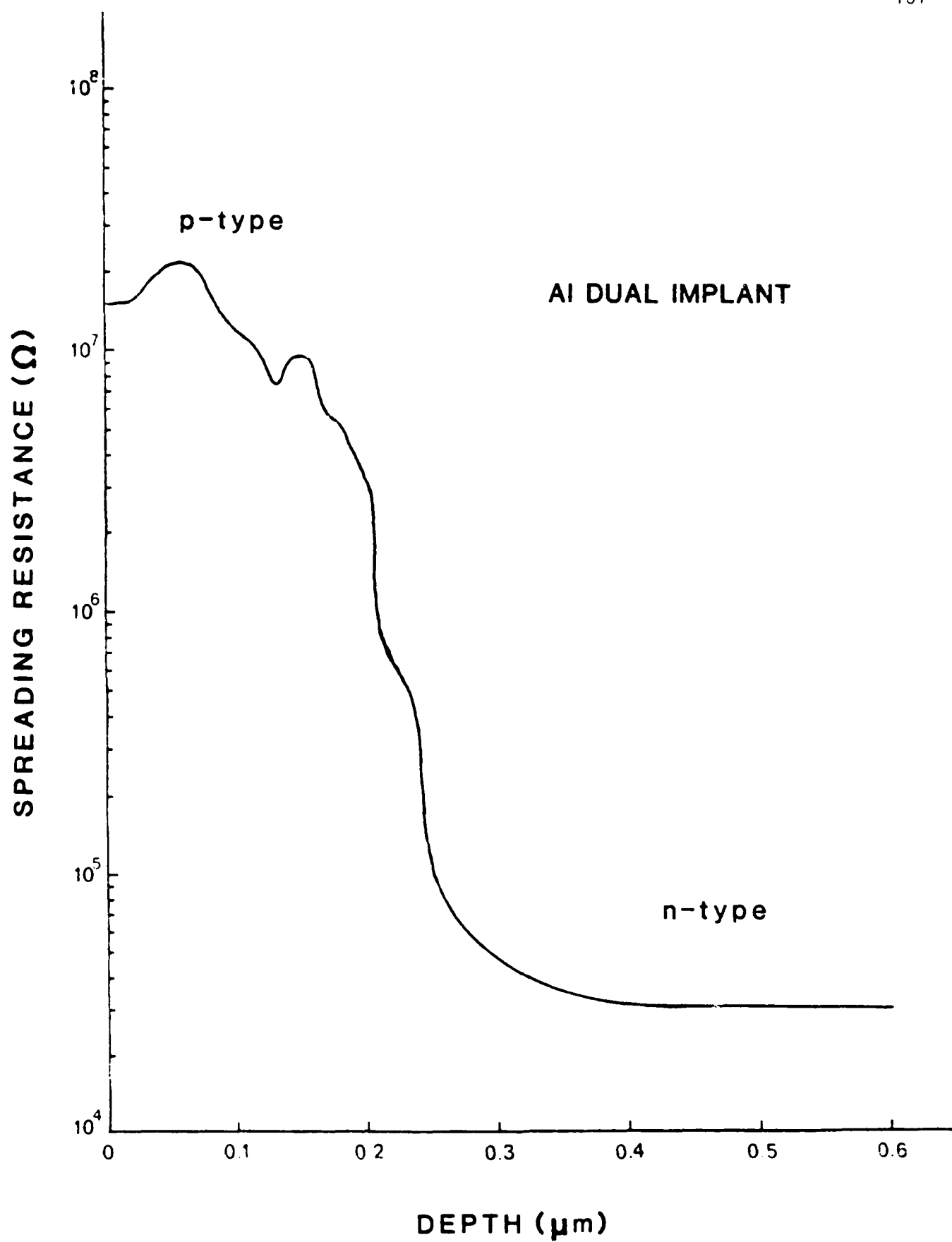


Figure 59. Spreading resistance as a function of depth from the sample surface of an annealed (2073K, 3.0×10^2 s) Al^+ dual implant region in p-SiC.

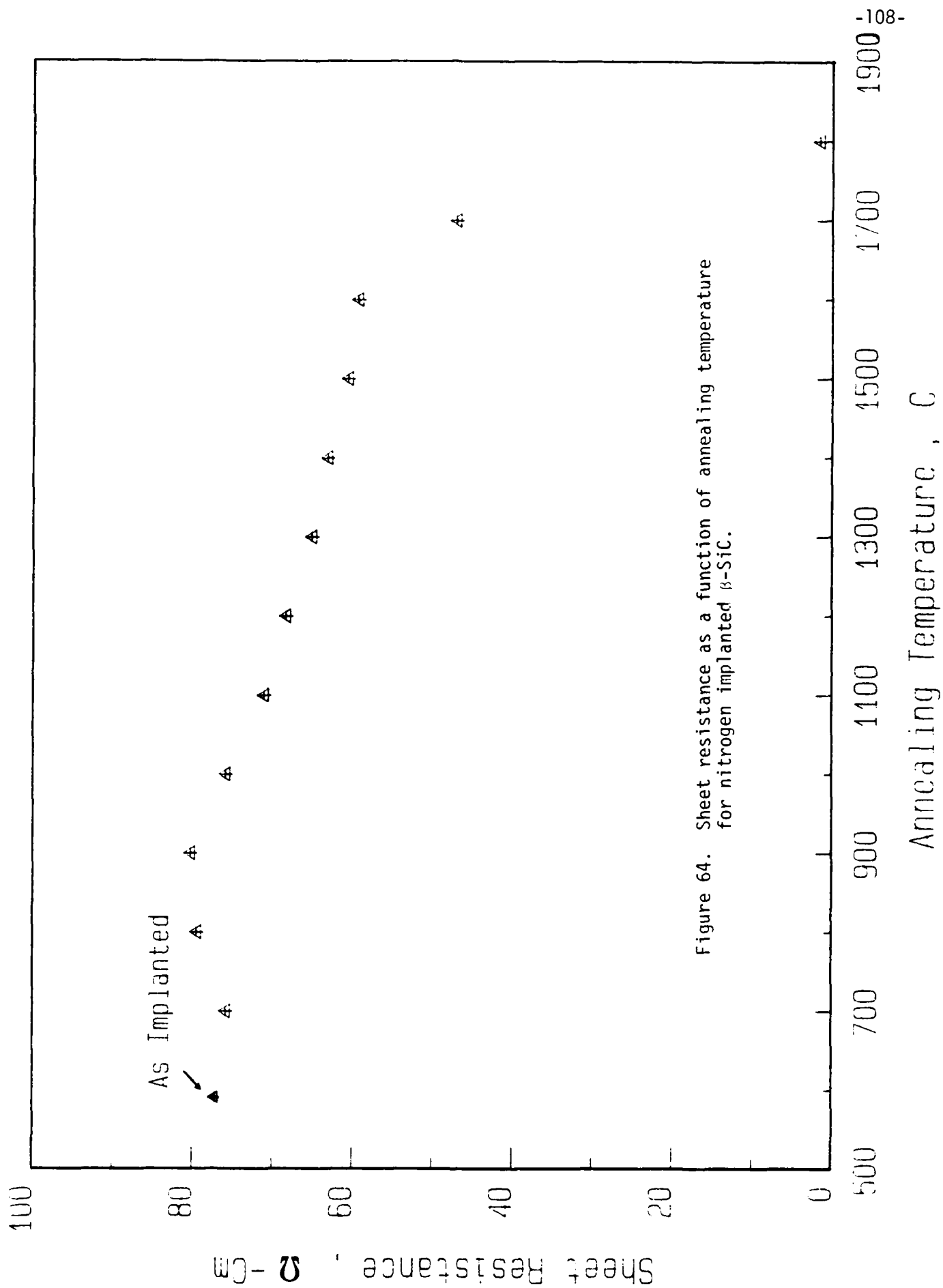
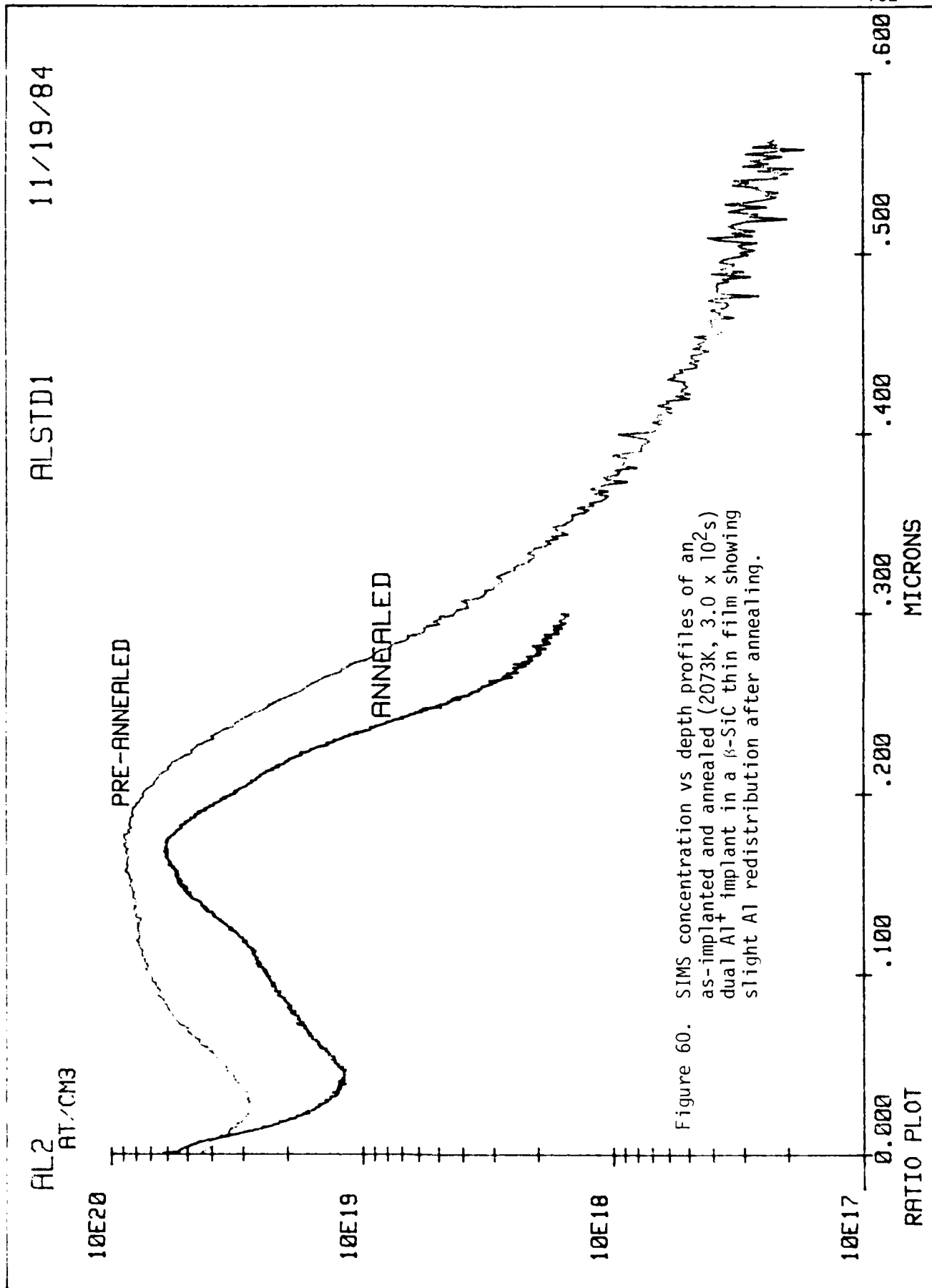


Figure 64. Sheet resistance as a function of annealing temperature for nitrogen implanted β -SiC.



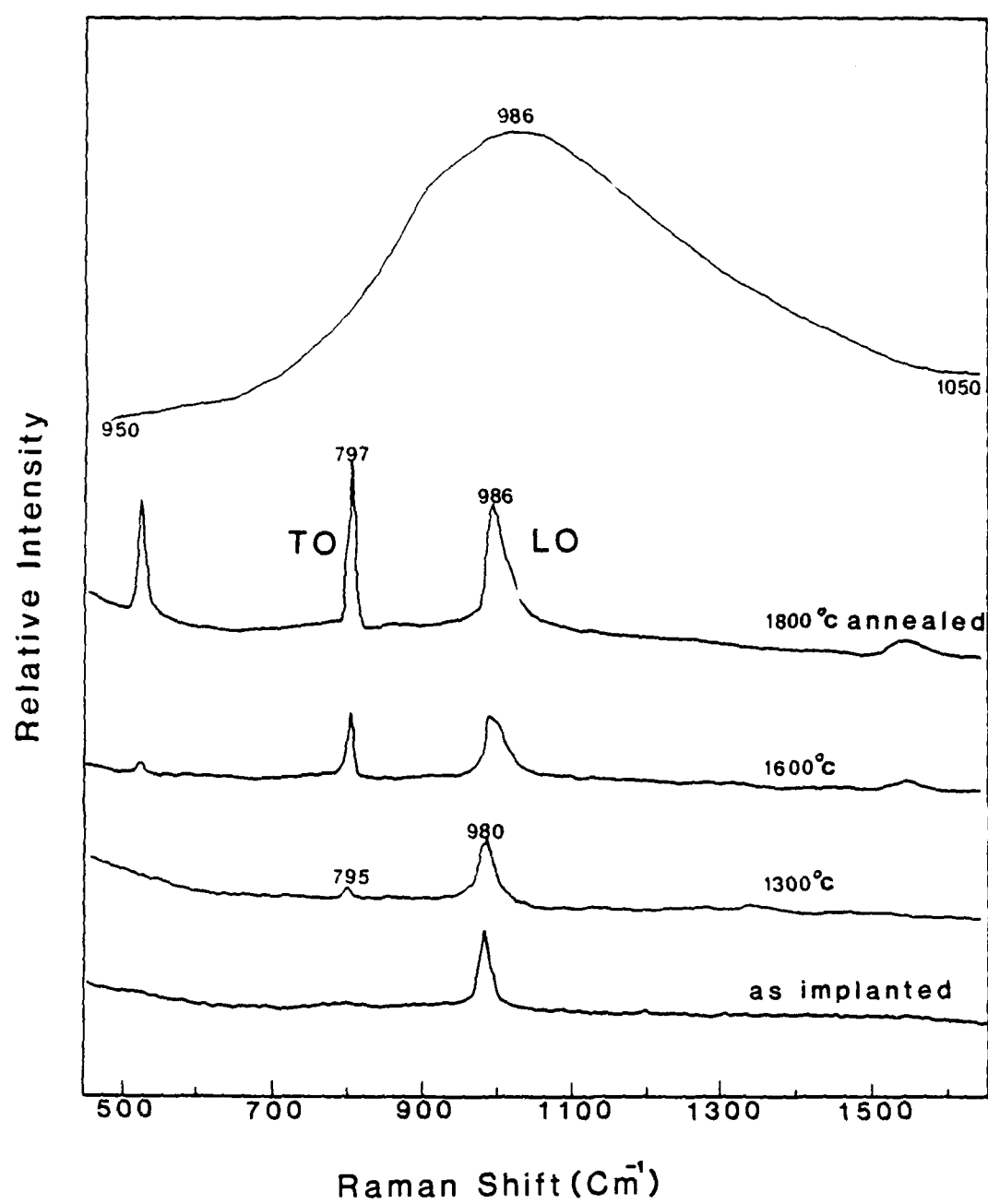


Figure 65. Raman spectra of nitrogen implanted and annealed samples.

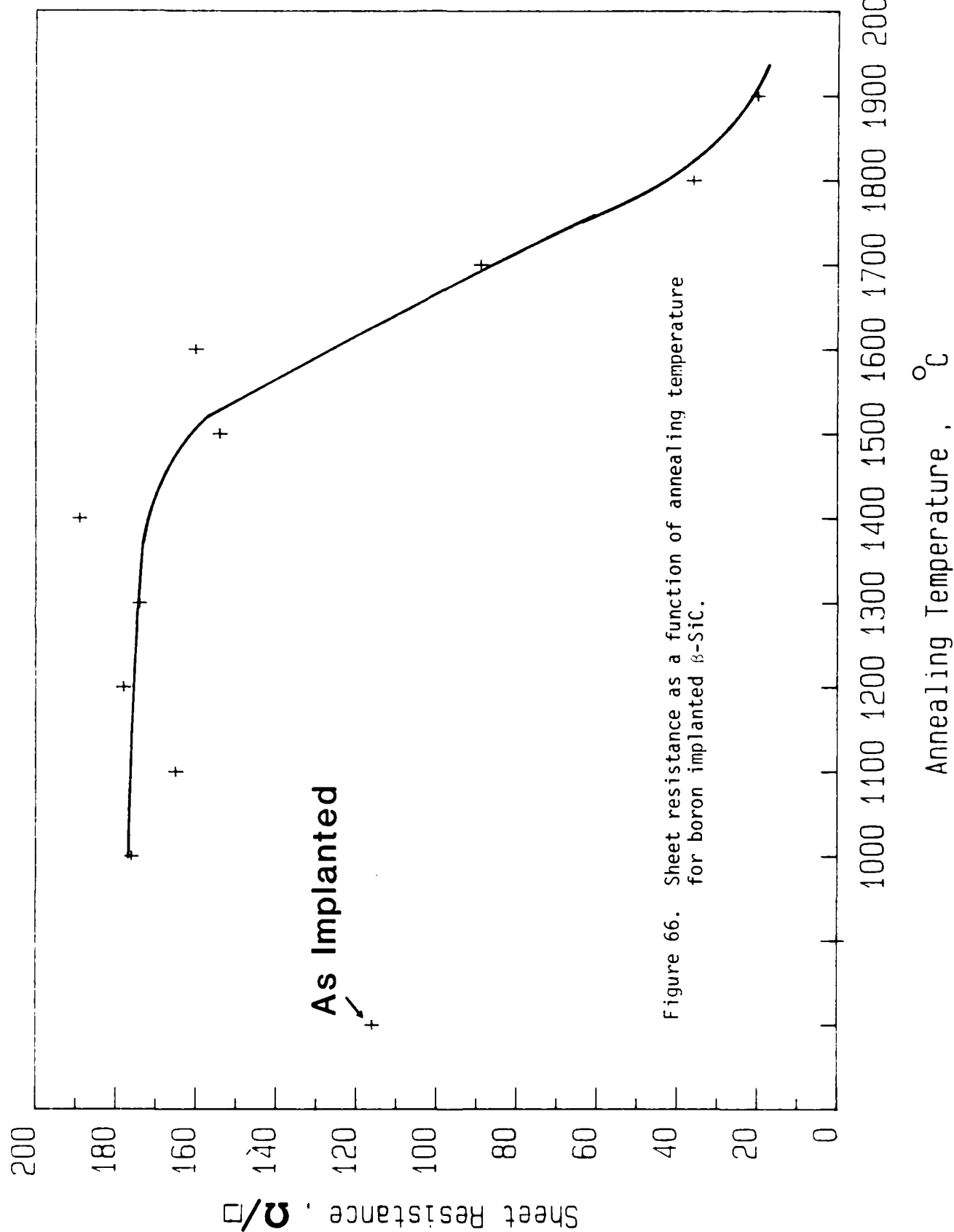
annealing. Using the dose and energy values noted in Table VII, the theoretical LSS dopant profiles were superimposed on the SIMS profile of concentration as a function of depth as shown in Figure 61. As one may note, there is excellent correspondence between the theoretical and experimental curves.

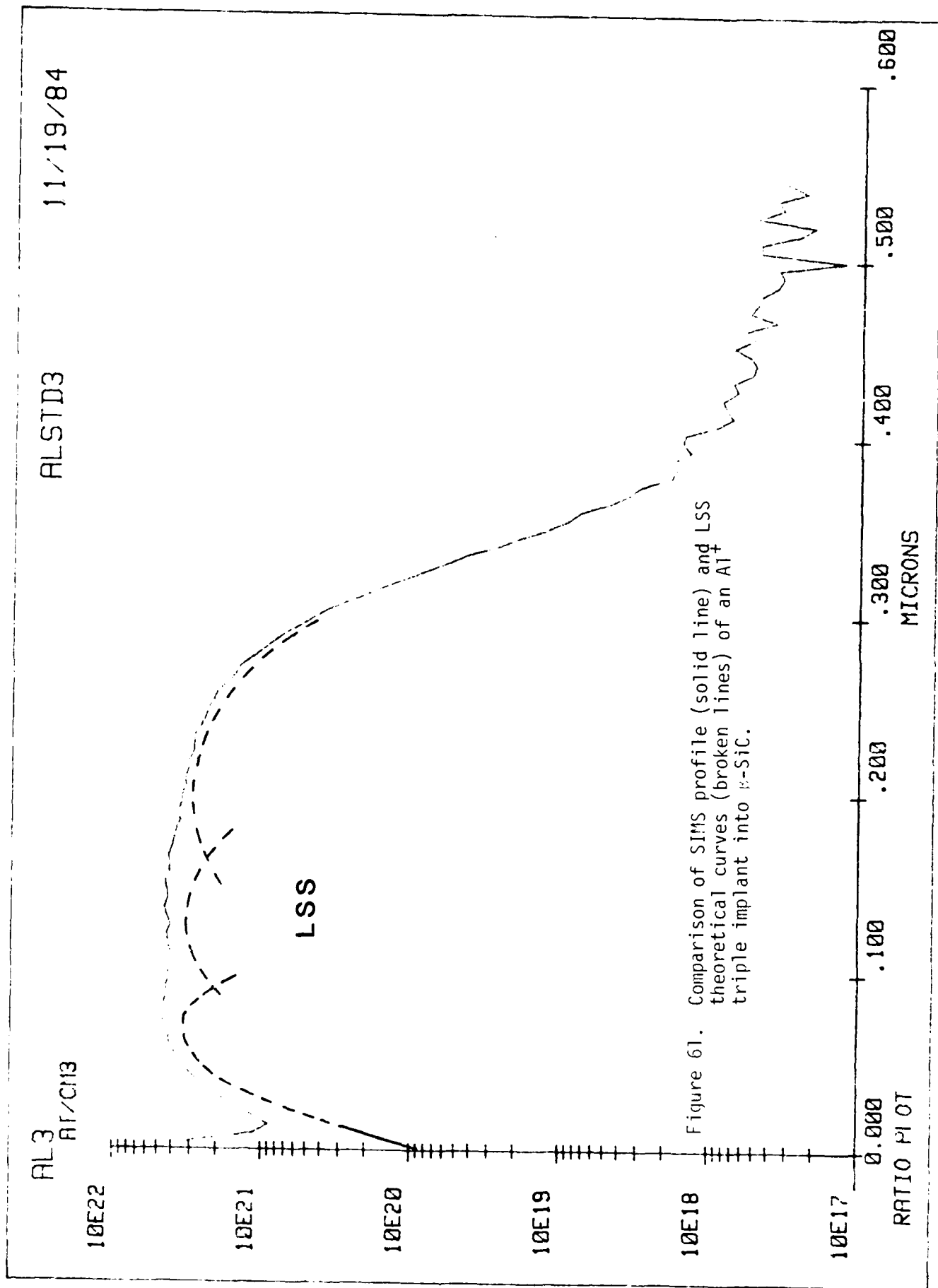
Spreading resistance measurements were also conducted on these implanted samples which had been annealed at 2073K. As shown in Figure 62, a surface p-type layer with a peak spreading resistance of $\sim 10^7$ ohms was determined. This value of spreading resistance equals that achieved with the aluminum dual implant (see Figure 59). Note that the peak atomic concentration in the dual implant was $\sim 1 \times 10^{20}/\text{cm}^3$ while that in the triple implant was $\sim 5 \times 10^{21}/\text{cm}^3$. At first an equal spreading resistance between the two implants may appear contradictory. However, a solubility of ~ 1.0 atomic % aluminum in SiC at 2173K limits the amount of dopant that can be accommodated in the crystal lattice. In turn, the concentration of dopant that can be activated is also limited.

The spreading resistance of the remaining n-type SiC was $\sim 2 \times 10^5$ ohms, as is also indicated in Figure 62. This is nearly an order of magnitude higher than that of the n-type SiC used for the aluminum double implant case (see Figure 59). However, this is expected; since, the carrier concentration in the undoped SiC used for the triple implant was measured at $n = 6 \times 10^{15}/\text{cm}^3$.

A cross-section TEM micrograph of the as implanted surface is shown in Figure 63a. As shown, dislocations and stacking faults terminate at the crystalline-implanted interface. In this instance a 0.47 μm deep amorphous layer resulted.

Figure 63b shows an XTEM micrograph of the implanted surface after annealing at 2073K for 3.0×10^2 s in argon. Quite clearly the amorphous layer has regrown by solid phase epitaxy. However, unlike GaAs and other compound semiconductors, no dislocation loops formed at the regrown interface nor microtwins in the regrown bulk. This may result from the already high defect density of the intrinsic material whereby new defects are in some way getterred. Nevertheless, these results are very promising.





However, capacitance-voltage measurements do indicate p-type conduction after annealing in the temperature range of 1473K-1873K. The p-type carrier concentration remained almost constant at $\sim 10^{16}/\text{cm}^3$ in this temperature range as shown in Figure 67. A rapid decrease in resistance was observed after annealing above 1973K. Ironically, these latter samples showed n-type conduction. The reason for this are not known at this writing.

Marsh¹³ also did not achieve p-type conduction in B-implanted samples annealed at high temperatures. He suggested that the possible reasons for this were: (a) out-diffusion of B, (b) decomposition of the SiC and (c) the presence of compensating n-type defects. The present authors also believe the formation of a B-containing carbide at the high temperatures may be responsible for the loss in p-type conduction.

Figure 68 shows the results of SIMS measurements of atomic concentration as a function of depth of the boron dual implanted and annealed samples. Annealing time was again 3.0×10^2 s at each temperature. The boron profile of the 1573K annealed sample was almost the same as that of as-implanted sample. But out diffusion of the implanted boron was observed after annealing at 1873K. Almost all the boron was diffused out after the 1973K anneal. Studies involving the direct observation of the structural change in these implanted and annealed samples are now underway by using XTEM.

The results of Raman spectroscopy on these dual B⁺ implants are shown in Figure 69. After implantation the characteristic SiC peaks disappeared. As the annealing temperature was increased, the characteristic L₀ and T₀ peaks became increasingly sharp. These changes indicate that the implant damage in the SiC lattice is being removed as the temperature is increased.

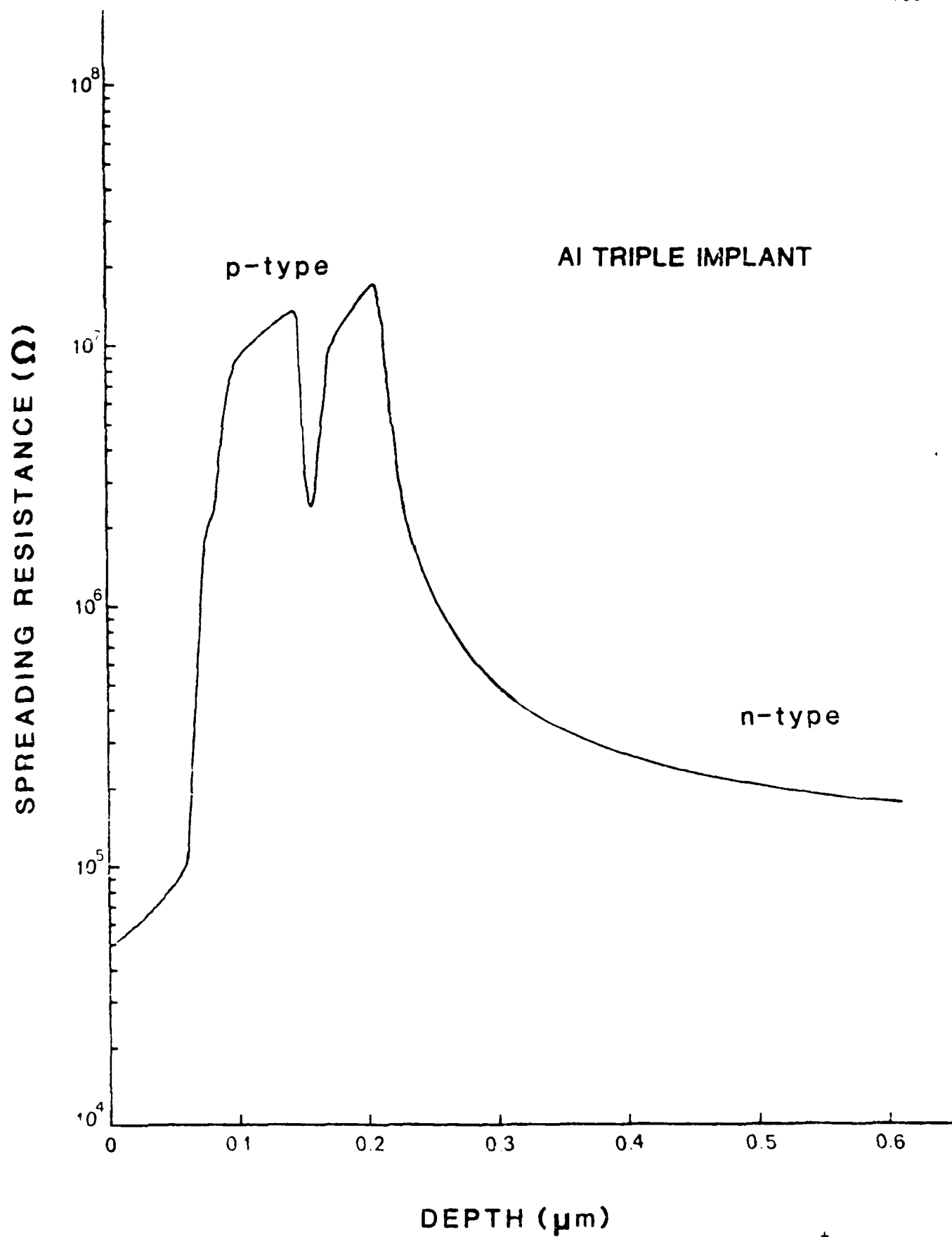


Figure 62. Spreading resistance as a function of depth for an Al^+ triple implant into 3-SiC.



MILLER FEEDBACK PROFILER PLOTTER

N EFF.

PROFILE PLOT

SAMPLE	840974
DATE	
PROFILER SETTINGS	
K	RANGE
A	cm ²
-C	PF
	TEMP. °K

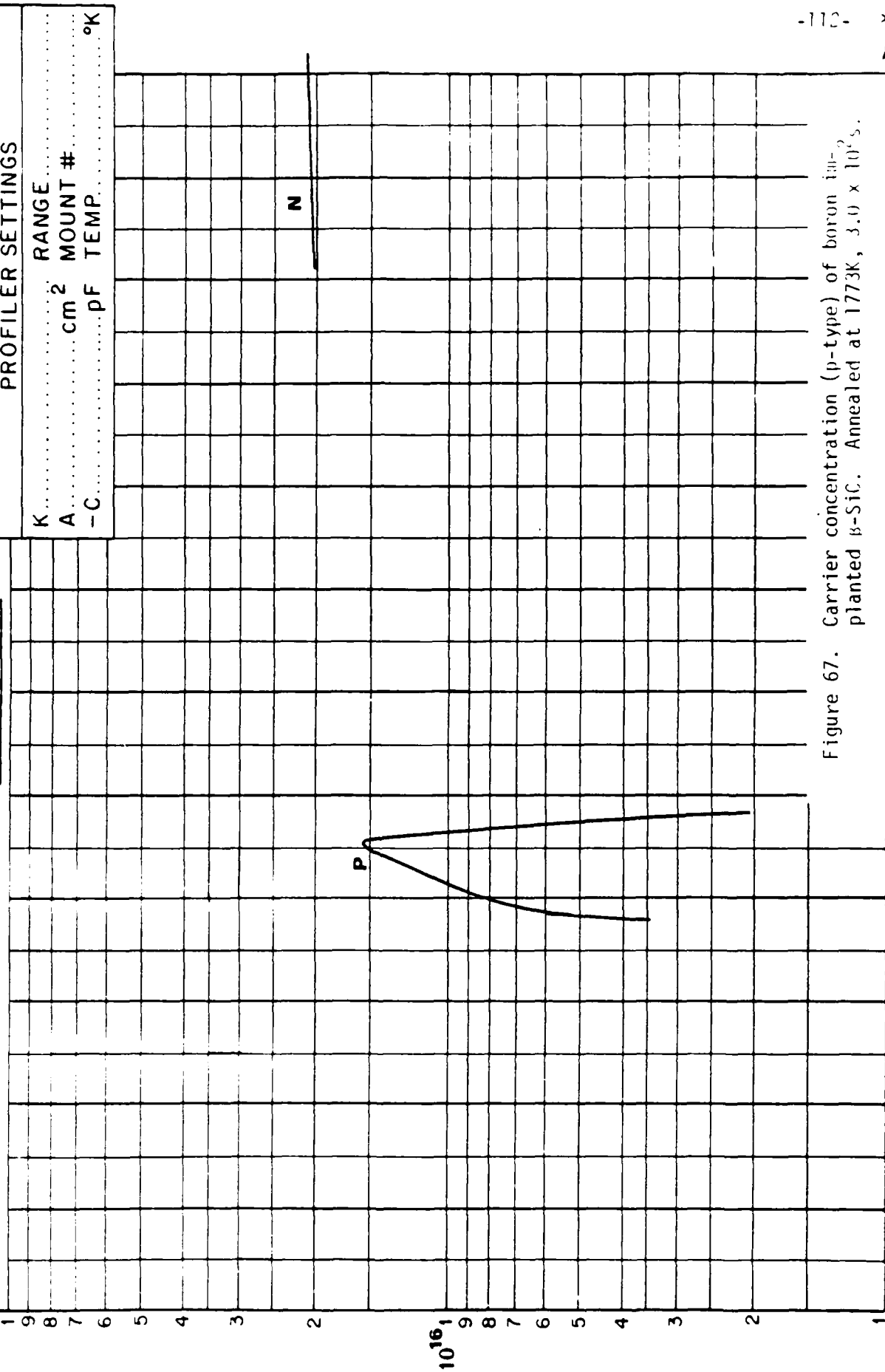
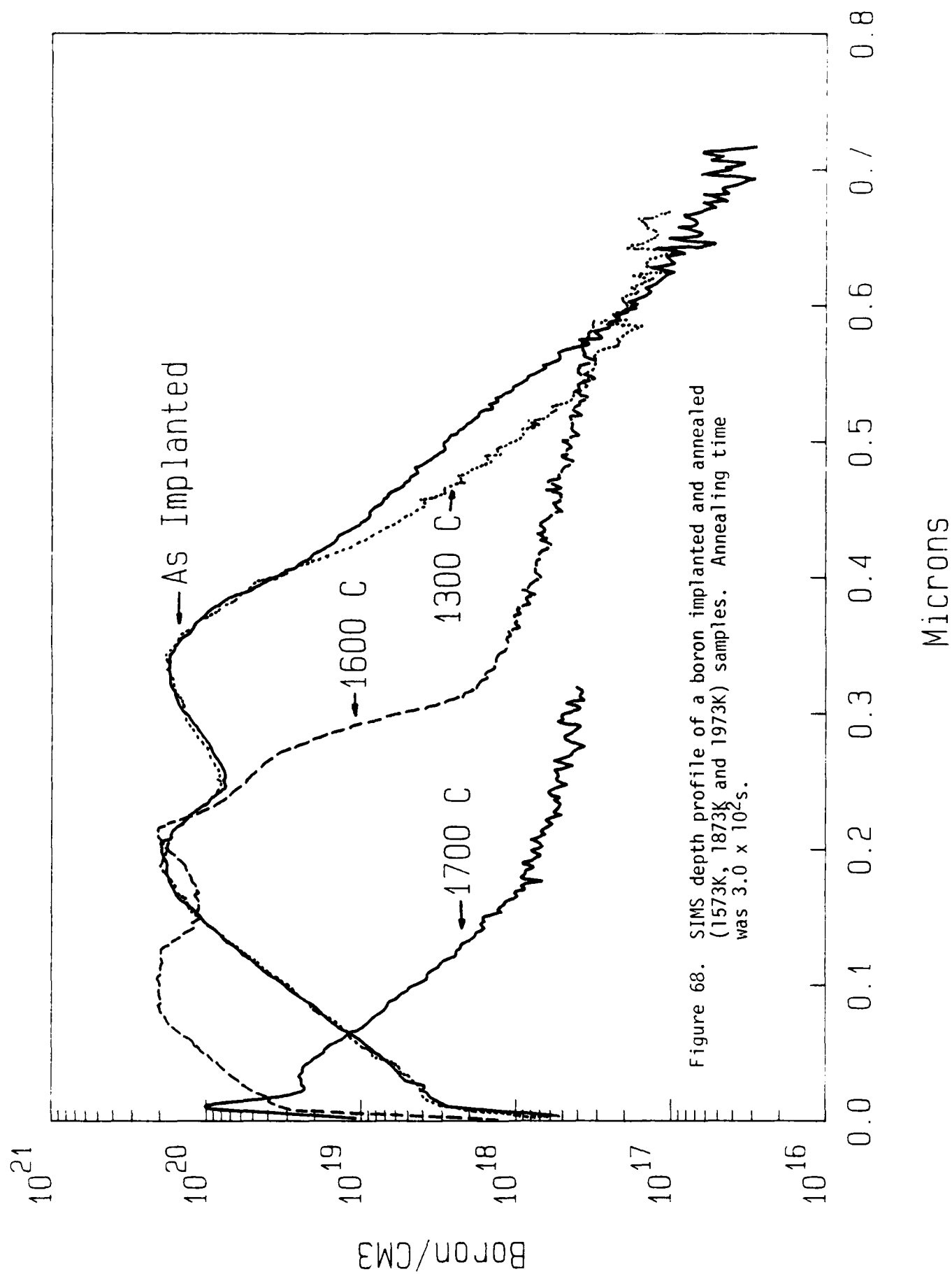


Figure 67. Carrier concentration (p-type) of boron implanted β -SiC. Annealed at 1773K, 3.0×10^{15} .

0.25

0.5

x



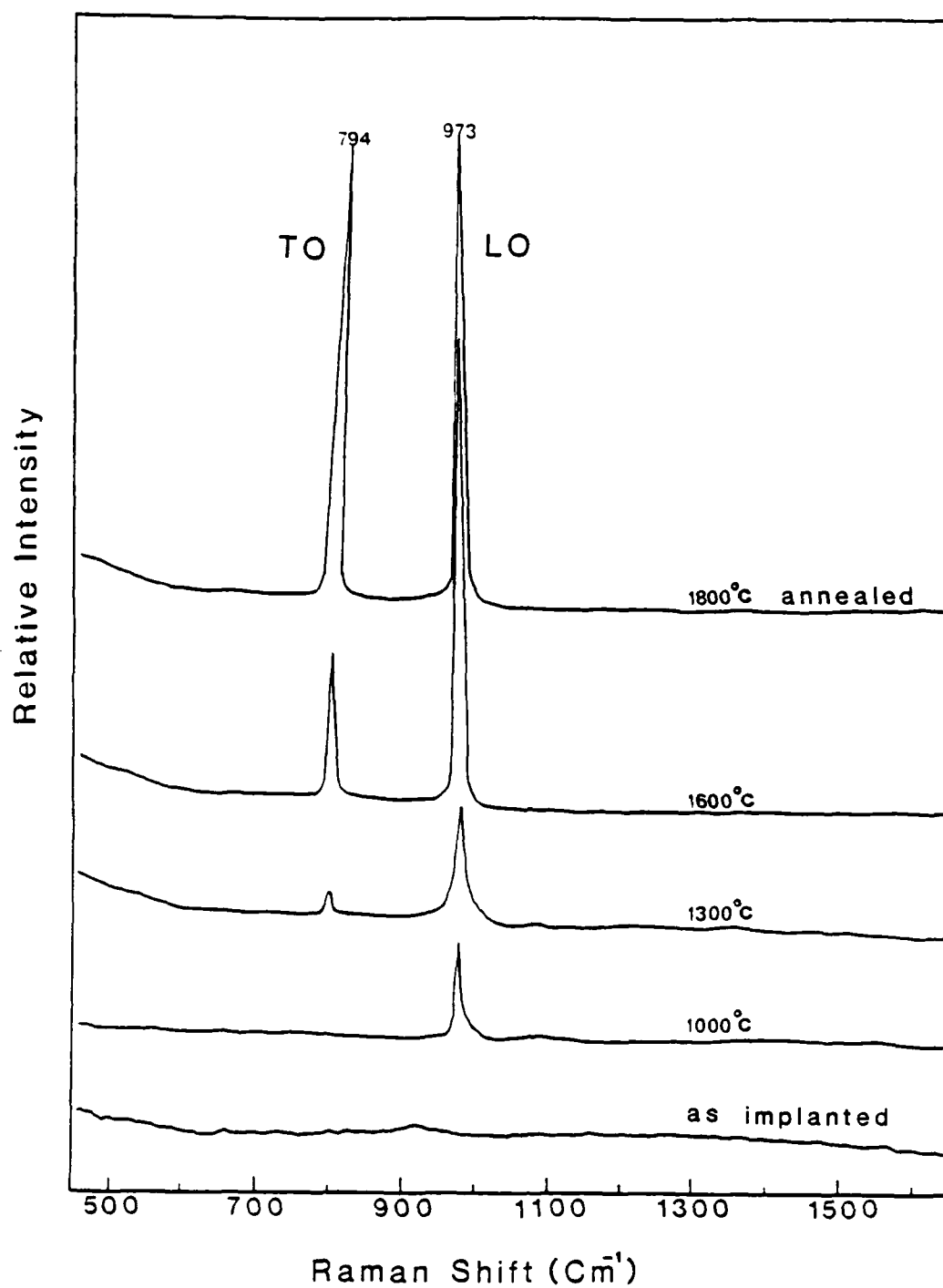


Figure 69. Raman spectra of boron implanted and annealed samples.

IX. OXIDATION STUDIES

The initial efforts in this particular program were concerned with the achievement of both wet and dry oxidation and the accurate determination of the oxide thickness. The oxidation system, as presently configured (see Figure 70), utilizes high purity O_2 or Ar in-

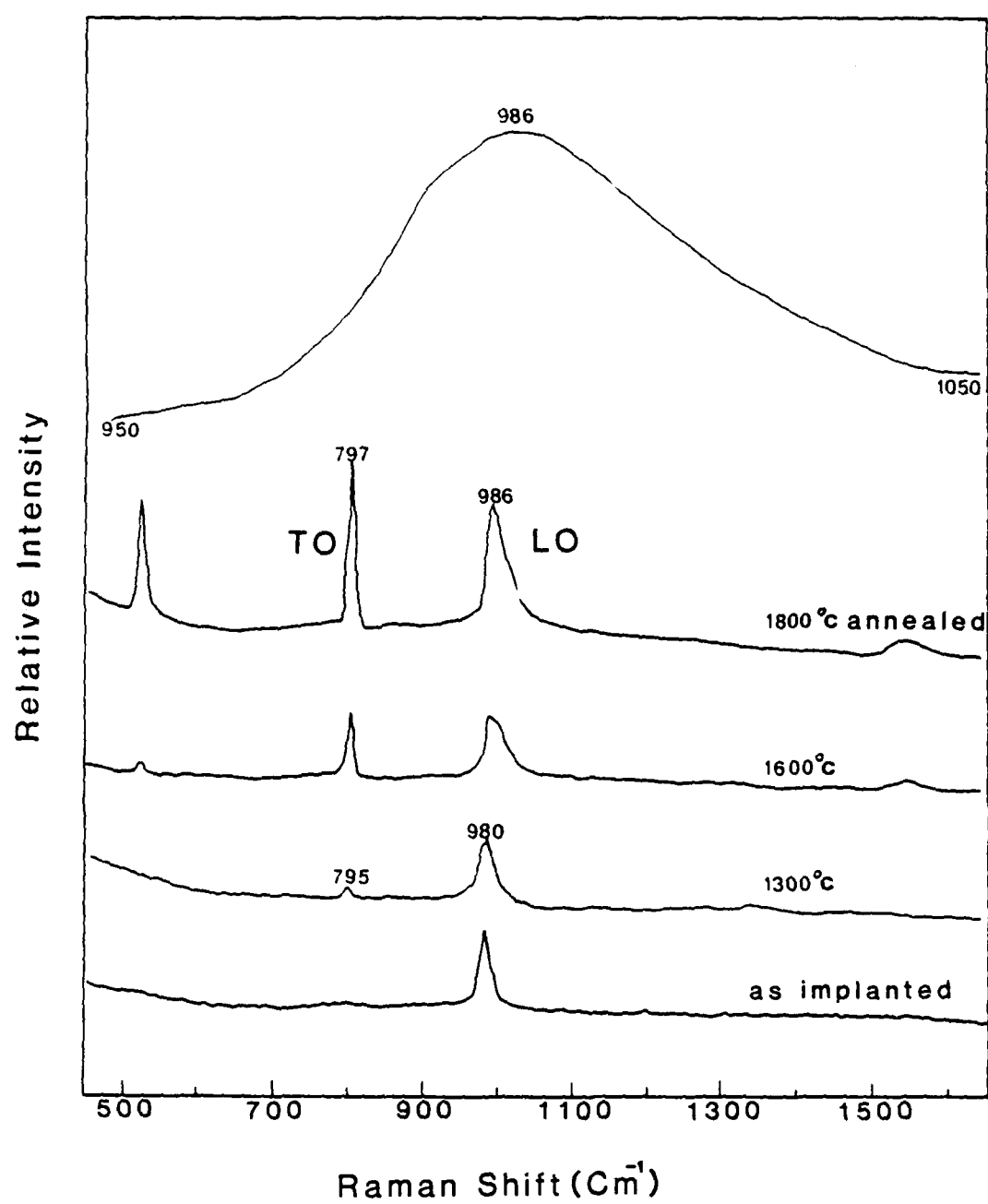


Figure 65. Raman spectra of nitrogen implanted and annealed samples.

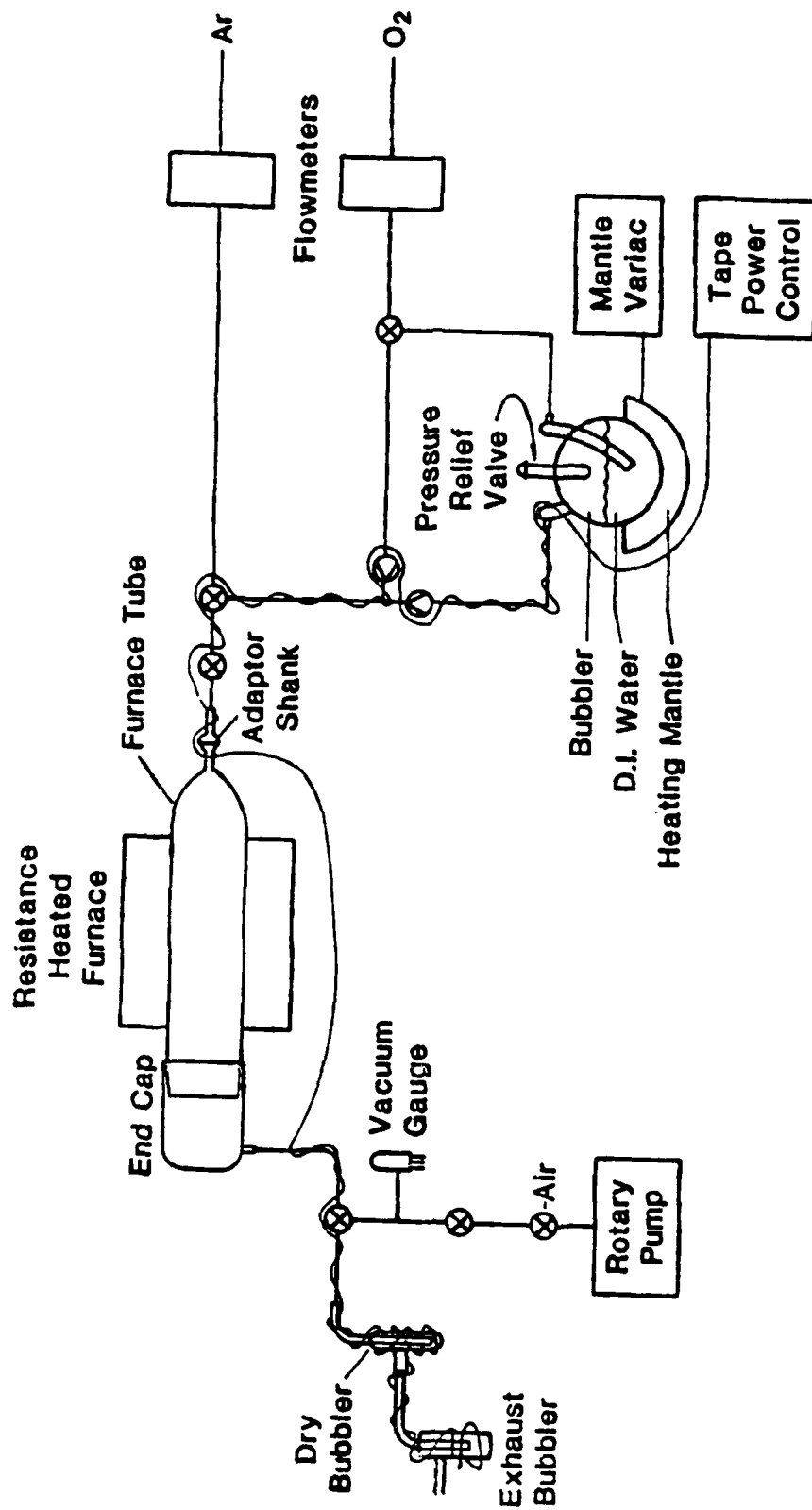


Figure 70. Schematic of the thermal oxidation system used to oxidize the β -SiC thin films.

However, capacitance-voltage measurements do indicate p-type conduction after annealing in the temperature range of 1473K-1873K. The p-type carrier concentration remained almost constant at $\sim 10^{16}/\text{cm}^3$ in this temperature range as shown in Figure 67. A rapid decrease in resistance was observed after annealing above 1973K. Ironically, these latter samples showed n-type conduction. The reason for this are not known at this writing.

Marsh¹³ also did not achieve p-type conduction in B-implanted samples annealed at high temperatures. He suggested that the possible reasons for this were: (a) out-diffusion of B, (b) decomposition of the SiC and (c) the presence of compensating n-type defects. The present authors also believe the formation of a B-containing carbide at the high temperatures may be responsible for the loss in p-type conduction.

Figure 68 shows the results of SIMS measurements of atomic concentration as a function of depth of the boron dual implanted and annealed samples. Annealing time was again 3.0×10^2 s at each temperature. The boron profile of the 1573K annealed sample was almost the same as that of as-implanted sample. But out diffusion of the implanted boron was observed after annealing at 1873K. Almost all the boron was diffused out after the 1973K anneal. Studies involving the direct observation of the structural change in these implanted and annealed samples are now underway by using XTEM.

The results of Raman spectroscopy on these dual B⁺ implants are shown in Figure 69. After implantation the characteristic SiC peaks disappeared. As the annealing temperature was increased, the characteristic L₀ and T₀ peaks became increasingly sharp. These changes indicate that the implant damage in the SiC lattice is being removed as the temperature is increased.

oxide was grown was actually Si, and thus be able to obtain an accurate measurement of oxide thickness. However, the SiC was found to be too transparent to provide sufficient reflectance at the SiC/oxide interface.

The next method employed to determine the oxide thickness was angle lapping of the oxide/film/Si substrate combination. The oxidized samples were lapped at a 36 minute angle (100X) with 0.25 μm diamond paste, and subsequently polished in Syton. They were examined under a microscope using a Nomarsky lens, photographed and the layers measured with a ruler. However, it was extremely difficult to determine the positions of the SiC/oxide interface as well as the top surface of the oxide. The inability to find the interface is due, in part, to the degree of surface roughness caused by the oxidation, which can be as much as 1500 \AA . More important, however, is the fact that the SiC does not provide enough reflectance to show the interface. The actual interface is somewhere between the point where the regular, smooth fringes in the SiC stop, and the first observed color fringe, but the exact position cannot be determined.

The third method attempted was to use a profilometer to measure a step in the oxide. In this method, the oxide layer is partially masked with wax and the exposed oxide is etched away with buffered oxide etchant. The wax is then removed, leaving an oxide layer with a step down to the SiC. A Dektak profilometer, utilizing a sensitive stylus, is then used to measure the oxide step. This method gave the best results, yet measurements were still quite inaccurate because of the surface roughness of the SiC, which was also replicated by the oxide. The measurements were still only accurate to within $\pm 500\text{\AA}$.

Because of this measuring inaccuracy, and other concerns, it was decided that the as-grown samples must be polished. Polishing was performed on a Syntron polishing system using 0.25 μm diamond paste on a nylon knap. The observed roughness on polished SiC is negligible. Step measurements of the oxide layers grown in this polished SiC were considerably easier and resulted in interpretable and repeatable data as shown in Figure 71. The SiC part of the profile is smooth, and the steps are abrupt. There is, however, some surface roughness on the oxide layer. The roughness increases with oxidation

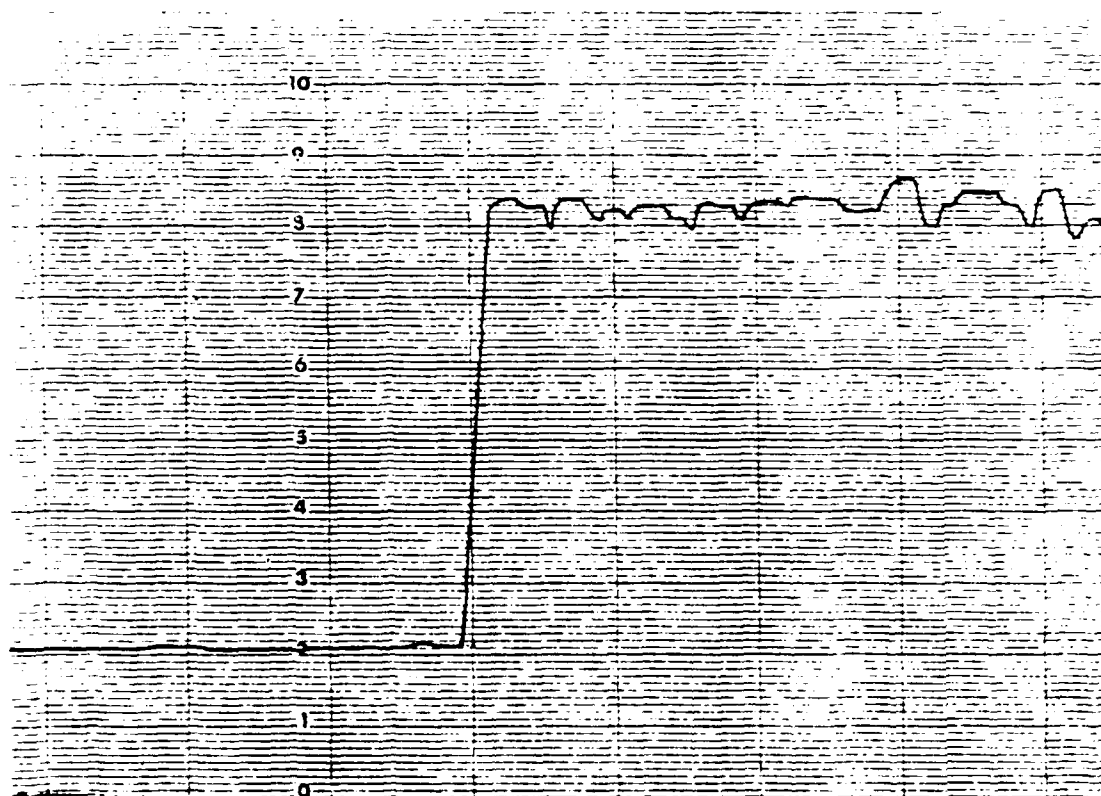


Figure 71. Profilometer determination of the oxide thickness thermally grown on a polished β -SiC thin film at 1200°C in flowing (60 ccm) wet O_2 for 780 minutes. Polished SiC film surface roughness is shown in the left portion of the diagram while a similar profile is shown for the oxide film in the right portion of the graph. Each minor division is equal to 200\AA .



MILLER FEEDBACK PROFILER PLOTTER

SAMPLE	840914
DATE	
PROFILER SETTINGS	
K	RANGE
A	cm ² MOUNT #
-C	PF TEMP °K

PROFILE PLOT

N_{EFF}

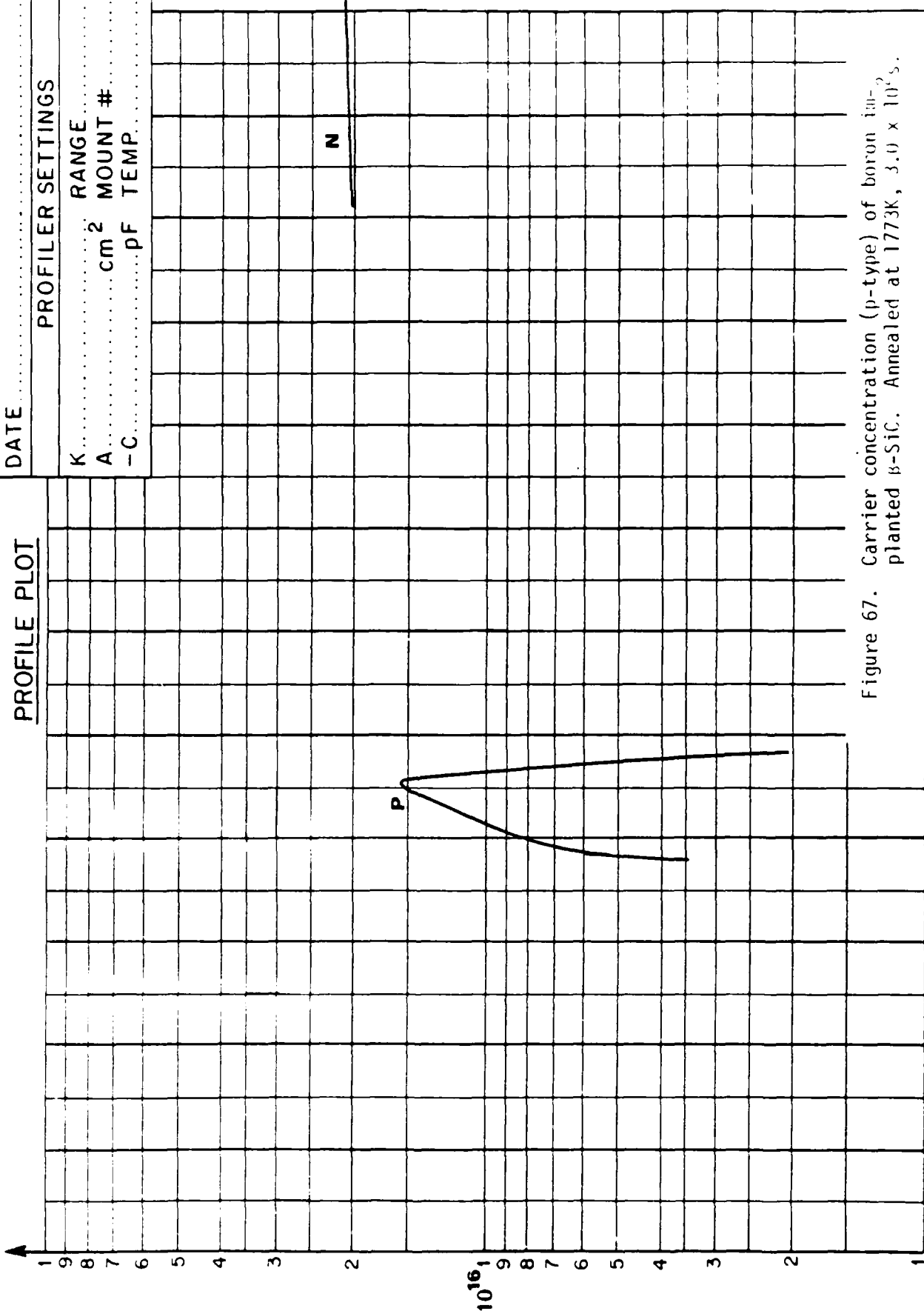


Figure 67. Carrier concentration (p-type) of boron implanted μ -SiC. Annealed at 1773K, 3.0×10^5 s.

0.25

0.5

x

-112-

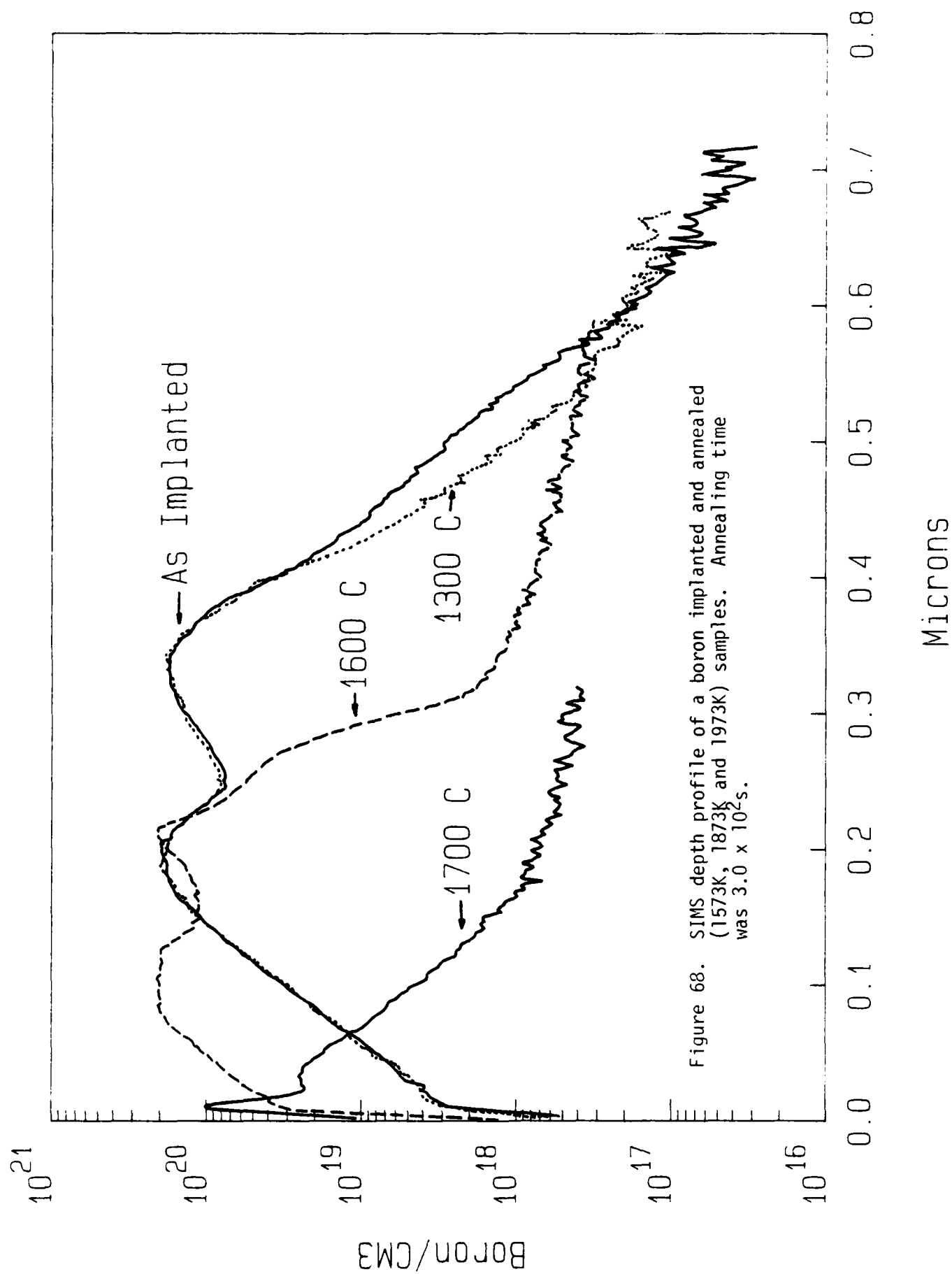
time and thickness. For a thickness of 2700\AA , the observed surface roughness is around 250\AA ; however, at a thickness of $12,300\text{\AA}$, the observed roughness is up to 1500\AA . Possible reasons for this roughening will be discussed later.

Angle lapping was also performed on polished samples. While the roughness was not a problem, it was still impossible to determine the position of the interface. As such it was decided that the profilometer provides the most accurate results.

The color of the oxide layer also changes with thickness, because there is constructive interference of only one visible wave length for a certain oxide thickness. The colors and thicknesses observed for SiO_2 on SiC follow exactly those observed in SiO_2 on Si . One can actually tell, to within $100\text{--}200\text{\AA}$, how thick an oxide layer is by simply noting the color. For example, it has been determined that the oxidation rate of B-doped SiC is markedly slower than that of intrinsic because of the observed color differences. The effects of doping on oxidation rates will be studied in the future.

The results of wet and dry oxidation studies on intrinsic $\beta\text{-SiC}$ films at 1273K, 1373K and 1473K are shown in Figs. 72 and 73. Wet oxidation was achieved by bubbling O_2 through deionized water at 98°C , at a flow rate of 60 ccm. Varying flow rates have been used, from 3 ccm to 60 ccm. It was found that, while oxidation was considerably slower at 3 ccm, there was no rate change between 20 and 60 ccm. Therefore, it is assumed that a flowrate of over 20 ccm should give the maximum oxidation rate at a given temperature. These curves exhibit the expected linear-parabolic nature of oxidation of SiC , with oxidation being faster in the initial regime, and slower after the diffusion of oxygen through the oxide layer becomes the controlling factor.

The rate of wet oxidation at 1473K is, as expected, much faster than the dry oxidation rate. However, wet oxidation at 1373K is only slightly faster than dry oxidation, and the dry process is actually faster than the wet at 1273K. This is a somewhat surprising result, and is explained later in conjunction with SIMS data.



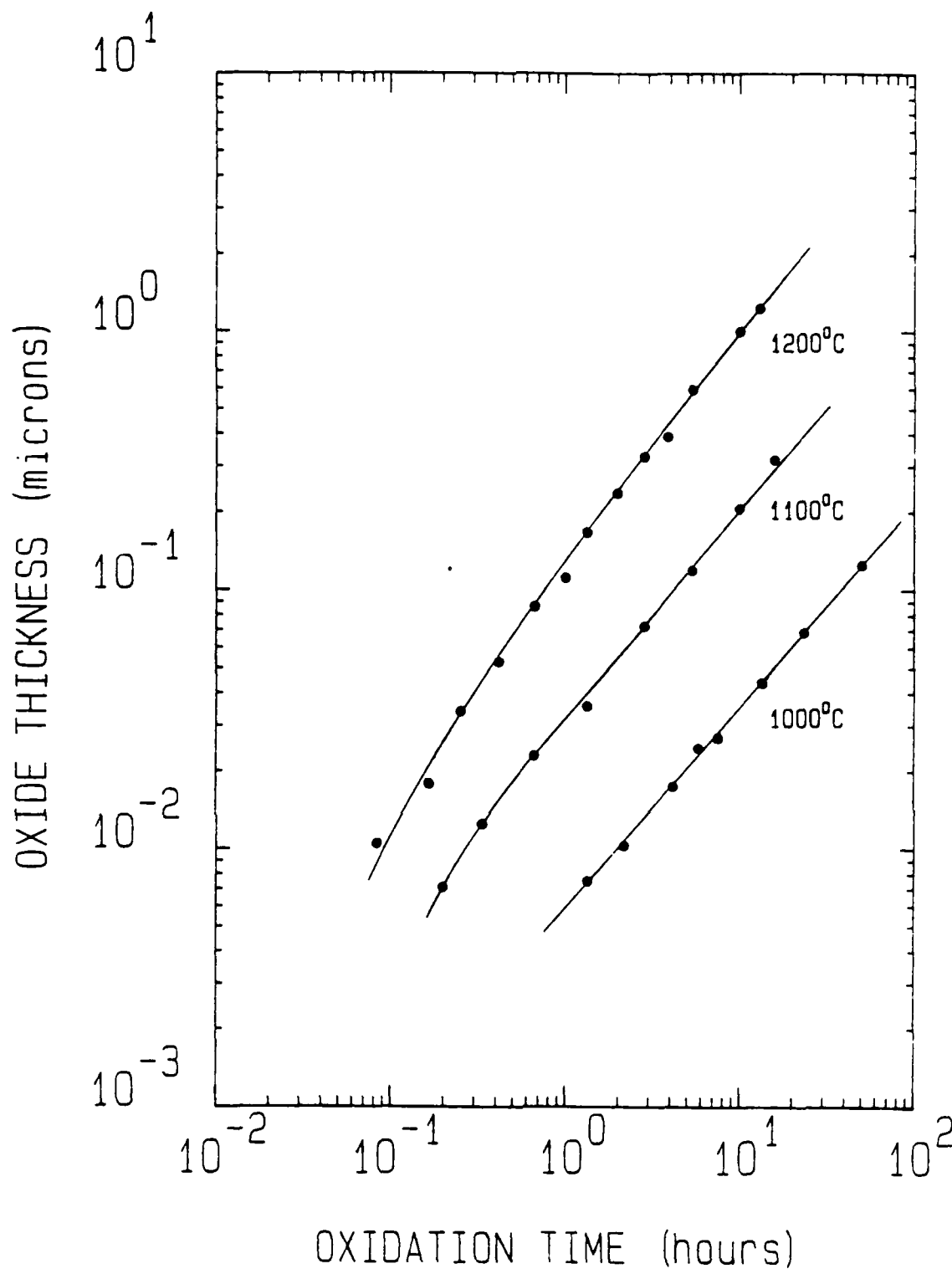
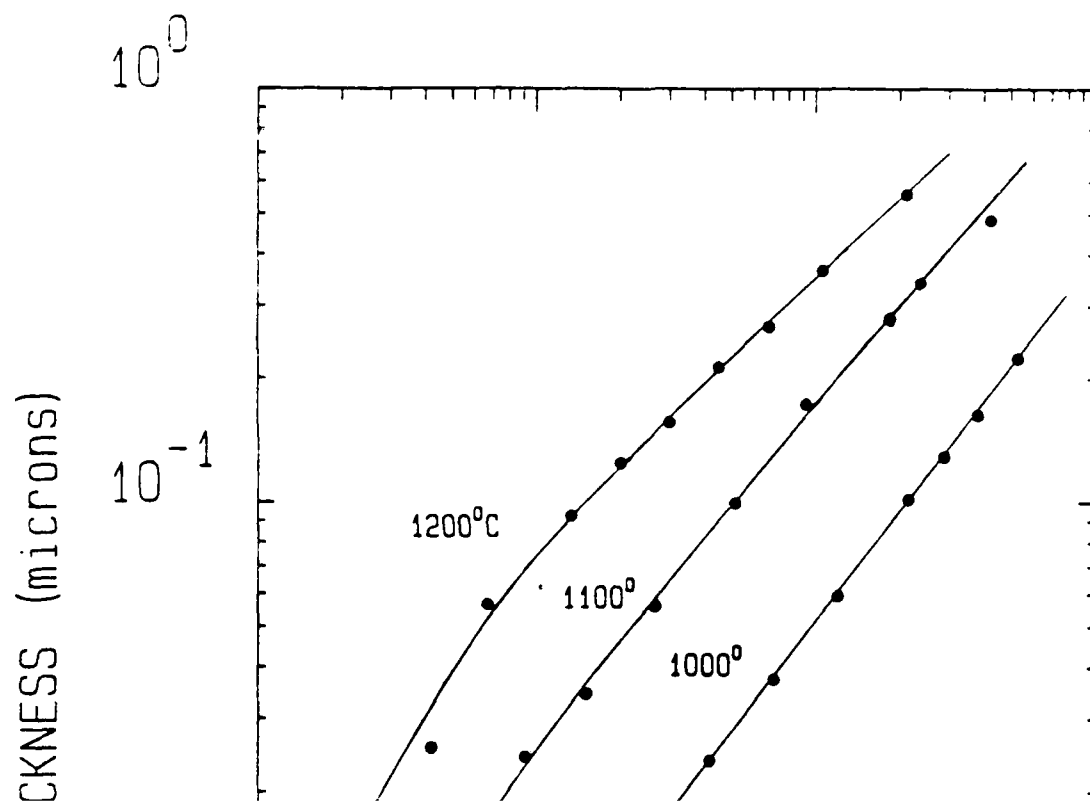


Figure 72. Log-log plot of oxide thickness as a function of time for growth of SiO₂ on SiC in a wet oxidation environment at 1273K, 1373K and 1473K.



IX. OXIDATION STUDIES

The initial efforts in this particular program were concerned with the achievement of both wet and dry oxidation and the accurate determination of the oxide thickness. The oxidation system, as presently configured (see Figure 70), utilizes high purity O_2 or Ar in-

The oxidation model used for SiC is the Deal-Grove model that is widely accepted in the case of Si. This model assumes that the oxidant (H_2O or O) diffuses through the oxide and reacts at the oxide-SiC interface. The oxidation rate follows the derived equation.

$$\frac{X_o}{A/2} = \left[1 + \frac{t + \tau}{A^2/4B} \right] - 1 \quad (3)$$

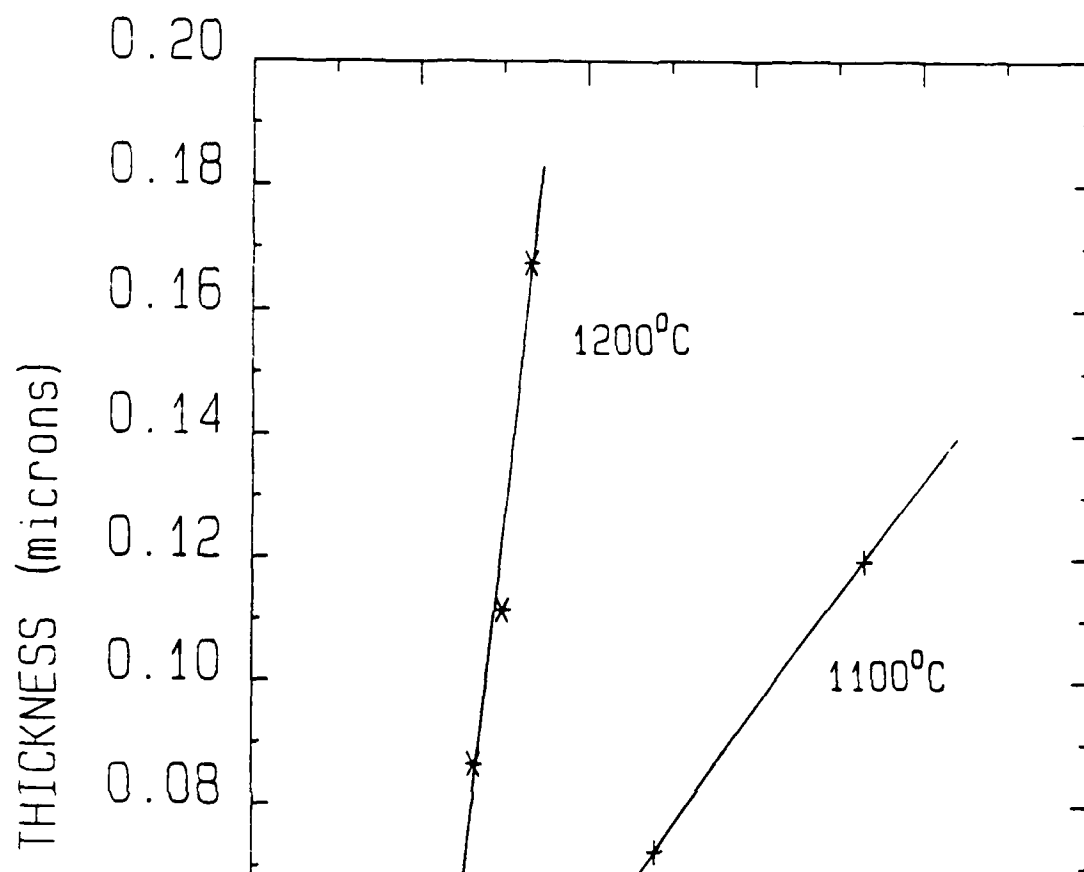
where

- X_o = oxide thickness
- t = oxidation time
- B = parabolic rate constant
- $\frac{B}{A}$ = linear rate constant
- $\tau = (X_i^2 + AX_i)/B$
- X_i = initial oxide thickness

The constant, τ , is a time that is added on to the actual oxidation time to account for either an initial oxide thickness or to adjust for certain peculiarities due to space charge effects in the initial stages of oxidation of a bare SiC surface. The linear and parabolic rate constants have been determined for both wet and dry oxygen. The case of wet oxidation will be discussed initially.

The data for wet oxidation has been placed on a linear graph in Figure 74. The constant, τ , can be determined by extrapolating the curve to where the oxide thickness equals zero. τ will equal the negative of the time intercept. As shown in Figure 74, the curves for each temperature extrapolate to $t = 0$, thus, $\tau = 0$ at all temperatures for wet oxidation. This agrees with Suzuki's¹⁴ data for 6-H SiC in wet oxidation.

The constants B and A can be calculated by plotting the thickness, X_o , versus $(t + \tau)/X_o$, as seen in Figure 75. The slope of the line is the constant B and the negative of the Y-intercept is the constant A . The values of the slopes and intercepts were determined by the least squares method. Some of the data is beyond the range of the graph, but is included in the calculation. One can see that both B and A decrease with temperature.



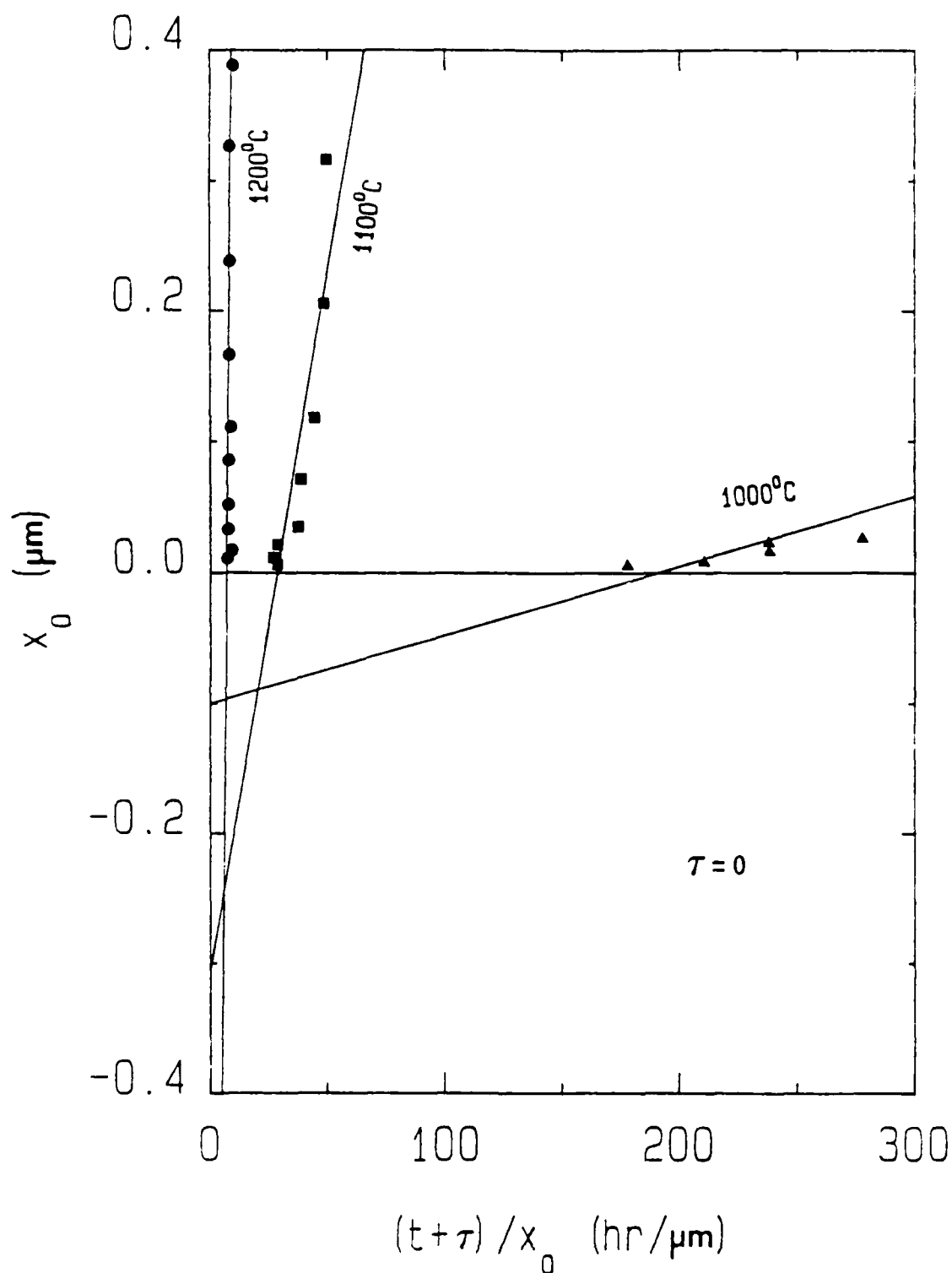


Figure 75. Evaluation of rate constants for oxidation of β -SiC in wet oxygen at 1273K, 1373K and 1473K slope of lines correspond to B in Eq. (3), intercepts at $t + \tau/x_0 = 0$ corresponds to -A in Eq. (3).

oxide was grown was actually Si, and thus be able to obtain an accurate measurement of oxide thickness. However, the SiC was found to be too transparent to provide sufficient reflectance at the SiC/oxide interface.

The next method employed to determine the oxide thickness was angle lapping of the oxide/film/Si substrate combination. The oxidized samples were lapped at a 36 minute angle (100X) with 0.25 μm diamond paste, and subsequently polished in Syton. They were examined under a microscope using a Nomarsky lens, photographed and the layers measured with a ruler. However, it was extremely difficult to determine the positions of the SiC/oxide interface as well as the top surface of the oxide. The inability to find the interface is due, in part, to the degree of surface roughness caused by the oxidation, which can be as much as 1500 \AA . More important, however, is the fact that the SiC does not provide enough reflectance to show the interface. The actual interface is somewhere between the point where the regular, smooth fringes in the SiC stop, and the first observed color fringe, but the exact position cannot be determined.

The third method attempted was to use a profilometer to measure a step in the oxide. In this method, the oxide layer is partially masked with wax and the exposed oxide is etched away with buffered oxide etchant. The wax is then removed, leaving an oxide layer with a step down to the SiC. A Dektak profilometer, utilizing a sensitive stylus, is then used to measure the oxide step. This method gave the best results, yet measurements were still quite inaccurate because of the surface roughness of the SiC, which was also replicated by the oxide. The measurements were still only accurate to within $\pm 500\text{\AA}$.

Because of this measuring inaccuracy, and other concerns, it was decided that the as-grown samples must be polished. Polishing was performed on a Syntron polishing system using 0.25 μm diamond paste on a nylon knap. The observed roughness on polished SiC is negligible. Step measurements of the oxide layers grown in this polished SiC were considerably easier and resulted in interpretable and repeatable data as shown in Figure 71. The SiC part of the profile is smooth, and the steps are abrupt. There is, however, some surface roughness on the oxide layer. The roughness increases with oxidation

The constants B and B/A are plotted logarithmically against the reciprocal of the absolute temperature in Figure 76. Both constants exhibit exponential temperature dependencies. The activation energy for the linear rate constant B/A is 61 kcal/mol, which is reasonably close to the 69.3 kcal/mol required to break a Si-C bond. The parabolic rate constant is not as cooperative, exhibiting an activation energy of 119 kcal/mol. The parabolic rate constant should closely approximate the activation energy for the diffusion of H_2O in SiO_2 , which is 18.3 kcal/mol. However, Suzuki¹⁴ obtained a value for B of 48 kcal/mol for 6-H SiC and theorized that the out diffusion of the reaction by-product CO through the oxide was the controlling factor. There is still a large discrepancy between Suzuki's value and that reported here. The reason for this disagreement will be explained below.

In order to determine the rate constants for the dry oxidation data, the same method is followed. The data is placed on a linear graph, as shown in Figure 77. In this case, the curves for 1473K and 1373K extrapolate to a positive value of 0.118 hrs., or about 7 mins. For 1273K, the curve extrapolates to negative 0.147 hrs., or almost 9 mins. The negative of these values equal τ .

With these values, B and A are determined by plotting X_0 vs $(t + \tau)/X_0$ as in the previous case. As can be seen in Figure 78, A (the $-y$ intercept) increases, while B (the slope) decreases, with decreasing temperature. The values were, again, determined by the least squares method.

In the plot of rate constant vs inverse of temperature in Figure 79, one can see that the activation energy of the linear rate constant B/A is 60 kcal/mol. This is almost identical to the value obtained in wet oxidation, indicating that the surface control mechanism is the same for the two oxidants. Again, this value is close to the accepted value for breaking a Si-C bond. The parabolic rate constant B has an activation energy of 34 kcal/mol. This can be compared with the value of 27.0 kcal/mol for the diffusivity of oxygen through fused silica. Considering that only three points have been determined, these values are relatively close, and it can be

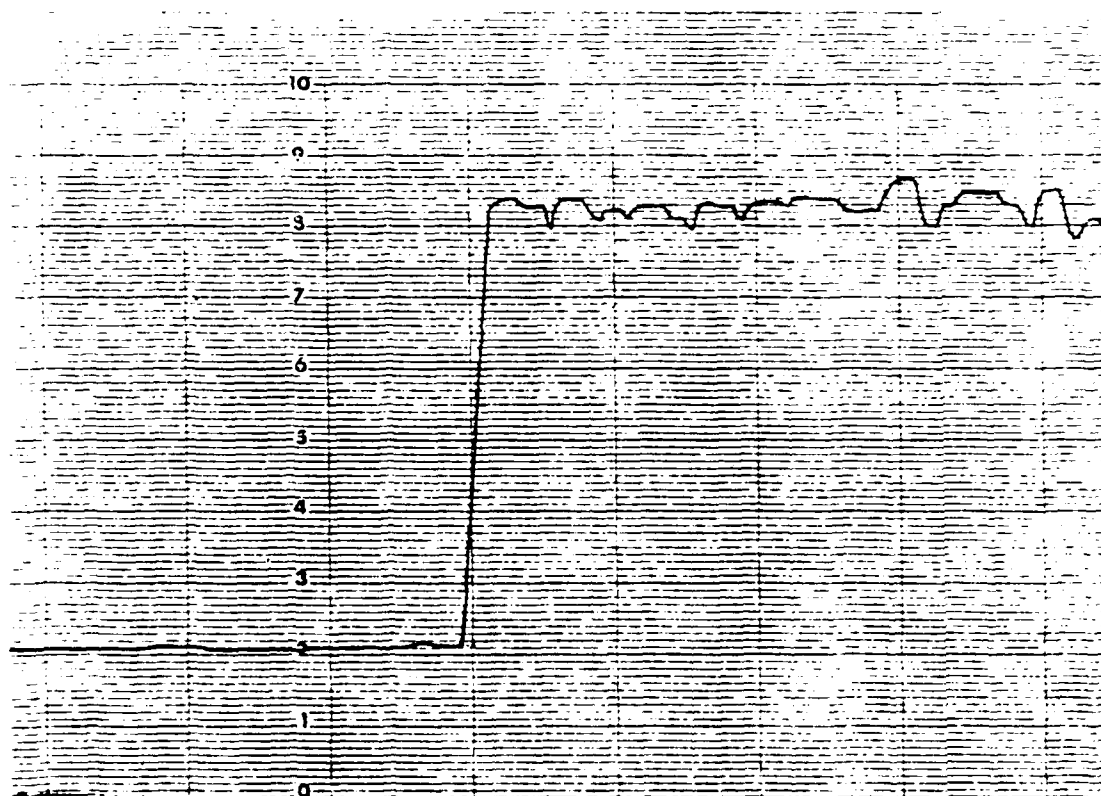


Figure 71. Profilometer determination of the oxide thickness thermally grown on a polished β -SiC thin film at 1200°C in flowing (60 ccm) wet O_2 for 780 minutes. Polished SiC film surface roughness is shown in the left portion of the diagram while a similar profile is shown for the oxide film in the right portion of the graph. Each minor division is equal to 200\AA .

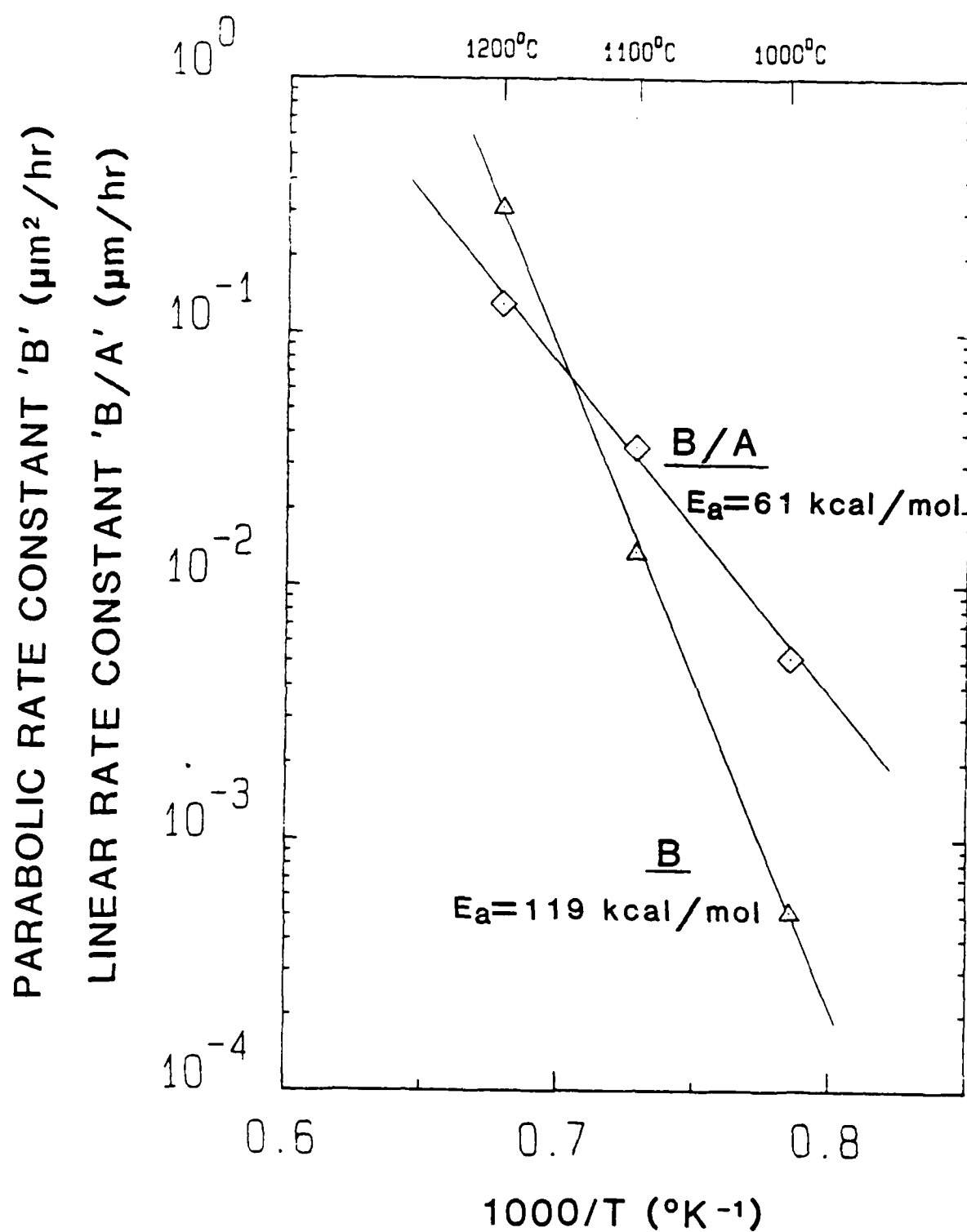


Figure 76. Temperature dependencies of the linear rate constant, B/A , and the parabolic rate constant, B , for wet oxidation of β -SiC.

time and thickness. For a thickness of 2700\AA , the observed surface roughness is around 250\AA ; however, at a thickness of $12,300\text{\AA}$, the observed roughness is up to 1500\AA . Possible reasons for this roughening will be discussed later.

Angle lapping was also performed on polished samples. While the roughness was not a problem, it was still impossible to determine the position of the interface. As such it was decided that the profilometer provides the most accurate results.

The color of the oxide layer also changes with thickness, because there is constructive interference of only one visible wave length for a certain oxide thickness. The colors and thicknesses observed for SiO_2 on SiC follow exactly those observed in SiO_2 on Si . One can actually tell, to within $100\text{--}200\text{\AA}$, how thick an oxide layer is by simply noting the color. For example, it has been determined that the oxidation rate of B-doped SiC is markedly slower than that of intrinsic because of the observed color differences. The effects of doping on oxidation rates will be studied in the future.

The results of wet and dry oxidation studies on intrinsic $\beta\text{-SiC}$ films at 1273K, 1373K and 1473K are shown in Figs. 72 and 73. Wet oxidation was achieved by bubbling O_2 through deionized water at 98°C , at a flow rate of 60 ccm. Varying flow rates have been used, from 3 ccm to 60 ccm. It was found that, while oxidation was considerably slower at 3 ccm, there was no rate change between 20 and 60 ccm. Therefore, it is assumed that a flowrate of over 20 ccm should give the maximum oxidation rate at a given temperature. These curves exhibit the expected linear-parabolic nature of oxidation of SiC , with oxidation being faster in the initial regime, and slower after the diffusion of oxygen through the oxide layer becomes the controlling factor.

The rate of wet oxidation at 1473K is, as expected, much faster than the dry oxidation rate. However, wet oxidation at 1373K is only slightly faster than dry oxidation, and the dry process is actually faster than the wet at 1273K. This is a somewhat surprising result, and is explained later in conjunction with SIMS data.

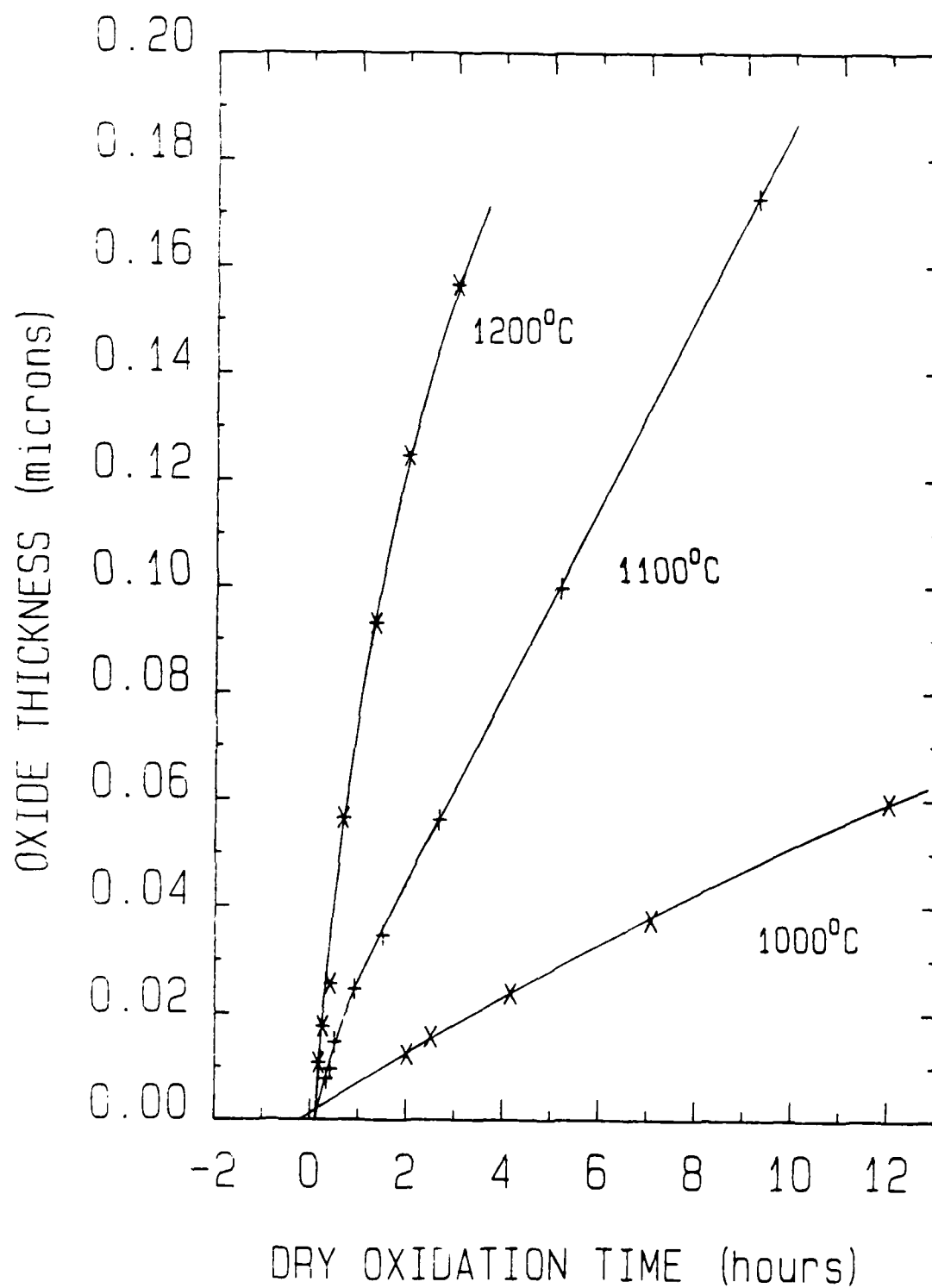


Figure 77. Linear plot of oxide thickness vs. oxidation time for dry oxidation of SiC at 1273K, 1373K and 1473K.

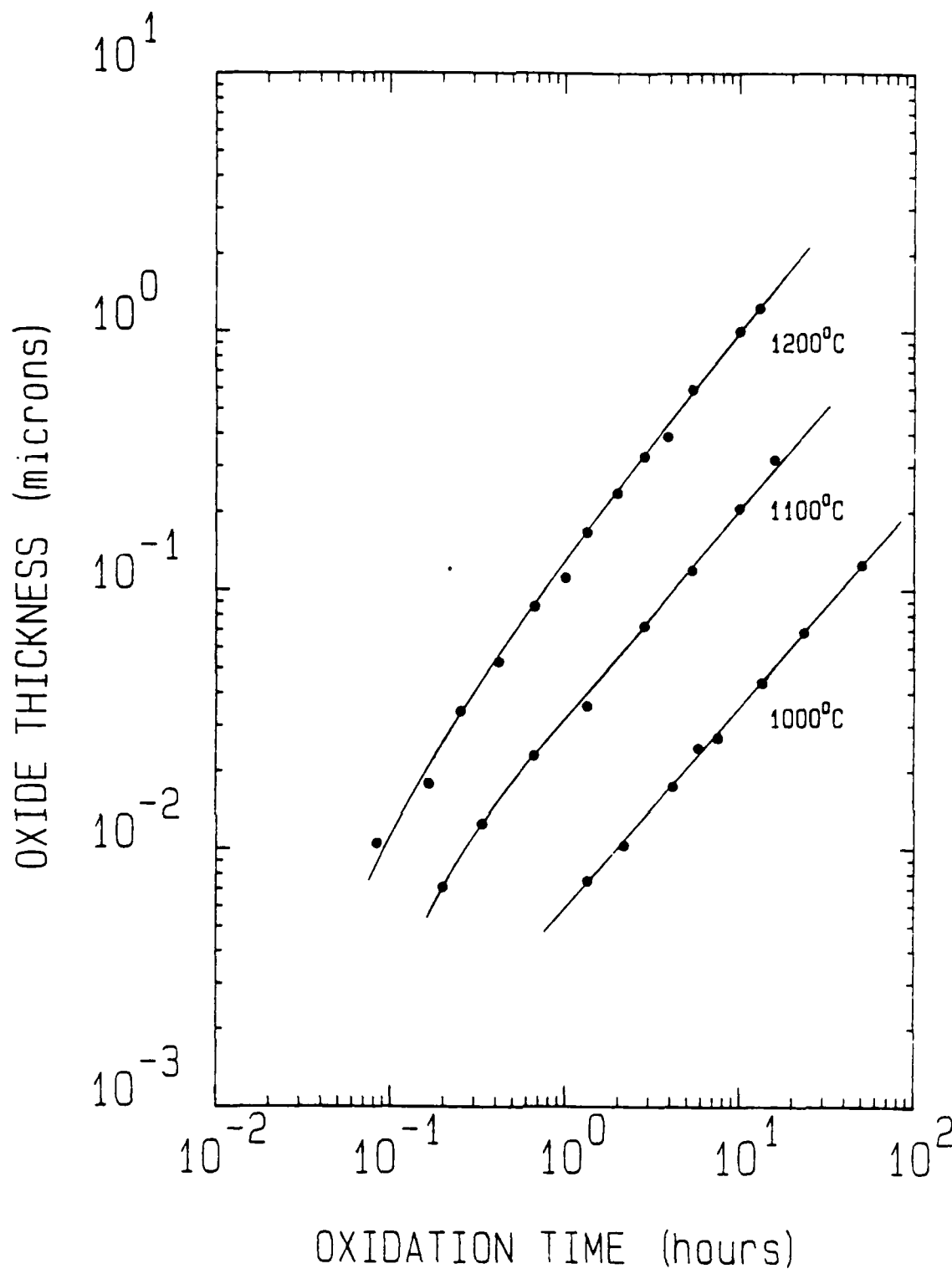


Figure 72. Log-log plot of oxide thickness as a function of time for growth of SiO_2 on $\alpha\text{-SiC}$ in a wet oxidation environment at 1273K, 1373K and 1473K.

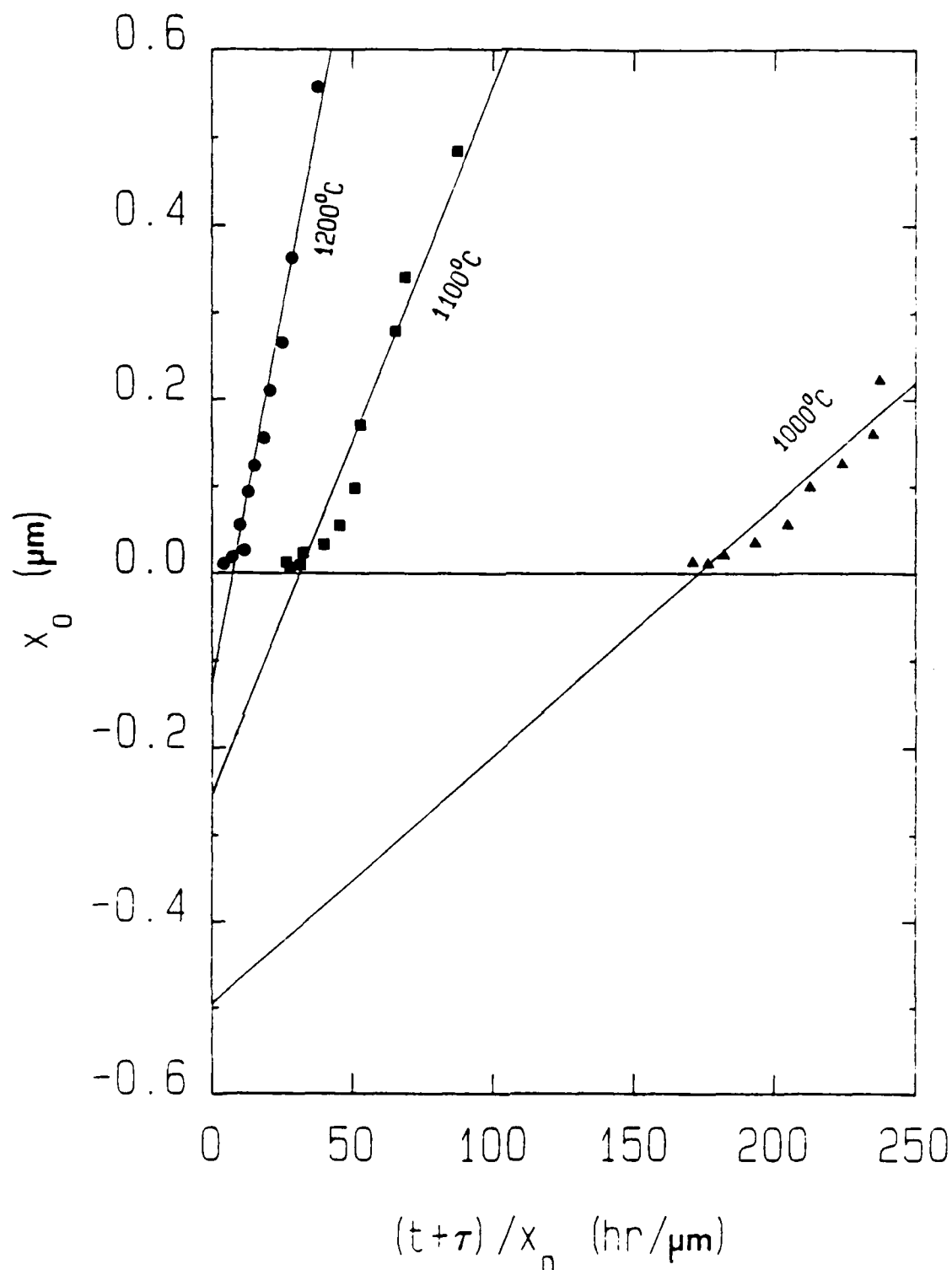


Figure 78. Evaluation of rate constants for oxidation of β -SiC in dry oxygen at 1273K, 1373K, and 1473K, using general relationship of Eq. (3).

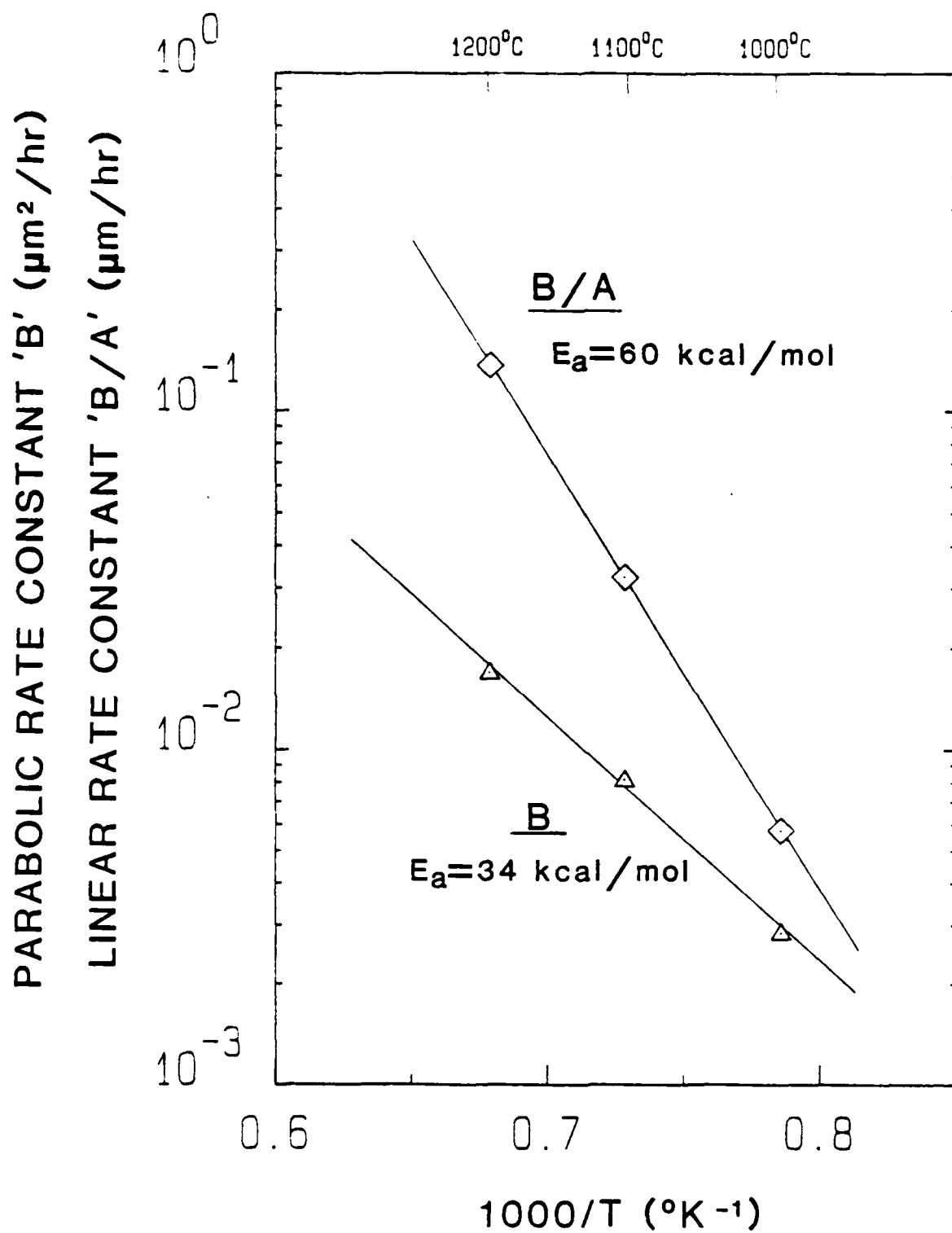


Figure 79. Temperature dependencies of the linear rate constant, B/A , and the parabolic rate constant, B , for dry oxidation of SiC .

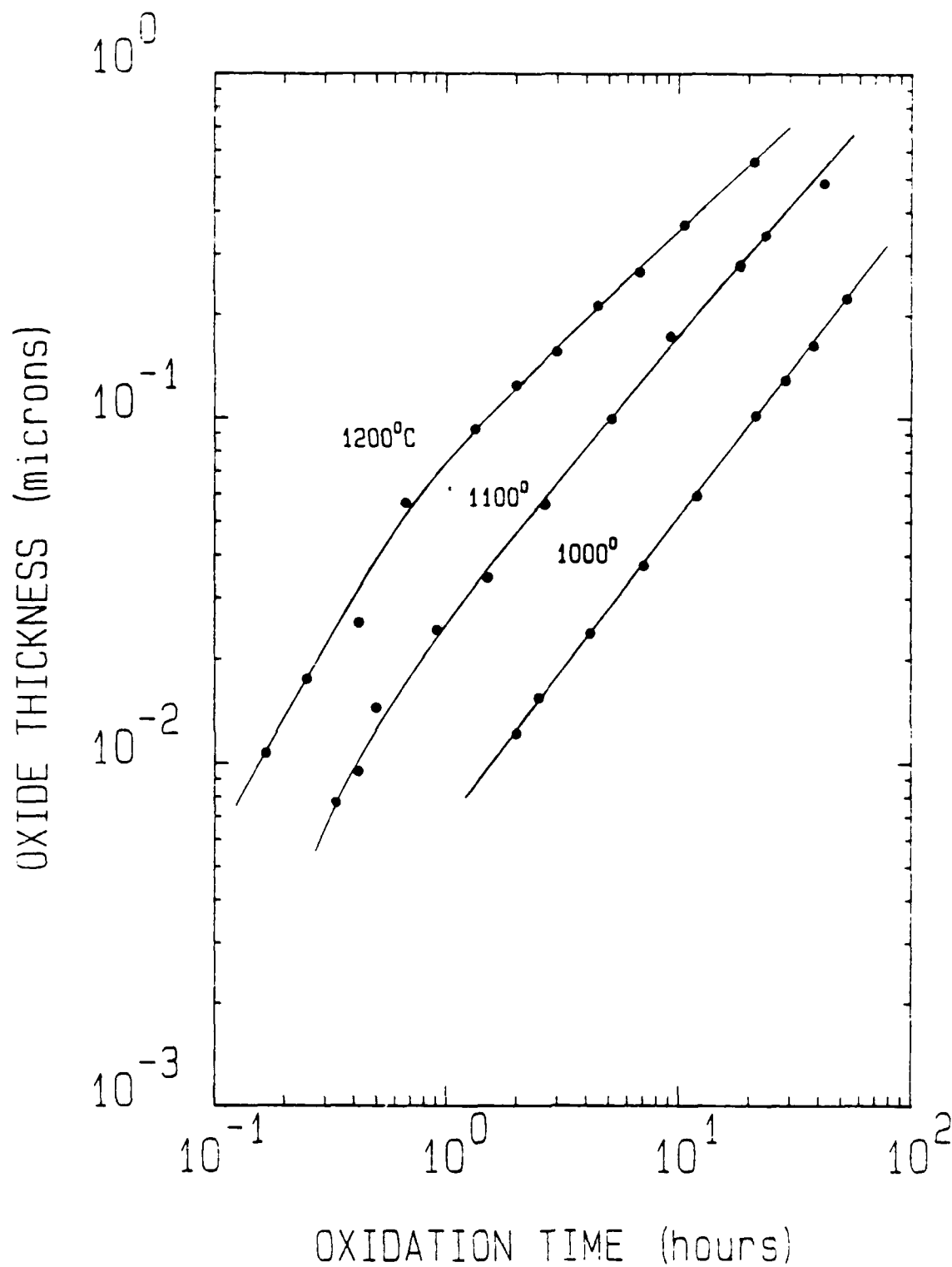


Figure 73. Log-log plot of oxide thickness as a function of oxidation time for dry oxidation of SiC at 1273K, 1373K and 1473K.

assumed that the diffusion of the oxidant, and not the out-diffusion of CO, is the rate limiting factor in dry oxidation.

All the data obtained for both wet and dry oxidation are normalized with respect to A and B in Figure 80. The solid black line is a calculated theoretical line corresponding to Eq. (3). The excellent agreement between theory and experimental results demonstrates that the model fits quite well. Also included are the two asymptotic forms of the general relationship. The linear law is seen to be valid at short times, relative to A and B, and the data approaches the parabolic law at relatively long periods of time. Of particular interest in this graph, is the fact that none of the wet data gets into a region where the parabolic law has a strong influence. Except for a few points, the wet data is, in fact, very close to the linear law regime. For this reason, the parabolic data, and resulting activation energy, for wet oxidation should be considered inaccurate until more experimentation can be conducted in the longer time-parabolic law regime.

SIMS analysis shows a striking difference in the carbon content of the wet and dry oxides. Figure 81 shows the depth profile of a wet oxide layer grown at 1373K for 320 mins. It can be seen that in SiC, Si and C have about the same yield under the profiling conditions. Although SIMS measurements of the yield of a species is very matrix dependent, a rough idea of the amount of C-containing species may be surmised from the data obtained from the oxide. Thus in the oxide side of the SIMS profile, it can be seen that the C ion yield is about one order of magnitude lower than the Si ion yield. If we assume that there are 2.3×10^{22} Si atoms/cm³ in the oxide, then the carbon ion yield, at its lowest point, is about 10^{21} C atoms/cm³). This carbon is presumed to be in the form of CO. This profile also shows an appreciable amount of oxygen penetration into the SiC. The oxygen level is still dropping in the SiC as deep as 1100Å.

The depth profile of a dry oxide layer which was grown for 310 mins. (about the same time as the wet oxide in Figure 81) is shown in Figure 82. Again, from the SiC side, one can see that the ion

The oxidation model used for SiC is the Deal-Grove model that is widely accepted in the case of Si. This model assumes that the oxidant (H_2O or O) diffuses through the oxide and reacts at the oxide-SiC interface. The oxidation rate follows the derived equation.

$$\frac{X_o}{A/2} = \left[1 + \frac{t + \tau}{A^2/4B} \right] - 1 \quad (3)$$

where

- X_o = oxide thickness
- t = oxidation time
- B = parabolic rate constant
- $\frac{B}{A}$ = linear rate constant
- $\tau = (X_i^2 + AX_i)/B$
- X_i = initial oxide thickness

The constant, τ , is a time that is added on to the actual oxidation time to account for either an initial oxide thickness or to adjust for certain peculiarities due to space charge effects in the initial stages of oxidation of a bare SiC surface. The linear and parabolic rate constants have been determined for both wet and dry oxygen. The case of wet oxidation will be discussed initially.

The data for wet oxidation has been placed on a linear graph in Figure 74. The constant, τ , can be determined by extrapolating the curve to where the oxide thickness equals zero. τ will equal the negative of the time intercept. As shown in Figure 74, the curves for each temperature extrapolate to $t = 0$, thus, $\tau = 0$ at all temperatures for wet oxidation. This agrees with Suzuki's¹⁴ data for 6-H SiC in wet oxidation.

The constants B and A can be calculated by plotting the thickness, X_o , versus $(t + \tau)/X_o$, as seen in Figure 75. The slope of the line is the constant B and the negative of the Y-intercept is the constant A . The values of the slopes and intercepts were determined by the least squares method. Some of the data is beyond the range of the graph, but is included in the calculation. One can see that both B and A decrease with temperature.

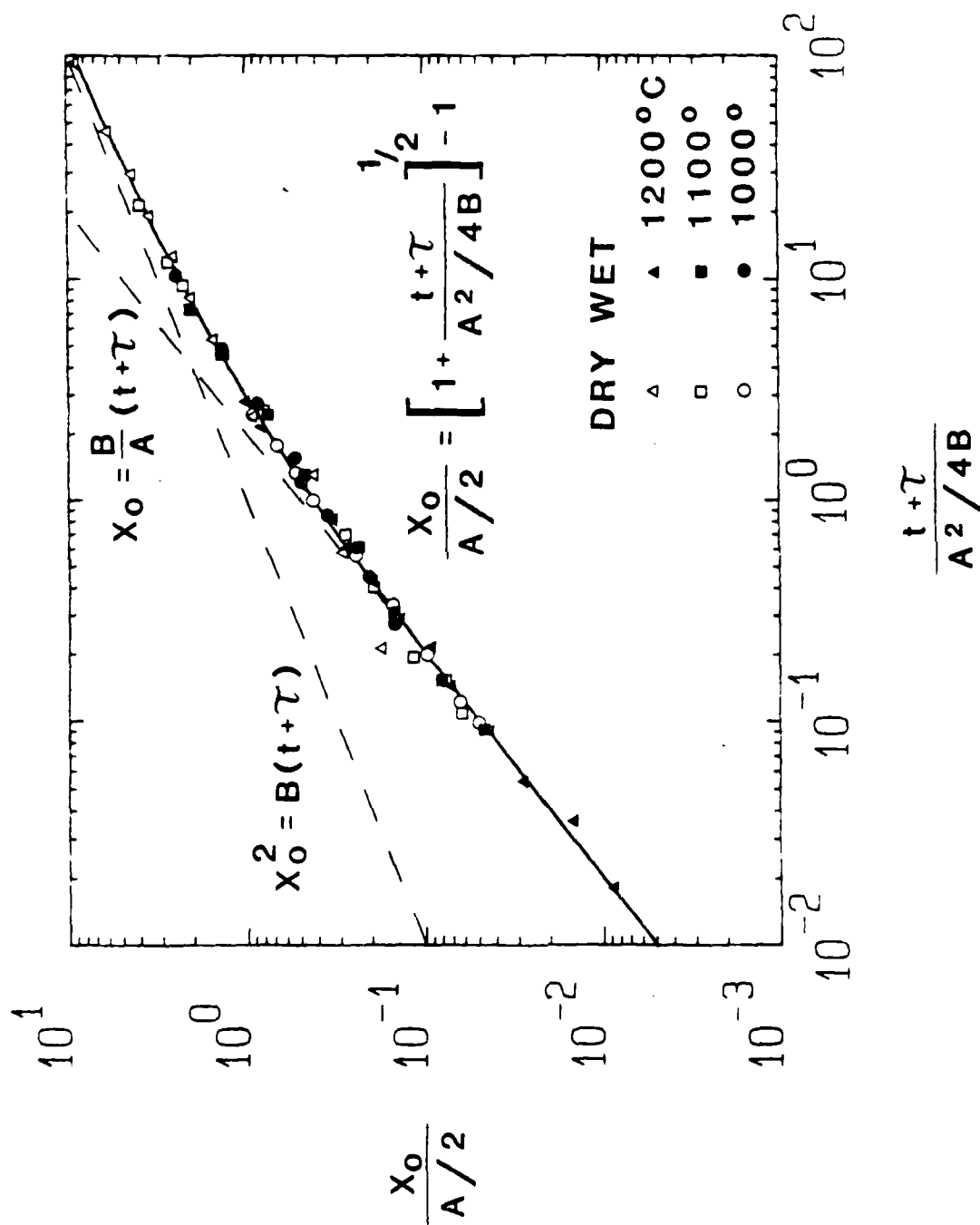
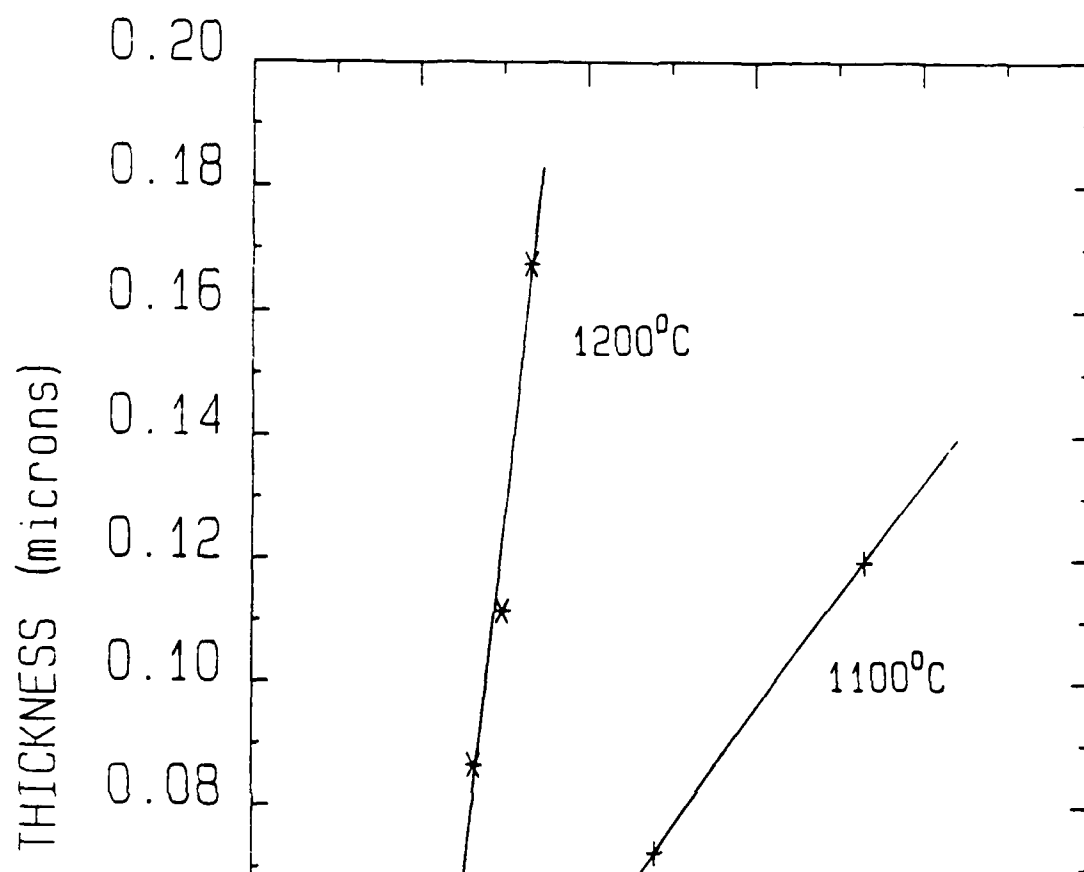


Figure 80. General relationship for thermal oxidation of β -SiC at 1273K, 1373K and 1473K. Solid line is the theoretical line as expressed in Eq. (3), the dotted lines are its two limiting forms.

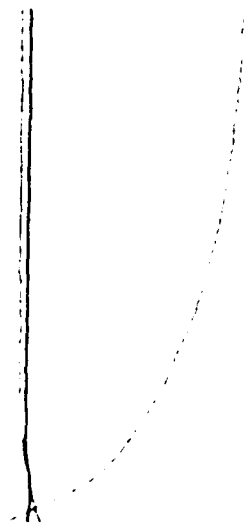


JRY11A

11/26/84

RAW DATA

0 H 20 Mn 55 S



Depth profile through a 1000Å thick
Si₃N₄ layer and into the p-SiC film.
Sample was grown at 1373K for 370 mins.

101

The constants B and B/A are plotted logarithmically against the reciprocal of the absolute temperature in Figure 76. Both constants exhibit exponential temperature dependencies. The activation energy for the linear rate constant B/A is 61 kcal/mol, which is reasonably close to the 69.3 kcal/mol required to break a Si-C bond. The parabolic rate constant is not as cooperative, exhibiting an activation energy of 119 kcal/mol. The parabolic rate constant should closely approximate the activation energy for the diffusion of H_2O in SiO_2 , which is 18.3 kcal/mol. However, Suzuki¹⁴ obtained a value for B of 48 kcal/mol for 6-H SiC and theorized that the out diffusion of the reaction by-product CO through the oxide was the controlling factor. There is still a large discrepancy between Suzuki's value and that reported here. The reason for this disagreement will be explained below.

In order to determine the rate constants for the dry oxidation data, the same method is followed. The data is placed on a linear graph, as shown in Figure 77. In this case, the curves for 1473K and 1373K extrapolate to a positive value of 0.118 hrs., or about 7 mins. For 1273K, the curve extrapolates to negative 0.147 hrs., or almost 9 mins. The negative of these values equal τ .

With these values, B and A are determined by plotting X_o vs $(t + \tau)/X_o$ as in the previous case. As can be seen in Figure 78, A (the $-y$ intercept) increases, while B (the slope) decreases, with decreasing temperature. The values were, again, determined by the least squares method.

In the plot of rate constant vs inverse of temperature in Figure 79, one can see that the activation energy of the linear rate constant B/A is 60 kcal/mol. This is almost identical to the value obtained in wet oxidation, indicating that the surface control mechanism is the same for the two oxidants. Again, this value is

yields of Si and C are about the same. In this case, however, the carbon ion yield drops off very quickly from the interface into the oxide. The carbon ion yield, at its lowest point, is now about three orders of magnitude lower than the silicon level, or around 2×10^{19} C atoms/cm³. Also, the amount of oxygen diffusion into the SiC appears to be much less, because the oxygen level seems to quickly level off to a background level. However this background level suggests that there is a fair amount of oxygen already present in the as-grown SiC. The depth of profiling into the SiC is much less in this case ($\approx 150\text{\AA}$ deep) than it was for the wet oxide sample because a lower intensity beam was used.

Because the CO content is so much higher in the wet oxide layer than in the dry oxide layer, it can be assumed that the H₂O is somehow blocking the out diffusion of CO. H₂O has a lower diffusivity in fused quartz than O₂ does, and only delivers half as much oxygen per molecule to the interface. The only reason wet oxidation is always faster, in the case of Si, is that the solubility of H₂O is much higher in SiO₂ than the solubility of O₂. In the case of SiC, a CO molecule is formed every time a Si atom reacts. Because there is so much H₂O allowed in the SiO₂ (3×10^{19} /cm³), it physically blocks more diffusion paths for the CO, and correspondingly, the CO blocks the same paths for the H₂O. Like an overcrowded freeway, this "piling up" of molecules slows the diffusion rate of both species, with the CO diffusion being the controlling parabolic factor with temperature, as proposed by Suzuki.

In dry oxidation, the amount of O₂ allowed in the SiO₂ is around 5×10^{16} /cm³, which is not enough to have any strong effect on the out diffusion of CO. This is confirmed by the SIMS analysis which shows much less "piling up" of CO in the oxide. Thus the controlling parabolic factor is the diffusion of O₂ through the oxide. This is supported by the fact that the activation energy of the dry parabolic rate constant is close to that of O₂ diffusion in fused quartz. Therefore, the reason that dry oxidation is actually faster than wet oxidation at 1273K is that, at that temperature, the diffusivities of H₂O and CO are lowered so much by the "piling up" effect, that dry oxidation, even with the lower oxidant solubility, is faster.

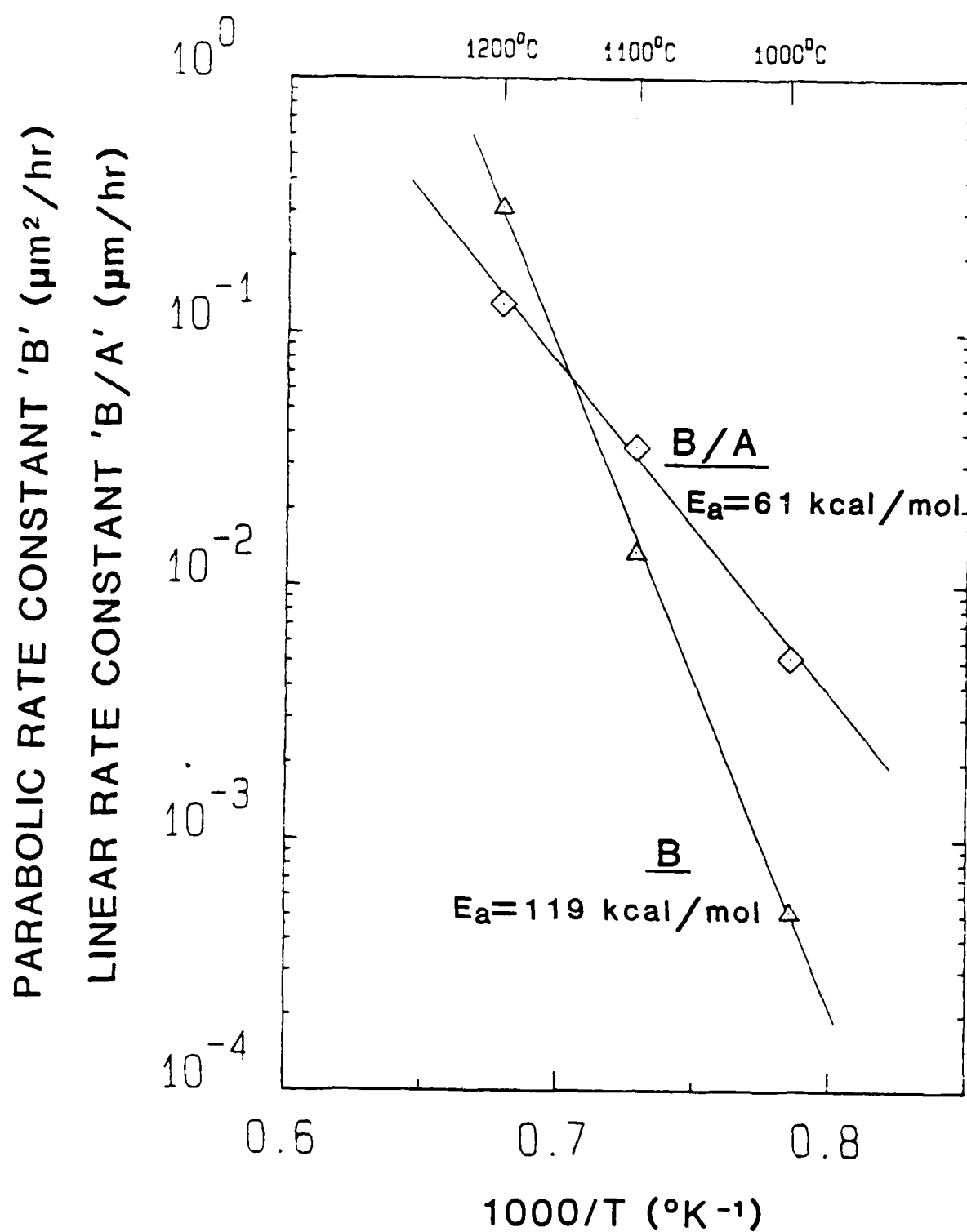
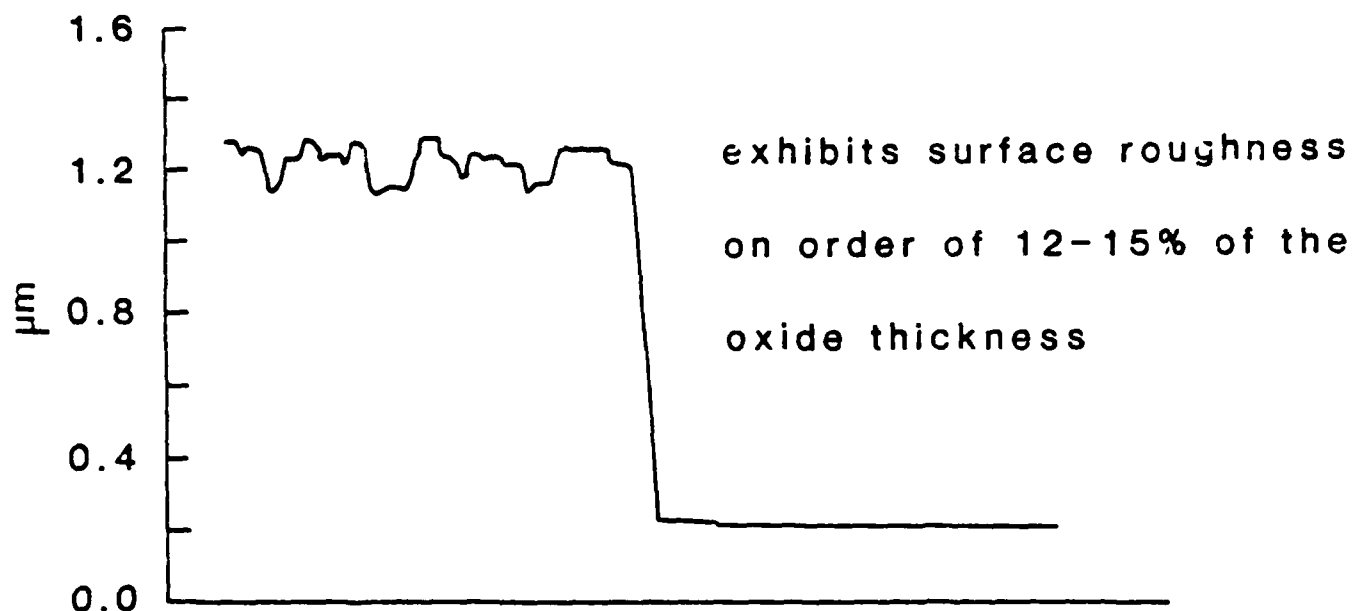


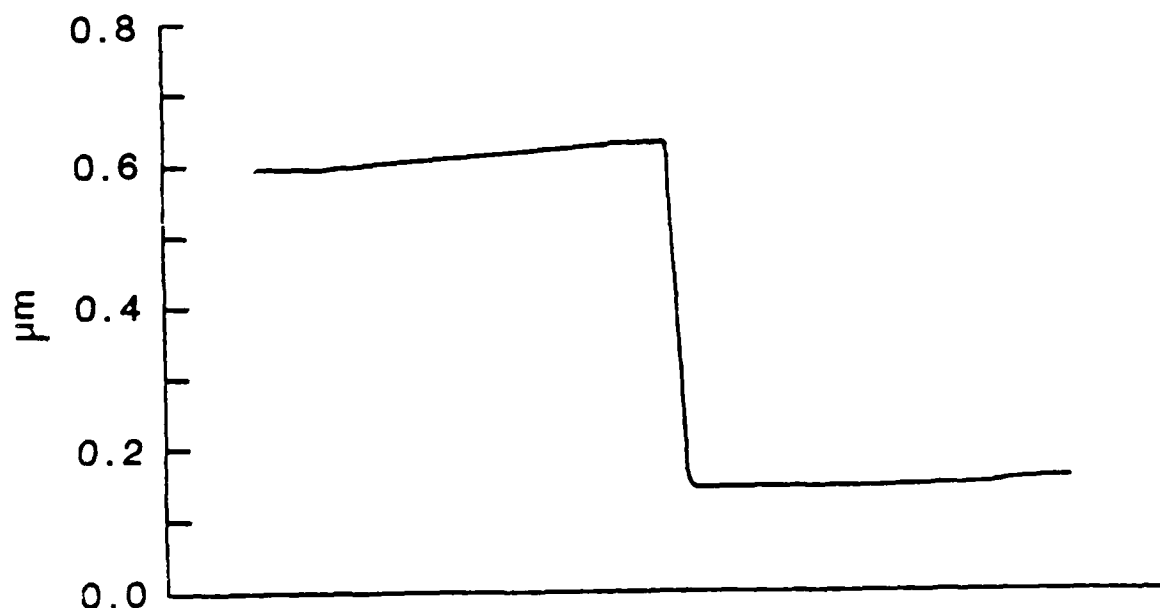
Figure 76. Temperature dependencies of the linear rate constant, B/A , and the parabolic rate constant, B , for wet oxidation of β -SiC.

Another interesting difference between wet and dry oxidation is the surface morphology. As stated earlier, in wet oxidation, profilometer measurements show that wet oxides typically show a large amount of surface roughness. A typical example is shown in Figure 83. The oxide produced using H_2O always exhibits a surface roughness that has peak to valley heights on the order of 12-15% of the oxide thickness. However, as shown in Figure 84, this roughness is not seen in dry oxidation. The dry oxides closely mimic the polished SiC surfaces on which they were grown. The cause of the roughness in wet oxidation is not known at this time, but one possibility is that, for some reason, partial crystallization occurs, and the roughness is caused by the presence of cristoballite crystals. This possibility will be checked by performing cross sectional TEM on the oxide layers, at which time the interface widths will also be determined.



1200°C-600 mins. (1 μm with 0.15 μm roughness)

Figure 83. Profilometer measurement of a wet oxide (left) step down to bare 8-SiC (right). Oxide grown at 1473K for 600 mins. (1 μm step with 0.15 μm oxide roughness).



1100°C-2550 mins. (0.485 μm)

Figure 84. Profilometer measurement of a dry oxide (left) step down to bare 8-SiC (right). Oxide grown at 1373K for 2550 mins. (0.485 μm step, no oxide roughness).

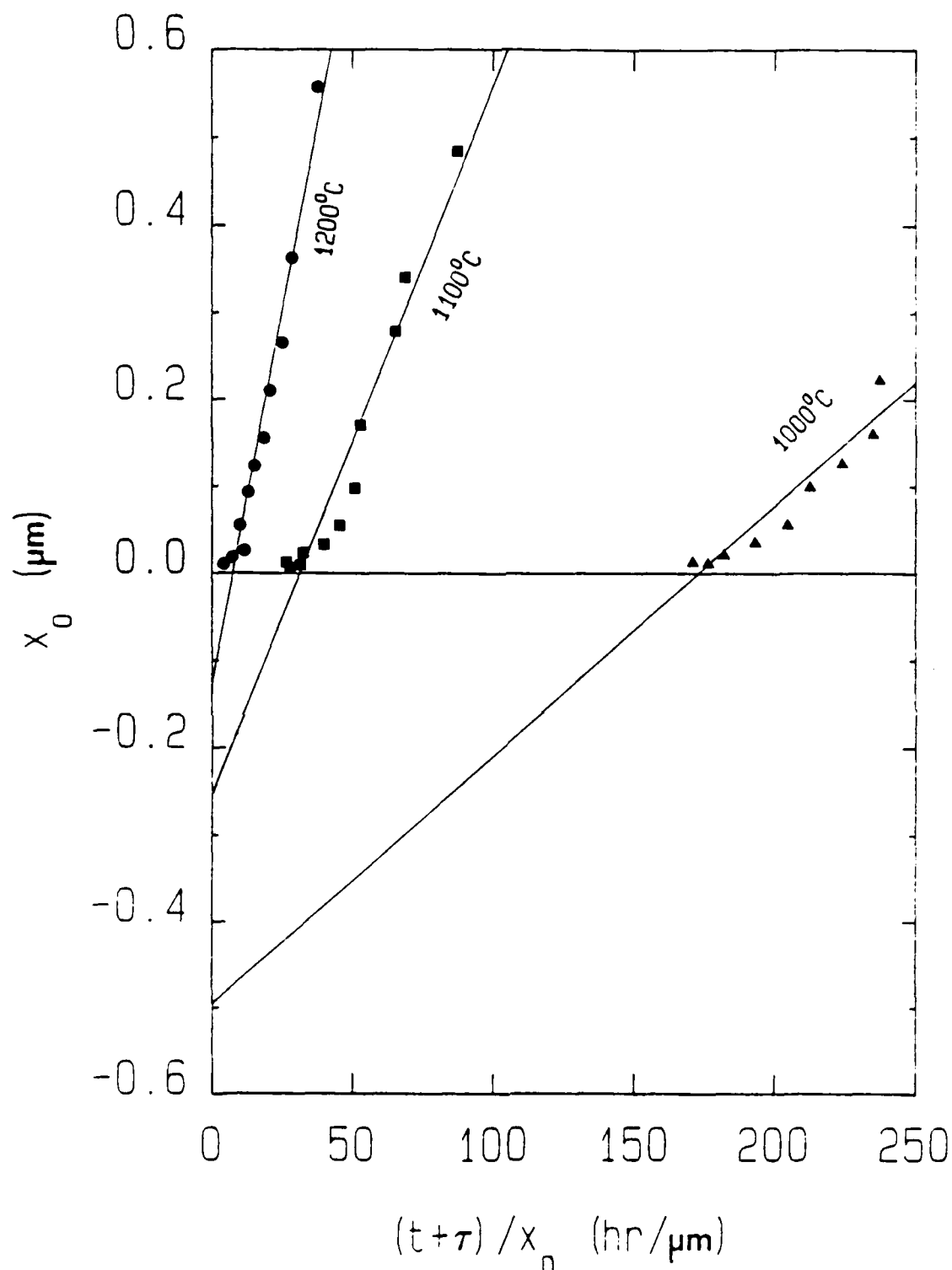


Figure 78. Evaluation of rate constants for oxidation of β -SiC in dry oxygen at 1273K, 1373K, and 1473K, using general relationship of Eq. (3).

X. PLASMA ETCHING STUDIES

Because of the need to perform surface removal and mesa etching, a method of etching SiC is needed. Because there is no suitable wet etchant for SiC, dry etching processes have been investigated. Sputter etching with Ar at 100 watts was found to give an etch rate of $33\text{\AA}/\text{min}$. While this yields a faster rate of removal than oxidation, it is undesirable because sputter etching involves physical damage, such as the formation of dislocations and amorphous regions. In silicon, damage has been found as deep as $500\text{--}750\text{\AA}$, from the sample surface¹⁵. This damage has negative effects on interface state densities, minority carrier generation times, breakdown voltages, barrier heights, and trapping levels.

To avoid this damage, plasma etching has been investigated. In this process, the sample was located on the ground electrode; thus, there was very little ion bombardment. The gas system used initially was $\text{CF}_4 + \text{O}_2$. The F etches Si via the formation of SiF_4 , while the O_2 reacts with the C in SiC, and the C in CF_4 , to form CO and CO_2 . This gas system was investigated by Matsui¹⁶ but employed for reactive ion-beam etching of SiC. This investigator found the optimum mixture to be at 40% O_2 .

The samples were masked with photoresist, and etched using a Technics Planar Etch II at 2 torr and 200 watts RF power. The resulting etch rates for varying O_2 mixing ratios have been very inconsistent. While there is a general increase in etch rate as % O_2 increases, it is impossible to derive a curve from the data. Even using the same mixing ratio, time, power, pressure, etc., it was impossible to obtain repeatedly the same rate. Etch rates in the range of $150\text{\AA}/\text{min}$ to $550\text{\AA}/\text{min}$ have been obtained.

These etch rates are significantly higher ($\sim 2\frac{1}{2}$ times higher) than those reported by Matsui et al.¹⁶ However, this could be caused by a difference in the power used. The cause for the non-reproducible results, at this time, is assumed to be poor flow control.

While the etch rates were desirably fast, all the samples had a dark surface layer present. The layer, approximately 1000\AA

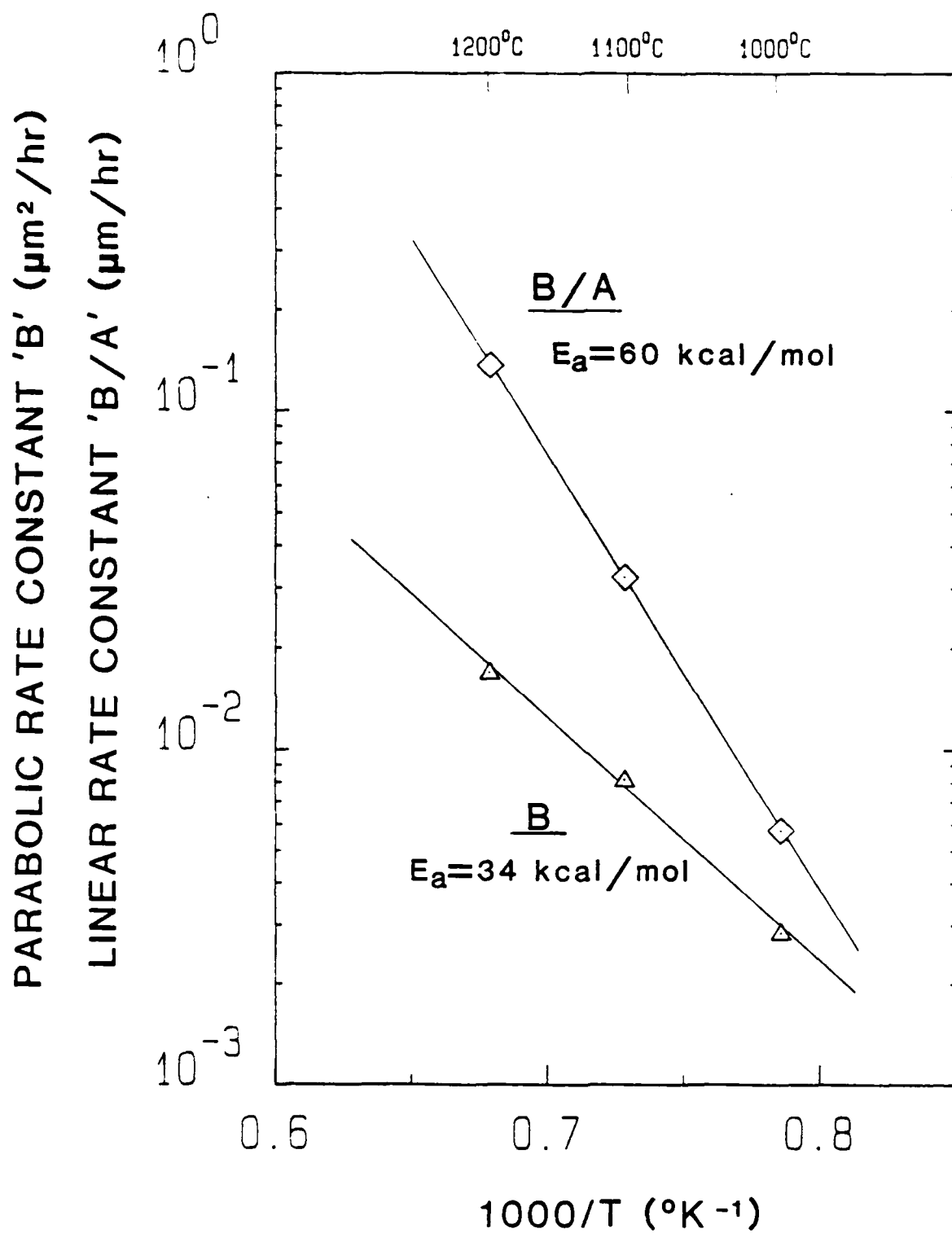


Figure 79. Temperature dependencies of the linear rate constant, B/A , and the parabolic rate constant, B , for dry oxidation of β -SiC.

thick after 20 minutes etching, was assumed, at first, to be C. However, the layer did not burn off at 1273K in air, nor did it etch away in hot nitric acid. After SIMS analysis, it was determined that the layer was actually redeposited SiC. There was virtually no difference between the bar graphs for unetched SiC (Figure 85) and the dark surface layer of etched SiC (Figure 86). It is assumed that the layer is amorphous or polycrystalline and is loosely bound to the single crystal SiC surface, because it scratches away easily. The redeposited layer can also be removed by (1) oxidizing for a sufficient time to consume 1000Å of SiC and (2) etching away the oxide layer leaving a bare, etched SiC surface. This type of layer was not reported by Matsui et al.¹⁶ However, it is assumed that this layer would not form in his process; since, reactive ion beam etching involves ion bombardment, which would splutter away any redeposited material. The thickness of the layer also increases as etch time increases, thus retarding the etch rate at longer times.

The "SiC" layer appears regardless of the power levels, although it is thinner at 50 watts than it is at 200 watts. However, the etch rate is also slower at 50 watts. It is possible that the redeposited layer could be avoided at lower pressures, because there would not be as many molecules to combine and redeposit. Etching at lower pressures has not been attempted at this point because it is very hard to control mixing ratios accurately below 2 torr with the flow meters on this system.

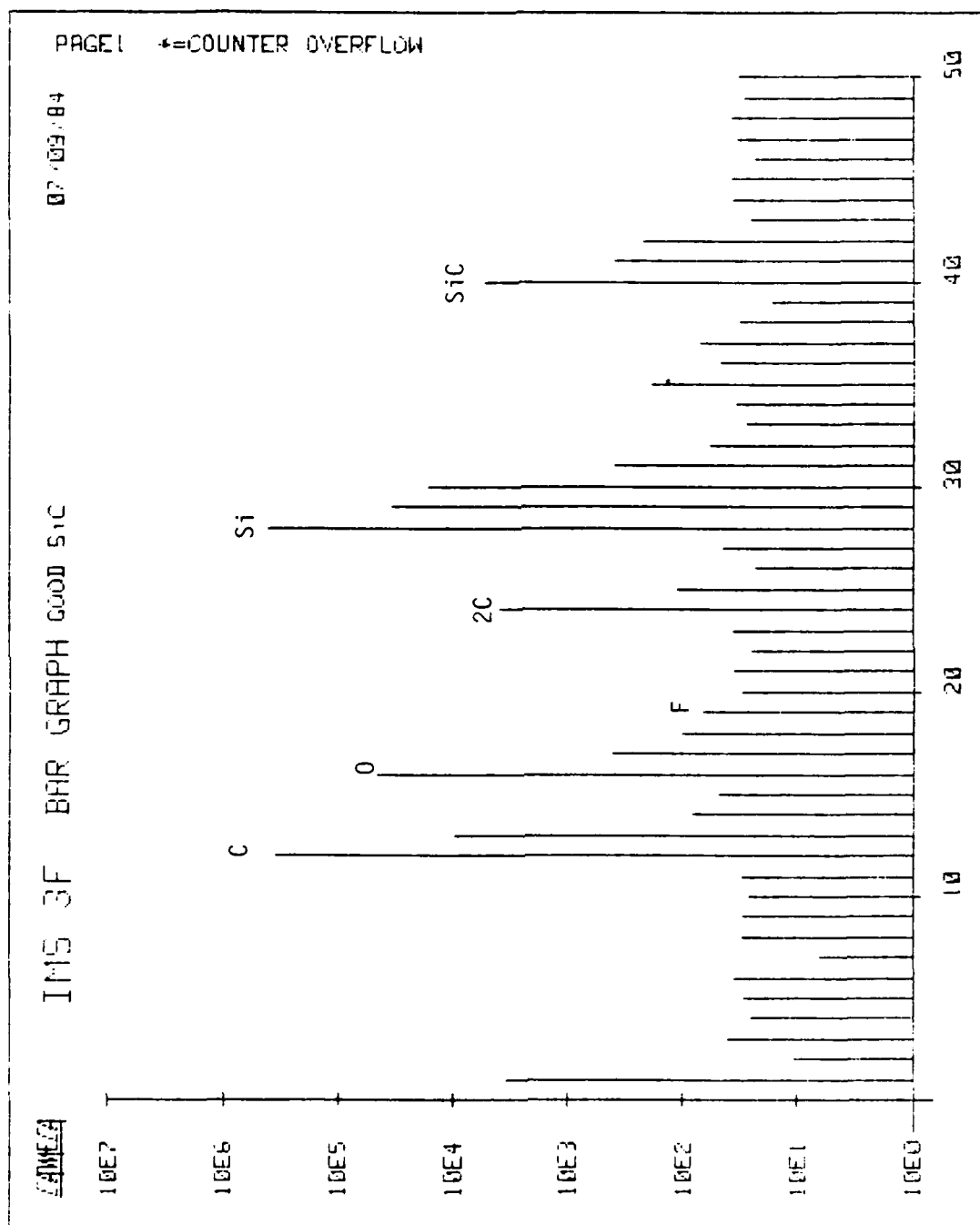


Figure 85. Bar graph resulting from SIMS chemical analysis (mass scan) showing count rate for the various elements or molecules having a mass/charge ratio shown on the abscissa for a nonplasma-etched intrinsic β -SiC single crystal thin film.

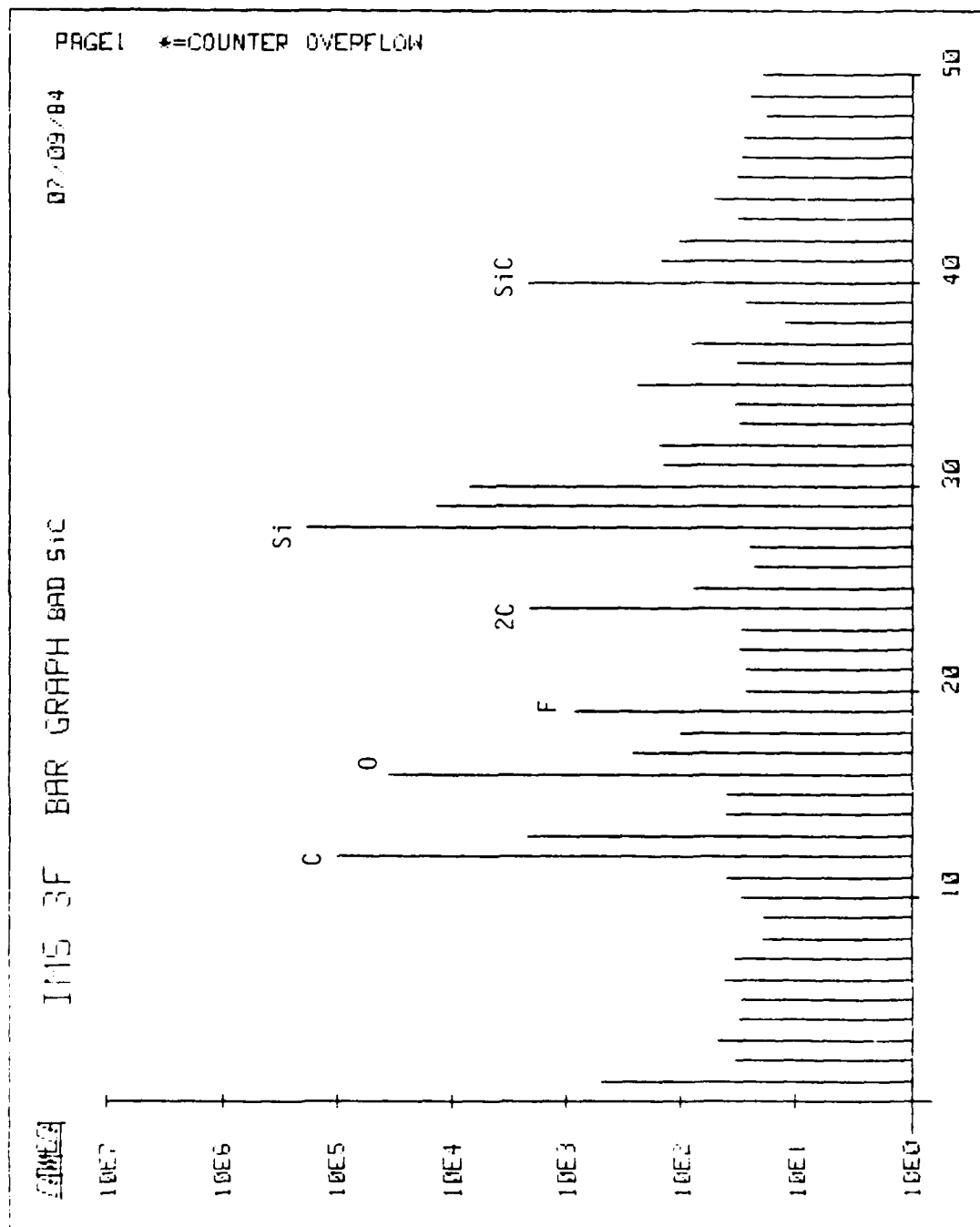


Figure 86. Bar graph resulting from SIMS chemical analysis (mass scan) showing count rate for the various elements or molecules having a mass/charge ratio shown on the abscissa for the surface layer produced by plasma etching of a β -SiC intrinsic single crystal thin film. Note similarity with Fig. 25.

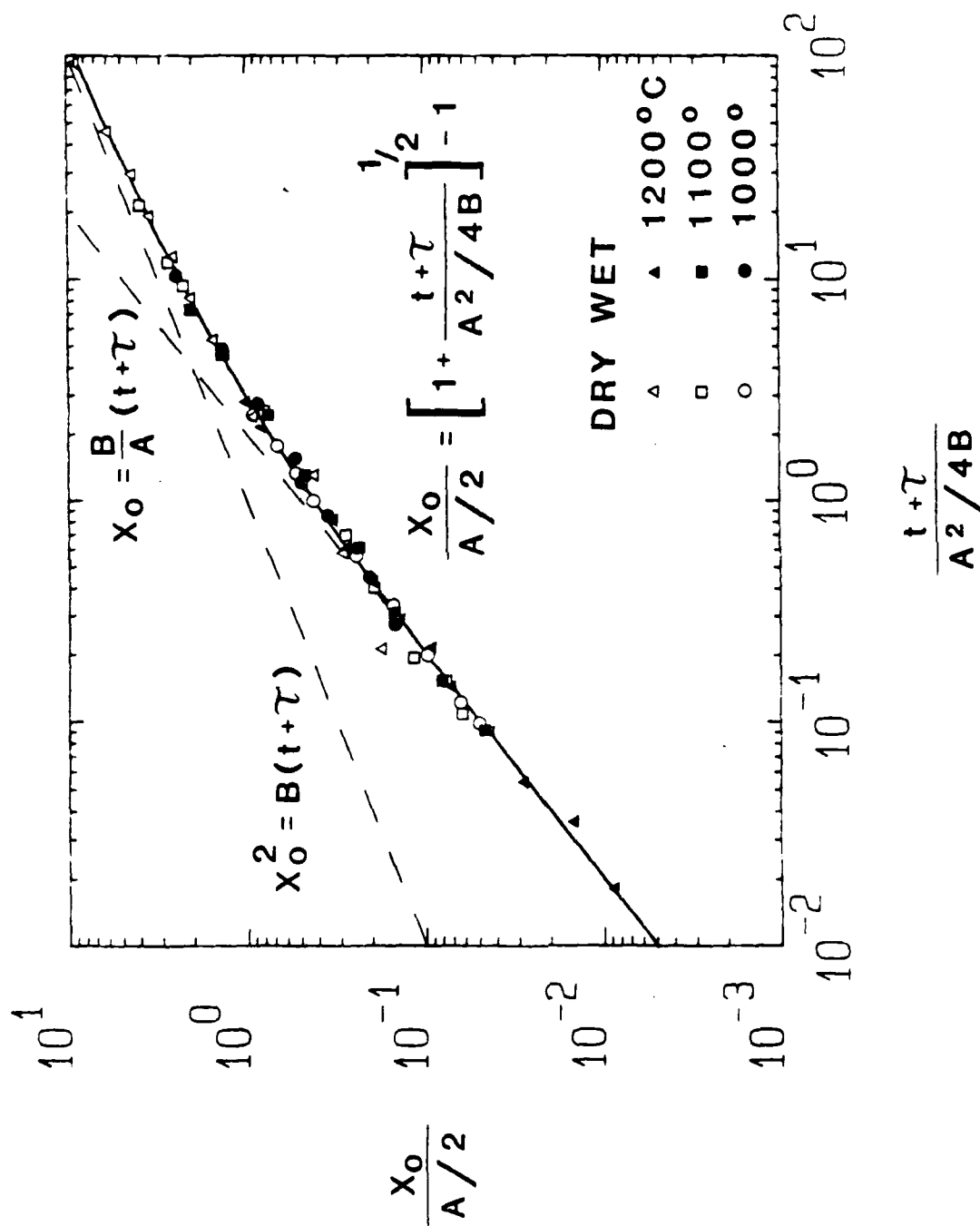


Figure 80. General relationship for thermal oxidation of β -SiC at 1273K, 1373K and 1473K. Solid line is the theoretical line as expressed in Eq. (3), the dotted lines are its two limiting forms.

XI. DEVICE FABRICATION

A. P-N Junction

A p-n junction has been fabricated during growth by the successive introduction of N and Al. The sample was removed from the CVD unit, oxidized to remove the high near surface concentration of dopant, etched in HF and re-introduced into the CVD unit for each successive doping. The 9.0 μm thick n^+ layer and the 2.0 μm thick n layer shown in Figure 87b were produced by doping with N derived from NH_3 . The 1.5 μm thick p-layer was doped with Al derived from trimethylaluminum.

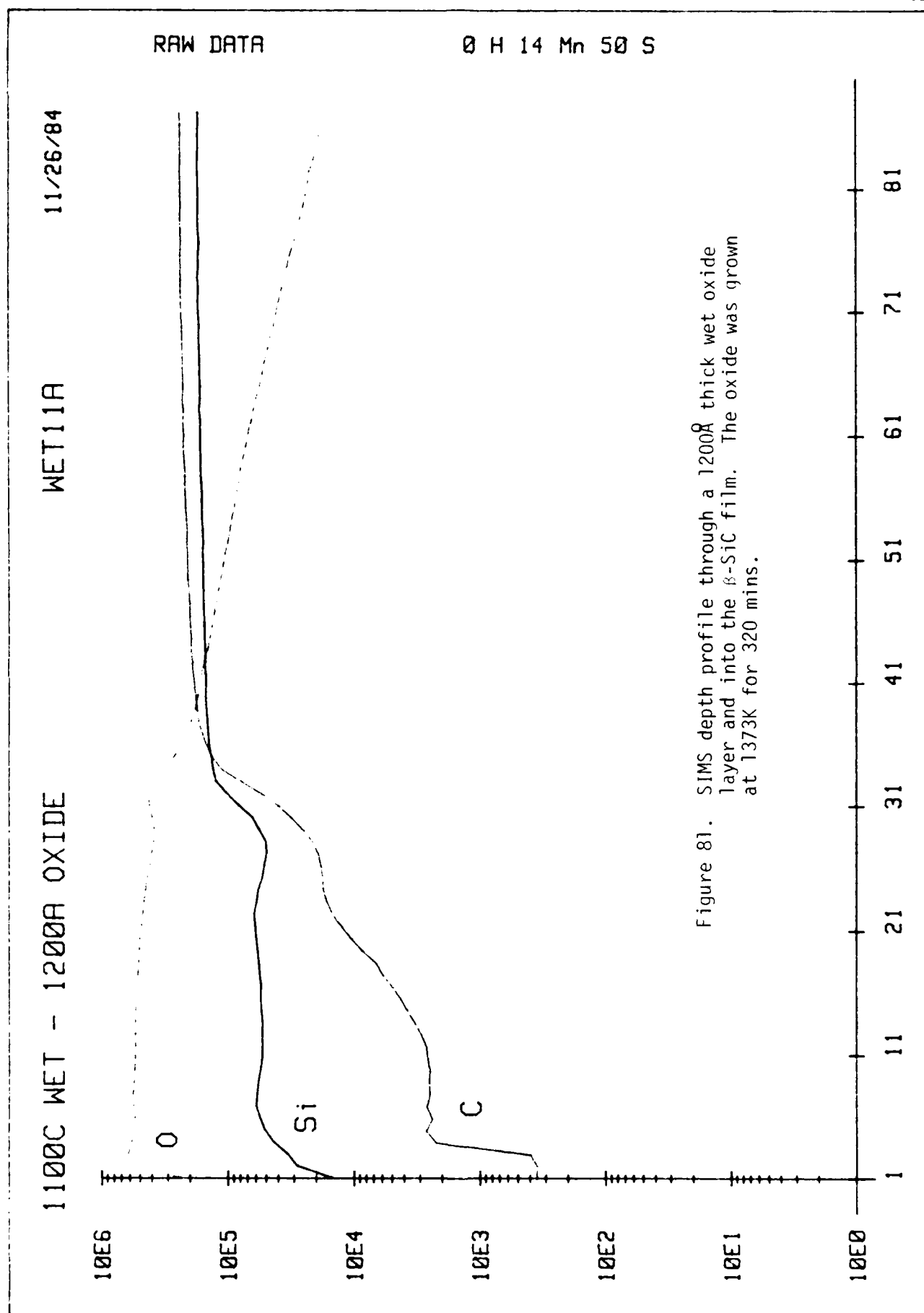
To eliminate any effects of surface disorder, the completed sample was oxidized via wet oxidation. This initial 0.6 μm thick oxide layer was then etched away using HF acid. Another 0.3 μm oxide layer was subsequently grown and a square window having a 400 μm edge was opened using photolithographic techniques.

A Au-Ta-Al alloy previously shown to produce an ohmic contact on p-type SiC was evaporated into the window. The Si substrate was removed using CP-4 solution, and a Au-Ta alloy previously shown to produce an ohmic contact on n-type SiC was evaporated onto the bottom of the N-doped layer.

The size of the square p-n junction is approximately 2 mm on a slide. The resulting current voltage curve for this junction is shown in Figure 87a. It reveals a fairly large leakage current, but it does possess a rectifying character. The reasons for the large leakage current are (1) the large contact area, (2) the lack of any passivation treatment and (3) the absence of a mesa shape.

The p-n junction depth profile was obtained using SIMS analysis, as shown in Figure 88. An Al concentration of $7 \times 10^{17}/\text{cm}^3$ is revealed to a distance 0.6 μm from the surface. The Al ion yield rises slightly at the p-n interface, probably as a result of oxide formation on the SiC during the transfer from the HF to the CVD chamber; this yield drops abruptly to $10^{15}/\text{cm}^3$ or background level.

At this p-n interface, the N concentration increases to $2 \times 10^{19}/\text{cm}^3$ in the n^+ layer.



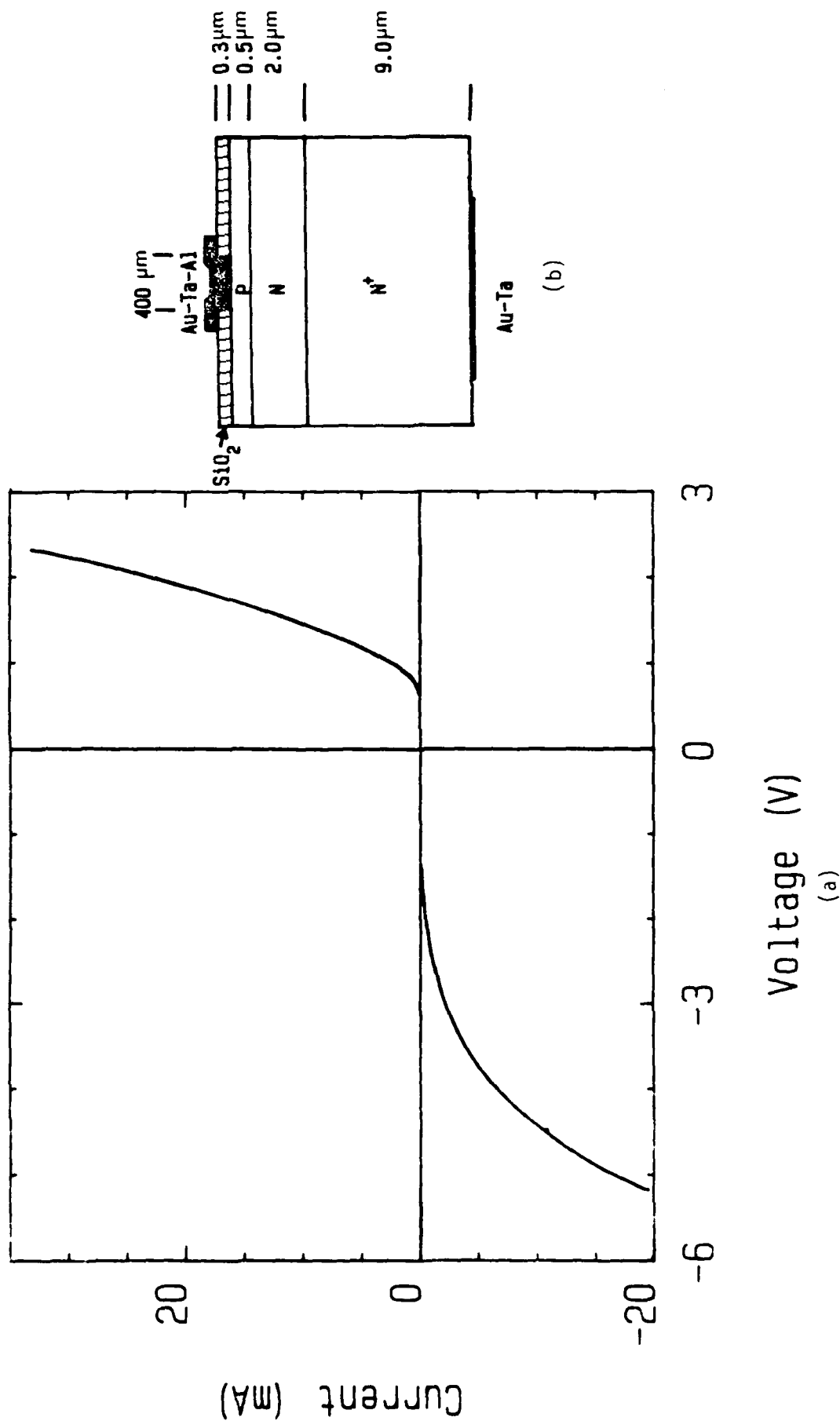


Figure 87. (a) The I-V characterization of the p-n junction diode which was fabricated by in situ doping of $\mu\text{-SiC}$ films with Al and N.

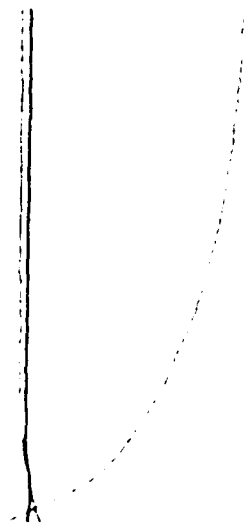
(b) The schematic diagram of p-n junction diode.

JRY11A

11/26/84

RAW DATA

0 H 20 Mn 55 S



Depth profile through a 1000Å thick
p-SiC film.
Sample was grown at 1373K for 370 mins.

101

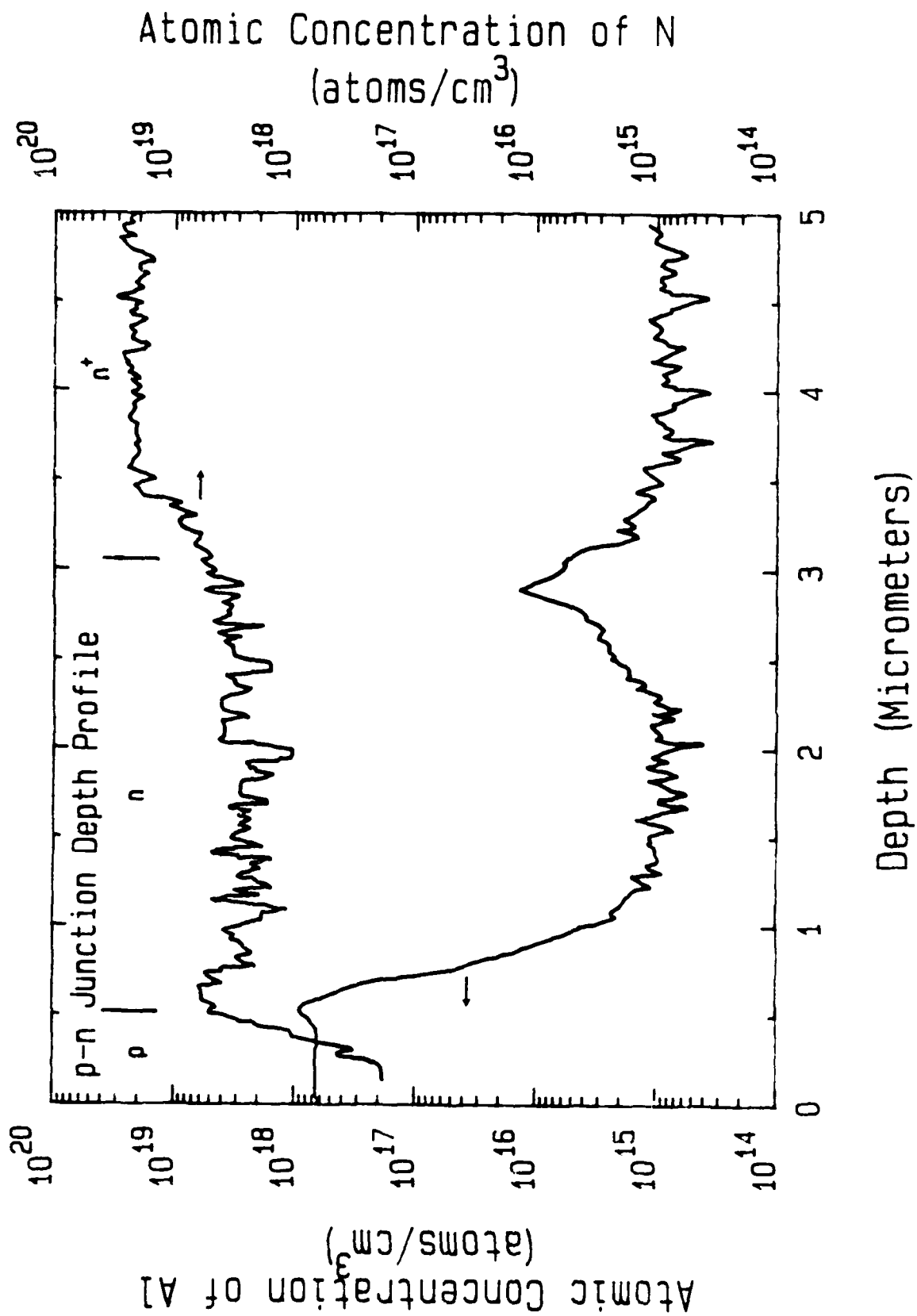


Figure 88. SIMS depth profile of p-n junction which was produced by in situ doping with Al and N.

yields of Si and C are about the same. In this case, however, the carbon ion yield drops off very quickly from the interface into the oxide. The carbon ion yield, at its lowest point, is now about three orders of magnitude lower than the silicon level, or around 2×10^{19} C atoms/cm³. Also, the amount of oxygen diffusion into

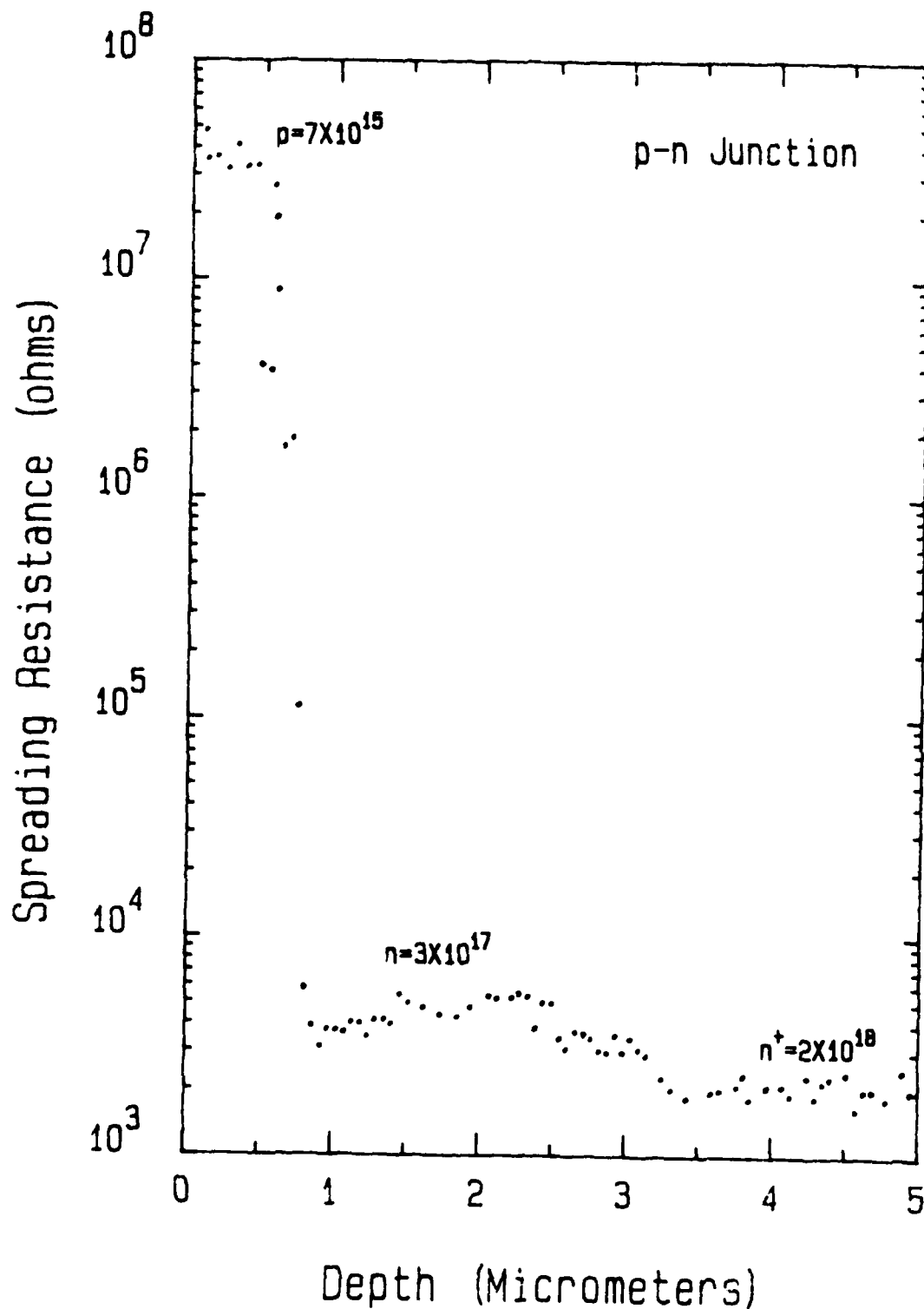


Figure 89. Spreading resistance profile vs depth of p-n junction diode which was doped during growth.

***** GRAPHICS PLOT *****
1028 1

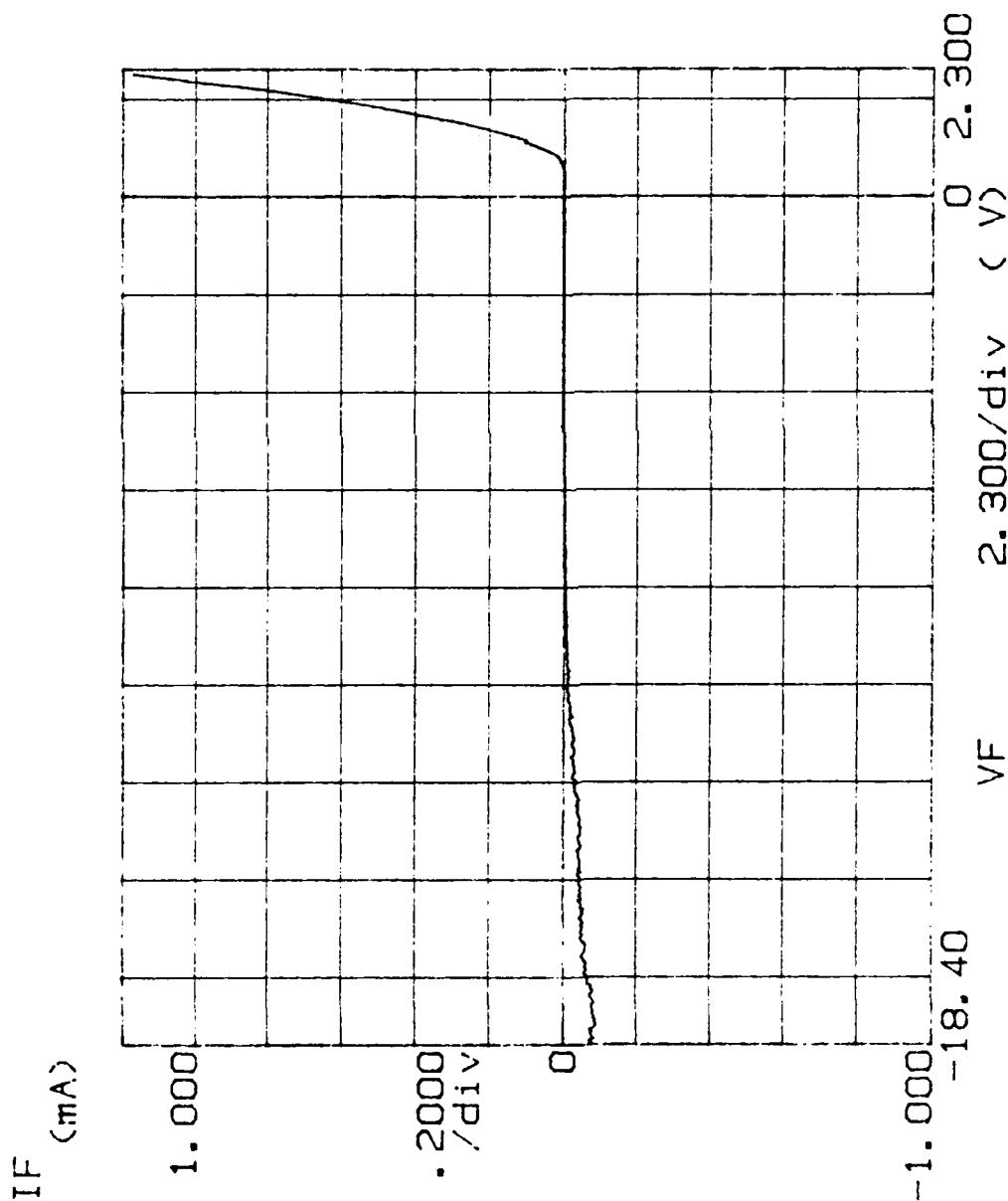
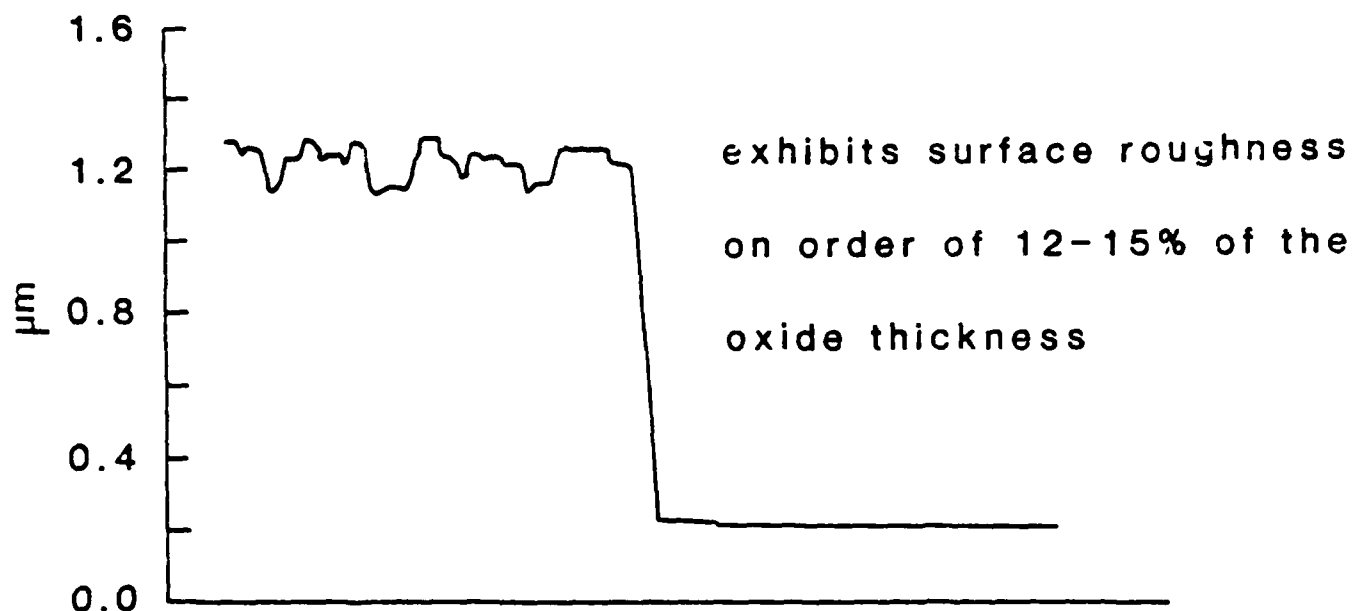
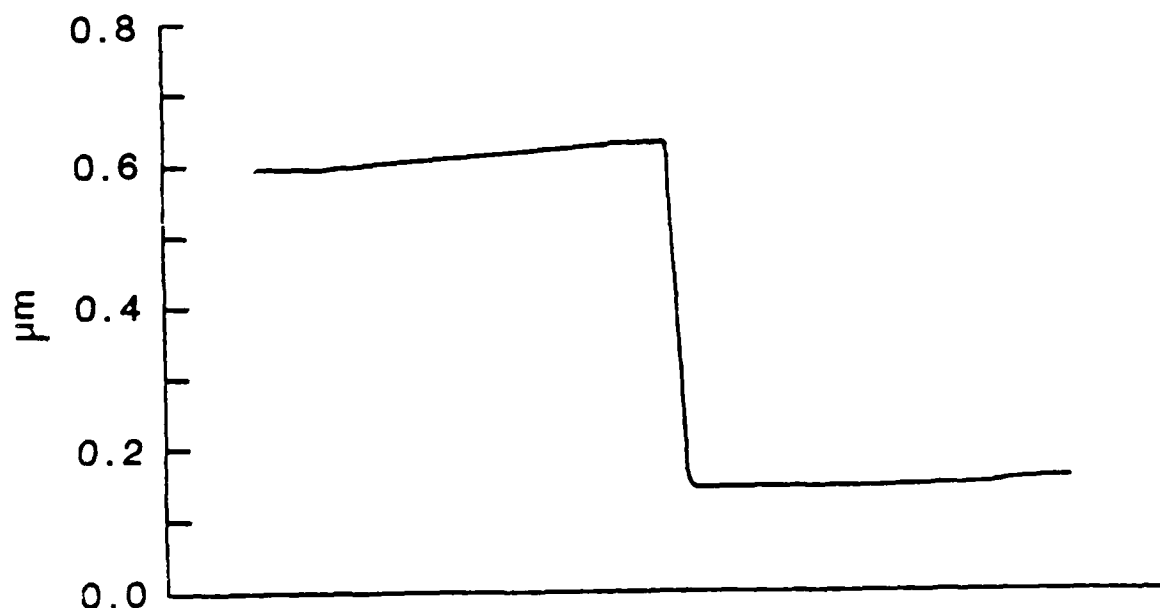


Figure 90. I-V characteristics of a Au- β -SiC Schottky diode. A Ta-Si alloy was used to make the ohmic contact. The area of the junction was $7.9 \times 10^{-5} \text{ cm}^2$.



1200°C-600 mins. (1 μm with 0.15 μm roughness)

Figure 83. Profilometer measurement of a wet oxide (left) step down to bare 8-SiC (right). Oxide grown at 1473K for 600 mins. (1 μm step with 0.15 μm oxide roughness).



1100°C-2550 mins. (0.485 μm)

Figure 84. Profilometer measurement of a dry oxide (left) step down to bare 8-SiC (right). Oxide grown at 1373K for 2550 mins. (0.485 μm step, no oxide roughness).

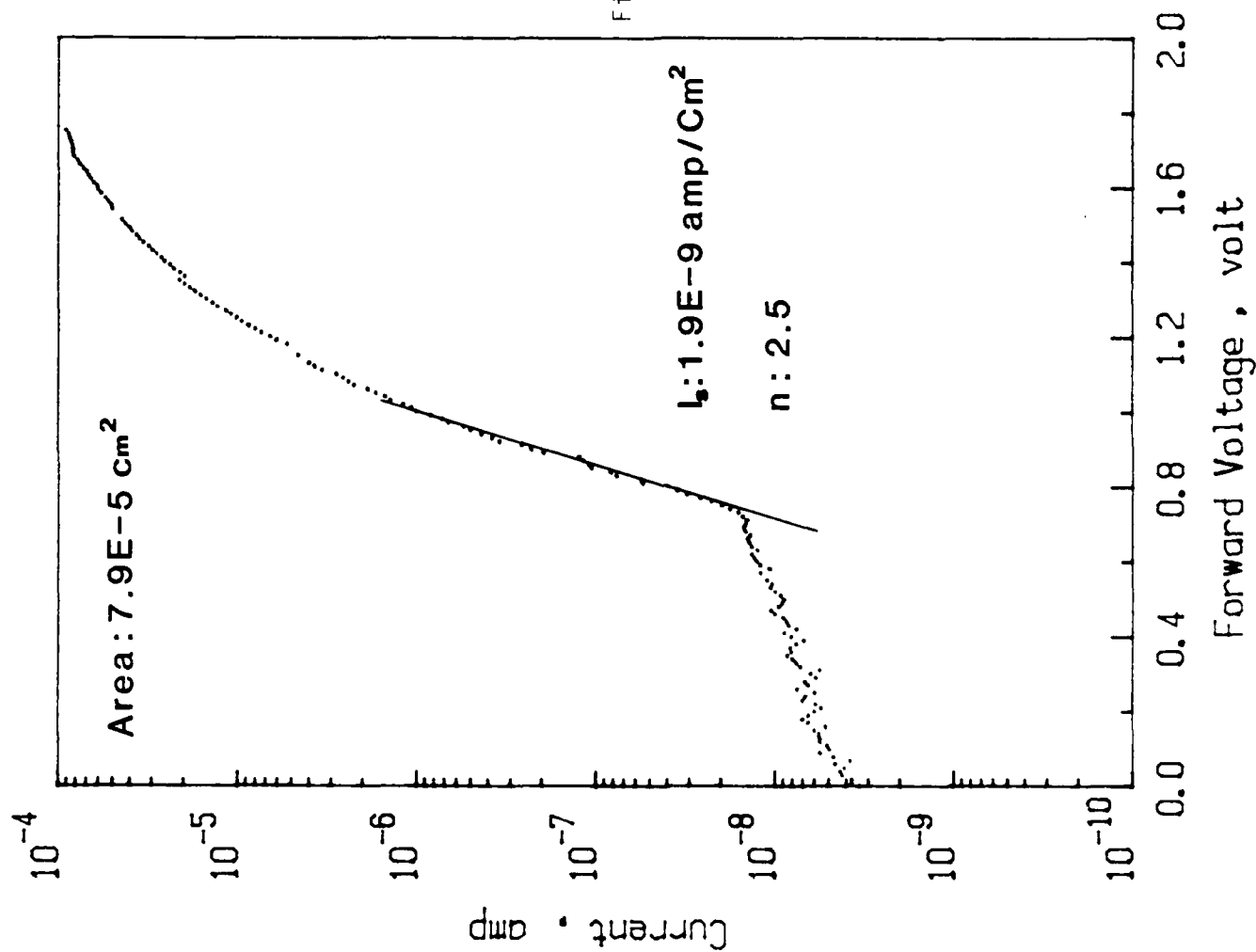


Figure 91.

The log current vs forward bias voltage relationship of a Au-p-SiC diode. The diode constant, n , is 2.5 and saturation current, I_{s2} , is $1.9 \times 10^{-9} \text{ am/cm}^2$.

X. PLASMA ETCHING STUDIES

Because of the need to perform surface removal and mesa etching, a method of etching SiC is needed. Because there is no suitable wet etchant for SiC, dry etching processes have been investigated. Sputter etching with Ar at 100 watts was found to give an etch rate of $33\text{\AA}/\text{min}$. While this yields a faster rate of removal than oxidation, it is undesirable because sputter etching involves physical damage, such as the formation of dislocations and amorphous regions. In silicon, damage has been found as deep as $500\text{--}750\text{\AA}$, from the sample surface¹⁵. This damage has negative effects on interface state densities, minority carrier generation times, breakdown voltages, barrier heights, and trapping levels.

To avoid this damage, plasma etching has been investigated. In this process, the sample was located on the ground electrode; thus, there was very little ion bombardment. The gas system used initially was $\text{CF}_4 + \text{O}_2$. The F etches Si via the formation of SiF_4 , while the O_2 reacts with the C in SiC, and the C in CF_4 , to form CO and CO_2 . This gas system was investigated by Matsui¹⁶ but employed for reactive ion-beam etching of SiC. This investigator found the optimum mixture to be at 40% O_2 .

The samples were masked with photoresist, and etched using a Technics Planar Etch II at 2 torr and 200 watts RF power. The resulting etch rates for varying O_2 mixing ratios have been very inconsistent. While there is a general increase in etch rate as % O_2 increases, it is impossible to derive a curve from the data. Even using the same mixing ratio, time, power, pressure, etc., it was impossible to obtain repeatedly the same rate. Etch rates in the range of $150\text{\AA}/\text{min}$ to $550\text{\AA}/\text{min}$ have been obtained.

These etch rates are significantly higher ($\sim 2\frac{1}{2}$ times higher) than those reported by Matsui et al.¹⁶ However, this could be caused by a difference in the power used. The cause for the non-reproducible results, at this time, is assumed to be poor flow control.

While the etch rates were desirably fast, all the samples had a dark surface layer present. The layer, approximately 1000\AA

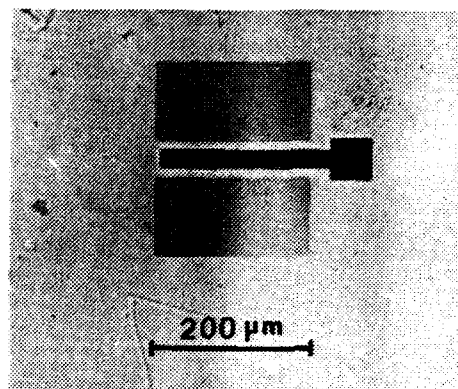
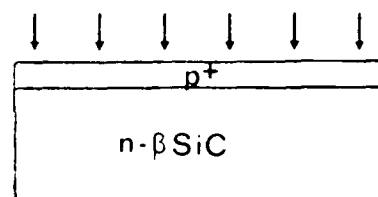


Figure 92. Fifty micron channel length mask for FET fabrication.

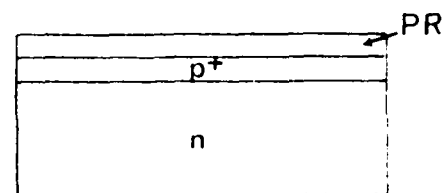
thick after 20 minutes etching, was assumed, at first, to be C. However, the layer did not burn off at 1273K in air, nor did it etch away in hot nitric acid. After SIMS analysis, it was determined that the layer was actually redeposited SiC. There was virtually no difference between the bar graphs for unetched SiC (Figure 85) and the dark surface layer of etched SiC (Figure 86). It is assumed that the layer is amorphous or polycrystalline and is loosely bound to the single crystal SiC surface, because it scratches away easily. The redeposited layer can also be removed by (1) oxidizing for a sufficient time to consume 1000Å of SiC and (2) etching away the oxide layer leaving a bare, etched SiC surface. This type of layer was not reported by Matsui et al.¹⁶ However, it is assumed that this layer would not form in his process; since, reactive ion beam etching involves ion bombardment, which would splutter away any redeposited material. The thickness of the layer also increases as etch time increases, thus retarding the etch rate at longer times.

The "SiC" layer appears regardless of the power levels, although it is thinner at 50 watts than it is at 200 watts. However, the etch rate is also slower at 50 watts. It is possible that the redeposited layer could be avoided at lower pressures, because there would not be as many molecules to combine and redeposit. Etching at lower pressures has not been attempted at this point because it is very hard to control mixing ratios accurately below 2 torr with the flow meters on this system.

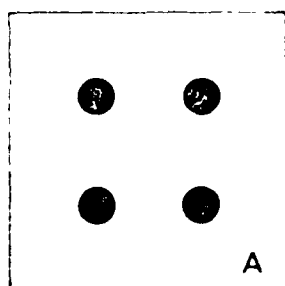
1. Implant p^+ layer in intrinsic substrate



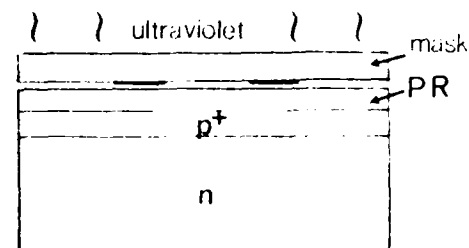
2. Apply layer of positive photoresist (PR)



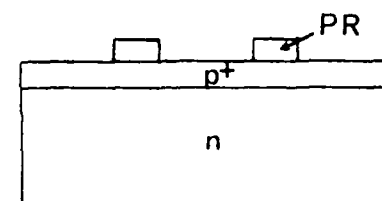
3. Expose PR through mask A



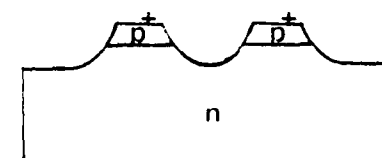
brightfield



4. Remove exposed PR

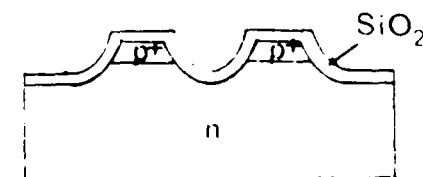


5. Plasma etch to form mesa structure; remove remaining PR

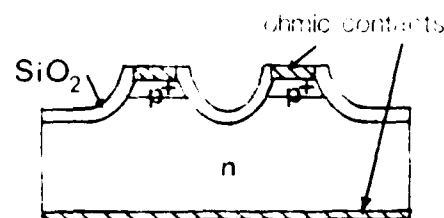


6. Anneal implant - 1800 °C in Ar

7. 1200 °C oxidation



8. Using PR and darkfield version of mask A, repeat steps 2-4; remove remaining PR



9. Apply ohmic contacts

Figure 93. Step wise procedure for the fabrication of a p^+ - n mesa structure diode.

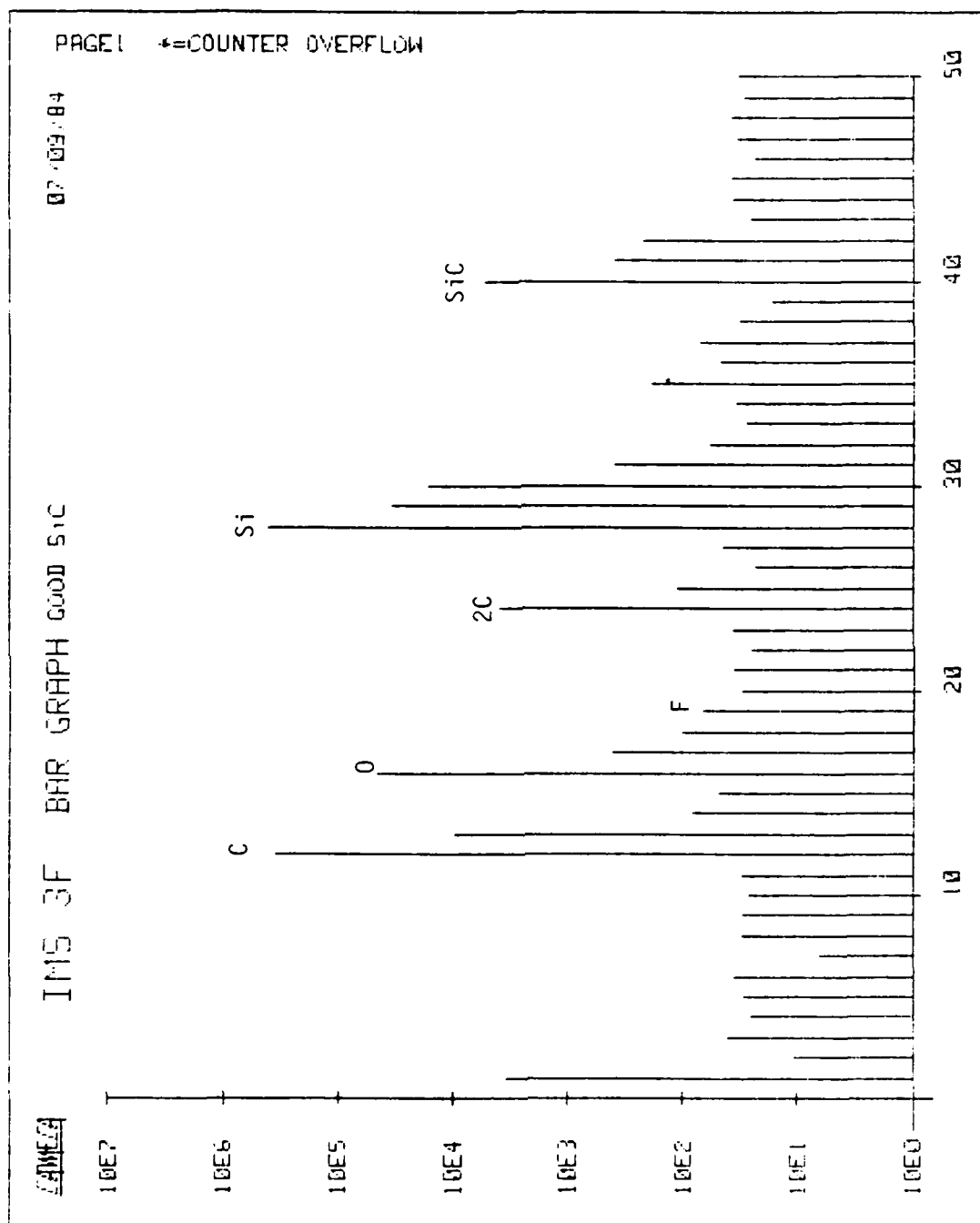


Figure 85. Bar graph resulting from SIMS chemical analysis (mass scan) showing count rate for the various elements or molecules having a mass/charge ratio shown on the abscissa for a nonplasma-etched intrinsic β -SiC single crystal thin film.

XII. REFERENCES

1. A. I. Kingon, L. J. Lutz, P. Liaw and R. F. Davis, J. Amer. Ceram. Soc. 66, 558 (1983).
2. R. W. Bartlett and R. A. Mueller, Mat. Res. Bull. 4, S341 (1969).
3. N. N. Long, D. S. Nedzvetskii, N. K. Prokofeva and M. B. Reifman, Opt. Spektosk, 29, 388 (1970).
4. S. Nishino, H. Suhara and H. Matsunami, in Extended Abstracts of the 15th Conference on Solid State Devices and Materials, Tokyo, 1983, pp. 317-320.
5. W. von Muench and E. Pettenpaul, J. Electrochem. Soc. 125, 294 (1978).
6. W. H. Sheperd, J. Electrochem. Soc. 115, 541 (1968).
7. H. Reiss, J. Chem. Phys. 21, 1209 (1953).
8. P. Rai-Choudry and E. I. Salkovitz, J. Cryst. Growth 7, 353 (1970).
9. D. R. Stull and H. Prophet, JANAF Thermochemical Tables, Second edition, NSRDS-NBS 37, National Bureau of Standards, USA (1971).
10. J. Bloem, J. Electrochem. Soc. 117, 1397 (1970).
11. D. Olego and M. Cardona, Phys. Rev. B. 25, 3878 (1982).
12. N. I. Rabin and V. I. Kasatochkin, Neorgaincheskie Materialy 14, 1545 (1978).
13. O. J. Marsh in "Silicon Carbide, 1973", R. Marshall, C. Ryan and J. Faust, eds., U. of South Carolina Press, Columbia, S. C. (1974), p. 471.
14. A. Suzuki, Jap. Jour. Appl. Phys. 21, 579 (1982).
15. S. W. Pang, "Dry Etching Induced Damage in Si and GaAs," Solid State Tech. 27, 249 (April 1984).
16. S. Matsui, et al., "Reactive Ion-Beam Etching of Silicon Carbide," Jap. J. of Appl. Phys., Vol. 20, No. 1, January 1981, pp. L38-L40.
17. D. L. Barrett and R. B. Campbell, J. Appl. Phys. 38, 53 (1967).

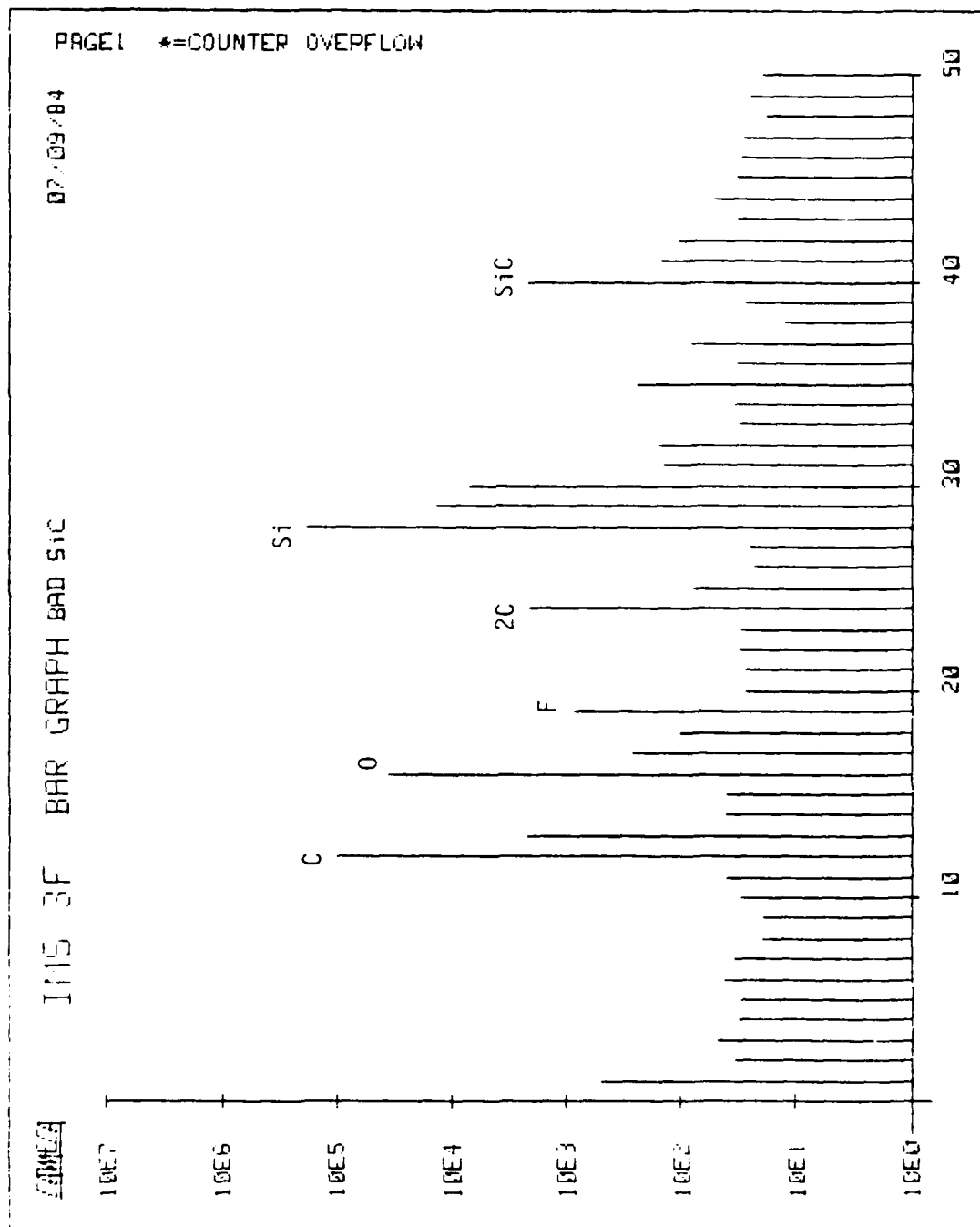


Figure 86. Bar graph resulting from SIMS chemical analysis (mass scan) showing count rate for the various elements or molecules having a mass/charge ratio shown on the abscissa for the surface layer produced by plasma etching of a β -SiC intrinsic single crystal thin film. Note similarity with Fig. 25.

XI. DEVICE FABRICATION

A. P-N Junction

A p-n junction has been fabricated during growth by the successive introduction of N and Al. The sample was removed from the CVD unit, oxidized to remove the high near surface concentration of dopant, etched in HF and re-introduced into the CVD unit for each successive doping. The 9.0 μm thick n^+ layer and the 2.0 μm thick n layer shown in Figure 87b were produced by doping with N derived from NH_3 . The 1.5 μm thick p-layer was doped with Al derived from trimethylaluminum.

To eliminate any effects of surface disorder, the completed sample was oxidized via wet oxidation. This initial 0.6 μm thick oxide layer was then etched away using HF acid. Another 0.3 μm oxide layer was subsequently grown and a square window having a 400 μm edge was opened using photolithographic techniques.

A Au-Ta-Al alloy previously shown to produce an ohmic contact on p-type SiC was evaporated into the window. The Si substrate was removed using CP-4 solution, and a Au-Ta alloy previously shown to produce an ohmic contact on n-type SiC was evaporated onto the bottom of the N-doped layer.

The size of the square p-n junction is approximately 2 mm on a slide. The resulting current voltage curve for this junction is shown in Figure 87a. It reveals a fairly large leakage current, but it does possess a rectifying character. The reasons for the large leakage current are (1) the large contact area, (2) the lack of any passivation treatment and (3) the absence of a mesa shape.

The p-n junction depth profile was obtained using SIMS analysis, as shown in Figure 88. An Al concentration of $7 \times 10^{17}/\text{cm}^3$ is revealed to a distance 0.6 μm from the surface. The Al ion yield rises slightly at the p-n interface, probably as a result of oxide formation on the SiC during the transfer from the HF to the CVD chamber; this yield drops abruptly to $10^{15}/\text{cm}^3$ or background level.

At this p-n interface, the N concentration increases to $2 \times 10^{19}/\text{cm}^3$ in the n^+ layer.

APPENDIX II

List of all Reports for the Period February 1, 1982 - January 31, 1985

<u>Type of Report</u>	<u>Period Covered by Report</u>	<u>Date Issued</u>
A. Annual Letter Report	2/1/82 - 8/31/82	8/31/82
B. Annual Letter Report	9/1/82 - 3/31/83	3/31/83
C. Annual Technical Report	9/1/82 - 8/31/83	8/31/83
D. Annual Letter Report	9/1/83 - 3/31/84	3/31/84
E. Annual Technical Report	9/1/83 - 8/31/84	8/31/84
F. Final Technical Report	2/1/82 - 1/31/85	1/31/85

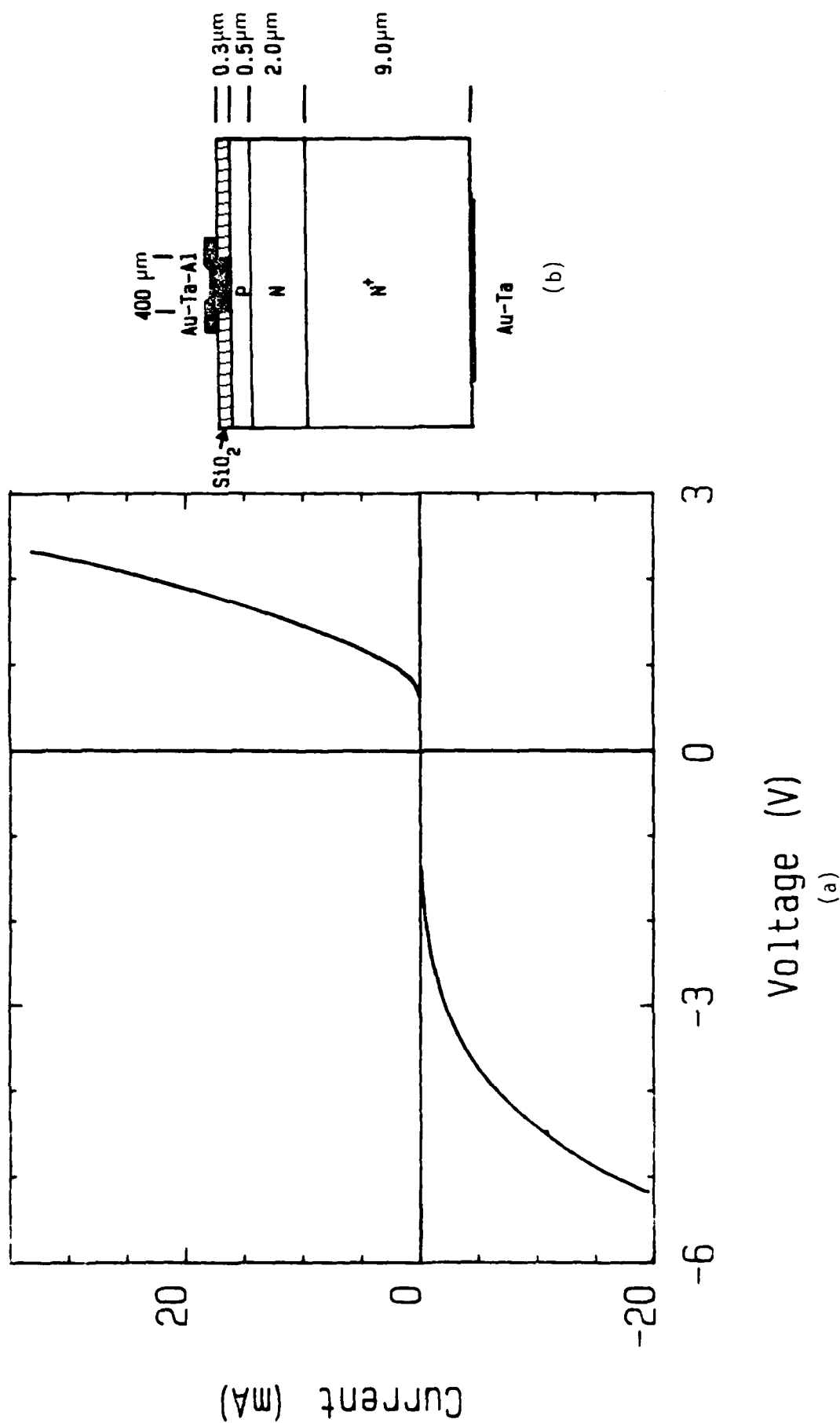


Figure 87. (a) The I-V characterization of the p-n junction diode which was fabricated by in situ doping of $\mu\text{-SiC}$ films with Al and N.

(b) The schematic diagram of p-n junction diode.

APPENDIX III

DISTRIBUTION LIST - FINAL TECHNICAL REPORT

CONTRACT N00014-82-K-0182

<u>Address</u>	<u>No. of Copies</u>
Dr . Max Yoder Office of Naval Research Electronics Program - Code 414 800 North Quincy Street Arlington, VA 22217	2
Ms. Nancy S. McHan ONR Resident Representative Georgia Institute of Technology 214 O'Keefe Building Atlanta, GA 30332	2
Director, Naval Research Laboratory ATTN: Code 2627 Washington, DC 20375	7
Defense Technial Information Center Bldg. 5 Cameron Station Alexandria, Virginia 22314	14
ONR Branch Office 536 South Clark Street Room 286 Chicago, IL 60605	2
Dr. J. Anthony Powell NASA Lewis 2100 Brookpark Rd. Cleveland, OH 44135	1
Dr. Ray Kaplan Code 6834 Department of the Navy Naval Research Laboratory Washington, DC 20375	1

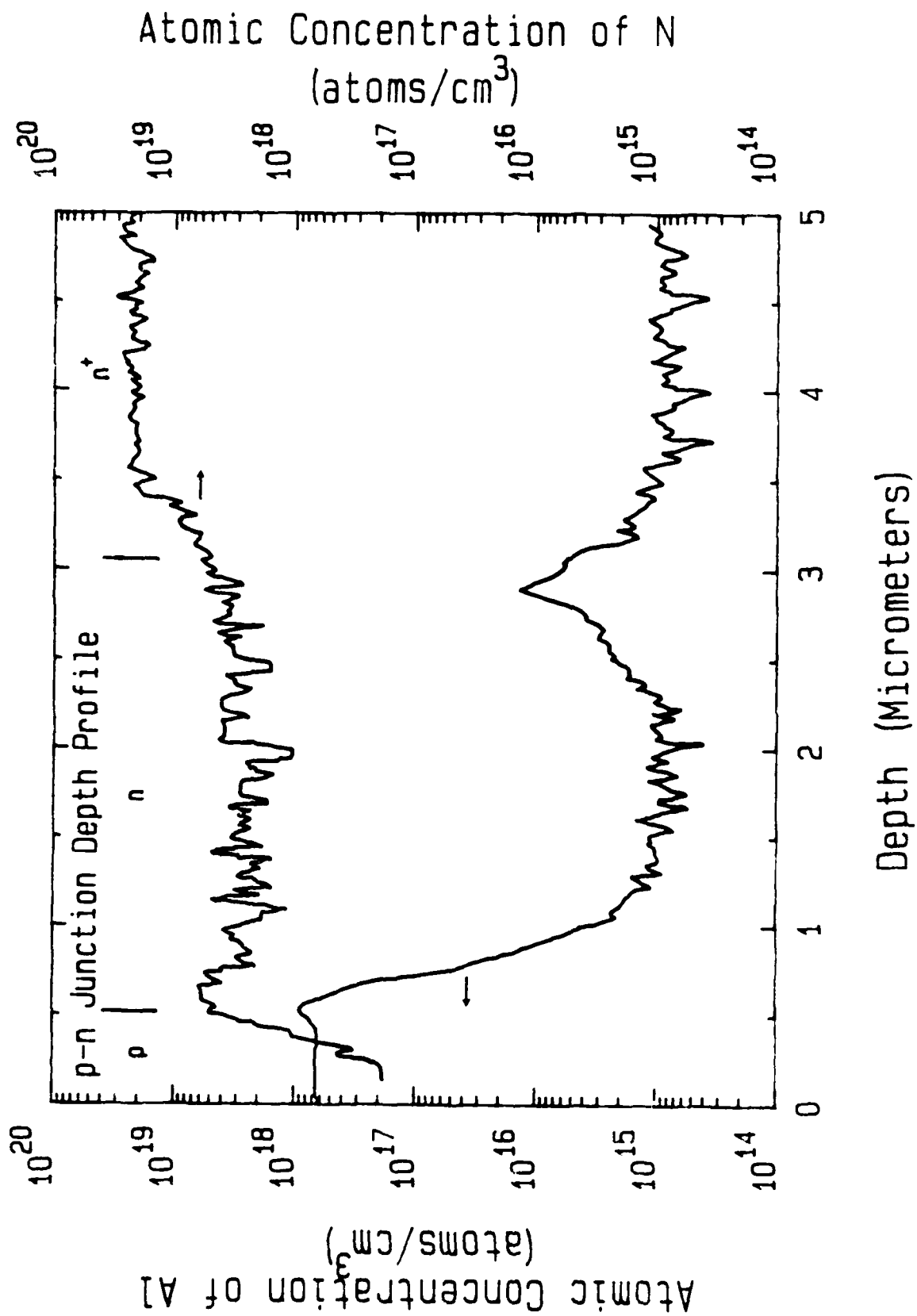


Figure 88. SIMS depth profile of p-n junction which was produced by in situ doping with Al and N.

END

FILMED

5-85

DTIC

A spreading resistance profile of this junction area was obtained at Solid State Measurements, Inc. and is shown in Figure 89. This profile is consistent with the SIMS data. The 0.5 μm thick p-layer shows a resistance of 4×10^7 ohms. This resistance decreases abruptly at the p-n interface to a value of 4×10^3 ohms. The n^+ layer has the resistance of 2×10^3 ohms. Using the ratios of active carrier concentration to doping concentration of 0.1 and 0.01 for N and Al, respectively, noted in the section on in situ doping, the active carrier concentrations in the p, n and n^+ regions would be $7 \times 10^{15}/\text{cm}^3$, $3 \times 10^{17}/\text{cm}^3$ and $2 \times 10^{18}/\text{cm}^3$, respectively.

B. Schottky Diode

A Schottky diode was produced on undoped SiC (n-type carrier concentration = $5 \times 10^{16}/\text{cm}^3$) by the evaporation of Au (rectifying) and the r-f sputtering of Ta-Si (ohmic) contacts. The latter was heated to 1123K for 1.2×10^3 s. The area of the Au dot was $7.9 \times 10^{-5} \text{ cm}^2$. As shown in Figure 90, the leakage current increased with applied voltage; however, actual breakdown did not occur up to - 100 volt (the maximum voltage of our measurement unit). The log current vs forward bias voltage relationship given in Figure 91 shows the value of the diode constant (i.e. slope), n, to be 2.5; the saturation current, I_s is $1.9 \times 10^{-9} \text{ amp/cm}^2$.

The barrier height, ϕ_B , for Au on β -SiC can be calculated from the relation can be calculated from the relation.

$$\phi_B = kT/q \ln \left[\frac{A^* T^2}{I_s} \right]$$

where A^* is the effective Richardson constant [$A^* = (m_n^*/m_0) \cdot A$] and I_s is the saturation current density of the diode. Using as the effective mass of the electron $m^* = 0.25 m_0$ and $A = 120 \text{ amp/cm}^2/\text{K}^2$, the barrier height is calculated to be 0.9 eV.

C. Future Devices

Two additional devices which we wish to make from the SiC films are MESFETs and a mesa structure diode. To fabricate the former, 20 μm , 50 μm and 100 μm channel length masks have been made of which the 50 μm mask is shown in Figure 92. Fabrication of this device is now underway.

Finally, Figure 93 shows the proposed step-by-step procedure to be used in the fabrication of a p^+-n mesa structure diode.

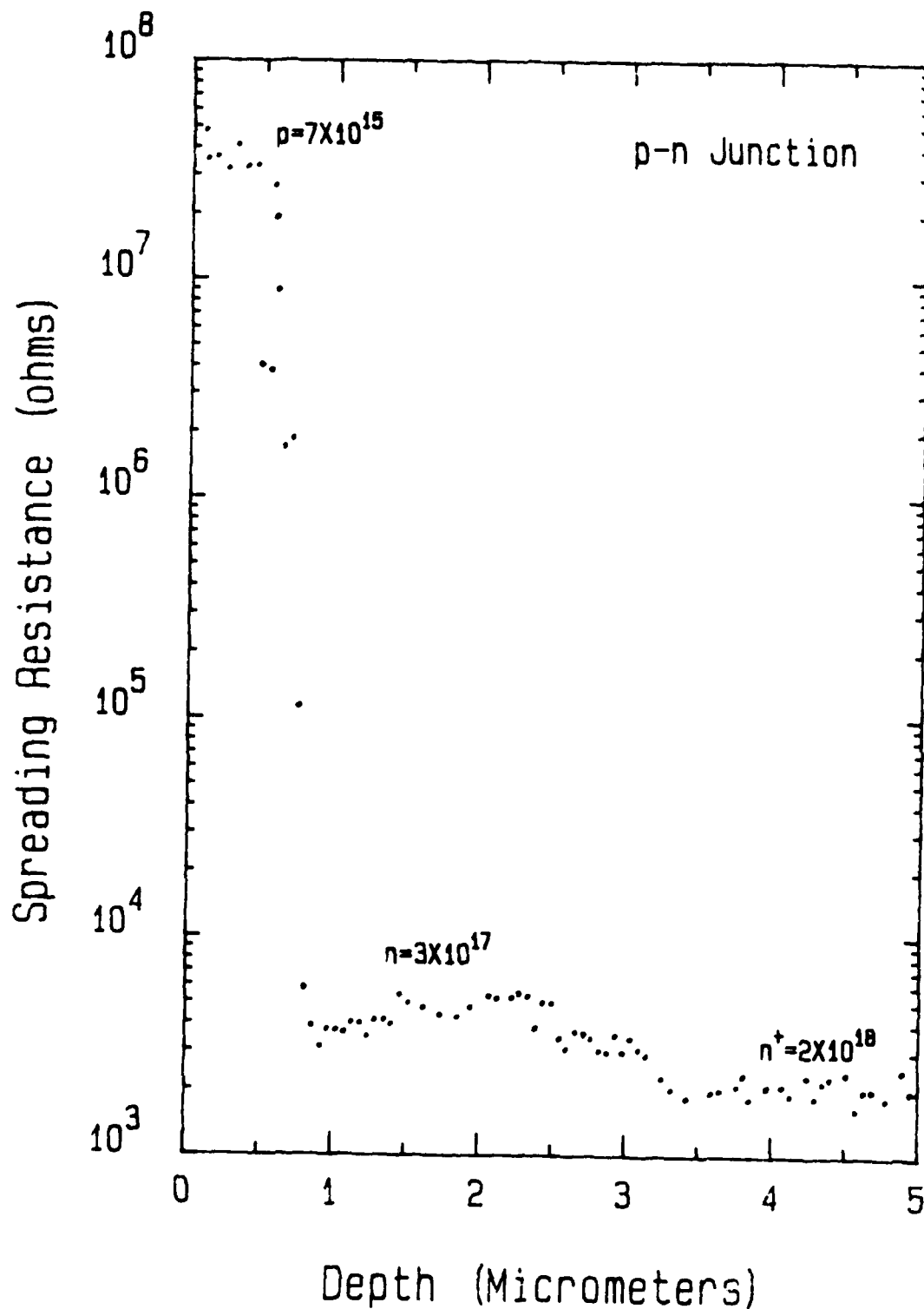


Figure 89. Spreading resistance profile vs depth of p-n junction diode which was doped during growth.

***** GRAPHICS PLOT *****
1028 1

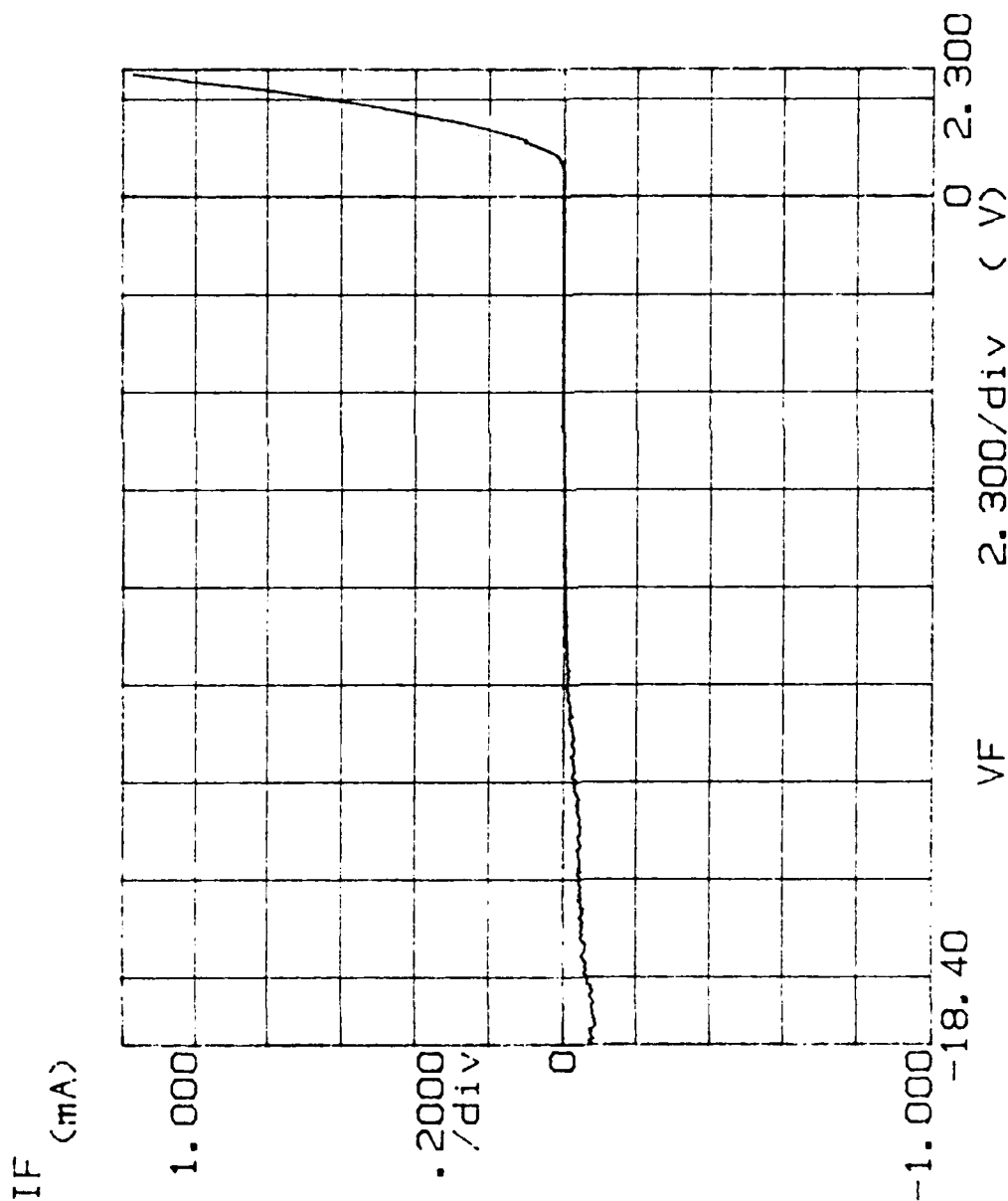


Figure 90. I-V characteristics of a Au- β -SiC Schottky diode. A Ta-Si alloy was used to make the ohmic contact. The area of the junction was $7.9 \times 10^{-5} \text{ cm}^2$.

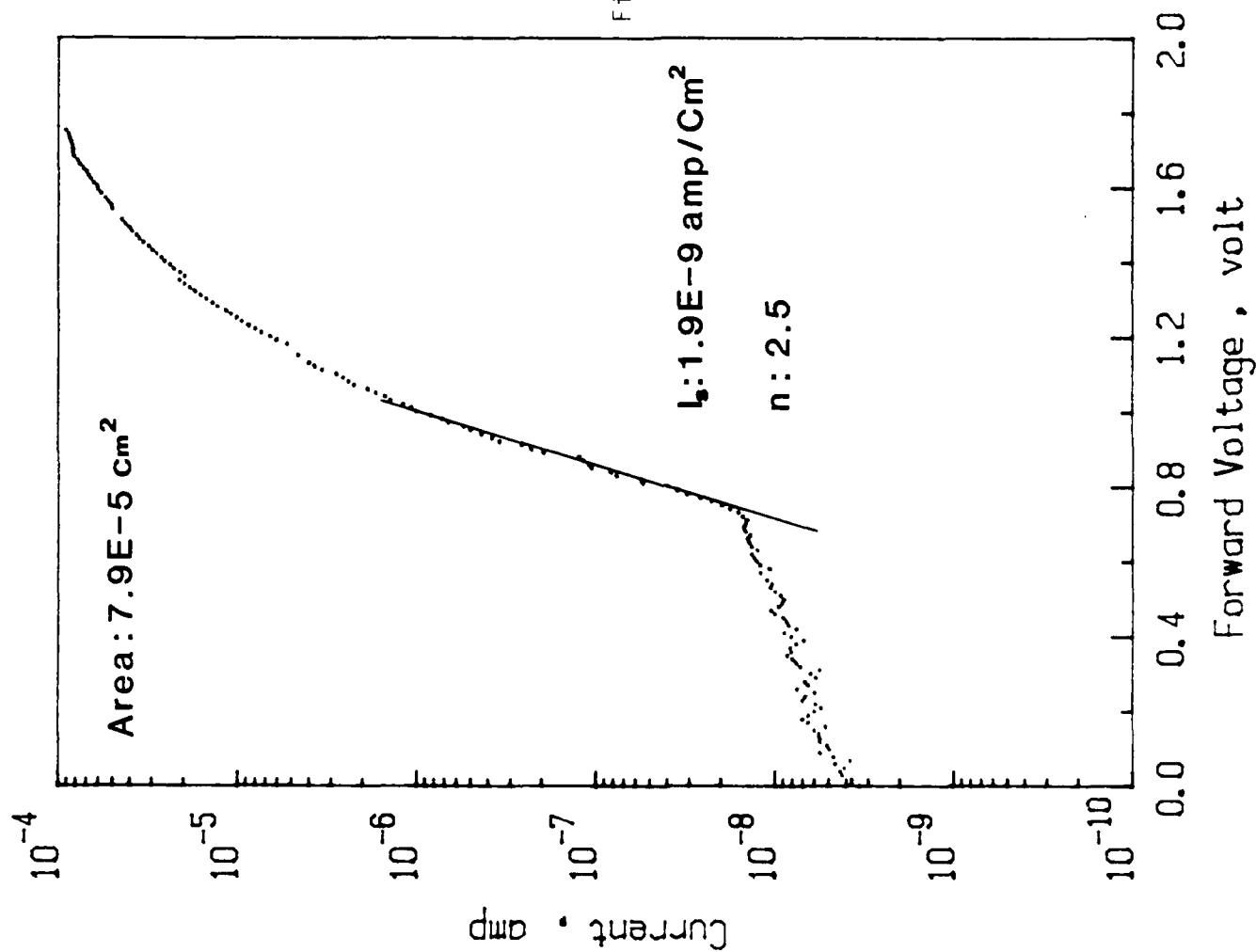


Figure 91.

The log current vs forward bias voltage relationship of a Au-p-SiC diode. The diode constant, n , is 2.5 and saturation current, I_{s2} , is $1.9 \times 10^{-9} \text{ am/cm}^2$.

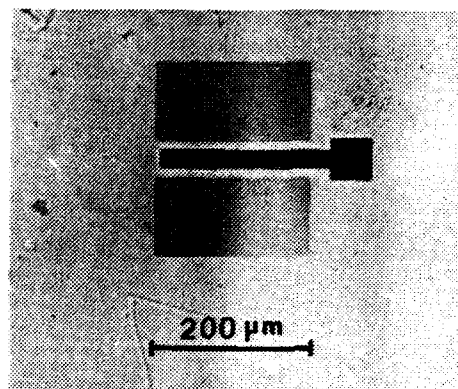
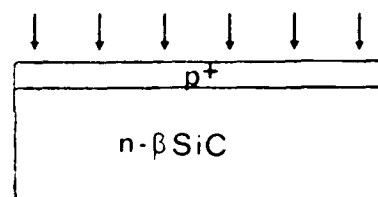
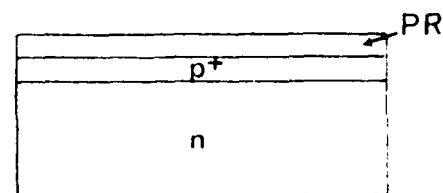


Figure 92. Fifty micron channel length mask for FET fabrication.

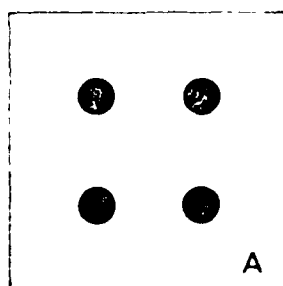
1. Implant p^+ layer in intrinsic substrate



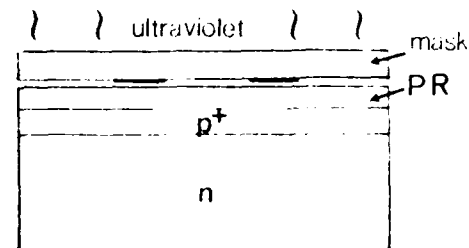
2. Apply layer of positive photoresist (PR)



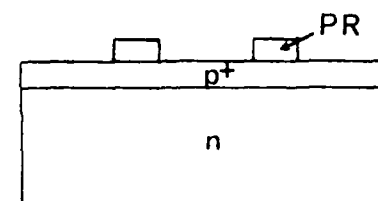
3. Expose PR through mask A



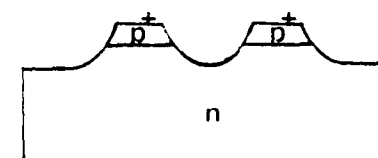
brightfield



4. Remove exposed PR

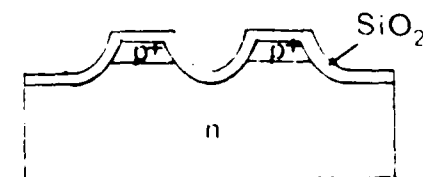


5. Plasma etch to form mesa structure; remove remaining PR

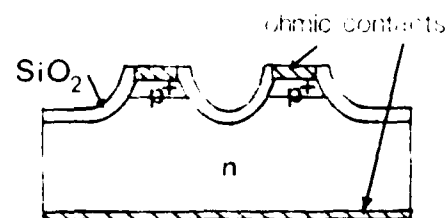


6. Anneal implant - 1800 °C in Ar

7. 1200 °C oxidation



8. Using PR and darkfield version of mask A, repeat steps 2-4; remove remaining PR



9. Apply ohmic contacts

Figure 93. Step wise procedure for the fabrication of a p^+ - n mesa structure diode.

XII. REFERENCES

1. A. I. Kingon, L. J. Lutz, P. Liaw and R. F. Davis, J. Amer. Ceram. Soc. 66, 558 (1983).
2. R. W. Bartlett and R. A. Mueller, Mat. Res. Bull. 4, S341 (1969).
3. N. N. Long, D. S. Nedzvetskii, N. K. Prokofeva and M. B. Reifman, Opt. Spektosk, 29, 388 (1970).
4. S. Nishino, H. Suhara and H. Matsunami, in Extended Abstracts of the 15th Conference on Solid State Devices and Materials, Tokyo, 1983, pp. 317-320.
5. W. von Muench and E. Pettenpaul, J. Electrochem. Soc. 125, 294 (1978).
6. W. H. Sheperd, J. Electrochem. Soc. 115, 541 (1968).
7. H. Reiss, J. Chem. Phys. 21, 1209 (1953).
8. P. Rai-Choudry and E. I. Salkovitz, J. Cryst. Growth 7, 353 (1970).
9. D. R. Stull and H. Prophet, JANAF Thermochemical Tables, Second edition, NSRDS-NBS 37, National Bureau of Standards, USA (1971).
10. J. Bloem, J. Electrochem. Soc. 117, 1397 (1970).
11. D. Olego and M. Cardona, Phys. Rev. B. 25, 3878 (1982).
12. N. I. Rabin and V. I. Kasatochkin, Neorgaincheskie Materialy 14, 1545 (1978).
13. O. J. Marsh in "Silicon Carbide, 1973", R. Marshall, C. Ryan and J. Faust, eds., U. of South Carolina Press, Columbia, S. C. (1974), p. 471.
14. A. Suzuki, Jap. Jour. Appl. Phys. 21, 579 (1982).
15. S. W. Pang, "Dry Etching Induced Damage in Si and GaAs," Solid State Tech. 27, 249 (April 1984).
16. S. Matsui, et al., "Reactive Ion-Beam Etching of Silicon Carbide," Jap. J. of Appl. Phys., Vol. 20, No. 1, January 1981, pp. L38-L40.
17. D. L. Barrett and R. B. Campbell, J. Appl. Phys. 38, 53 (1967).

APPENDIX I

A. Published

1. A. I. Kingon, L. J. Lutz, P. Liaw and R. F. Davis, "Thermodynamic Calculations for the Chemical Vapor Deposition of Silicon Carbide", J. Am. Ceram. Soc.
2. A. I. Kingon, L. J. Lutz and R. F. Davis, "Thermodynamic Calculations for the Chemical Vapor Deposition of Silicon Nitride", J. Am. Ceram. Soc.
3. A. I. Kingon and R. F. Davis, "The Application of Thermodynamic Calculations to Chemical Vapor Deposition Processes", Materials Science Research, Vol. 17, Plenum, New York, 1984, 317-328.
4. P. Liaw and R. F. Davis, "Thermal Stresses in Heteroepitaxial Beta Silicon Carbide Thin Films Grown on Silicon Substrates", J. Electrochem. Soc. 95, 2145 (1984).

B. Accepted for Publication

1. P. Liaw and R. F. Davis, "Epitaxial Growth and Characterization of β -SiC Thin Films", Accepted for publication by the Journal of the Electrochemical Society.
2. H. J. Kim, X. B. Cox, R. Linton and R. F. Davis, "Growth and Characterization of Silicon Surfaces Reacted with C_2H_4 ", Submitted for publication to Thin Solid Films.
3. C. H. Carter, Jr., J. Bentley and Robert F. Davis, "The Occurrence of Defects in Silicon Carbide as a Result of Processing Mode". Presented at the Materials Research Society Symposium on Defect Properties and Processing of High Technology Non-Metallic Materials", Boston, MA, 1983. To be published in the Proceedings of the Symposium.
4. J. M. Williams, B. R. Appleton, C. J. McHargue, P. S. Sklad, G. M. Begun, P. Angelini and R. F. Davis, "Ion Implantation Effects in SiC". Presented at the International Conference on Ion Beam Modification of Materials, Cornell University, Ithaca, NY, 1984. To be published in the Proceedings of the Conference.
5. K. L. More, J. Ryu, C. H. Carter, Jr., J. Bentley and R. F. Davis, "Defects in Silicon Carbide: Their Electrical and Physical Consequences". Presented at the International Conf. on Defects in Insulating Crystals", University of Utah, Salt Lake City, 1984. To be published in the Proceedings of the Symposium.

APPENDIX II

List of all Reports for the Period February 1, 1982 - January 31, 1985

<u>Type of Report</u>	<u>Period Covered by Report</u>	<u>Date Issued</u>
A. Annual Letter Report	2/1/82 - 8/31/82	8/31/82
B. Annual Letter Report	9/1/82 - 3/31/83	3/31/83
C. Annual Technical Report	9/1/82 - 8/31/83	8/31/83
D. Annual Letter Report	9/1/83 - 3/31/84	3/31/84
E. Annual Technical Report	9/1/83 - 8/31/84	8/31/84
F. Final Technical Report	2/1/82 - 1/31/85	1/31/85

APPENDIX III

DISTRIBUTION LIST - FINAL TECHNICAL REPORT

CONTRACT N00014-82-K-0182

<u>Address</u>	<u>No. of Copies</u>
Dr . Max Yoder Office of Naval Research Electronics Program - Code 414 800 North Quincy Street Arlington, VA 22217	2
Ms. Nancy S. McHan ONR Resident Representative Georgia Institute of Technology 214 O'Keefe Building Atlanta, GA 30332	2
Director, Naval Research Laboratory ATTN: Code 2627 Washington, DC 20375	7
Defense Technial Information Center Bldg. 5 Cameron Station Alexandria, Virginia 22314	14
ONR Branch Office 536 South Clark Street Room 286 Chicago, IL 60605	2
Dr. J. Anthony Powell NASA Lewis 2100 Brookpark Rd. Cleveland, OH 44135	1
Dr. Ray Kaplan Code 6834 Department of the Navy Naval Research Laboratory Washington, DC 20375	1

END

FILMED

5-85

DTIC